UNIVERSITY OF CALIFORNIA

Santa Barbara

Understanding and correlating heteroatom distributions in zeolite frameworks with catalytic activity

A dissertation submitted in partial satisfaction of the

requirements for the degree Doctor of Philosophy

in Chemical Engineering

by

Michael Brandon Schmithorst

Committee in charge:

Professor Bradley F. Chmelka, Chair

Professor Phillip Christopher

Professor Eric McFarland

Professor Galen Stucky

December 2023

The dissertation of Michael Brandon Schmithorst is approved.

Phillip Christopher

Eric McFarland

Galen Stucky

Bradley F. Chmelka, Committee Chair

December 2023

Understanding and correlating heteroatom distributions in zeolite frameworks with catalytic activity

Michael Brandon Schmithorst

ACKNOWLEDGEMENTS

I have grown tremendously as a scientist over the past five years of my Ph.D., and that is in large part thanks to the people who have helped me and supported me along the way. First, I would like to thank my advisor, Professor Brad Chmelka for pushing me to be the best version of myself as a scientist throughout my Ph.D. Thanks to Brad, I have become a more thoughtful researcher, a better writer, and a better speaker over the course of my Ph.D. I appreciate the opportunity to work on such interesting projects and also how Brad's extensive connections gave me the opportunity to collaborate with a broad range of industrial and academic partners.

Additionally, I would like to thank my committee members Prof. Phil Christopher, Prof. Eric McFarland, and Prof. Galen Stucky for their guidance over the years in my annual committee meetings. Suggestions from Phil, Eric, and Galen have all led to important considerations of how I have designed experiments and thought about results. I would also like to thank Phil and Eric for allowing me to use equipment in their labs at different points in my Ph.D. to aid with my research.

I have many collaborators to thank for their help over the years. First, I would like to thank my colleagues Dr. Subramanian Prasad, Dr. Ahmad Moini, Dr. Vivek Vattipalli, Dr. Karsten Seidel, Dr. Takayaki Iida, and Dr. Rui Zhang for their support. In particular, I need to acknowledge Prasad's role in my Ph.D.—at times he felt like a fifth committee member, and I appreciate all of his advice. Additionally, I appreciate the opportunity to work on a project as part of the BASF California Research Alliance and meet many interesting scientists at semiannual review meetings.

I also have many academic collaborators to thank. I am grateful to Prof. Eva Olsson and Dr. Lunjie Zeng for hosting me for two months at Chalmers University of Technology in Gothenburg, Sweden and giving me access to their labs. I would like to thank Evgeniia Ikonnikova and Dr. Tom Willhammar from Stockholm University and Bryan Cruz Delgado and Prof. Raj Gounder from Purdue University for their contributions to the copper chabazite project. I'd also like to thank Danyu Wang and Prof. Michael Tsapatsis at Johns Hopkins University, Sopuruchukwu Ezenwa and Prof. Raj Gounder from Purdue University, and Phong Nguyen, Prof. Rachel Segalman, and Prof. Michael Chabinyc from UC Santa Barbara for giving me the opportunity to collaborate with them on their work.

There are many people at UC Santa Barbara who have helped me in less formal ways over the course of my Ph.D. I'd like to thank all of the members of the Chmelka group that I have overlapped with: Prof. Zachariah Berkson, Dr. Nathan Prisco, Dr. Shona Becwar, Dr. Tsatsral Battsengel, Dr. Maxwell Berkow, Dr. Philipp Selter, Dr. Federica Boscaro, Dr. Arun Patel, Matthew Lertola, Anna Pischer, Ramya Ragunathan, Hosu Gwak, Alyssa McNarney, and Victoria Diaz. In particular, I want to acknowledge Philipp, Zach, Nathan, and Tsatsa for research guidance, Max and Shona for emotional support, and Anna and Alyssa for giving me confidence my work will be continued in good hands. I'd like to thank Dr. Chithra Asokan, Dr. Gregory Zakem, and Jordan Finzel for advice on building a reactor, and Dr. Raynald Giovine for NMR knowledge. I'd also like to thank all the research staff at UCSB, particularly Jaya Nolt and Dr. Jerry Hu.

I'd like to thank my friends and family for all their love and support over the past five years, both from near and afar. Lastly, I'd like to thank Sally Jiao, without whom none of this would have been possible.

VITA OF MICHAEL BRANDON SCHMITHORST
December 2023

PhD Candidate in Chemical Engineering

SUMMARY

Chemical engineering PhD candidate experienced in academic research with excellent problem-solving and technical communication skills. Expert in material characterization and catalytic performance testing of heterogeneous zeolite catalysts.

EDUCATION

Doctor of Philosophy in Chemical Engineering **2018 – present**
University of California, Santa Barbara, Santa Barbara, CA, USA grad est. Dec. 2023
Thesis: *Understanding and correlating heteroatom distributions in zeolite frameworks with catalytic activity*
Advisor: Professor Bradley Chmelka, PhD

Bachelor of Science in Engineering in Chemical Engineering
2014 – 2018
University of South Carolina, Columbia, South Carolina, USA
GPA: 4.0
USC Honors College
Graduated *summa cum laude*
Tau Beta Pi SC Beta Chapter Outreach Chair

RELEVANT WORK EXPERIENCE

ACADEMIC RESEARCH
Graduate Student Researcher, Chmelka Research Group
UC Santa Barbara, Santa Barbara, CA
2018 – present
Performed research on zeolite catalysts for automotive pollution mitigation and hydrocarbon conversion, with a focus on understanding how atomic-level features of these catalysts and their interactions with adsorbates influence reaction properties using scanning transmission electron microscopy, advanced solid-state NMR and other spectroscopic techniques. Collaborated with scientists from industry sponsors and within academia on several projects. Mentored one UC Santa Barbara undergraduate student on projects receiving multiple funded undergraduate research awards.

Undergraduate Researcher, Ritter Research Group
University of South Carolina, Columbia, SC 2017 – 2018
Investigated the effectiveness of reflux steps on separation efficiency in separation of CO_2 and N_2 by rapid pressure swing adsorption. Modeled fundamental properties of the investigated pressure swing adsorption system. Presented results at 2017 AIChE Annual Meeting (awarded 3rd place poster).

Undergraduate Researcher, Center for Strategic Approaches to the Generation of Electricity
University of South Carolina, Columbia, SC 2015 – 2017
Designed procedure for additive manufacturing of materials with embedded nanoparticles for monitoring residual stress. Built a low-cost 3D printer made of recycled materials for use in Introduction to Chemical Engineering class.

TEACHING AND MENTORING

Graduate Scholars Program Mentor, Graduate Division
UC Santa Barbara, Santa Barbara, CA 2021 – 2023
Mentored small groups of first-year STEM PhD students from underrepresented backgrounds and provided advice on excelling in graduate school and referrals to campus resources for graduate students.

Teaching Assistant, Department of Chemical Engineering
UC Santa Barbara, Santa Barbara, CA 2019 – 2021
Worked as a teaching assistant for Separations, Reaction Engineering, and Introduction to Chemical Engineering. Designed and delivered several lectures and review sessions for Separations and Reaction Engineering. Awarded Outstanding Teaching Assistant in Chemical Engineering for 2020-21.

Undergraduate Teaching Assistant, Department of Chemical Engineering
University of South Carolina, Columbia, SC 2016 – 2018
Worked as a teaching assistant for undergraduate classes on fluid mechanics and unit operations. Assisted students with lab work and graded homework and lab reports.

Peer Tutor, Student Success Center
University of South Carolina, Columbia, SC 2016 – 2017
Tutored students in lower division core STEM classes including general chemistry, introductory physics, organic chemistry, and a variety of chemical engineering classes.

PUBLICATIONS

1. Ezenwa, Castro, Hoffman, Locht, Attebery, Jan, Schmithorst, Chmelka, Hibbitts, Gounder. Synthetic Placement of Active Sites in Zeolites for Selective Toluene Methylation to para-Xylene. *Submitted.* **2023.**
2. Berkow, Gwak, Idso, Schmithorst, Rhodes, Price, Gianola, Han, Chmelka. Co-assembly of functionally-active proteorhodopsin membrane protein molecules in mesostructured silica-surfactant films. *Chemistry of Materials, 35 (20), 8502-8516*. **2023.**
3. Schmithorst, Prasad, Moini, Chmelka. Direct detection of paired aluminum heteroatoms in chabazite zeolite catalysts and their significance for methanol dehydration reactivity. *Journal of the American Chemical Society, 143 (33), 18215-18220*. **2023.**
4. Wang, Schmithorst, Li, Luo, Park, Xu, Bukowski, Chmelka, Kokkoli, Tsapatsis. Enantioselective catalysts based on metal-organic framework supported nucleotides. *Microporous and Mesoporous Materials 360, 112703.* **2023**.

5. Nguyen, Schmithorst, Mates, Segalman, Chabinyc. Diffusion of Bronsted acidic dopants in conjugated polymers. *Journal of Materials Chemistry C 11, 7462-7470*. **2023.**
6. Selter, Schmithorst, Chmelka. Hopping dynamics and diffusion of atoms, molecules, and ions in nanoporous solids by exchange NMR spectroscopy. *Adsorption 27 (5), 857-874.* **2021.**

MANUSCRIPTS IN PREPARATION

1. Schmithorst, Prasad, Moini, Chmelka, Effects of framework Al distributions on selective catalytic reduction of NO_x by Cu-chabazite. Manuscript in preparation for *Journal of the American Chemical Society*
2. Schmithorst, Berkson, Stoev, Chmelka. Role of diverse acid sites on the cracking activity and deactivation of zeolite H^+-USY. Manuscript in preparation for *Angewandte Chemie*.

PATENTS and INVENTIONS

1. Schmithorst, Prasad, Moini, Chmelka, Vattipalli. Zeolite catalysts with paired heteroatoms and methods thereof. *U.S. Application No. 63/263,599*. **2021.**

AWARDS

1. 3rd place, Best Oral Presentation Challenge, BASF California Research Alliance Semiannual Review, Fall 2023.
2. *Visiting Scholar Fellowship*, funded by the Cooperative for Advanced Materials in Energy-Related Applications (CAMERA) grant, International Research Experiences for Students (IRES) program, **National Science Foundation**. Chalmers University of Technology, Gothenburg, Sweden, 2022.
3. *Outstanding Teaching Assistant in Chemical Engineering*. Department of Chemical Engineering, UC Santa Barbara, 2021.
4. *Undergraduate Awards:* 2018 Outstanding Senior in Chemical Engineering, Science Undergraduate Research Fellowship recipient, National Merit Scholar, Tau Beta Pi Record Scholarship recipient, USC President's List (2014-2018), 3rd place in Separations II in Student Poster Competition at 2017 AIChE National Conference

CONFERENCE PRESENTATIONS

ORAL PRESENTATIONS

1. BASF California Research Alliance Semiannual Review, Santa Barbara, CA. *Atomic-level understanding of deNO$_x$ performance & deactivation of Cu-CHA catalysts*. 18 October 2023. (**3rd place talk**)
2. UCSB-Chalmers Colloquium on Materials Science and Engineering, Santa Barbara, CA. *Understanding the adsorption and deNO$_x$ properties of zeolite catalysts at an atomic level*. 31 January 2023.
3. American Institute of Chemical Engineers Annual Meeting, Phoenix, AZ. *Distributions of Al atoms in chabazite zeolite frameworks & their effects on catalytic reaction properties*. 13 November 2022.
4. BASF California Research Alliance Semiannual Review, Santa Barbara, CA. *Distributions of Al atoms in chabazite zeolite frameworks & their effects on catalytic reaction properties*. 3 November 2022.

5. 15th Annual Clorox-Amgen Graduate Student Symposium, Santa Barbara, CA. *Distributions of Al atoms in chabazite zeolite frameworks & their effects on catalytic reaction properties*. 15 September 2022.
6. International Zeolite Conference, Valencia, ES. *Distributions of Al atoms in chabazite zeolite frameworks & their effects on catalytic reaction properties*. 5 July 2022.
7. BASF California Research Alliance Semiannual Review, Berkeley, CA. *Distributions of Al atoms in chabazite zeolite frameworks & their effects on catalytic reaction properties*. 4 May 2022.
8. American Institute of Chemical Engineers Annual Meeting, Boston, MA. *Distributions of Al atoms in chabazite zeolite frameworks & their effects on catalytic reaction properties*. 11 November 2021.
9. BASF California Research Alliance Semiannual Review, Berkeley, CA. *Molecular compositions and structures of heteroatom and cation-exchange sites in zeolite catalysis by ssNMR.* 25 October 2019.
10. UCSB 1st year Research Presentations Symposium, Santa Barbara, CA. *Understanding and modifying the atomic-level surface chemistry of zeolite catalysts.* 24 September 2019.

POSTERS

1. BASF North American Research Forum, Wyandotte, MI. Direct evidence of paired framework heteroatoms in a zeolite and their significance for catalytic reactivity. 9 May 2023.
2. Experimental NMR Conference, Pacific Grove, CA. 2D *J*- and dipolar-mediated correlation NMR techniques for structural characterization of dilute heteroatom sites in zeolite catalysts. 17 April 2023.
3. BASF California Research Alliance Semiannual Review, Virtual. *The effects of metal cations on the adsorption, reaction, and stability of zeolite catalysts*. 28 April 2021.
4. BASF California Research Alliance Semiannual Review, Virtual. *The effects of metal cations on the adsorption, reaction, and stability of zeolite catalysts*. 5 November 2020.
5. AICHE Student Meeting Student Poster Competition, Minneapolis, MN. *Separation of CO_2 and N_2 by rapid PSA using 13X zeolite and a dual reflux cycle*. 30 October 2017. (**3rd place poster**)

ABSTRACT

Understanding and correlating heteroatom distributions in zeolite frameworks with catalytic activity

by

Michael Brandon Schmithorst

Zeolites are a class of crystalline, nanoporous aluminosilicates used for many applications, including water softening, gas separations, hydrocarbon conversions, and a wide range of other reaction chemistries. The diverse applications of zeolites arise from local negative charges introduced by four-coordinate aluminum heteroatoms in the zeolite framework, which are charge-balanced by exchangeable cations in the zeolite pores. Exchanging in different cations enables the many different industrial applications of zeolites. Thus, understanding and controlling the complicated distributions of aluminum heteroatoms in the zeolite framework enables the catalytic reaction properties to be modified and improved through manipulation of cation locations and distributions. However, characterization of such distributions and their direct influences on catalysis is challenging. In this dissertation, I demonstrate how advanced characterization techniques provide unprecedented insights on aluminum distributions, in both zeolite nanopores and hierarchical zeolites with multiple pore sizes.

Local aluminum configurations in zeolite nanopores are hypothesized to affect the catalytic performance of the small-pore zeolite chabazite, which is used in its Cu^{2+}-exchanged

form industrially as a $deNO_x$ catalyst in diesel exhaust systems. It has been proposed that closely paired aluminum configurations (separated by 1-2 bridging Si-O-Si) are desirable. However, the non-stoichiometric and non-periodic ordering of aluminum in the zeolite framework makes characterizing these aluminum pairing distributions in zeolites intractable by many characterization techniques. By using advanced solid-state nuclear magnetic resonance spectroscopy (NMR) analyses, two industrially relevant chabazite catalysts are shown to have different relative amounts of paired-framework aluminum atoms that are not detected by conventional methods. The differences in aluminum pairing correlate with differences in catalytic activity and help to guide industrial zeolite syntheses for improved Cu-chabazite $deNO_x$ catalysts. In addition, effects of hydrothermal aging on Cu and Al distributions in a Cu-CHA zeolite are investigated by advanced electron microscopy and NMR techniques. Advanced NMR techniques show that the distributions of and interactions between adsorbed species under $deNO_x$ reaction conditions evolve due to hydrothermal treatment. In addition, it is shown that distributions of paired aluminum species in the zeolite framework evolve as a result of hydrothermal treatment.

In addition to local aluminum configurations within nanopores, catalytic activity can be influenced by aluminum distributions between different pore sizes. Commercial H^+-exchanged zeolite Y (H^+-Y), a large-pore catalyst, has been used as hydrocarbon cracking catalysts for decades, and is a classic example of a zeolite catalyst with complicated distributions of aluminum. The industrial form of the H^+-Y catalyst is modified to create mesoporous defects in the zeolite crystallites, which improve the mass transport of large hydrocarbon reactants to active sites and directly expose some framework aluminum, and thus active sites, to the mesopores. To better understand the role of mesopore active sites in cracking

chemistry, the mesopore sites on a H^+-Y catalyst were selectively passivated and compared with an otherwise identical unpassivated catalyst for hexane cracking activity. Passivation results in a decrease in initial activity but overall reduction in amount of coke formation on the catalyst. Solid-state NMR measurements show that the passivation results in a modification of mesopore defect acid sites, and additionally show that bulkier polyaromatic hydrocarbon species form on the unmodified catalyst. Overall, the results discussed in this dissertation will aid in the design of zeolite catalysts with more desirable distributions of aluminum heteroatoms and reaction properties.

TABLE OF CONTENTS

Chapter 1

Introduction and overview

Background

Heterogeneous catalysis, the conversion of gaseous or liquid phase compounds over a solid catalyst, is a ubiquitous process in the modern chemical industry.[1] The combustion fuels we use for travel, the polymers and plastics that are used in many consumer products, and even many of the active compounds used in pharmaceuticals are all derived from petroleum by a series of hydrocarbon conversion reactions over heterogeneous catalysts.[2] In addition, heterogeneous catalysts are used in environmental pollution controls to control emissions of byproducts including carbon monoxide, hydrocarbons, and nitrogen and sulfur oxides which are associated with negative health and environmental outcomes.[3] As we more fully understand the effects that humanity's emissions have on the climate, it has become evident that it is necessary to both shift to more sustainable sources of chemical precursors and improve our environmental emission controls.[4] Both of these challenges require the development of new materials for heterogeneous catalysis.

Zeolites are a class of crystalline, microporous aluminosilicates with a wide variety of commercial uses in the chemical industry.[5] Though naturally occurring, various synthetic zeolites have been made since the first half of the 20th century and have been commercialized since the 1950s.[6] The uses of synthetic zeolites include cation exchange in water softening applications, adsorbents in gas separations such as oxygen production from air, and as catalysts in a variety of reaction chemistries including the cracking of bulky hydrocarbons into useful chemical precursors.[7–9] The wide range of applications for zeolites arise from the tunability of

nanoscale features to the zeolite structure—specifically the variety of zeolite pore structures available and the distributions of aluminum heteroatoms in the aluminosilicate framework.

To date, over 200 unique zeolite crystal structures have successfully been synthesized.[10] These different zeolite framework types have one-, two-, or three-dimensional pore structures of different diameters connecting internal voids that vary in size and shape depending on framework type. As most of these pores and voids are less than one nanometer in diameter, they inhibit the diffusion of small gaseous species. This results in a size and shape selectivity, where only certain types of molecules can diffuse in and out of the pores, or the diffusivities of similarly sized molecules are rendered drastically different.[11] In addition, confinement effects from van der Waals forces in the zeolite pores can selectively stabilize certain transition states in complex reaction pathways, altering selectivity and activity.[12] As an example, it has been observed that methylation of olefins proceeds at different rates over different zeolite pore topologies due to confinement effects.[13] While over 200 zeolite pore topologies have been identified, very few are commercially synthesized and deployed due to complex and expensive syntheses.[14] However, this relatively small number of pore topologies provides enough diversity to adequately tune adsorption and reaction properties.

In addition to pore topology, the distribution of active adsorption and reaction sites in zeolites is an important parameter to control and tune activity. Active adsorption and reaction sites in zeolites typically exist as species hosted in the pores of the zeolite. While these active sites can be small metal clusters constrained and stabilized by van der Waals interactions with the zeolite pores, more commonly they are single atom cations.[15] These cations charge balance local negative charges on the zeolite framework, which result from the inclusion of four-coordinate aluminum atoms in the framework. Strong acid sites can be introduced to a zeolite

by charge-balancing framework aluminum with H^+ cations. H^+-zeolites are used for a variety of hydrocarbon conversion reactions.[16] A wide variety of metal cations can also be exchanged into the zeolite pores to access different reaction chemistries and adsorption selectivities. In the H^+-form, faujasite-framework-type zeolites have long been used as cracking catalysts.[9] When exchanged with Li^+, the same framework type is industrially used for air separations into N_2 and O_2 based on the higher affinity of Li^+ for N_2 adsorption.[8] These different cations enable the wide range of applications for zeolites and make them suitable for further development to respond to demands for different reaction chemistries and conditions.

As aluminum heteroatoms charge balance cations that act as active sites for catalysis in zeolites, controlling the distributions of these aluminum heteroatoms may provide an additional lever to control reaction properties. Historically, this has been done by varying the total aluminum content in a zeolite to vary the average distance between sites. In some frameworks, such as the medium-pore zeolite ZSM-5 (MFI), this can be done synthetically.[17] In other frameworks, such as Zeolite Y (FAU), different aluminum contents are accessed by post-synthetic leaching of aluminum from the framework.[18] While these methods are suitable for providing some control to catalytic activity, it is desirable to control aluminum distributions at a constant bulk Si/Al ratio to better fine tune catalytic properties.[19] This can be accomplished in two ways. For one, selective formation of closely proximate aluminum species may enable exchange of divalent metal cations into a zeolite pore structure or enable reaction chemistries that rely on multiple Bronsted acid sites.[20] In addition, selective insertion of aluminum at specific T-sites in zeolites with multiple distinct tetrahedral aluminum and silicon sites may help to tune activity.[21] However, controlled syntheses to direct aluminum insertion in zeolite frameworks have remained elusive until recently.

Synthetic zeolites are made by combining silicon and aluminum sources in a highly caustic solution under hydrothermal conditions. Structure-directing agents (SDA), both in the form of inorganic cations and organic molecules with cationic functional groups, control the type of zeolite framework formed by stabilizing the pore structure during synthesis.[22] In addition, the SDA cations charge balance the aluminum inserted into the zeolite framework, and thus exert some control over the aluminum distributions in synthetic zeolites.[21] Previous work has indicated that usage of different organic structure-directing agents in zeolite synthesis alters the locations of aluminum in the framework based on observed differences in adsorbed probe molecules.[23] In addition, recent computational work has shown that varying the organic structure-directing agent used in synthesis results in significantly different free energy landscapes for aluminum insertion into different sites.[24–26] However, confidently characterizing these distributions in synthesized zeolites has been challenging.

As previously mentioned, zeolites are often modified post-synthesis to change aluminum distributions. This is commonly done by treatment with high-temperature water vapor.[27] The four-coordinate aluminum in the zeolite framework is susceptible to hydrolysis from the framework under these conditions.[28] The removal of aluminum from the framework can result in local collapse of the crystal structure.[29] As a result, these hydrothermally treated zeolites have complex distributions of micropores and mesopores, along with distributions of crystalline framework and extraframework aluminum that both can impart acidity to the zeolite. Understanding the influences of these complex distributions of pore size and acid site location and strength on catalyst activity has been challenging.

Solid-state nuclear magnetic resonance spectroscopy (NMR) is a technique that is ideally suited for studying these complex distributions of aluminum heteroatoms and

adsorption sites in zeolites.[30] In solid-state NMR, nuclear magnetic spins aligned in a magnetic field are perturbed from equilibrium by radiofrequency pulses applied at specific frequencies. The resulting decay of the perturbed nuclear magnetic vector back to equilibrium can be detected, resulting in a free induction decay pattern which can be Fourier transformed to produce frequency-domain information. As each nuclear isotope precesses in a magnetic field at a different frequency, the information obtained from NMR is nucleus-specific, which aids in deciphering chemical information from materials with complex distributions of ordered and disordered species. NMR is sensitive to the electron structure of the detected nuclei, and thus the same nucleus in a different chemical environment produces a distinct frequency, known as its chemical shift.[31,32] This chemical shift frequency is commonly reported in units of Hz/MHZ or parts-per-million (ppm). Several nuclei relevant for zeolite catalysts, including ^{1}H (100% natural abundance), ^{27}Al (100% natural abundance), ^{29}Si (4.7% natural abundance), ^{13}C (1.1% natural abundance, and ^{15}N (0.3% natural abundance), making solid-state NMR in ideal technique to probe the local chemical environments of zeolite framework moieties and adsorbate species, though some nuclei require enrichment.

In addition to basic solid-state NMR experiments providing information on local chemical environments, advanced NMR techniques can be used to correlate local chemical environments from proximate species between the same nucleus in different chemical environments or different nuclei.[33–35] These techniques have long been used in solution-state NMR to aid in solving the structures of proteins and other biomolecules.[36] Over the last couple of decades, advances to solid-state NMR pulse sequences have enabled similar analyses on solids, even in systems with dilute nuclei or spin systems involving quadrupolar nuclei, such as ^{27}Al.[37–39] In addition, advances in NMR signal enhancement from techniques including

dynamic nuclear polarization (DNP) have facilitated the detection of very dilute adsorbate species on heterogeneous surfaces.[40,41] In zeolites, these multinuclear NMR techniques have been used to confidently detect and assign framework moieties associated with different types of adsorption environments, and to examine the types of adsorbed species present in zeolites and their associations with different framework moieties.[30,42–49] In addition, advanced NMR techniques have also been used to track rates of exchange and diffusion of adsorbates within zeolites and other porous solids.[50–54]

In this dissertation, a series of studies that advance the atomic-level understanding of differences in adsorption and reaction properties in industrially-relevant zeolite materials are presented. Advanced solid-state NMR techniques are used to understand differences in distributions of aluminum heteroatoms in zeolite frameworks—both local distributions in crystalline sites and between micropore and mesopore sites in zeolites that have been subjected to hydrothermal treatment. These atomic-level observations are correlated with bulk reaction and adsorption properties to understand how different structures may influence catalytic activity. In addition, complementary state-of-the-art characterization techniques including high-resolution scanning transmission electron microscopy and 3D electron diffraction crystallography are used to better explain differences in reaction properties between zeolites. These analyses are applied to zeolites used industrially as pollution abatement catalysts and as hydrocarbon cracking catalysts. In addition, many of the structural characterization techniques demonstrated are anticipated to be transferrable to other zeolites, potentially enabling better understanding of atomic-level origins of catalytic properties in a wide variety of systems. The rest of the introduction chapter consists of brief summaries of the remaining chapters of this dissertation.

Thesis Overview

Chapter 2. Direct detection of paired aluminum heteroatoms in chabazite zeolite catalysts and their significance for methanol dehydration reactivity

Distributions of aluminum heteroatoms in a zeolite framework influence the locations of exchangeable cations that account for the diverse adsorption and reaction properties of zeolite catalysts. For the small pore zeolite chabazite, two different reaction have been suggested to depend on the amounts of paired configurations of aluminum atoms separated by one or two tetrahedrally-coordinated silicon atoms. In the H^+-exchanged form of chabazite, these closely paired aluminum atoms have been suggested to enhance the rates of methanol and ethanol dehydration reactions.[55–57] In the Cu-exchanged form, chabazite is used industrially as a deNO_x catalyst.[58,59] It has been proposed that Cu^{2+} cations charge-balanced by two proximate framework aluminum species have different reaction properties than those charge-balanced by only one framework aluminum.[60,61] While the effects of these closely paired aluminum species on reaction properties is clear, accurately quantifying these paired aluminum configurations is challenging due to the non-stoichiometric compositions and non-periodic distributions of aluminum atoms in the zeolite framework. The typical method used in the literature to quantify these distributions is titration by divalent metal cations, commonly Co^{2+}.[62–64] However, computational studies have come to different conclusions about which types of sites these cations titrate to, making interpretation of this data challenging.[65,66] Here, for two H^+-chabazite with similar bulk aluminum contents and Co^{2+} exchange levels, but different methanol dehydration activity, a series of 2D NMR experiments are demonstrated to detect differences in levels of aluminum pairing configurations. 2D ^{27}Al-^{29}Si *J*-mediated NMR spectra, sensitive to the local environments of covalently bonded ^{27}Al-O-^{29}Si moieties,

unambiguously show differences in levels of second-nearest-neighbor (^{27}Al-O-^{29}Si-O-^{27}Al, 2NN) paired aluminum configurations. In addition, 2D ^{29}Si-^{29}Si *J*-mediated NMR spectra, similarly sensitive to the local environments of covalently bonded ^{29}Si-O-^{29}Si moieties, show differences in levels of third-nearest-neighbor (^{27}Al-O-^{29}Si-O-^{29}Si-O-^{27}Al, 3NN) paired aluminum configurations. Basic Monte Carlo simulations are employed to estimate the amounts of paired aluminum represented by the detected NMR signals in these experiments. The methods demonstrated here are anticipated to be widely transferable to other zeolite framework types and heteroatoms.

Chapter 3. Influences of hydrothermal treatment on copper aluminum distributions in a Cu-chabazite deNO_x catalyst

Automobile exhaust is a major source of air pollution, particularly in densely populated areas. Since the 1970 Clean Air Act, catalytic converters have been required on all automobiles to control the amounts of carbon monoxide, unburned hydrocarbons, soot, and nitric oxides (NO_x). However, effective catalytic reduction of NO_x to N_2 in diesel systems has until recently been challenging due to the excess oxygen present in diesel exhaust.[3] Currently, NO_x is converted to N_2 by injecting a co-feed of NH_3 to the exhaust stream to perform selective catalytic reduction of NO_x by NH_3 (SCR) by the following reaction:[67,68]

$$4NO + 4NH_3 + O_2 \rightarrow 4N_2 + 6H_2O$$

This reaction is performed over a Cu^{2+}-exchanged chabazite zeolite (Cu-CHA), a small pore (0.4 nm) aluminosilicate zeolite, where Cu^{2+} cations act as the catalyst for the SCR reaction and undergo a Cu^{2+} to Cu^{+} redox cycle.[69] While these catalysts are deployed commercially, better atomic-level understanding of their performance is important to improve key design challenges for the catalyst.

A significant issue with Cu-CHA is that, under high-temperature hydrothermal conditions that it is intermittently exposed to in the catalytic converter, the catalyst structure decays.[70,71] Two pathways are proposed for this. For one, aluminum in hydrolyzed from the zeolite framework under these conditions, resulting in a loss of charge-balancing sites for Cu cations.[70] In addition, the single-atom Cu species may irreversibly sinter to form Cu agglomerates under these high temperature conditions.[72,73] However, the distributions of active species left over after extreme degradation from steam treatment, and the types of species that are most susceptible to deactivation are not well understood. In this chapter, a series of advanced characterization methods are applied to a Cu-CHA catalyst after varied aging treatments. A combination of high-angle annular dark field scanning transmission electron microscopy (HAADF-STEM) and electron paramagnetic resonance (EPR) were used to track the distributions of single-atom Cu species and Cu agglomerates as a function of steaming conditions. In addition, ^{15}N NMR of adsorbed species after treatment under SCR reaction conditions reveal differences in distributions of adsorption sites in catalysts as a function of aging, along with their interactions. 2D ^{27}Al-^{29}Si NMR correlation analyses reveal that closely paired aluminum species seem to be preferentially preserved during hydrothermal treatment in the presence of Cu cations. These results provide useful design rules for Cu-CHA materials with higher Cu and Al resistance to high temperature hydrothermal treatment.

Chapter 4. Role of diverse acid sites on the cracking activity and deactivation of zeolite H^+-USY

For decades, useful hydrocarbons have been created from heavy crude oil by cracking reactions that break large organic molecules into smaller ones that are useful either as fuels or as chemical precursors.[9] Cracking reactions are typically performed over catalyst composites

that include the large pore zeolite Y (FAU framework type) as a major active component.[74] The form of zeolite Y used is typically steam-treated to reduce the amount of aluminum in the zeolite framework.[75] This results in a complex distribution of aluminum species resulting in acid sites located on both mesopores and micropores.[29,76] While these steam treatments have long been observed to improve the performance of the zeolite, the complexities of reaction and diffusion limitations in these materials have been challenging to deconvolute. In particular, the role of aluminum distributions in deactivation by buildup of carbonaceous coke deposits is not well understood.[77] Active research is being performed to better understand how these complex acid site distributions influence reaction properties, as our need to address climate change is shifting the types of feedstocks used in cracking reactions and new catalyst preparations are needed to address these changes in feedstock composition.[9,78,79]

In this study, 2D ^{27}Al-^{29}Si NMR correlations reveal a complex distribution of alumina-silica chemical environments on a typical commercial dealuminated zeolite Y (deAl-Y), with some environments attributed to species on the mesopore surface. It was hypothesized that the mesopore surface acid sites are more susceptible to deactivation by coke formation. To better understand the influence of these mesopore acid sites on overall activity, the deAl-Y was silylated with a bulky organosilane too large to enter the zeolite micropores. Compared to the unmodified catalyst, the silylated deAl-Y exhibited less initial deactivation and higher olefin selectivity in a model hexane cracking reaction. The amount of hard coke, a carbonaceous deactivation byproduct, was significantly reduced on the silylated deAl-Y catalyst, as determined by thermogravimetric analyses. ^{1}H NMR analyses of hydrocarbon species adsorbed on the catalyst after different times on stream reveal that the distributions of aromatic species in the unmodified and modified zeolite evolve differently, with aromatic species on the

unmodified catalyst becoming more polyaromatic over time. ^{27}Al-filtered ^{1}H NMR spectra reveal that these species are located near aluminum, and thus are likely adsorbed reaction byproducts. These results help to inform future design of zeolite catalysts in systems where coke formation may be undesirable.

Chapter 5. Methods for tracking zeolite crystallization by NMR

Zeolites are synthesized under caustic, hydrothermal conditions from aluminum and silica precursors in the presence of cationic inorganic and organic molecules functioning as structure-directing agents. Interactions between these cationic structure directing agents and the forming zeolite framework determine the siting of aluminum in the zeolite framework, with both kinetic and thermodynamic driving forces playing a role in zeolite framework stability.[80] Changing the structure-directing agents used during synthesis changes the thermodynamic favorability of different aluminum sites and distributions.[24] Modifying the silicon and aluminum sources can also change these distributions by changing dissolution kinetics. It has been shown that using zeolites as aluminum and silicon sources produces different distributions of aluminum than using small molecule precursors.[81,82]

While these differing thermodynamic and kinetic driving forces are well-known, their relative importance under zeolite synthesis conditions is not well understood. Here, methods for characterizing aluminum and silicon species both *ex situ* and *in situ* are explored for standard siliceous and aluminosilicate chabazite syntheses. Powder X-ray diffraction, scanning electron microscopy, and ^{29}Si NMR were used to track the evolution of crystallinity, particle size, and framework species local chemical environments in samples quenched at different synthesis times prior to observed complete synthesis. In addition, advanced solid-state NMR 2D ^{27}Al-^{29}Si and ^{29}Si-^{1}H correlation analyses revealed differences in distributions of

framework species in mid-synthesis and fully crystalline chabazite materials. *In situ* NMR methods for tracking the evolution of ^{29}Si chemical environments under zeolite synthesis conditions were also explored. This chapter demonstrates a workflow that could be applied to novel zeolite syntheses, such as those involving interzeolite transformations, in order to better understand the complex dissolution and recrystallization processes involved with these syntheses.

Chapter 6. Conclusions and future directions

This chapter collects the overall conclusions from Chapters 2-5 for the convenience of the reader and discusses future possibilities for building on this work or applying methods to different, interesting systems.

References

(1) Fechete, I.; Wang, Y.; Védrine, J. C. The Past, Present and Future of Heterogeneous Catalysis. *Catalysis Today* **2012**, *189* (1), 2–27. https://doi.org/10.1016/j.cattod.2012.04.003.

(2) Bennett, S. J.; Pearson, P. J. G. From Petrochemical Complexes to Biorefineries? The Past and Prospective Co-Evolution of Liquid Fuels and Chemicals Production in the UK. *Chemical Engineering Research and Design* **2009**, *87* (9), 1120–1139. https://doi.org/10.1016/j.cherd.2009.02.008.

(3) Nova, I.; Tronconi, E. *Urea-SCR Technology for deNOx After Treatment of Diesel Exhausts*; Nova, I., Tronconi, E., Eds.; Fundamental and Applied Catalysis; Springer New York: New York, NY, 2014. https://doi.org/10.1007/978-1-4899-8071-7.

(4) Calvin, K.; Dasgupta, D.; Krinner, G.; Mukherji, A.; Thorne, P. W.; Trisos, C.; Romero, J.; Aldunce, P.; Barrett, K.; Blanco, G.; Cheung, W. W. L.; Connors, S.; Denton, F.; Diongue-Niang, A.; Dodman, D.; Garschagen, M.; Geden, O.; Hayward, B.; Jones, C.; Jotzo, F.; Krug, T.; Lasco, R.; Lee, Y.-Y.; Masson-Delmotte, V.; Meinshausen, M.; Mintenbeck, K.; Mokssit, A.; Otto, F. E. L.; Pathak, M.; Pirani, A.; Poloczanska, E.; Pörtner, H.-O.; Revi, A.; Roberts, D. C.; Roy, J.; Ruane, A. C.; Skea, J.; Shukla, P. R.; Slade, R.; Slangen, A.; Sokona, Y.; Sörensson, A. A.; Tignor, M.; Van Vuuren, D.; Wei, Y.-M.; Winkler, H.; Zhai, P.; Zommers, Z.; Hourcade, J.-C.; Johnson, F. X.; Pachauri, S.; Simpson, N. P.; Singh, C.; Thomas, A.; Totin, E.; Arias, P.; Bustamante, M.; Elgizouli, I.; Flato, G.; Howden, M.; Méndez-Vallejo, C.; Pereira, J. J.; Pichs-Madruga, R.; Rose, S. K.; Saheb, Y.; Sánchez Rodríguez, R.; Ürge-Vorsatz, D.; Xiao, C.; Yassaa, N.; Alegría, A.; Armour, K.; Bednar-Friedl, B.; Blok, K.; Cissé, G.; Dentener, F.; Eriksen, S.; Fischer, E.; Garner, G.; Guivarch, C.; Haasnoot, M.; Hansen, G.; Hauser, M.; Hawkins, E.; Hermans, T.; Kopp, R.; Leprince-Ringuet, N.; Lewis, J.; Ley, D.; Ludden, C.; Niamir, L.; Nicholls, Z.; Some, S.; Szopa, S.; Trewin, B.; Van Der Wijst, K.-I.; Winter, G.; Witting, M.; Birt, A.; Ha, M.; Romero, J.; Kim, J.; Haites, E. F.; Jung, Y.; Stavins, R.; Birt, A.; Ha, M.; Orendain, D. J. A.; Ignon, L.; Park, S.; Park, Y.; Reisinger, A.; Cammaramo, D.; Fischlin, A.; Fuglestvedt, J. S.; Hansen, G.; Ludden, C.; Masson-Delmotte, V.; Matthews, J. B. R.; Mintenbeck, K.; Pirani, A.; Poloczanska, E.; Leprince-Ringuet, N.; Péan, C. *IPCC, 2023: Climate Change 2023: Synthesis Report. Contribution of Working Groups I, II and III to the Sixth Assessment Report of the Intergovernmental Panel on Climate Change [Core Writing Team, H. Lee and J. Romero (Eds.)]. IPCC, Geneva, Switzerland.*, First.; Intergovernmental Panel on Climate Change (IPCC), 2023. https://doi.org/10.59327/IPCC/AR6-9789291691647.

(5) Breck, D. W. *Zeolite Molecular Sieves: Structure, Chemistry, and Use*; Wiley: New York, 1973.

(6) Flanigen, E. M. Chapter 2 Zeolites and Molecular Sieves an Historical Perspective. In *Studies in Surface Science and Catalysis*; van Bekkum, H., Flanigen, E. M., Jansen, J.

C., Eds.; Introduction to Zeolite Science and Practice; Elsevier, 1991; Vol. 58, pp 13–34. https://doi.org/10.1016/S0167-2991(08)63599-5.

(7) Ghobarkar, H.; Schäf, O.; Guth, U. Zeolites—from Kitchen to Space. *Progress in Solid State Chemistry* **1999**, *27* (2–4), 29–73. https://doi.org/10.1016/S0079-6786(00)00002-9.

(8) Rege, S. U.; Yang, R. T. Limits for Air Separation by Adsorption with LiX Zeolite. *Ind. Eng. Chem. Res.* **1997**, *36* (12), 5358–5365. https://doi.org/10.1021/ie9705214.

(9) Vogt, E. T. C.; Weckhuysen, B. M. Fluid Catalytic Cracking: Recent Developments on the Grand Old Lady of Zeolite Catalysis. *Chemical Society Reviews* **2015**, *44* (20), 7342–7370. https://doi.org/10.1039/c5cs00376h.

(10) Guo, P.; Yan, N.; Wang, L.; Zou, X. Database Mining of Zeolite Structures. *Crystal Growth and Design* **2017**, *17* (12), 6821–6835. https://doi.org/10.1021/acs.cgd.7b01410.

(11) Olsbye, U.; Svelle, S.; Bjørgen, M.; Beato, P.; Janssens, T. V. W.; Joensen, F.; Bordiga, S.; Lillerud, K. P. Conversion of Methanol to Hydrocarbons: How Zeolite Cavity and Pore Size Controls Product Selectivity. *Angewandte Chemie International Edition* **2012**, *51* (24), 5810–5831. https://doi.org/10.1002/anie.201103657.

(12) Chai, Y.; Dai, W.; Wu, G.; Guan, N.; Li, L. Confinement in a Zeolite and Zeolite Catalysis. *Acc. Chem. Res.* **2021**, *54* (13), 2894–2904. https://doi.org/10.1021/acs.accounts.1c00274.

(13) Van der Mynsbrugge, J.; De Ridder, J.; Hemelsoet, K.; Waroquier, M.; Van Speybroeck, V. Enthalpy and Entropy Barriers Explain the Effects of Topology on the Kinetics of Zeolite-Catalyzed Reactions. *Chemistry – A European Journal* **2013**, *19* (35), 11568–11576. https://doi.org/10.1002/chem.201301272.

(14) Sherman, J. D. Synthetic Zeolites and Other Microporous Oxide Molecular Sieves. *Proceedings of the National Academy of Sciences* **1999**, *96* (7), 3471–3478. https://doi.org/10.1073/pnas.96.7.3471.

(15) Wang, H.; Wang, L.; Xiao, F. S. Metal@zeolite Hybrid Materials for Catalysis. *ACS Central Science* **2020**, *6* (10), 1685–1697. https://doi.org/10.1021/ACSCENTSCI.0C01130.

(16) Xu, B.; Sievers, C.; Hong, S. B.; Prins, R.; van Bokhoven, J. A. Catalytic Activity of Brønsted Acid Sites in Zeolites: Intrinsic Activity, Rate-Limiting Step, and Influence of the Local Structure of the Acid Sites. *Journal of Catalysis* **2006**, *244* (2), 163–168. https://doi.org/10.1016/j.jcat.2006.08.022.

(17) Ali, M. A.; Brisdon, B.; Thomas, W. J. Synthesis, Characterization and Catalytic Activity of ZSM-5 Zeolites Having Variable Silicon-to-Aluminum Ratios. *Applied Catalysis A: General* **2003**, *252* (1), 149–162. https://doi.org/10.1016/S0926-860X(03)00413-7.

(18) Fernandez, C.; Stan, I.; Gilson, J. P.; Thomas, K.; Vicente, A.; Bonilla, A.; Pérez-Ramírez, J. Hierarchical ZSM-5 Zeolites in Shape-Selective Xylene Isomerization: Role

of Mesoporosity and Acid Site Speciation. *Chemistry – A European Journal* **2010**, *16* (21), 6224–6233. https://doi.org/10.1002/CHEM.200903426.

(19) Knott, B. C.; Nimlos, C. T.; Robichaud, D. J.; Nimlos, M. R.; Kim, S.; Gounder, R. Consideration of the Aluminum Distribution in Zeolites in Theoretical and Experimental Catalysis Research. *ACS Catal.* **2018**, *8* (2), 770–784. https://doi.org/10.1021/acscatal.7b03676.

(20) Li, S.; Li, H.; Gounder, R.; Debellis, A.; Müller, I. B.; Prasad, S.; Moini, A.; Schneider, W. F. First-Principles Comparison of Proton and Divalent Copper Cation Exchange Energy Landscapes in SSZ-13 Zeolite. *The Journal of Physical Chemistry C* **2018**, *122* (41), 23564–23573. https://doi.org/10.1021/acs.jpcc.8b07213.

(21) Román-Leshkov, Y.; Moliner, M.; Davis, M. E. Impact of Controlling the Site Distribution of Al Atoms on Catalytic Properties in Ferrierite-Type Zeolites. *The Journal of Physical Chemistry C* **2011**, *115* (4), 1096–1102. https://doi.org/10.1021/jp106247g.

(22) Lobo, R. F.; Zones, S. I.; Davis, M. E. Structure-Direction in Zeolite Synthesis. *J. Incl. Phenom. Macrocycl. Chem.* **1995**, *21* (1), 47–78. https://doi.org/10.1007/BF00709411.

(23) Yi, X.; Xiao, Y.; Li, G.; Liu, Z.; Chen, W.; Liu, S. B.; Zheng, A. From One to Two: Acidic Proton Spatial Networks in Porous Zeolite Materials. *Chemistry of Materials* **2020**, *32* (3), 1332–1342. https://doi.org/10.1021/acs.chemmater.0c00005.

(24) Schwalbe-Koda, D.; Kwon, S.; Paris, C.; Bello-Jurado, E.; Jensen, Z.; Olivetti, E.; Willhammar, T.; Corma, A.; Román-Leshkov, Y.; Moliner, M.; Gómez-Bombarelli, R. A Priori Control of Zeolite Phase Competition and Intergrowth with High-Throughput Simulations. *Science* **2021**, *374* (6565), 308–315. https://doi.org/10.1126/science.abh3350.

(25) Jensen, Z.; Kwon, S.; Schwalbe-Koda, D.; Paris, C.; Gómez-Bombarelli, R.; Román-Leshkov, Y.; Corma, A.; Moliner, M.; Olivetti, E. A. Discovering Relationships between OSDAs and Zeolites through Data Mining and Generative Neural Networks. *ACS Cent. Sci.* **2021**, *7* (5), 858–867. https://doi.org/10.1021/acscentsci.1c00024.

(26) Di Iorio, J. R.; Li, S.; Jones, C. B.; Nimlos, C. T.; Wang, Y.; Kunkes, E.; Vattipalli, V.; Prasad, S.; Moini, A.; Schneider, W. F.; Gounder, R. Cooperative and Competitive Occlusion of Organic and Inorganic Structure-Directing Agents within Chabazite Zeolites Influences Their Aluminum Arrangement. *Journal of the American Chemical Society* **2020**, *142* (10), 4807–4819. https://doi.org/10.1021/jacs.9b13817.

(27) Williams, B. A.; Babitz, S. M.; Miller, J. T.; Snurr, R. Q.; Kung, H. H. The Roles of Acid Strength and Pore Diffusion in the Enhanced Cracking Activity of Steamed Y Zeolites. *Applied Catalysis A: General* **1999**, *177* (2), 161–175. https://doi.org/10.1016/S0926-860X(98)00264-6.

(28) van Bokhoven, J. A.; van der Eerden, A. M. J.; Koningsberger, D. C. Three-Coordinate Aluminum in Zeolites Observed with In Situ X-Ray Absorption Near-Edge

Spectroscopy at the Al K-Edge: Flexibility of Aluminum Coordinations in Zeolites. *J. Am. Chem. Soc.* **2003**, *125* (24), 7435–7442. https://doi.org/10.1021/ja0292905.
(29) Dutartre, R.; de Ménorval, L. C.; Di Renzo, F.; McQueen, D.; Fajula, F.; Schulz, P. Mesopore Formation during Steam Dealumination of Zeolites: Influence of Initial Aluminum Content and Crystal Size. *Microporous Materials* **1996**, *6* (5), 311–320. https://doi.org/10.1016/0927-6513(96)00039-9.
(30) Li, S.; Lafon, O.; Wang, W.; Wang, Q.; Wang, X.; Li, Y.; Xu, J.; Deng, F. Recent Advances of Solid-State NMR Spectroscopy for Microporous Materials. *Advanced Materials* **2020**, *32* (44), 2002879. https://doi.org/10.1002/adma.202002879.
(31) Levitt, M. H. *Spin Dynamics: Basics of Nuclear Magnetic Resonance*, 2. ed., repr.; Wiley: Chichester, 2011.
(32) Keeler, J. *Understanding NMR Spectroscopy*, 2nd ed.; John Wiley and Sons: Chichester, U.K, 2010.
(33) Lesage, A.; Bardet, M.; Emsley, L. Through-Bond Carbon-Carbon Connectivities in Disordered Solids by NMR. *Journal of the American Chemical Society* **1999**, *121* (47), 10987–10993. https://doi.org/10.1021/ja992272b.
(34) Massiot, D.; Fayon, F.; Alonso, B.; Trebosc, J.; Amoureux, J. P. Chemical Bonding Differences Evidenced from J-Coupling in Solid State NMR Experiments Involving Quadrupolar Nuclei. *Journal of Magnetic Resonance* **2003**, *164* (1), 160–164. https://doi.org/10.1016/S1090-7807(03)00134-4.
(35) Hu, B.; Trébosc, J.; Amoureux, J. P. Comparison of Several Hetero-Nuclear Dipolar Recoupling NMR Methods to Be Used in MAS HMQC/HSQC. *Journal of Magnetic Resonance* **2008**, *192* (1), 112–122. https://doi.org/10.1016/j.jmr.2008.02.004.
(36) Renault, M.; Cukkemane, A.; Baldus, M. Solid-State NMR Spectroscopy on Complex Biomolecules. *Angewandte Chemie International Edition* **2010**, *49* (45), 8346–8357. https://doi.org/10.1002/anie.201002823.
(37) Chen, L.; Lu, X.; Wang, Q.; Lafon, O.; Trébosc, J.; Deng, F.; Amoureux, J. P. Distance Measurement between a Spin-1/2 and a Half-Integer Quadrupolar Nuclei by Solid-State NMR Using Exact Analytical Expressions. *Journal of Magnetic Resonance* **2010**, *206* (2), 269–273. https://doi.org/10.1016/j.jmr.2010.07.009.
(38) Giovine, R.; Trébosc, J.; Pourpoint, F.; Lafon, O.; Amoureux, J. P. Magnetization Transfer from Protons to Quadrupolar Nuclei in Solid-State NMR Using PRESTO or Dipolar-Mediated Refocused INEPT Methods. *Journal of Magnetic Resonance* **2019**, *299*, 109–123. https://doi.org/10.1016/J.JMR.2018.12.016.
(39) Lu, X.; Lafon, O.; Trébosc, J.; Tricot, G.; Delevoye, L.; Méar, F.; Montagne, L.; Amoureux, J. P. Observation of Proximities between Spin-12 and Quadrupolar Nuclei: Which Heteronuclear Dipolar Recoupling Method Is Preferable. *Journal of Chemical Physics* **2012**, *137* (14), 144201. https://doi.org/10.1063/1.4753987.
(40) Lesage, A.; Lelli, M.; Gajan, D.; Caporini, M. A.; Vitzthum, V.; Miéville, P.; Alauzun, J.; Roussey, A.; Thieuleux, C.; Mehdi, A.; Bodenhausen, G.; Copéret, C.; Emsley, L.

Surface Enhanced NMR Spectroscopy by Dynamic Nuclear Polarization. *Journal of the American Chemical Society* **2010**, *132* (44), 15459–15461. https://doi.org/10.1021/ja104771z.

(41) Rossini, A. J.; Zagdoun, A.; Lelli, M.; Lesage, A.; Copéret, C.; Emsley, L. Dynamic Nuclear Polarization Surface Enhanced NMR Spectroscopy. *Acc. Chem. Res.* **2013**, *46* (9), 1942–1951. https://doi.org/10.1021/ar300322x.

(42) Gao, P.; Wang, Q.; Xu, J.; Qi, G.; Wang, C.; Zhou, X.; Zhao, X.; Feng, N.; Liu, X.; Deng, F. Brønsted/Lewis Acid Synergy in Methanol-to-Aromatics Conversion on Ga-Modified ZSM-5 Zeolites, As Studied by Solid-State NMR Spectroscopy. *ACS Catalysis* **2018**, *8* (1), 69–74. https://doi.org/10.1021/acscatal.7b03211.

(43) Li, S.; Zheng, A.; Su, Y.; Zhang, H.; Chen, L.; Yang, J.; Ye, C.; Deng, F. Brønsted/Lewis Acid Synergy in Dealuminated HY Zeolite: A Combined Solid-State NMR and Theoretical Calculation Study. *Journal of the American Chemical Society* **2007**, *129* (36), 11161–11171. https://doi.org/10.1021/ja072767y.

(44) Wang, C.; Xu, J.; Deng, F. Mechanism of Methanol-to-Hydrocarbon Reaction over Zeolites: A Solid-State NMR Perspective. *ChemCatChem* **2020**, *12* (4), 965–980. https://doi.org/10.1002/CCTC.201901937.

(45) Wang, C.; Wang, Q.; Xu, J.; Qi, G.; Gao, P.; Wang, W.; Zou, Y.; Feng, N.; Liu, X.; Deng, F. Direct Detection of Supramolecular Reaction Centers in the Methanol-to-Olefins Conversion over Zeolite H-ZSM-5 by ^{13}C-^{27}Al Solid-State NMR Spectroscopy. *Angewandte Chemie International Edition* **2016**, *55* (7), 2507–2511. https://doi.org/10.1002/anie.201510920.

(46) Berkson, Z. J.; Hsieh, M.; Smeets, S.; Gajan, D.; Lund, A.; Lesage, A.; Xie, D.; Zones, S. I.; McCusker, L. B.; Baerlocher, C.; Chmelka, B. F. Preferential Siting of Aluminum Heteroatoms in the Zeolite Catalyst Al-SSZ-70. *Angewandte Chemie International Edition* **2019**, *58* (19), 6255–6259. https://doi.org/10.1002/anie.201813533.

(47) Chen, K.; Zornes, A.; Nguyen, V.; Wang, B.; Gan, Z.; Crossley, S. P.; White, J. L. ^{17}O Labeling Reveals Paired Active Sites in Zeolite Catalysts. *Journal of the American Chemical Society* **2022**, *144* (37), 16916–16929. https://doi.org/10.1021/jacs.2c05332.

(48) Chen, K.; Gan, Z.; Horstmeier, S.; White, J. L. Distribution of Aluminum Species in Zeolite Catalysts: ^{27}Al NMR of Framework, Partially-Coordinated Framework, and Non-Framework Moieties. *Journal of the American Chemical Society* **2021**, *143* (17), 6669–6680. https://doi.org/10.1021/JACS.1C02361.

(49) Pugh, S. M.; Wright, P. A.; Law, D. J.; Thompson, N.; Ashbrook, S. E. Facile, Room-Temperature ^{17}O Enrichment of Zeolite Frameworks Revealed by Solid-State NMR Spectroscopy. *Journal of the American Chemical Society* **2020**, *142* (2), 900–906. https://doi.org/10.1021/JACS.9B10528.

(50) Schaefer, D. J.; Favre, D. E.; Wilhelm, M.; Weigel, S. J.; Chmelka, B. F. Site-Hopping Dynamics of Benzene Adsorbed on Ca-LSX Zeolite Studied by Solid-State Exchange ^{13}C NMR. *Journal of the American Chemical Society* **1997**, *119* (39), 9252–9267.

(51) Kärger, J.; Pfeifer, H. N.M.R. Self-Diffusion Studies in Zeolite Science and Technology. *Zeolites* **1987**, *7* (2), 90–107. https://doi.org/10.1016/0144-2449(87)90067-4.
(52) Heink, W.; Kärger, J.; Ernst, S.; Weitkamp, J. P.F.G. N.M.R. Study of the Influence of the Exchangeable Cations on the Self-Diffusion of Hydrocarbons in Zeolites. *Zeolites* **1994**, *14* (5), 320–325. https://doi.org/10.1016/0144-2449(94)90104-X.
(53) Kortunov, P.; Vasenkov, S.; Kärger, J.; Valiullin, R.; Gottschalk, P.; Fé Elía, M.; Perez, M.; Stöcker, M.; Drescher, B.; McElhiney, G.; Berger, C.; Gläser, R.; Weitkamp, J. The Role of Mesopores in Intracrystalline Transport in USY Zeolite: PFG NMR Diffusion Study on Various Length Scales. *J. Am. Chem. Soc.* **2005**, *127* (37), 13055–13059. https://doi.org/10.1021/ja053134r.
(54) Liu, Y.; Zhang, W.; Liu, Z.; Xu, S.; Wang, Y.; Xie, Z.; Han, X.; Bao, X. Direct Observation of the Mesopores in ZSM-5 Zeolites with Hierarchical Porous Structures by Laser-Hyperpolarized ^{129}Xe NMR. *J. Phys. Chem. C* **2008**, *112* (39), 15375–15381. https://doi.org/10.1021/jp802813x.
(55) Di Iorio, J. R.; Nimlos, C. T.; Gounder, R. Introducing Catalytic Diversity into Single-Site Chabazite Zeolites of Fixed Composition via Synthetic Control of Active Site Proximity. *ACS Catalysis* **2017**, *7* (10), 6663–6674. https://doi.org/10.1021/acscatal.7b01273.
(56) Marsden, G.; Kostetskyy, P.; Sekiya, R. S.; Hoffman, A.; Lee, S.; Gounder, R.; Hibbitts, D.; Broadbelt, L. J. Quantifying Effects of Active Site Proximity on Rates of Methanol Dehydration to Dimethyl Ether over Chabazite Zeolites through Microkinetic Modeling. *ACS Materials Au* **2022**, *2* (2), 163–175. https://doi.org/10.1021/ACSMATERIALSAU.1C00057/.
(57) Hoffman, A. J.; Bates, J. S.; Di Iorio, J. R.; Nystrom, S. V.; Nimlos, C. T.; Gounder, R.; Hibbitts, D. Rigid Arrangements of Ionic Charge in Zeolite Frameworks Conferred by Specific Aluminum Distributions Preferentially Stabilize Alkanol Dehydration Transition States. *Angewandte Chemie International Edition* **2020**, *59* (42), 18686–18694. https://doi.org/10.1002/anie.202007790.
(58) Gao, F.; Kwak, J. H.; Szanyi, J.; Peden, C. H. F. Current Understanding of Cu-Exchanged Chabazite Molecular Sieves for Use as Commercial Diesel Engine DeNO_x Catalysts. *Topics in Catalysis* **2013**, *56*, 1441–1459. https://doi.org/10.1007/s11244-013-0145-8.
(59) Beale, A. M.; Gao, F.; Lezcano-Gonzalez, I.; Peden, C. H. F.; Szanyi, J. Recent Advances in Automotive Catalysis for NO_x Emission Control by Small-Pore Microporous Materials. *Chemical Society Reviews* **2015**, *44* (20), 7371–7405. https://doi.org/10.1039/c5cs00108k.
(60) Gao, F.; Szanyi, J. On the Hydrothermal Stability of Cu/SSZ-13 SCR Catalysts. *Applied Catalysis A: General* **2018**, *560*, 185–194. https://doi.org/10.1016/j.apcata.2018.04.040.
(61) Shih, A. J.; González, J. M.; Khurana, I.; Pérez Ramírez, L.; Peña, A.; Kumar, A.; Villa, A. L. Influence of ZCuOH, Z_2Cu, and Extraframework Cu_xO_y Species in Cu-SSZ-13 on

N_2O Formation during the Selective Catalytic Reduction of NO_x with NH_3. *ACS Catalysis* **2021**, *11*, 10362–10376. https://doi.org/10.1021/acscatal.1c01871.

(62) Dědeček, J.; Kaucky, D.; Wichterlová, B.; Gonsiorová, O. Co^{2+} Ions as Probes of Al Distribution in the Framework of Zeolites. ZSM-5 Study. *PCCP* **2002**, *4*, 5406–5413. https://doi.org/10.1039/b203966b.

(63) Pashkova, V.; Klein, P.; Dedecek, J.; Tokarová, V.; Wichterlová, B. Incorporation of Al at ZSM-5 Hydrothermal Synthesis. Tuning of Al Pairs in the Framework. *Microporous and Mesoporous Materials* **2015**, *202*, 138–146. https://doi.org/10.1016/J.MICROMESO.2014.09.056.

(64) Chen, K.; Abdolrahmani, M.; Horstmeier, S.; Pham, T. N.; Nguyen, V. T.; Zeets, M.; Wang, B.; Crossley, S.; White, J. L. Brønsted–Brønsted Synergies between Framework and Noncrystalline Protons in Zeolite H-ZSM-5. *ACS Catalysis* **2019**, *9* (7), 6124–6136. https://doi.org/10.1021/ACSCATAL.9B01583.

(65) Mlekodaj, K.; Dedecek, J.; Pashkova, V.; Tabor, E.; Klein, P.; Urbanova, M.; Karcz, R.; Sazama, P.; Whittleton, S. R.; Thomas, H. M.; Fishchuk, A. V.; Sklenak, S. Al Organization in the SSZ-13 Zeolite. Al Distribution and Extraframework Sites of Divalent Cations. *The Journal of Physical Chemistry C* **2019**, *123* (13), 7968–7987. https://doi.org/10.1021/ACS.JPCC.8B07343.

(66) Nimlos, C. T.; Hoffman, A. J.; Hur, Y. G.; Lee, J.; Di Iorio, J. R.; Hibbitts, D. D.; Gounder, R. Experimental and Theoretical Assessments of Aluminum Proximity in MFI Zeolites and Its Alteration by Organic and Inorganic Structure-Directing Agents. *Chemistry of Materials* **2020**, *32* (21), 9277–9298. https://doi.org/10.1021/acs.chemmater.0c03154.

(67) Bull, I.; Xue, W.-M.; Burk, P.; Boorse, S.; Jaglowski, W. M.; Koermer, G. S.; Moini, A.; Patchett, J. A.; Dettling, J. C.; Caudle, M. T. Copper CHA Zeolite Catalysts. US7601662B2, 2009.

(68) Kwak, J. H.; Tonkyn, R. G.; Kim, D. H.; Szanyi, J.; Peden, C. H. F. Excellent Activity and Selectivity of Cu-SSZ-13 in the Selective Catalytic Reduction of NO_x with NH_3. *Journal of Catalysis* **2010**, *275* (2), 187–190. https://doi.org/10.1016/j.jcat.2010.07.031.

(69) Chen, L.; Janssens, T. V. W.; Vennestrøm, P. N. R.; Jansson, J.; Skoglundh, M.; Grönbeck, H. A Complete Multisite Reaction Mechanism for Low-Temperature NH_3-SCR over Cu-CHA. *ACS Catalysis* **2020**, *10* (10), 5646–5656. https://doi.org/10.1021/ACSCATAL.0C00440.

(70) Kwak, J. H.; Tran, D.; Burton, S. D.; Szanyi, J.; Lee, J. H.; Peden, C. H. F. Effects of Hydrothermal Aging on NH_3-SCR Reaction over Cu/Zeolites. *Journal of Catalysis* **2012**, *287*, 203–209. https://doi.org/10.1016/j.jcat.2011.12.025.

(71) Kim, Y. J.; Lee, J. K.; Min, K. M.; Hong, S. B.; Nam, I. S.; Cho, B. K. Hydrothermal Stability of CuSSZ13 for Reducing NO_x by NH_3. *Journal of Catalysis* **2014**, *311*, 447–457. https://doi.org/10.1016/J.JCAT.2013.12.012.

(72) Song, J.; Wang, Y.; Walter, E. D.; Washton, N. M.; Mei, D.; Kovarik, L.; Engelhard, M. H.; Prodinger, S.; Wang, Y.; Peden, C. H. F.; Gao, F. Toward Rational Design of Cu/SSZ-13 Selective Catalytic Reduction Catalysts: Implications from Atomic-Level Understanding of Hydrothermal Stability. *ACS Catalysis* **2017**, *7* (12), 8214–8227. https://doi.org/10.1021/acscatal.7b03020.
(73) Uchisawa, J.; Obuchi, A.; Yamamoto, A.; Suzuki, S.; Mizushima, N.; Hayashi, S. Effect of Water Vapor on the Accelerated Deterioration Treatment of Cu-SSZ-13 as Catalysts for Selective Catalytic Reduction. *Industrial and Engineering Chemistry Research* **2021**, *60* (43), 15454–15463. https://doi.org/10.1021/ACS.IECR.1C02599/.
(74) Breck, D. W. Crystalline Zeolite Y. US3130007A, April 21, 1964.
(75) Engelhardt, G.; Lohse, U.; Samoson, A.; Mägi, M.; Tarmak, M.; Lippmaa, E. High Resolution ^{29}Si N.M.R. of Dealuminated and Ultrastable Y-Zeolites. *Zeolites* **1982**, *2* (1), 59–62. https://doi.org/10.1016/S0144-2449(82)80042-0.
(76) Yu, Z.; Zheng, A.; Wang, Q.; Chen, L.; Xu, J.; Amoureux, J.-P.; Deng, F. Insights into the Dealumination of Zeolite HY Revealed by Sensitivity-Enhanced ^{27}Al DQ-MAS NMR Spectroscopy at High Field. *Angewandte Chemie International Edition* **2010**, *49* (46), 8657–8661. https://doi.org/10.1002/anie.201004007.
(77) Vogt, E. T. C.; Fu, D.; Weckhuysen, B. M. Carbon Deposit Analysis in Catalyst Deactivation, Regeneration, and Rejuvenation. *Angewandte Chemie International Edition* **2023**, *62* (29), e202300319. https://doi.org/10.1002/anie.202300319.
(78) Weitkamp, J. Catalytic Hydrocracking—Mechanisms and Versatility of the Process. *ChemCatChem* **2012**, *4* (3), 292–306. https://doi.org/10.1002/CCTC.201100315.
(79) Adawi, H. I.; Zheng, Y.; Sarazen, M. L. Underpinnings of Carbonaceous Deposition among Structurally Diverse Hierarchical Zeolites during Hydrocarbon Upgrading. *Crystal Growth & Design* **2023**, *23* (4), 2675–2688. https://doi.org/10.1021/acs.cgd.2c01488.
(80) Cundy, C. S.; Cox, P. A. The Hydrothermal Synthesis of Zeolites: Precursors, Intermediates and Reaction Mechanism. *Microporous and Mesoporous Materials* **2005**, *82* (1–2), 1–78. https://doi.org/10.1016/j.micromeso.2005.02.016.
(81) Devos, J.; A. Shah, M.; Dusselier, M. On the Key Role of Aluminium and Other Heteroatoms during Interzeolite Conversion Synthesis. *RSC Advances* **2021**, *11* (42), 26188–26210. https://doi.org/10.1039/D1RA02887A.
(82) Robijns, S.; Devos, J.; Donckels, T.; de Oliveira-Silva, R.; De Witte, N.; Sakellariou, D.; Van Assche, T. R. C.; Dusselier, M. Steering Interzeolite Conversion with Alkali Metal Cations: Lithium Maximizes Al Proximity in SSZ-13 Zeolite Genesis. *Crystal Growth and Design* **2023**, *23* (1), 289–299. https://doi.org/10.1021/ACS.CGD.2C01009.

Chapter 2

Direct detection of paired aluminum heteroatoms in chabazite zeolite catalysts and their significance for methanol dehydration reactivity

Adapted with permission from Schmithorst, M. B.; Prasad, S.; Moini, A.; Chmelka, B. F. Direct Detection of Paired Aluminum Heteroatoms in Chabazite Zeolite Catalysts and Their Significance for Methanol Dehydration Reactivity. *J. Am. Chem. Soc.* **2023**, *145* (33), 18215-18220. DOI: 10.1021/jacs.3c05708. Article is available via: https://pubs.acs.org/articlesonrequest/AOR-U9HMNHWSNTKV4GNARWIV

Abstract

The distributions of heteroatoms within zeolite frameworks have important influences on the locations of exchangeable cations that account for the diverse adsorption and reaction properties of zeolite catalysts. In particular for aluminosilicate zeolites, paired configurations of aluminum atoms separated by one or two tetrahedrally-coordinated silicon atoms are important for charge-balancing pairs of H^+ cations, which are active for methanol dehydration, or divalent metal cations, such as Cu^{2+}, which selectively catalyze the reduction of NO_x, both technologically important reactions. Such paired heteroatom configurations, however, are challenging to detect and probe, due to the typically non-stoichiometric compositions and non-periodic distributions of aluminum atoms within aluminosilicate zeolite frameworks. Nevertheless, distinct configurations of paired framework aluminum atoms are unambiguously detected and resolved in solid-state 2D ^{27}Al–^{29}Si and ^{29}Si–^{29}Si NMR spectra, which are sensitive to the local environments of covalently bonded ^{27}Al–O–^{29}Si and ^{29}Si–O–^{29}Si moieties, respectively. Specifically, two H^+-chabazite zeolites with the same bulk framework aluminum contents are shown to have different types and populations of closely paired

aluminum species, which correlate with higher activity for methanol dehydration. The methodologies and insights are broadly applicable to analyses of heteroatom sites, their distributions, and adsorption and reaction properties in other zeolite framework types.

Introduction

Understanding the composition-structure-activity relationships of nanoporous aluminosilicate zeolite catalysts has been a long-sought goal to improve their performance, although much has remained elusive at an atomic-level. In particular, the numbers, types, and efficacies of adsorption or reaction sites in zeolites are governed by the quantities and distributions of non-stoichiometric Al heteroatoms within their respective zeolite structures. Such Al atoms are tetrahedrally-coordinated and covalently bonded via bridging oxygen atoms to four Si atoms in zeolite frameworks. As each framework Al atom imparts a local negative charge to the zeolite framework, the numbers and locations of charge-balancing exchangeable cations are crucially linked. Where such cations are H^+, zeolites manifest strong Bronsted acidities, such as those used industrially for fluidized catalytic cracking of hydrocarbons (e.g., H^+-USY) or methanol-to-gasoline or xylene-isomerization processes (H^+-ZSM-5).[1–3] For divalent cations, such as Ca^{2+} or Mg^{2+}, as taken up by zeolite A in water-softening applications, or $Pt(NH_3)_4^{2+}$ or Cu^{2+} ions used to introduce catalytically-active metal species into zeolite nanopores, pairs of nearby framework Al atoms are required to accommodate the divalent charges of the metal species.[4,5] A timely example is the small-pore zeolite chabazite (CHA), which has been studied extensively over the past decade in Cu-exchanged forms for the selective catalytic reduction (SCR) of NO_x in diesel exhaust.[6–13] Importantly, the properties of Cu-chabazite catalysts have been shown to depend on the state of exchanged Cu(II) species, with Cu^{2+} cations considered most desirable.[14,15] Such Cu^{2+} cations are thought to be stabilized

by pairs of nearby framework Al heteroatoms in the aluminosilicate CHA framework, which due to Lowenstein's Rule, are hypothesized to be in second-nearest-neighbor (2NN, **Al**–O–Si–O–**Al**, Al separated by 0.5–0.6 nm) or third-nearest-neighbor (3NN, **Al**–O–Si–O–Si–O–**Al**, Al separated by 0.6-0.8 nm) configurations.[16,17] The non-stoichiometric and non-uniform distributions of Al heteroatoms have made such configurations exceedingly challenging to analyze.

The most widely used method for assessing the presence of paired framework Al atoms in chabazite or other zeolites has been the titration of paired anionic framework charges with divalent cations, typically Co^{2+}, which has been shown to exchange into specific sites.[18–20] However, there are conflicting reports in the literature with regard to the type(s) of cation sites into which Co^{2+} exchanges in chabazite nanopores,[21,22] which are frequently attributed to Co^{2+} cations associated with paired configurations of Al atoms in six-membered CHA rings.[23,24] X-ray scattering and scanning transmission electron microscopy have recently been used to identify distributions of tetrahedrally-coordinated Al atoms among crystallographically distinct framework sites in highly siliceous zeolites.[25,26] Solid-state nuclear magnetic resonance (NMR) spectroscopy has been used to probe framework Al proximities in highly siliceous or modified zeolites, primarily via through-space dipolar interactions, which provide information on the nanoscale proximities of ^{29}Si, ^{27}Al, ^{17}O, or ^{1}H nuclei, though cannot distinguish between framework versus extra-framework moieties or local bonding configurations.[27–30] The resolution and usefulness of these approaches are thus limited, especially for high-aluminum-content zeolites.

By comparison, powerful two-dimensional (2D) correlation NMR analyses that rely on through-covalent-bond scalar (*J*) interactions overcome many of these limitations.[31–33]

Specifically, 2D *J*-mediated ^{27}Al–^{29}Si and ^{29}Si–^{29}Si correlation spectra enable the detection and resolution of isotropic chemical shifts from natural abundance (4.7%) ^{29}Si nuclei that are correlated with signals from *J*-coupled ^{27}Al nuclei, providing detailed information on the bonding environments and connectivities of framework heteroatom moieties selectively.[34–36] In particular, this approach enables second- and third-nearest-neighbor configurations of paired framework Al atoms to be unambiguously detected, resolved, and compared for different CHA zeolite catalysts with similar, high aluminum contents, but significantly different macroscopic reaction properties.

Results and Discussion

The importance of "paired" versus isolated heteroatom sites in zeolites is manifested by the different rates of catalytic reactions, such as methanol dehydration to dimethylether. For example, previous modeling and indirect measurements inferred from Co^{2+} titration have indicated that the rate of methanol dehydration over H^+-chabazite may be faster over catalysts in which framework Al heteroatoms are nearby one another, compared to when they are isolated.[37–39] Here, two H^+-chabazite catalysts were tested for the rates at which methanol was converted to dimethylether under identical conditions. The two zeolites were both synthesized using trimethyladamantylammonium hydroxide as the organic structure-directing agent, although H^+-CHA-1 was synthesized via inter-zeolite conversion using FAU zeolite as a precursor, while H^+-CHA-2 was synthesized by conventional methods using molecular precurors.[40–42] The resulting products had very similar bulk compositions (Si/Al~10) and were indistinguishable by conventional scattering or NMR characterization techniques (Figures S1-S4), or their 2D ^{1}H–^{1}H NMR spectra (Figure S5). Notably, standard Co^{2+} exchange analyses resulted in low Co^{2+}/Al ratios of <0.02 for both catalysts (Table S1). Kinetic analyses were

conducted in a batch reactor and monitored *in situ* by acquiring direct-excitation ^{13}C magic-angle-spinning (MAS) NMR spectra and comparing transient changes in the well-resolved integrated intensities of ^{13}C signals at 52 ppm and 62 ppm from adsorbed methanol and dimethylether molecules, respectively (Figs. S6-S9). Based on the integrated intensities of these two signals, the conversions of methanol over time at 125 ºC and at 150 ºC for H^+-CHA-1 and H^+-CHA-2 are shown in Figure 1. The rates of methanol dehydration at both temperatures are significantly higher for H^+-CHA-1 than those measured for H^+-CHA-2, despite their similar and very low populations of sites titrated by Co^{2+}. These differences in activity are discussed in more detail in Figure S10 and Table S2.

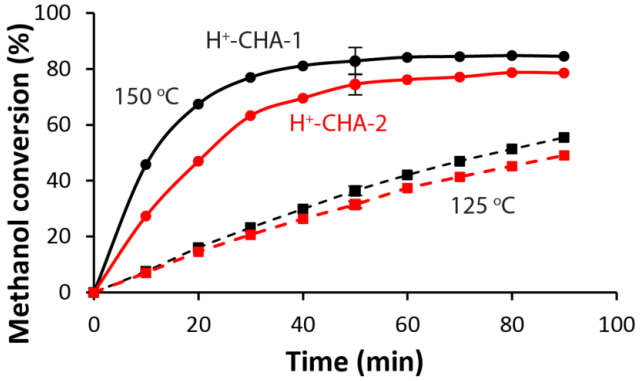

Figure 1. Methanol conversion as a function of time during dehydration over H^+-CHA-1 (black) and H^+-CHA-2 (red) at 150 ºC (circles) and at 125 ºC (squares), as determined from integrated intensities of *in situ* direct-excitation ^{13}C NMR spectra in Figures S6-S9. Under these conditions, CH3OH turnover numbers per Al atom were established to be >1, as discussed in the Supporting Information.

The two catalysts, however, exhibit significant differences in the nanoscale proximities of their framework Al moieties. These are revealed by a combination of solid-state 2D ^{27}Al–^{29}Si and ^{29}Si–^{29}Si *J*-mediated NMR correlation spectra, which provide direct measurements of the connectivities, proximities, and the relative amounts of paired Al atoms in the zeolite frameworks. Such spectra show correlated signals only from *J*-coupled ^{29}Si and ^{27}Al nuclei

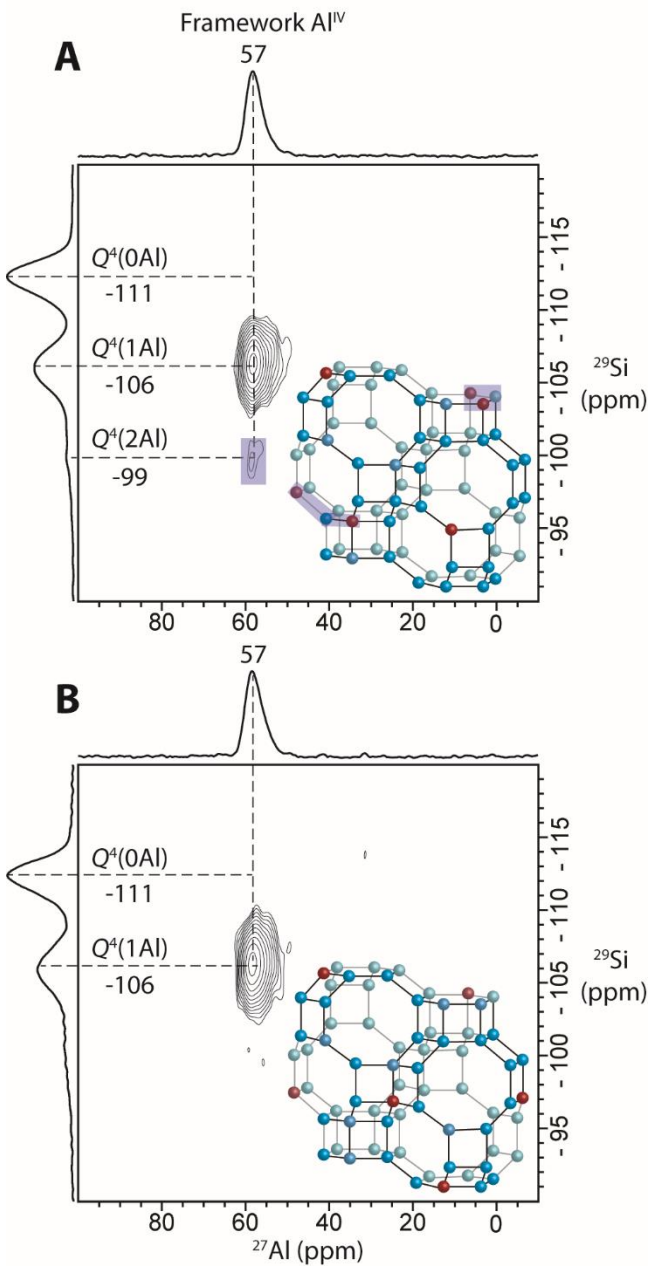

Figure 2. Solid-state 2D ^{27}Al–^{29}Si *J*-HMQC NMR spectra of (A) hydrated H^{+}-CHA-1 and (B) hydrated H^{+}-CHA-2. Correlated ^{29}Si and ^{27}Al intensities in (A) highlighted in blue correspond to paired-2NN Al configurations. The inset schematic diagrams show (A) possible 2NN configurations with silicon atoms (blue), aluminum atoms (red), and black lines representing bridging oxygen atoms, whereas (B) shows only isolated framework Al atoms. 1D ^{29}Si{^{1}H} CP-MAS spectra are shown to the left of each 2D spectrum, and ^{27}Al projections are shown on top. The spectra were acquired at 9.4 T, 100 K, and 8 kHz MAS.

that are covalently bonded through a single ^{29}Si–O–^{27}Al bond.[43] With this technique, paired-2NN aluminum configurations can be confidently identified from the isotropic ^{29}Si chemical shifts associated with correlated ^{29}Si and ^{27}Al intensity from *J*-coupled nuclei in ^{27}**Al**–O–^{29}Si–O–^{27}**Al** framework moieties. Figure 2A,B shows solid-state 2D ^{27}Al–^{29}Si *J*-mediated HMQC spectra for H^+-CHA-1 and H^+-CHA-2, which exhibit key differences in correlated intensity that manifest different distributions of framework Al atoms. Specifically, Figure 2A shows two well-resolved regions of correlated intensity for H^+-CHA-1 at 57 ppm in the ^{27}Al dimension, corresponding to four-coordinate framework Al atoms, correlated to ^{29}Si NMR signals at –106 ppm and at–99 ppm, from Q^4(1Al) moieties and Q^4(2Al) moieties, respectively; the latter unambiguously establishes the presence of paired-2NN ^{27}**Al**–O–^{29}Si–O–^{27}**Al** configurations in H^+-CHA-1. In contrast, the analogous spectrum of H^+-CHA-2 in Figure 2B shows correlated intensity only between the framework $^{27}Al^{IV}$ signal at 57 ppm and the ^{29}Si signal at –106 ppm from Q^4(1Al) species, with no detectable correlated intensity at –99 ppm associated with paired Q^4(2Al) moieties. Together, these two spectra establish that H^+-CHA-1 has more paired-2NN aluminum configurations than H^+-CHA-2.

Third-nearest-neighbor (3NN) **Al**–O–^{29}Si–O–^{29}Si–O–**Al** configurations of paired Al atoms in zeolite frameworks have been significantly more challenging to detect. This is due, in part, to the low probability of finding pairs of ^{29}Si atoms (4.7% natural abundance) that bridge covalently bonded Q^4(1Al) framework moieties, as well as their weak ^{29}Si–O–^{29}Si *J*-couplings. Nevertheless, 2D ^{29}Si–^{29}Si{^{1}H} CP-*J*-mediated NMR spectra acquired at 100 K provide a crucial combination of enhanced Boltzmann signal sensitivity and enhanced spectral resolution. These analyses correlate the isotropic ^{29}Si chemical shifts associated with pairs of *J*-coupled Q^4(1Al) ^{29}Si nuclei in **Al**–O–^{29}Si–O–^{29}Si–O–**Al** (3NN) framework configurations.

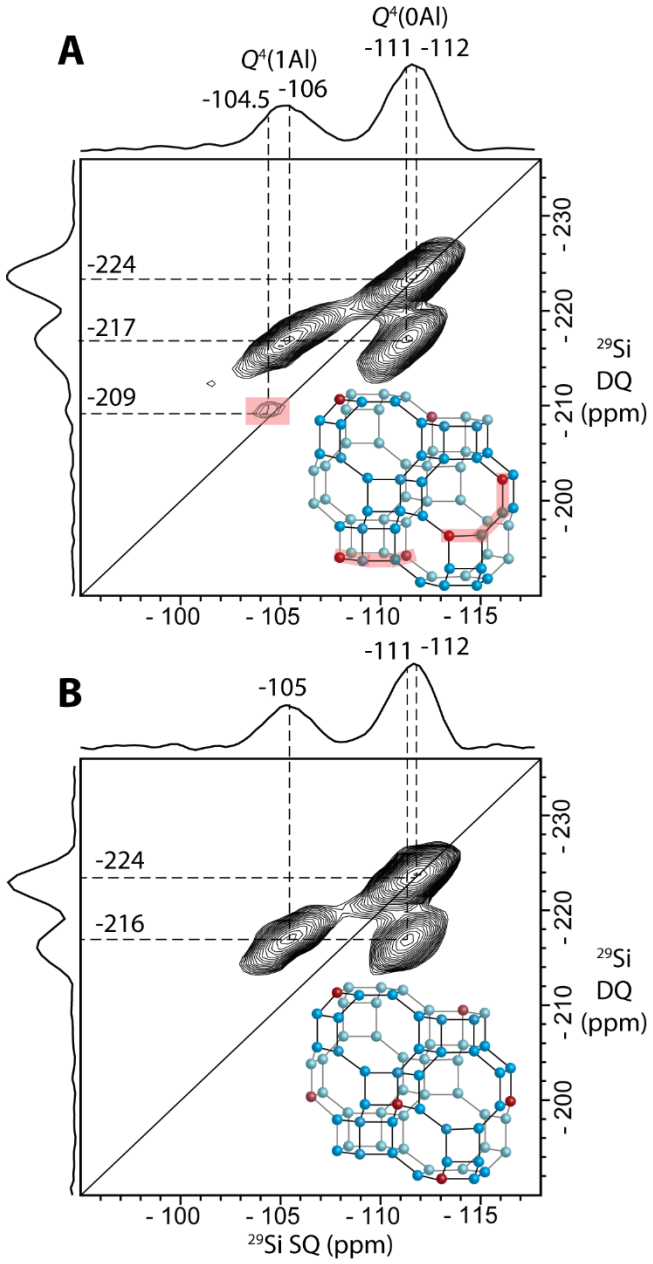

Figure 3. Solid-state 2D ^{29}Si–^{29}Si{^{1}H} *J*-mediated single-quantum-double-quantum NMR spectra of (A) hydrated H^{+}-CHA-1 and (B) hydrated H^{+}-CHA-2. Correlated intensity in (A) highlighted in red corresponds to Q^4(1Al)–Q^4(1Al) ^{29}Si framework moieties that bridge paired-3NN Al configurations, such as those depicted in the inset diagram in (A), which are absent in (B). 1D SQ and DQ projections are shown above and to the left, respectively, of each 2D spectrum. The spectra were acquired at 9.4 T, 100 K, and 8 kHz MAS.

These are manifested by correlated ^{29}Si signals in the isotropic single-quantum (SQ) dimension, which appear at the sum of their isotropic chemical shifts in the double-quantum (DQ) dimension of the 2D frequency map.[44] Figure 3A,B shows solid-state 2D ^{29}Si-^{29}Si{^{1}H} *J*-mediated NMR spectra for H^{+}-CHA-1 and H^{+}-CHA-2, respectively, with key differences that reflect different distributions of framework Al atoms. Specifically, Figure 3A shows three well-resolved regions of correlated ^{29}Si NMR signal intensity from *J*-coupled ^{29}Si nuclei in H^{+}-CHA-1 (i) along the double-diagonal line at –112 ppm in the single-quantum dimension –224 ppm in the double-quantum dimension) from covalently bonded Q^4(0Al) moieties in siliceous regions of the framework, (ii) off-diagonal correlated signals centered at –106 ppm and -111 ppm in the SQ dimension (–217 ppm, DQ dimension) from covalently bonded Q^4(1Al) and Q^4(0Al) framework moieties, respectively, and most importantly (iii) at –104.5 ppm along the double-diagonal from covalently bonded Q^4(1Al) moieties in **Al**–O–^{29}Si–O–^{29}Si–O–**Al** (3NN) configurations within the CHA framework (Fig. 3A, inset). No ^{29}Si signals associated with Q^4(2Al) or Q^3(0Al) moieties were detected, likely due to their low overall populations. For H^{+}-CHA-2, the analogous spectrum in Figure 3B acquired under identical conditions shows similar correlated ^{29}Si signals in the regions corresponding to *J*-coupled Q^4(0Al) –Q^4(0Al) and Q^4(1Al) –Q^4(0Al) framework moieties with approximately the same intensities as observed for H^{+}-CHA-1. Notably, however, correlated intensity corresponding to covalently bonded Q^4(1Al)–Q^4(1Al) ^{29}Si moieties is not present. Thus, H^{+}-CHA-1 has greater quantities of paired-3NN, as well as paired-2NN, configurations of Al atoms in its aluminosilicate framework compared to H^{+}-CHA-2.

To assess the extents to which the detected 2NN and 3NN Al configurations for H^{+}-CHA-1 and H^{+}-CHA-2 deviate from random Al distributions, chabazite structures with a

Si/Al=10 were simulated based on random aluminum distributions and repulsive Al-Al interactions.[16] The expected proportions of framework moieties (Tables S4–S7) differ from those measured for H^+-CHA-1 and H^+-CHA-2 (Figures S11, S12, Table S3). Comparisons show that the undetectable levels of 2NN and 3NN Al configurations in H^+-CHA-2 are consistent with expectations for Si/Al=10 based on repulsive Al-Al interactions. However, H^+-CHA-1 has a significantly greater fraction of paired-Al configurations than the simulation results predict, which suggests that synthesis using FAU zeolite as a precursor promotes local aluminum pairing. The simulated aluminum distributions corroborate the extent of Al pairing from the NMR analyses (Figures 2, 3) for H^+-CHA-1, and provide bounds to estimate the low levels of paired-2NN (10–20% of total Al) and moderate-to-high levels of paired-3NN Al configurations (60-80% Al) in this catalyst. In contrast, the levels of pairing in H^+-CHA-2 are too low to be quantified by these analyses.

Conclusions

Solid-state 2D NMR *J*-mediated correlation analyses enable second-nearest-neighbor and third-nearest-neighbor paired-aluminum configurations to be detected and unambiguously resolved in chabazite zeolite frameworks. These measurements exploit the through-covalent-bond selectivities of *J*-coupled ^{27}Al–O–^{29}Si and ^{29}Si–O–^{29}Si nuclei to directly detect paired-Al configurations that are distinct from isolated framework aluminum atoms. Two H^+-chabazite catalysts with similar Si/Al ratios were determined to have different extents of framework aluminum pairing, with a greater extent also shown to correlate with a higher rate of methanol dehydration despite similar Co^{2+} exchange levels. Thus, these 2D NMR correlation analyses provide information on the local pairing of aluminum heteroatoms in chabazite zeolite frameworks that is complementary to that obtained by divalent-cation-titration methods. Such

atomic-level insights provide important new design criteria for optimizing the syntheses of zeolite catalysts where proximate paired cations are the active moieties, as is the case for catalytic dehydration of methanol over H^+-CHA or selective catalytic reduction of NO_x over Cu^{2+}-CHA. The approach and insights here are expected to be transferrable broadly to other zeolite framework types, where paired framework heteroatoms contribute importantly to macroscopic catalyst adsorption or reaction properties.

Supporting Information

Materials and Methods

Materials. H^+-CHA-1 and H^+-CHA-2 were obtained in their H^+-exchanged forms from BASF (Iselin, New Jersey, USA). The two zeolites were synthesized using trimethyladamantylammonium hydroxide as the organic structure-directing agent, although H^+-CHA-1 was synthesized via inter-zeolite conversion (IZC) using FAU zeolite as a precursor, while H^+-CHA-2 was synthesized by conventional methods using molecular precurors.[40,41] The resulting products had very similar compositions (framework Si/Al~10, based on quantitative direct-excitation ^{29}Si MAS NMR spectra, see Figure S3) and were indistinguishable by conventional characterization techniques (Figures S1–S4).

Scattering characterization. Powder X-ray diffraction patterns were acquired on a Panalytical Empyrean Powder Diffractometer with a Cu-Kα radiation source, over a range of 2θ angles from 4° to 70°; a background was subtracted from the datasets.

NMR spectroscopy. Direct-excitation solid-state one-dimensional (1D) ^{29}Si and ^{27}Al NMR spectra of hydrated chabazite zeolites were acquired at 18.8 T under ambient temperature conditions on a 800 MHz Bruker Avance NMR spectrometer. The ^{29}Si NMR spectra were obtained using a 3.2 mm zirconia rotor at a magic-angle-spinning (MAS) frequency of 20 kHz. For the ^{29}Si NMR spectra, 168 scans were acquired with a 50 kHz 90° pulse and a 200 s recycle delay. During acquisition, SPINAL-64 heteronuclear decoupling was applied to ^{1}H nuclei.[45] The ^{27}Al NMR spectra were obtained using a 2.5 mm zirconia rotor at a MAS frequency of 30 kHz. For the ^{27}Al MAS NMR spectra, 4096 scans were acquired with a 0.5 μs excitation pulse corresponding to a 5° flip angle for an inherent ^{27}Al nutation curve, and a 0.2 s recycle delay. Prior to both ^{27}Al and ^{29}Si NMR measurements, the zeolite materials were stored for at least

24 h in a sealed container containing a saturated solution of potassium chloride to maintain a relative humidity of 85% to ensure full hydration of each chabazite zeolite. The ^{29}Si and ^{1}H NMR spectra were referenced to tetramethylsilane (TMS) at 0 ppm by using tetrakis(trimethylsilyl)silane (TKS) as a secondary standard (–9.84 ppm for ^{29}Si, 0.25 ppm for ^{1}H). The ^{27}Al NMR spectra were referenced to a 0.5 M aqueous solution of $Al(NO_3)$ at 0 ppm.

Direct-excitation solid-state 1D ^{1}H MAS NMR spectra with EASY background suppression and 2D ^{1}H–^{1}H single-quantum–double-quantum (SQ-DQ) NMR spectra of dehydrated chabazite zeolite powders were acquired at 18.8 T under ambient temperature conditions on a 800 MHz Bruker Avance NMR spectrometer using a 1.3 mm zirconia rotor spinning at 50 kHz. Prior to these measurements, H^+-chabazite powders were dehydrated under vacuum at 450 ^{o}C for 6 h with a temperature ramp of 2 ^{o}C/min, and MAS rotors were packed in a glove box to prevent rehydration. For the direct-excitation ^{1}H MAS NMR spectra, 128 scans were acquired with a 83.3 kHz 90^{o} pulse and a 3.5 s recycle delay. EASY background suppression was applied with a 50 ms delay after acquisition,[46] the background suppression was found to be necessary to remove a large background signal from the NMR probehead. For the 2D ^{1}H–^{1}H SQ-DQ NMR spectra, 64 increments of 64 scans were acquired with a t_1 increment of 80 μs. The BaBa-xy16 homonuclear double-quantum recoupling pulse sequence was used to recouple pairs of ^{1}H spins through their ^{1}H–^{1}H dipole-dipole couplings.[47] 83.3 kHz 90^{o} pulses were used for the BaBa-xy16 recoupling, and the total recoupling time was 0.4 ms. A 100 μs *z*-filter and 90^{o}-180^{o} spin-echo with 83.3 kHz r.f. pulses were used for detection.

Co^{2+} titration exchange analyses. For Co^{2+} exchange, the H^+-form of each chabazite zeolite powder was diluted at a ratio of 200 g solution/gram of zeolite and stirred in a 0.25 M $Co(NO_3)_2$ aqueous solution ($Co(NO_3)_2 \cdot 6H_2O$, Spectrum Chemical, ACS reagent grade) for 4 h at room

temperature. The powder was filter dried and rinsed with an excess of Milli-Q water, after which the filtrate was dried in an oven in air at 80 ^{o}C for 4 h. The exchanged zeolite was then calcined in a dry air flow of 0.5 SLM in a furnace with a temperature ramp of 2 ^{o}C/min up to 500 ^{o}C, at which temperature the furnace was held for 4 h. The exchanged, calcined zeolite powder was then diluted in $Ca(CO)_3$ and compressed into a disk-shaped pellet using a hydraulic press. The quantities of silicon, aluminum, and cobalt in these pellets were measured by laser ablation inductively-coupled plasma mass spectrometry.

Methanol dehydration reaction measurements. Kinetic analyses of methanol dehydration to dimethylether and water were conducted at 125 ^{o}C and 150 ^{o}C in a batch reactor within a specially designed NMR probehead. This enabled quantitative measurements of adsorbed reactant and product species to be conducted as a function of reaction time by acquiring *in situ* direct-excitation ^{13}C magic-angle spinning (MAS) NMR spectra under reaction conditions. Prior to NMR experiments, H^+-chabazite powders were dehydrated under vacuum at 450 ^{o}C for 6 h with a temperature ramp of 2 ^{o}C/min. After dehydration, 60 mg of dry powder was packed in a 7.5 mm NMR rotor designed for high-temperature, high-pressure applications, and 10 μL of ^{13}C-enriched methanol (Sigma Aldrich, 99% ^{13}C) were added, corresponding to a ratio of 3.0 mol $^{13}CH_3OH$/mol Al. The rotor was quickly sealed to prevent hydration. *In situ* direct-excitation 1D ^{13}C MAS NMR measurements were performed at a magnetic field of 11.7 T on a 500 MHz Bruker Avance NMR Spectrometer equipped with a double-resonance 7.5 mm NMR probehead from Revolution NMR, LLC at a MAS frequency of 5 kHz. Rotors were inserted into the probehead in the spectrometer and spun up to a 5 kHz MAS frequency at room temperature, after which the probehead was rapidly heated to either 125 or 150 ^{o}C, using temperature calibrations based on the ^{207}Pb NMR signal of $Pb(NO_3)_2$. As soon as the target

temperature was reached (1–2 min), the first ^{13}C NMR spectrum was acquired. For each direct-excitation ^{13}C MAS NMR spectrum, 32 scans were acquired with a recycle delay of 5 s between scans and a suitable delay between experiments such that the start of each ^{13}C NMR experiment was 10 min apart. A radiofrequency of 31.25 kHz was used for the ^{13}C 90° pulse, and SPINAL64 heteronuclear decoupling was applied to ^{1}H nuclei during acquisition. The time reported for each spectrum reflects the time elapsed from reaching the target temperature at the start of the NMR experiment. Conversions were calculated based on integrated line fits of the NMR data using DMFit,[49] and conversion was reported based on the amount of methanol measured in the first (0 min) ^{13}C NMR experiment.

Analyses of paired-Al framework atoms by 2D NMR. 2D *J*-mediated ^{27}Al-^{29}Si *J*-HMQC and 2D *J*-mediated ^{29}Si-^{29}Si CP refocused INADEQUATE NMR analyses were performed at 9.4 T at 100 K on a 400 MHz Bruker Ascend NMR spectrometer equipped with a triple-resonance Bruker NMR probehead using 3.2 mm zirconia MAS rotor at a spinning frequency of 8 kHz. For the 2D ^{27}Al-^{29}Si *J*-HMQC experiments, 64 increments of 512 scans with a t_1 increment of 250 μs were acquired with a recycle delay of 1 s between scans. 100 kHz (radiofrequency) r.f. pulses were applied to ^{29}Si, and 27.8 kHz r.f. pulses were applied to ^{27}Al. A 1-ms double-frequency-sweep shaped pulse was applied to ^{27}Al nuclei at the start of the pulse sequence and swept between 100 kHz and 1 MHz relative to the carrier frequency.[51] Prior to ^{29}Si-^{29}Si{^{1}H} CP refocused INADEQUATE experiments, powder samples were mixed with deionized water at a ratio of 1 g H_2O to 4 g powder to ensure full hydration of the zeolite. For 2D ^{29}Si-^{29}Si{^{1}H} CP refocused INADEQUATE experiments, 40 increments of 2048 scans with a t_1 increment of 250 μs were acquired. The recycle delay between scans was set to 1.12 s, equivalent to $1.4 \cdot T_1$, based on the ^{1}H T_1 measured using a saturation recovery experiment

with $^{29}Si\{^{1}H\}$ cross-polarization. A 50 kHz r.f. pulse was used for initial ^{1}H excitation, followed by a 5-ms cross-polarization contact pulse to transfer polarization from ^{1}H to ^{29}Si via heteronuclear ^{1}H–^{29}Si dipole-dipole couplings. The contact pulse frequencies for ^{29}Si and ^{1}H were empirically optimized to produce maximum signal, and a 50–100% linear ramp of the power applied to ^{1}H was used. For 90° and 180° pulses on ^{29}Si in the sequence, 50 kHz r.f. pulses were used. SPINAL64 heteronuclear decoupling was applied to ^{1}H after the contact pulse until the end of signal acquisition.

Basic characterization

To verify no differences in long-range ordering between H^{+}-CHA-1 and H^{+}-CHA-2, powder X-ray diffraction patterns were acquired of both materials and are shown in Figure S1. Both diffraction patterns are indexable to chabazite, with no evidence of reflections from additional crystalline phases or amorphous species.

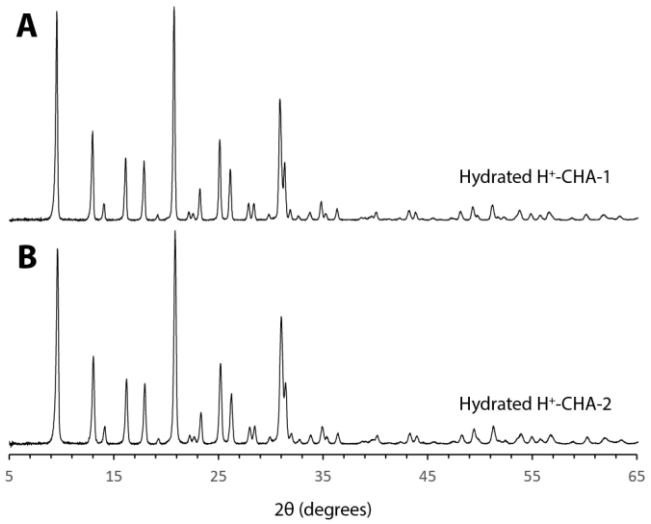

Figure S1. Wide-angle X-ray diffraction patterns for (A) hydrated H^{+}-CHA-1 and (B) hydrated H^{+}-CHA-2.

Solid-state 1D direct-excitation ^{27}Al NMR spectra of H^{+}-CHA-1 and H^{+}-CHA-2 were acquired to verify that there were not significant differences in the amount of extraframework

Al species. These spectra are shown in Figure S2. Two distinct ^{27}Al signals are resolved in each spectrum, along with spinning sidebands for the signal at 59 ppm that are marked with *. The intense ^{27}Al signal at 59 ppm corresponds to tetrahedrally-coordinated Al^{IV} atoms in the chabazite framework. The weak signal at 0 ppm is assigned to Al^{VI} species from either framework Al atoms that are strongly coordinated to two water molecules or from extraframework Al atoms that may form during the calcination process. In both materials, framework Al^{IV} atoms represent the vast majority of Al atoms present in each catalyst, with <5% of Al^{VI} species in each material.

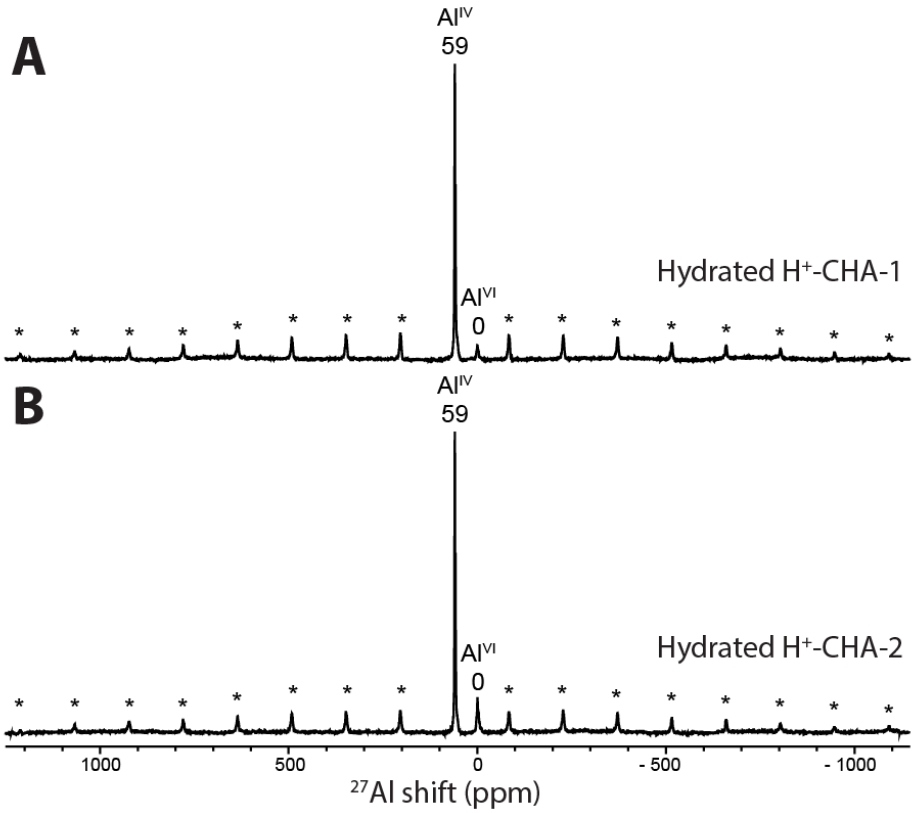

Figure S2. Direct-excitation solid-state ^{27}Al MAS NMR spectra of (A) hydrated H^+-CHA-1 and (B) hydrated H^+-CHA-2. The spectra were acquired under identical conditions at 298 K, 18.8 T and 30 kHz MAS with a recycle delay of 0.2 s.

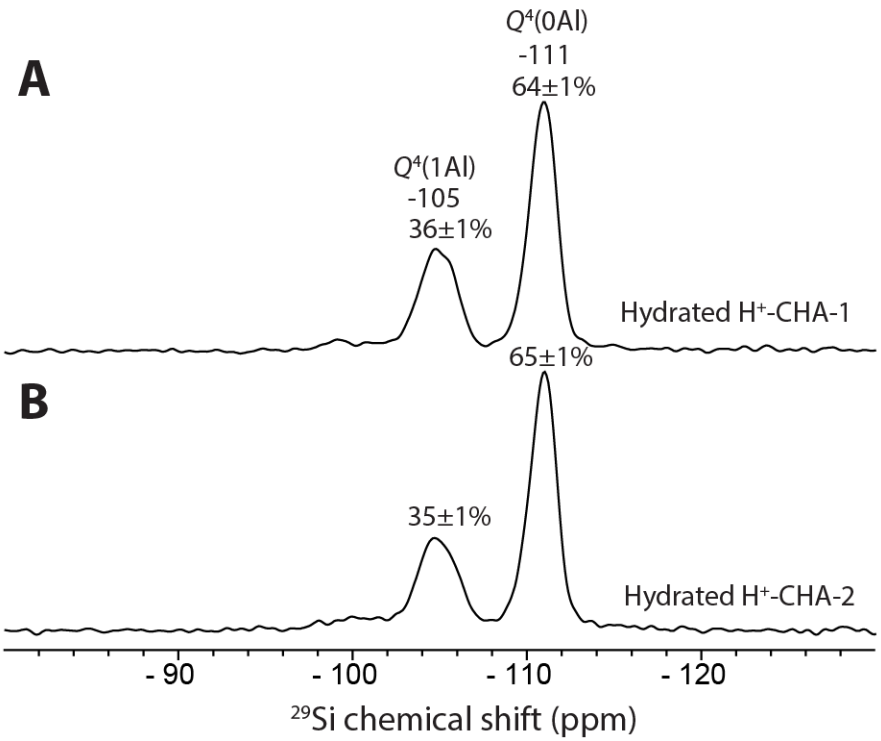

Figure S3. Direct-excitation solid-state ^{29}Si MAS NMR spectra of (A) hydrated H^+-CHA-1 and (B) hydrated H^+-CHA-2. The spectra were acquired under identical conditions at 298 K, 18.8 T, and 20 kHz MAS with a recycle delay of 200 s.

Solid-state 1D direct-excitation ^{29}Si NMR spectra were also acquired of H^+-CHA-1 and H^+-CHA-2 for comparison, and are shown in Figure S3. The spectra each contain two intense ^{29}Si signals at –105 ppm and –111 ppm, corresponding to Q^4(1Al) and Q^4(0Al) framework moieties, respectively (Q^m(nAl) represents a ^{29}Si atom that is covalently bonded via bridging oxygen atoms to m other nearest Si or Al tetrahedral site atoms, n of which are Al.) Additional intensity is evident in both spectra around –100 ppm, which is likely attributable to Q^3 silanols on crystallite surfaces, though could also be assigned to Q^4(2Al) moieties. Due to this ambiguity and low intensity, we have not included these species in the integration here. By integrating the Q^4(0Al) and Q^4(1Al) ^{29}Si NMR signals, framework Si/Al ratios can be calculated from the knowledge that a Q^4(0Al) moiety has four Si nearest neighbors, and a Q^4(1Al) moiety has three Si nearest neighbors and one Al nearest neighbor. Based on these

considerations, the framework Si/Al ratio for each catalyst is determined to be approximately 10.

Solid-state 1D direct-excitation ^{1}H NMR spectra were acquired of dehydrated H^{+}-CHA-1 and H^{+}-CHA-2 to compare levels of defects in the two materials. These spectra are shown in Figure S4. The two spectra consist of three regions of ^{1}H signal intensity at 1.7, 2.6, and 3.9 ppm corresponding to silanol, aluminum hydroxyl, and Bronsted acid-site ^{1}H species, respectively. (In addition, a signal is observed at 0.0 ppm marked by "‡" that is attributed to trace amounts of vacuum grease introduced to the materials during dehydration. The ^{1}H NMR spectra of H^{+}-CHA-1 and H^{+}-CHA-2 are almost identical. However, the intensity of the silanol ^{1}H NMR signal at 1.7 ppm is greater for H^{+}-CHA-2 than H^{+}-CHA-1.

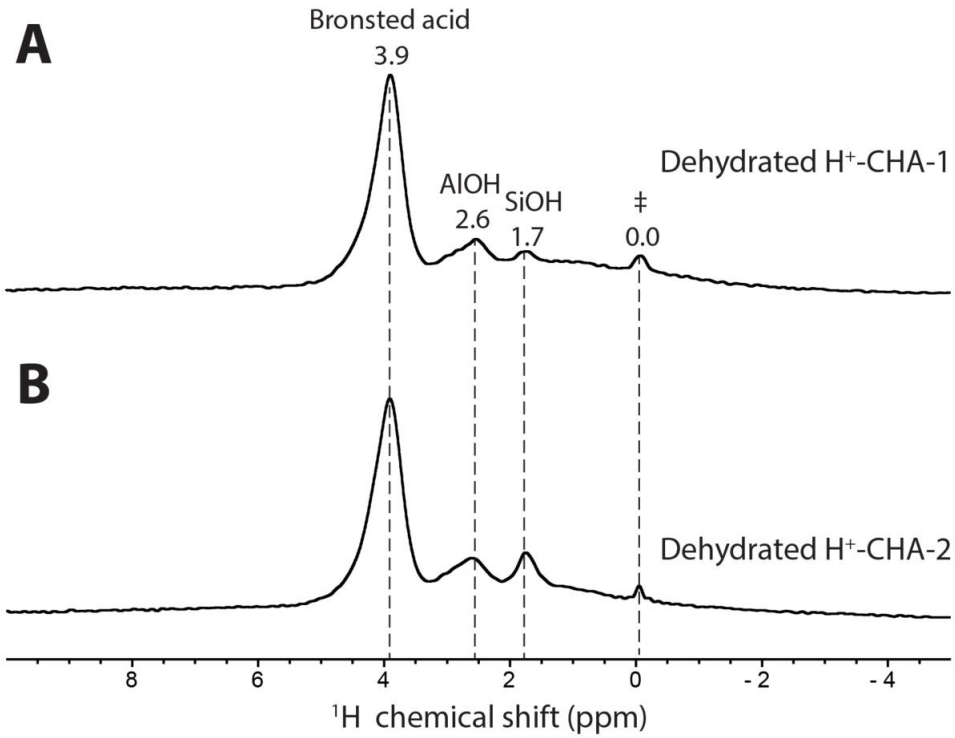

Figure S4. Direct-excitation solid-state ^{1}H MAS NMR spectra of (A) dehydrated H^{+}-CHA-1 and (B) dehydrated H^{+}-CHA-2. The spectra were acquired under identical conditions at 298 K, 18.8 T, and 50 kHz MAS.

If silanol defects are located near Bronsted acid sites, they may modify the activity of these sites for acid-catalyzed reactions, such as methanol dehydration.[48] To investigate whether the silanol defects present in H^+-CHA-1 and H^+-CHA-2 are located near Bronsted acid sites, and thus whether their different fractions of silanol species may contribute to their different reaction properties, 2D ^{1}H-^{1}H SQ-DQ NMR spectra were acquired and are shown in Figure S5. In these analyses, the isotropic ^{1}H chemical shifts associated with pairs of ^{1}H species in sub-nanoscale proximity are correlated. More specifically, the proximities ($\lesssim$0.5 nm) of dipole-dipole-coupled ^{1}H nuclei are established by correlating their isotropic chemical shifts in the single-quantum (SQ) dimension, which appear as the sum of their chemical shifts in the double-quantum (DQ) dimension. Thus, pairs of ^{1}H nuclei with the same chemical shift appear on the double-diagonal line drawn in Figure S5, whereas pairs of ^{1}H nuclei with different chemical shifts in different local environments exhibit correlated signals that are symmetrically displaced horizontally off the double-diagonal line. Four well-resolved ^{1}H signals attributed to H^+-chabazite appear in Figure S5A,B. Correlated ^{1}H intensity on the double-diagonal line at (SQ 3.9 ppm, DQ 7.8 ppm) corresponds to Bronsted acid sites in sub-nanoscale proximity to one another. More interestingly, correlated off-double-diagonal ^{1}H intensity at (SQ 3.9 ppm, DQ 6.5 ppm) and (SQ 2.6 ppm, DQ 6.5 ppm) corresponds to proximate Bronsted acid and AlOH species. Similarly, the correlated ^{1}H intensity along the double-diagonal line at (SQ 2.6 ppm, DQ 5.2 ppm) corresponds to AlOH species in sub-nanoscale proximity of one another and that at (SQ 1.7 ppm, DQ 3.4 ppm) corresponds to proximate silanol species. Most importantly, no intensity correlations are observed between silanol ^{1}H species and either AlOH or Bronsted acid ^{1}H species for both of the H^+-CHA-1 and H^+-CHA-2 materials. This indicates that there are not significant amounts of silanol species within ca. 0.5 nm proximity of acid

sites active for methanol dehydration. Thus, the differences in silanol populations between H^+-CHA-1 and H^+-CHA-2 observed in Figure S4 are not expected to influence methanol dehydration activity of the catalysts.

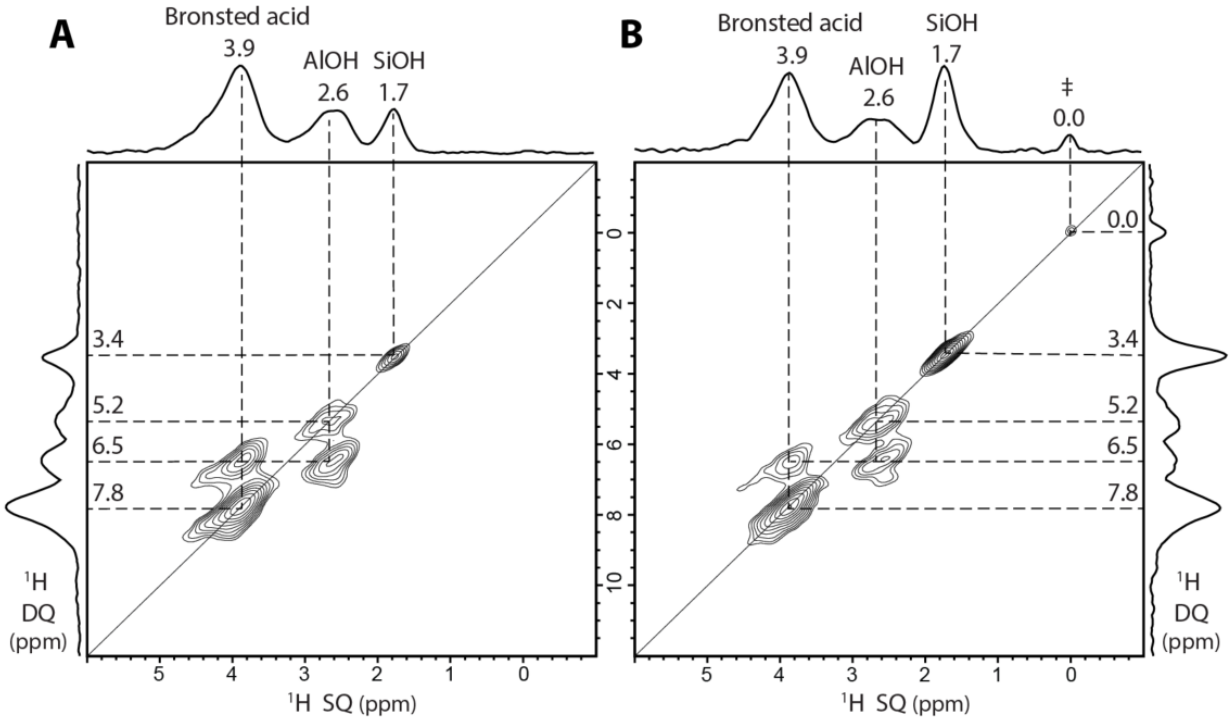

Figure S5. Solid-state 2D ^{1}H-^{1}H dipolar-mediated single-quantum–double-quantum NMR spectra of (A) dehydrated H^+-CHA-1 and (B) dehydrated H^+-CHA-2. The spectra were acquired under identical conditions at room temperature, 18.8 T, and 50 kHz MAS. The signal labeled with "‡" at 0.0 ppm is attributed to trace amounts of vacuum grease from the dehydration process.

Co^{2+} titration is a commonly used method to assess the levels of paired aluminum species in chabazite zeolites, based on the assumption that Co^{2+} will only exchange into charge-balancing cation positions for certain paired framework aluminum configurations, not isolated aluminum species. Table S1 summarizes the observed Co^{2+} exchange levels for H^+-CHA-1 and H^+-CHA-2. Both materials exhibit exceedingly low levels of Co^{2+}-exchanged sites, suggesting very low levels of paired framework aluminum configurations in both materials.

Table S1. Co/Al atomic ratios for the Co^{2+}-exchanged chabazite catalysts

Sample	Co/Al
Co,H^+-CHA-1	0.0161(3)
Co,H^+-CHA-2	0.0092(4)

Reaction studies

Batch methanol dehydration reactions were tracked *in situ* by solid-state 1D direct-excitation ^{13}C NMR. For both H^+-CHA-1 and H^+-CHA-2, the reaction was tracked at 125 ^oC and 150 ^oC, as shown in Figures S6-S9. Two regions of ^{13}C NMR signal were observed. ^{13}C NMR signal observed at 52 ppm was assigned to adsorbed methanol species. ^{13}C NMR signal observed at 62 ppm was assigned to adsorbed dimethyl ether. As the integrated intensities of these ^{13}C NMR spectra are quantitative, methanol conversions as a function of time could easily be calculated from the change in integrated intensity for the two bands of NMR signal at 52 and 62 ppm. For the measurements performed at 150 ^oC, the methanol conversion at 90 min was 84% over H^+-CHA-1 and 79% over H^+-CHA-2, both corresponding to over 2 moles of methanol reacted per mole of aluminum. For the 125 ^oC reaction measurements, conversions of 55% and 49% were reached over H^+-CHA-1 and H^+-CHA-2, respectively. Both conversions correspond to over 1 mole of methanol reacted per mole Al. These ratios of methanol reacted per aluminum serve as lower bounds, as some Al species may not be accessible, and more turnovers are expected to occur over paired sites.

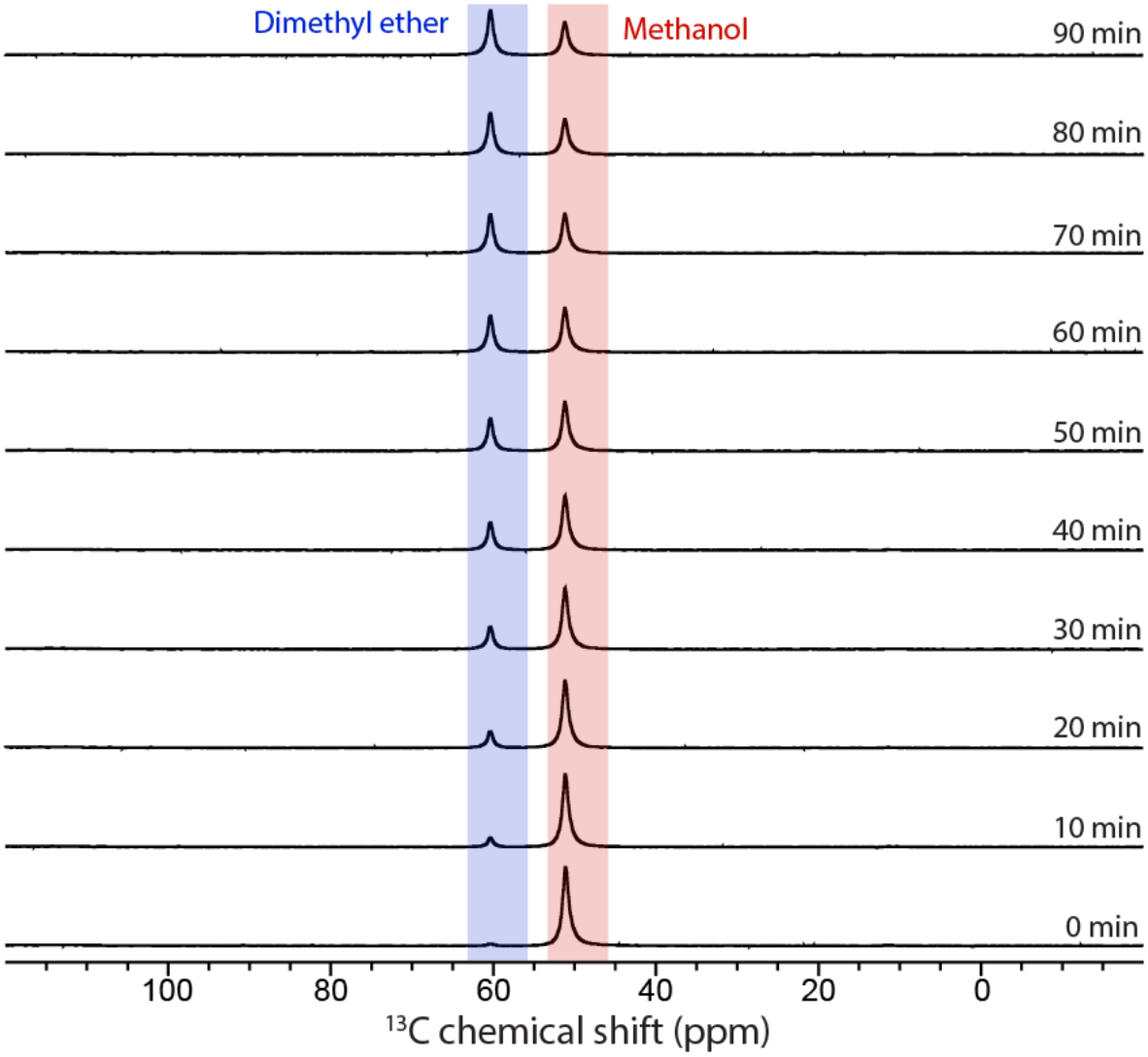

Figure S6. *In situ* direct-excitation 1D ^{13}C MAS NMR spectra of methanol reacting to form dimethylether over H^+-CHA-1 after different amounts of time in a batch reactor at 398 K (125 ^oC), 11.7 T, and 5 kHz MAS with a recycle delay of 5 s. The relative integrated intensities of the signals within the blue and red bands were used to determine the conversion as a function of time, as presented in Figure 1 of the manuscript.

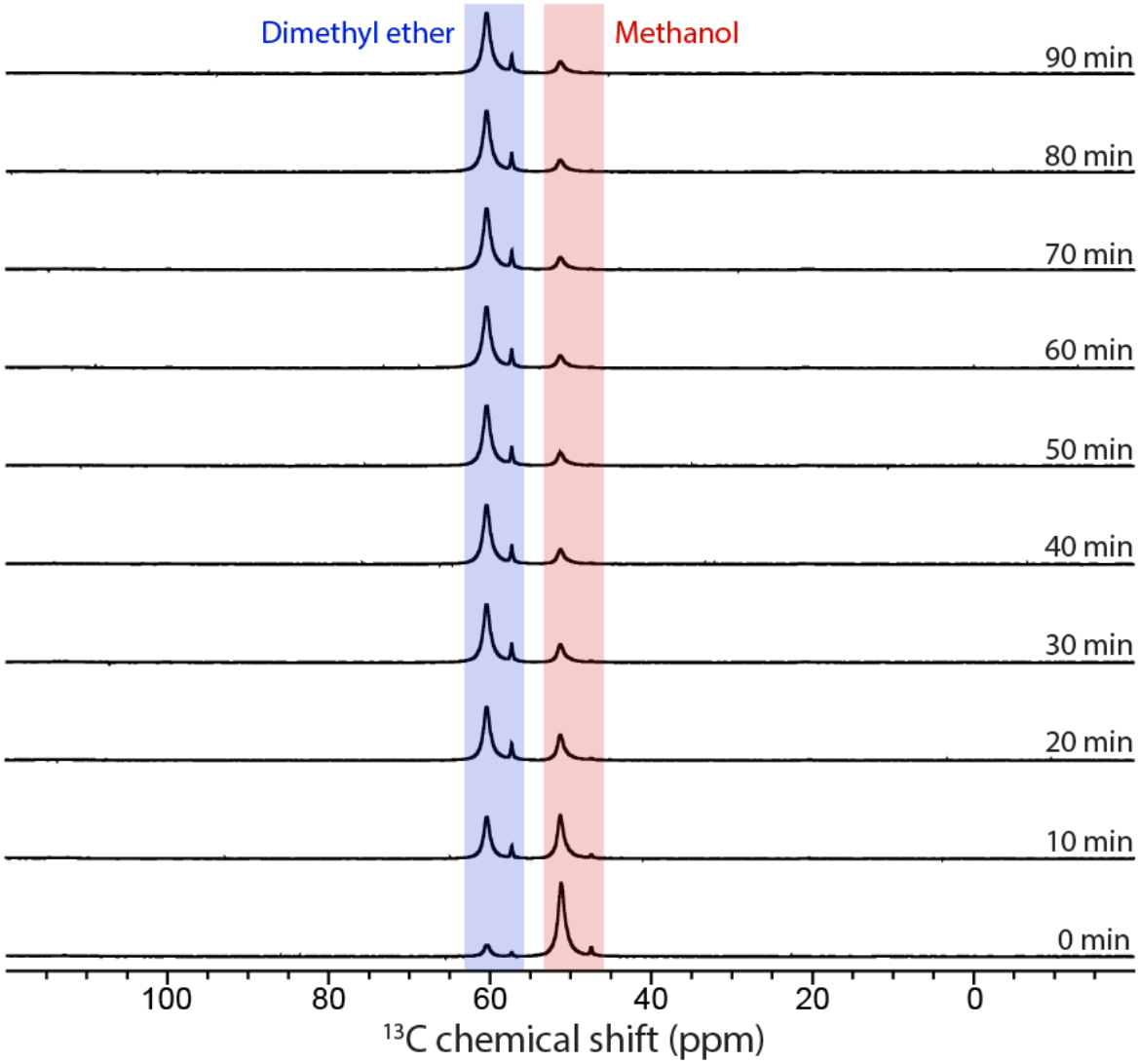

Figure S7. *In situ* direct-excitation 1D ^{13}C MAS NMR spectra of methanol reacting to form dimethylether over H^+-CHA-1 after different amounts of time in a batch reactor at 423 K (150 ^oC), 11.7 T, and 5 kHz MAS with a recycle delay of 5 s. The relative integrated intensities of the signals within the blue and red bands were used to determine the conversion as a function of time, as presented in Figure 1 of the manuscript.

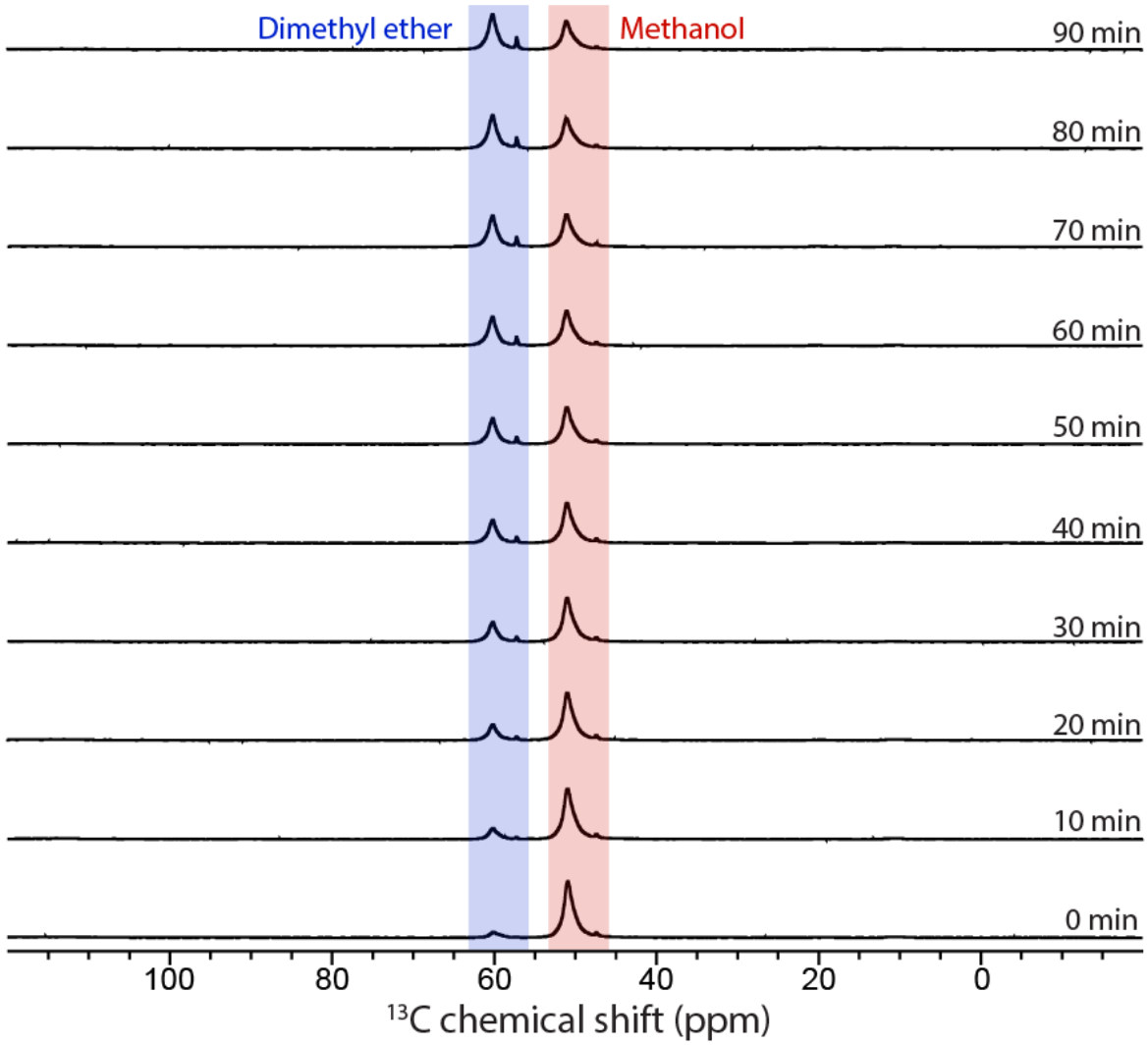

Figure S8. *In situ* direct-excitation 1D ^{13}C MAS NMR spectra of methanol reacting to form dimethylether over H^+-CHA-2 after different amounts of time. The spectra were acquired at 398 K (125 ^oC), 11.7 T, and 5 kHz MAS with a recycle delay of 5 s. The relative integrated intensities of the signals within the blue and red bands were used to determine the conversion as a function of time, as presented in Figure 1 of the manuscript.

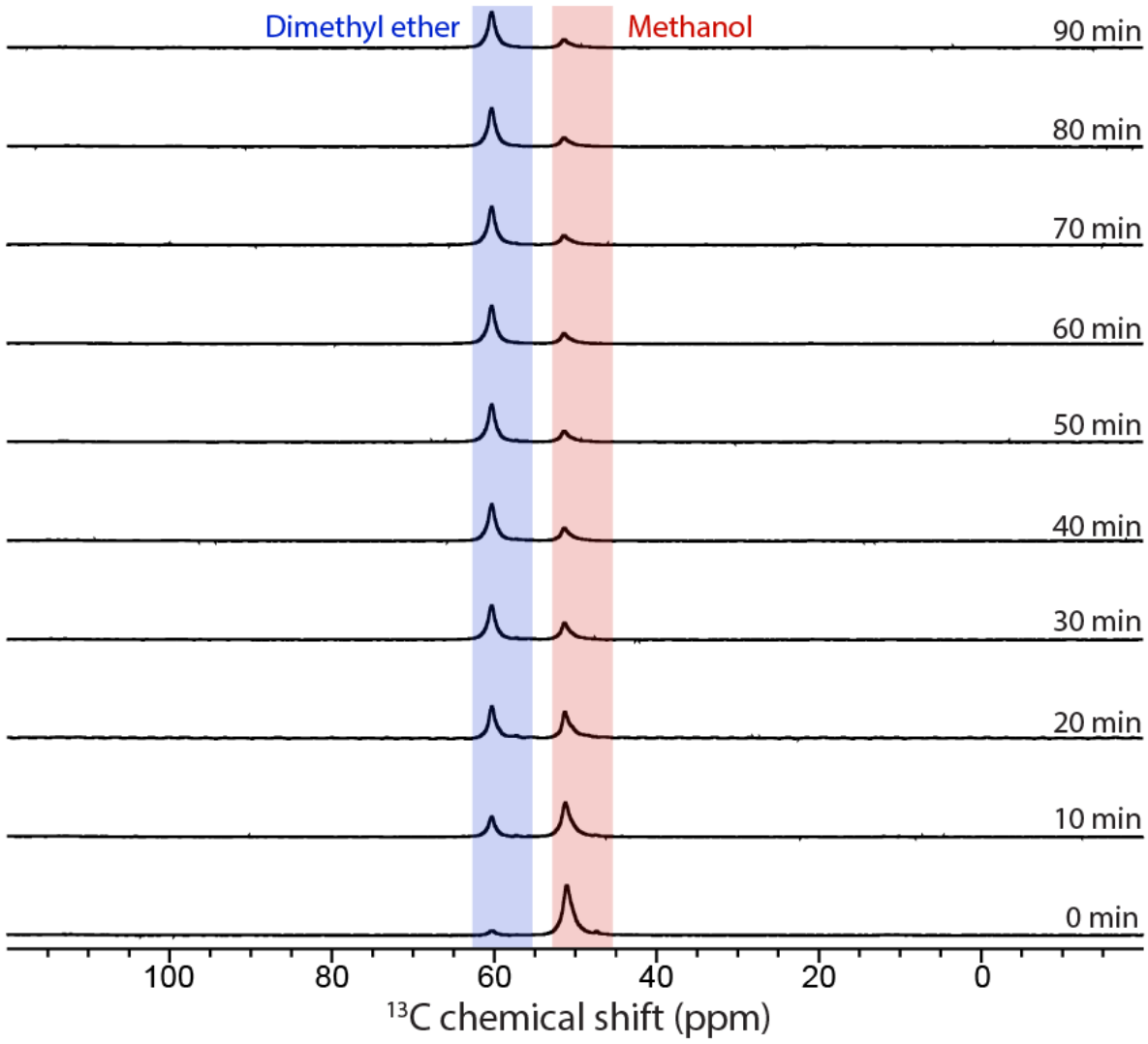

Figure S9. *In situ* direct-excitation 1D ^{13}C MAS NMR spectra of methanol reacting to form dimethylether over H^+-CHA-2 after different amounts of time in a batch reactor at 423 K (150 ^{o}C), 11.7 T, and 5 kHz MAS with a recycle delay of 5 s. The relative integrated intensities of the signals within the blue and red bands were used to determine the conversion as a function of time, as presented in Figure 1 of the manuscript.

Kinetic data were fit to a simple reversible rate expression that accounts for the different rates of methanol dehydration to dimethylether observed for the two catalysts. The rate expression depends on the amounts of adsorbed methanol and dimethylether and is given by:

$$-r_{\mathrm{CH3OH}} = k_{\mathrm{app,f}} N_{\mathrm{CH3OH}} - k_{\mathrm{app,r}} N_{\mathrm{DME}}$$

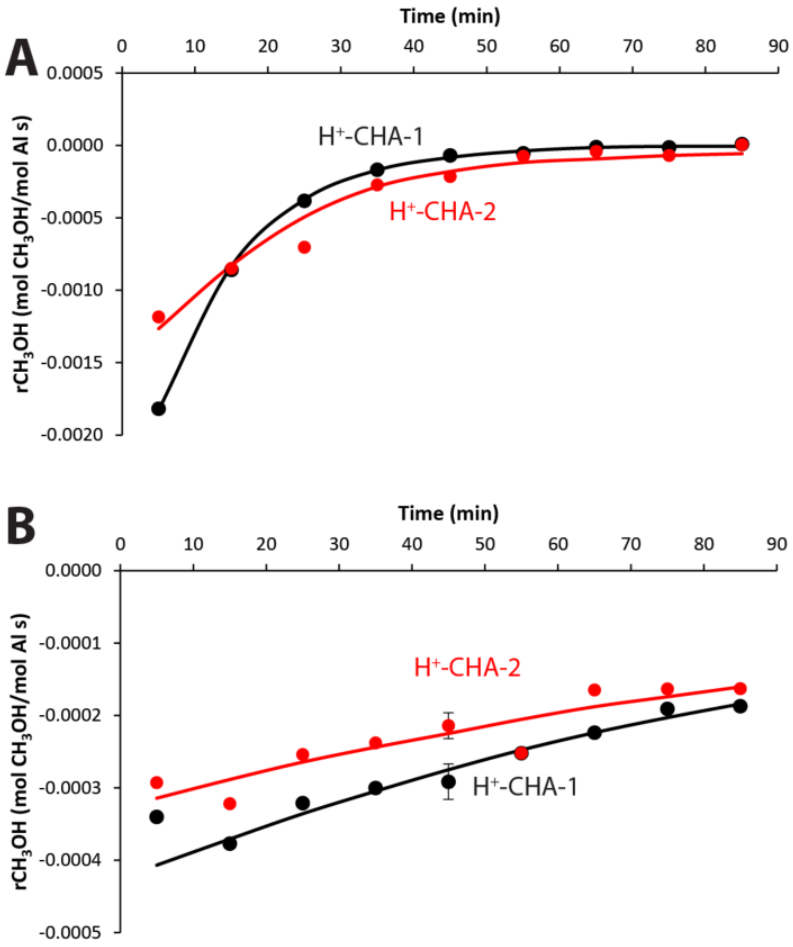

Figure S10. Methanol dehydration rates as a function of time for catalysts H^+-CHA-1 and H^+-CHA-2 at (A) 150 °C and (B) 125 °C. The rates on the *y*-axis were calculated from the integrated intensities (by taking the slopes between two time points) of the well-resolved ^{13}C NMR signals for methanol and dimethylether in the time-resolved *in situ* ^{13}C MAS NMR spectra in Figures S6-S9. The total NMR signal intensity was determined from the initial 10 μL of liquid ^{13}C-methanol at room temperature loaded into the MAS NMR rotor, which served as a batch reactor. Representative uncertainty bars are shown for the reaction rates at 45 min. The uncertainty bars in (A) are too small to be seen on the scale used.

where $k_{app,f}$ (s^{-1}) is the apparent forward rate coefficient with a first-order dependence on the amount of adsorbed methanol on the catalyst per mole of aluminum, N_{CH3OH} (mol CH_3OH/mol Al), and $k_{app,r}$ (mol CH_3OH/(mol DME s) is the apparent reverse rate coefficient with a first-order dependence on the amount of dimethylether adsorbed on the catalyst per mole of Al, N_{DME} (mol DME/mol Al). The amounts of reactants adsorbed on the catalyst were calculated

by taking the 10 μL of liquid methanol initially added to the rotor at room temperature to account for 100% of the ^{13}C signal observed in the *in-situ* NMR measurements; the small fractions of reactants and products present in the gas phase in the NMR rotor were neglected. The total ^{13}C NMR signal remained constant over the course of the reaction, consistent with the amounts of relevant species in the rotor headspace were not contributing significantly to the signals measured or changing significantly. The first-order dependence on the moles of adsorbed methanol is consistent with previous studies of methanol dehydration to dimethylether in differential reactors.[37,50] The first-order dependence on the moles of product dimethylether associated with the reverse reaction is not a factor in these studies due to the low conversions. Nevertheless, this dependence is consistent with the dominant mechanism proposed from a recent computational microkinetic model proposed for methanol dehydration over Bronsted-acid-exchanged zeolites.[38] The rate expression was fit to the acquired kinetic data over time by assuming the reaction rate at the midpoint between two collected data points could be linearly interpolated. The results of this fitting and the fitted rate coefficients are shown in Figure S10 and Table S2. As reaction rates were only measured at two temperatures, precise activation energies for the reaction over each catalyst were not obtained. Nevertheless, activation energies for $k_{app,f}$ calculated from data acquired at 125 ^{o}C and 150 ^{o}C are on the order of 100 kJ/mol for both catalysts, which is consistent with recent work by Marsden, *et al.*[38]

Table S2. Apparent rate coefficients for methanol dehydration at 150 ^{o}C or 125 ^{o}C over the H^{+}-CHA catalysts

	150 ^{o}C		125 ^{o}C	
	H^{+}-CHA-1	H^{+}-CHA-2	H^{+}-CHA-1	H^{+}-CHA-2
$k_{app,f}$ (s^{-1})	11.8	6.5	1.7	1.4
$k_{app,r}$ (mol CH_3OH / (mol DME s))	3.6	2.8	0.2	0.2

Additional 2D NMR analysis and simulations

Based on greater confidence provided by 2D NMR signal assignments, more precise fits of solid-state 1D direct-excitation were performed and are shown in Figure S11. The integrated intensities from these fits are shown in Table S3. The information from Figure 2 provide confidence in deconvoluting the Q^4(2Al) and Q^3(0Al) ^{29}Si NMR signals, which were excluded from the estimated deconvolution in Figure S3 due to their low intensity. In particular, the Q^4(2Al) signal corresponds to 2NN paired aluminum configurations. Notably, the deconvolution indicates a larger amount of external surface silanols in H^+-CHA-2 than H^+-CHA-1. This is consistent with the analyses of the ^{1}H NMR spectra of dehydrated H^+-CHA-1 and H^+-CHA-2 in Figure S4. In addition, deconvolutions of the indirect dimension of the 2D ^{29}Si-^{29}Si *J*-mediated NMR spectra in Figure 3 integrated around the Q^4(1Al) region were performed and are shown in Figure S11. The double-quantum signal at –209 ppm corresponds to Q^4(1Al)–Q^4(1Al) framework moieties in paired-3NN aluminum configurations. As in Figure 3, paired-3NN aluminum configurations are detected in H^+-CHA-1 but not H^+-CHA-2. It should be noted that the signal intensities are related to individual Q^4(1Al) ^{29}Si nuclei in bonded pairs, rather than number of pairs, so the number of Q^4(1Al)–Q^4(1Al) bonds are double-counted by these analyses. As a result, approximately 5% of the total signal in (A) results from Q^4(1Al)–Q^4(1Al) bonds and 95% results from Q^4(1Al)–Q^4(0Al) bonds, though this comparison is not absolutely quantitative.

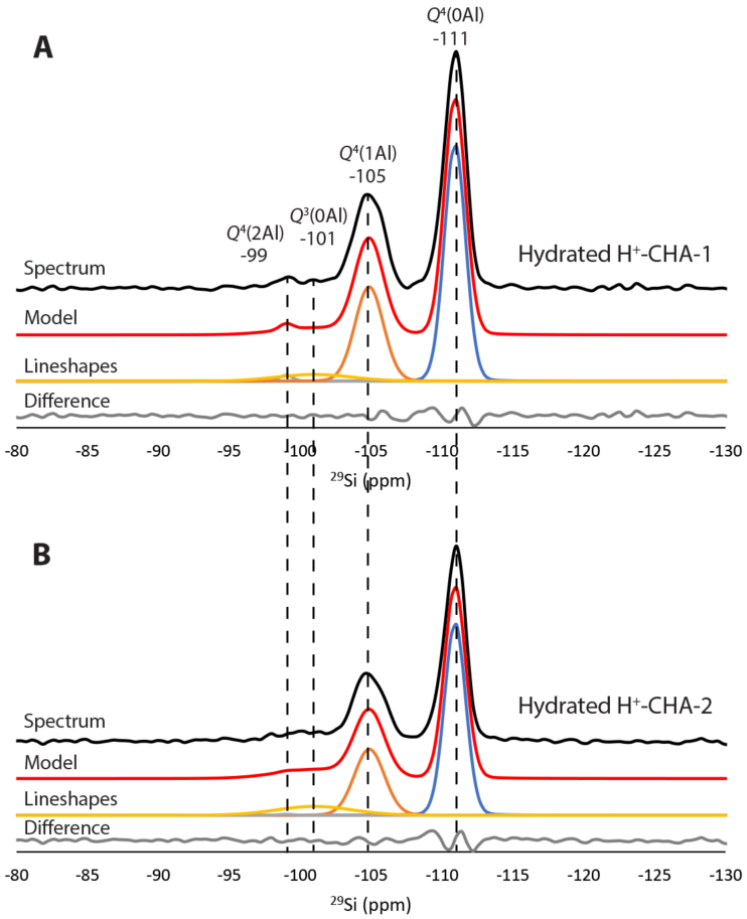

Figure S11. Spectral deconvolutions of direct-excitation ^{29}Si MAS NMR spectra for (A) hydrated H$^+$-CHA-1 and (B) hydrated H$^+$-CHA-2 based on the respective isotropic chemical shifts and linewidths established by the 2D ^{27}Al-^{29}Si *J*-HMQC NMR analyses in Figure 2 for each $Q^n(m\text{Al})$ species.

Table S3. Relative populations of framework ^{29}Si moieties in the H$^+$-CHA catalysts, as determined from deconvolution of ^{29}Si MAS NMR spectra in Figure S11.

Framework moiety	^{29}Si signal, ppm	H$^+$-CHA-1	H$^+$-CHA-2
Q^4(0Al)	–111	61%	60%
Q^4(1Al)	–105	32%	30%
Q^4(2Al)	–99	1%	0%
Q^3(0Al)	–101	6%	10%

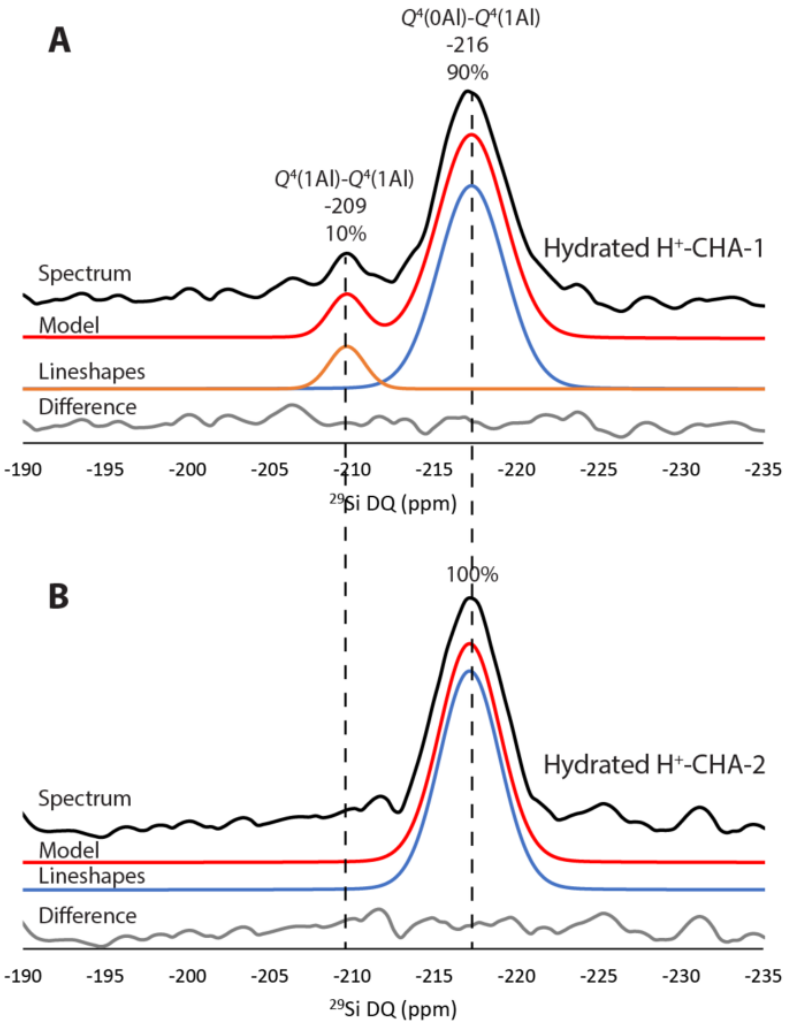

Figure S12. Spectral deconvolutions of the vertical double-quantum (DQ) projections of 2D ^{29}Si-^{29}Si{^{1}H} *J*-mediated CP-INADEQUATE NMR spectra in Figure 3 over the single-quantum range –103 to –108 ppm for (A) hydrated H^+-CHA-1 and (B) hydrated H^+-CHA-2.

Simulations of a chabazite structure with a Si/Al ratio of 10 were performed to calculate the relative quantities of Q^4(0Al), Q^4(1Al), Q^4(2Al), Q^4(3Al), and Q^4(4Al) ^{29}Si moieties, along with covalently bonded pairs of Q^4(1Al)–Q^4(1Al) and Q^4(1Al)–Q^4(0Al) moieties, based on both random aluminum distributions and repulsive Al-Al interactions, following methods from Di Iorio, *et al.*[23] The fractions of framework aluminum species in the simulated crystallite participating in either second-nearest-neighbor or third-nearest-neighbor paired Al configurations were also calculated. The Atomic Simulation Environment and Multiscale

Atomic Zeolite Simulation Environment libraries in Python were used for the simulations.[52,53] A 972 T-site supercell of chabazite with periodic boundary conditions based on the CHA crystal structure from the International Zeolite Association was populated with 88 Al atoms at random locations, for an approximate Si/Al ratio of 10. The only restriction placed on the Al insertion was to forbid Al-O-Al bonding that would violate Lowenstein's rule.[17] The quantities of Q^4(0Al), Q^4(1Al), Q^4(2Al), Q^4(3Al), and Q^4(4Al) Si moieties, along with Q^4(1Al)–Q^4(1Al) and Q^4(1Al)–Q^4(0Al) Si configurations, were calculated for 500 chabazite structures generated in this manner to obtain distributions of moieties that were randomly distributed within a crystallite framework. The results are tabulated in Table S4, with uncertainties in parentheses representing the 95% certainty bounds of the distributions of moieties from 500 repetitions.

Table S4. NMR-relevant moieties for simulated crystal with random Al distributions

	Q^4(0Al)	Q^4(1Al)	Q^4(2Al)	Q^4(3Al)	Q^4(4Al)	Q^4(1Al)–Q^4(1Al)	Q^4(1Al)–Q^4(0Al)
Amounts	581(13)	258(23)	42(11)	3(4)	0	84(25)	589(55)
Percentages	66%	29%	5%	0%	0%	12%	88%

Monte Carlo simulations were used to generate a chabazite structure with Al–Al repulsion-biased aluminum distributions. A 972 T-site chabazite structure with 88 randomly distributed aluminum atoms was generated, as described above. The total energy of the supercell was calculated from a formula for repulsive Al–Al interactions adapted from work by Di Iorio, *et al.* and Li, *et al.*:[16,23]

$$E_{\mathrm{Al-Al}} = 7.08\left(\frac{1}{d_{\mathrm{Al-Al}}} - \frac{1}{d_{\max}}\right) \quad ,$$

where $E_{\text{Al-Al}}$ is the energy associated with atomic Al–Al interactions in eV, $d_{\text{Al-Al}}$ is the distance between two Al atoms in Ångstroms, and $d_{\max}$ is the cutoff distance chosen for the simulation.

This cutoff distance was set at 10.85 Å to be consistent with previous work. The total energy of the system is $E_{\text{Al-Al}}$, which was summed over all possible Al-Al pairs in the supercell.

To create an aluminum distribution that minimized the total energy of the supercell, Al atoms in the supercell were randomly selected and a swap was attempted with one of the selected Al atom's nearest-neighbor Si atoms selected at random. The swap acceptance probability was given by:

$$P = \min\left(1, \exp\left(-\frac{\Delta E_{\text{Al-Al}}}{k_{\text{B}}T}\right)\right)$$

where $\Delta E_{\text{Al-Al}}$ corresponds to the difference in energy resulting from the swap, k_{B} is Boltzmann's constant, and T is the absolute temperature, set arbitrarily to 423 K, a typical temperature for zeolite synthesis. The swap was not attempted if the resulting configuration would violate Lowenstein's rule. 5×10^5 total attempted swaps were made. The total energy of the system equilibrated after about 1×10^5 attempted swaps, as shown in Figure S13. After 2.5×10^5 attempted swaps, the quantities of Q^4(0Al), Q^4(1Al), Q^4(2Al), Q^4(3Al), and Q^4(4Al)

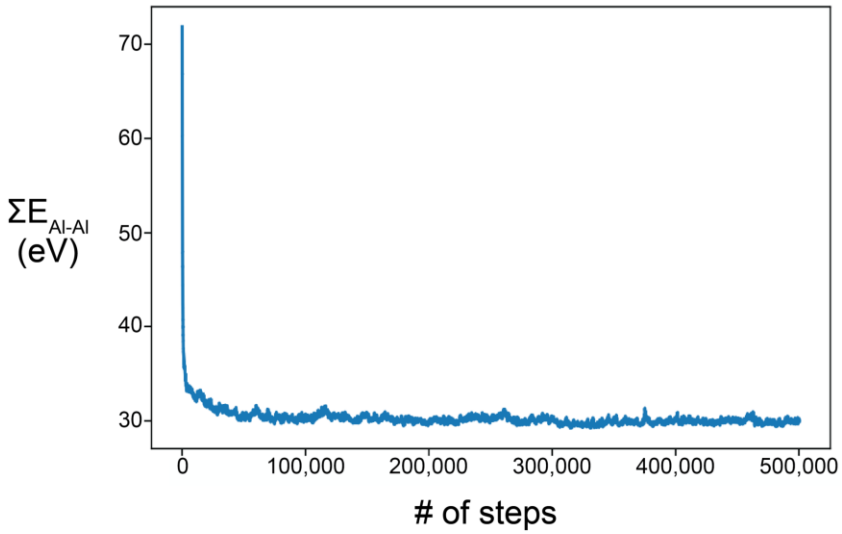

Figure S13. Plot of total energy due to distance-based Al–Al pair interactions as a function of steps or attempted swaps. The system equilibrates after approximately 100,000 steps, after which small oscillations are observed due to swaps with minor energy penalties. This plot is representative of all five simulation runs.

Si moieties along with Q^4(1Al)–Q^4(1Al) and Q^4(1Al)–Q^4(0Al) configurations were calculated every 1000 attempted swaps, for a total of 250 data points recorded from a simulation run. Five simulation runs were performed, and the results were consistent across different random starting points; these values are tabulated in Tables S5 and S6.

Table S5 summarizes the results of five runs of the Monte Carlo simulation for Al distributions in chabazite with repulsive Al–Al interactions. Notably, the distributions of moieties are very similar for each run, and the sampling within each run after equilibrium is reached shows only small deviations in the relative amounts of moieties due to kinetic effects, as represented to 95% certainty shown in the parentheses. Table S6 shows the same values but expressed as percentages for easy comparisons to the experimentally determined relative amounts of these moieties in H^+-CHA-1 and H^+-CHA-2 shown in Table S3 and Figure S12.

Table S5. Numbers of NMR-relevant moieties in a 972 T-site chabazite crystal formed with repulsive Al–Al interactions for 5 different simulation runs.

Run	Q^4(0Al)	Q^4(1Al)	Q^4(2Al)	Q^4(3Al)	Q^4(4Al)	Q^4(1Al)–Q^4(1Al)	Q^4(1Al)–Q^4(0Al)
1	533(2)	350(3)	1(2)	0	0	58(9)	936(15)
2	533(2)	350(4)	1(2)	0	0	56(9)	936(16)
3	533(2)	350(4)	1(2)	0	0	55(12)	940(22)
4	533(2)	350(3)	1(2)	0	0	54(12)	943(21)
5	533(1)	351(2)	0(1)	0	0	50(8)	953(15)

Table S6. NMR-relevant moieties from simulation runs for a chabazite crystal as a percentage of total moieties.

Run	Q^4(0Al)	Q^4(1Al)	Q^4(2Al)	Q^4(3Al)	Q^4(4Al)	Q^4(1Al)–Q^4(1Al)	Q^4(1Al)–Q^4(0Al)
1	60%	40%	0%	0%	0%	6%	94%
2	60%	40%	0%	0%	0%	6%	94%
3	60%	40%	0%	0%	0%	6%	94%
4	60%	40%	0%	0%	0%	5%	95%
5	60%	40%	0%	0%	0%	5%	95%
mean	60%	40%	0%	0%	0%	6%	94%

The counting statistics of NMR-relevant ^{29}Si moieties for random distributions of aluminum in a chabazite framework with Si/Al = 10 indicate much higher fractions of Q^4(2Al) moieties and Q^4(1Al)–Q^4(1Al) bonded pairs than are detected in either H^+-CHA-1 or H^+-CHA-2 (Table S3, Figure S12). This indicates that the distributions of aluminum in both catalysts are non-random.

The Monte Carlo simulation results indicate that for a chabazite crystallization process (with Si/Al = 10) that is controlled primarily by Al–Al repulsive interactions, significant fractions of Q^4(2Al) moieties, corresponding to second-nearest-neighbor aluminum configurations, are unlikely to form, in contrast to the large amounts observed for a simulated chabazite with a random aluminum distribution. This is consistent with the results in Figure 2B and Table S3 for H^+-CHA-2. The detectable Q^4(2Al) moieties in H^+-CHA-1 (Figure 2A, Table S3) suggest that additional factors other than repulsive aluminum interactions contribute to the distribution of CHA framework aluminum atoms that is observed.

In addition, the aluminum distributions resulting from the Monte Carlo simulations indicate that the number of Q^4(1Al)–Q^4(1Al) moieties relative to the number of Q^4(1Al)–Q^4(0Al) moieties should be relatively small for a chabazite material with a Si/Al = 10, if repulsive Al-Al interactions are a primary factor in determining the framework aluminum distribution. This is again consistent with the experimental results for H^+-CHA-2 in Figures 3B and S12. No correlated signal intensity is detected from Q^4(1Al)–Q^4(1Al) ^{29}Si moieties, in comparison to the expected 5-6% relative to the total Q^4(1Al)–Q^4(1Al) and Q^4(1Al)–Q^4(0Al) moieties predicted by the simulation. This is possibly due to the low signal-to-noise of Figure S12, and the semi-quantitative signals produced by the 2D ^{29}Si-^{29}Si *J*-mediated NMR experiment. The proximity of ^{27}Al atoms to ^{29}Si moieties results in faster nuclear spin-lattice (T_1) and spin-spin

(T_2) relaxation, i.e., a Q^4(1Al) moiety exhibits a shorter ^{29}Si T_1 value than a Q^4(0Al) moiety in the same material.[54] As a result, the observed double-quantum ^{29}Si NMR signal associated with Q^4(1Al)–Q^4(1Al) moieties may be weaker relative to the observed DQ ^{29}Si NMR signal associated with Q^4(0Al)–Q^4(1Al) moieties, thereby underestimating the fraction of paired-3NN Al moieties. In contrast, the appreciable DQ ^{29}Si NMR signal intensity associated with Q^4(1Al)–Q^4(1Al) moieties observed in Figures 3A and S12 indicates a significant deviation from the different model-predicted populations of these moieties in Table S6 for H^+-CHA-1. The true population of Q^4(1Al)–Q^4(1Al) moieties in this material is likely higher than the 10% overall signal intensity observed in Figure S12.

Determining the fractions of total framework aluminum atoms in paired-2NN and paired-3NN aluminum configurations within chabazites from the NMR analyses in Figures 2 and 3 is challenging, in part because some of the paired aluminum moieties may not be isolated from each other. This is expected to be the case for the high-aluminum-content zeolites, such as H^+-CHA-1 and H^+-CHA-2, considered here, for which an unspecified fraction of paired-2NN and paired-3NN Al moieties may share covalent bonds with the same Q^4(1Al) ^{29}Si moieties in the chabazite lattice. Nevertheless, from the simulations of random versus distanced-biased aluminum distributions in chabazite frameworks with a Si/Al = 10, the percentages of the aluminum atoms in second-nearest-neighbor and third-nearest-neighbor paired configurations for each distribution model can be directly computed. For these analyses, the percentage of aluminum atoms in a paired-2NN configuration refers to the percentage of Al atoms, out of 88 Al atoms in a simulated chabazite lattice with Si/Al=10 and 972 T-sites, that participate in at least one **Al**-O-^{29}Si-O-**Al** bonding configuration. Similarly, the percentage of aluminum atoms in a paired-3NN configuration refers to the percentage of Al atoms in at least one **Al**-O-^{29}Si-

O-^{29}Si-O-**Al** bonding configuration. These are summarized for both simulated distributions in Table S7 and provide context for understanding what the proportions of the different ^{29}Si NMR signals related to aluminum pairing physically represent for both H^+-CHA-1 and H^+-CHA-2. For the distance-biased simulation, almost no Q^4(2Al) moieties are predicted and correspondingly a very low percentage (2%) of aluminum atoms in paired-2NN aluminum configurations (**Al**-O-^{29}Si-O-**Al**) are expected. In addition, the distance-based model predicts 6% Q^4(1Al)–Q^4(1Al) bonded pairs (Table S6), relative to the total number of [Q^4(1Al)–Q^4(0Al) + Q^4(1Al)–Q^4(1Al)] pairs, which corresponds to 65% of Al atoms in paired-3NN configurations (**Al**-O-^{29}Si-O-^{29}Si-O-**Al**). In contrast, the 6% Q^4(2Al) moieties from the random-aluminum-distribution model (Table S4) corresponds to 60% of aluminum atoms in paired-2NN configurations. Similarly, the 12% predicted Q^4(1Al)–Q^4(1Al) covalently bonded pairs for this model (Table S4), relative to the total number of [Q^4(1Al)–Q^4(0Al) + Q^4(1Al)–Q^4(1Al)] pairs, corresponds to 79% of the aluminum atoms in paired-3NN configurations.

Table S7. Percentages of Al participating in paired bonding configurations for simulated and experimentally measured aluminum distributions in chabazite (Si/Al = 10)

	2NN	3NN
Random	60%	79%
Distance-biased	2%	65%
Experiment,[a] H^+-CHA-1	10-20%	60-80%
Experiment,[a] H^+-CHA-2	Below detection limit	Below detection limit

[a] from solid-state ^{29}Si and ^{27}Al NMR analyses

The experimental analysis is based on the 2D^{27}Al-^{29}Si and 2D ^{29}Si-^{29}Si *J*-mediated NMR analyses in Figures 2 and 3 of the main manuscript, which unambiguously measure covalently bonded Al atoms in the aluminosilicate CHA framework and rely on the heightened resolution and quantifiability of key Q^4(1Al) moieties provided by ^{29}Si NMR. The trends for these NMR-relevant ^{29}Si moieties and aluminum atoms in paired configurations are supported by

simulations and yield estimates for the percentages of aluminum atoms in paired-2NN and paired-3NN aluminum configurations, which are significantly different for the two chabazite catalysts (Table S7). Based on simulations of random and distance-biased aluminum distributions in chabazite, it can be inferred that the 1% total Q^4(2Al) ^{29}Si NMR signal for H^+-CHA-1 (Table S3) corresponds to 10-20% of Al atoms in paired-2NN configurations. In addition, the 5% Q^4(1Al)–Q^4(1Al) bonded pairs (Figure S12), relative to the total number of [Q^4(1Al)–Q^4(0Al) + Q^4(1Al)–Q^4(1Al)] pairs for H^+-CHA-1 can be inferred to correspond to 60-80% of Al in paired-3NN configurations. The uncertainty range for these values is due to the undercounting of Q^4(1Al)–Q^4(1Al) bonded pairs discussed above. For H^+-CHA-2, the paired-aluminum levels are below the noise threshold of NMR detectability and are therefore low but cannot be otherwise quantified. The simulated aluminum distributions corroborate the NMR analysis, indicating that only minimal amounts (if any) of the aluminum atoms are present in paired-2NN configurations in this catalyst. Simulated aluminum distributions indicate that framework aluminum atoms could be present in paired-3NN configurations in H^+-CHA-2, although the experimental NMR results show that, if present, they are also below the sensitivity limit of detection. In summary, the H^+-CHA-1 catalyst has significantly larger percentages of both paired-2NN and paired-3NN Al atoms in its zeolite framework, compared to the H^+-CHA-2 catalyst, despite their similar bulk aluminum contents (Si/Al=10). These distributions differ from those expected for random or distance-biased models, which suggests that more complicated factors govern the incorporation of Al heteroatoms into the crystallizing chabazite during syntheses than are currently understood. The influences of such paired distributions of framework Al atoms on chemical reaction properties have, to our knowledge, not previously been established so directly.

References

(1) Vogt, E. T. C.; Weckhuysen, B. M. Fluid Catalytic Cracking: Recent Developments on the Grand Old Lady of Zeolite Catalysis. *Chemical Society Reviews* **2015**, *44* (20), 7342–7370. https://doi.org/10.1039/c5cs00376h.

(2) Yarulina, I.; Chowdhury, A. D.; Meirer, F.; Weckhuysen, B. M.; Gascon, J. Recent Trends and Fundamental Insights in the Methanol-to-Hydrocarbons Process. *Nature Catalysis* **2018**, *1* (6). https://doi.org/10.1038/s41929-018-0078-5.

(3) Fernandez, C.; Stan, I.; Gilson, J. P.; Thomas, K.; Vicente, A.; Bonilla, A.; Pérez-Ramírez, J. Hierarchical ZSM-5 Zeolites in Shape-Selective Xylene Isomerization: Role of Mesoporosity and Acid Site Speciation. *Chemistry – A European Journal* **2010**, *16* (21), 6224–6233. https://doi.org/10.1002/CHEM.200903426.

(4) Ghobarkar, H.; Schäf, O.; Guth, U. Zeolites—from Kitchen to Space. *Progress in Solid State Chemistry* **1999**, *27* (2–4), 29–73. https://doi.org/10.1016/S0079-6786(00)00002-9.

(5) Weitkamp, J. Catalytic Hydrocracking—Mechanisms and Versatility of the Process. *ChemCatChem* **2012**, *4* (3), 292–306. https://doi.org/10.1002/CCTC.201100315.

(6) Gao, F.; Kwak, J. H.; Szanyi, J.; Peden, C. H. F. Current Understanding of Cu-Exchanged Chabazite Molecular Sieves for Use as Commercial Diesel Engine $DeNO_x$ Catalysts. *Topics in Catalysis* **2013**, *56*, 1441–1459. https://doi.org/10.1007/s11244-013-0145-8.

(7) Paolucci, C.; Parekh, A. A.; Khurana, I.; Di Iorio, J. R.; Li, H.; Albarracin Caballero, J. D.; Shih, A. J.; Anggara, T.; Delgass, W. N.; Miller, J. T.; Ribeiro, F. H.; Gounder, R.; Schneider, W. F. Catalysis in a Cage: Condition-Dependent Speciation and Dynamics of Exchanged Cu Cations in SSZ-13 Zeolites. *Journal of the American Chemical Society* **2016**, *138* (18), 6028–6048. https://doi.org/10.1021/JACS.6B02651.

(8) Paolucci, C.; Khurana, I.; Parekh, A. A.; Li, S.; Shih, A. J.; Li, H.; Di Iorio, J. R.; Albarracin-Caballero, J. D.; Yezerets, A.; Miller, J. T.; Delgass, W. N.; Ribeiro, F. H.; Schneider, W. F.; Gounder, R. Dynamic Multinuclear Sites Formed by Mobilized Copper Ions in NO_x Selective Catalytic Reduction. *Science* **2017**, *357* (6354), 898–903. https://doi.org/10.1126/science.aan5630.

(9) Song, J.; Wang, Y.; Walter, E. D.; Washton, N. M.; Mei, D.; Kovarik, L.; Engelhard, M. H.; Prodinger, S.; Wang, Y.; Peden, C. H. F.; Gao, F. Toward Rational Design of Cu/SSZ-13 Selective Catalytic Reduction Catalysts: Implications from Atomic-Level Understanding of Hydrothermal Stability. *ACS Catalysis* **2017**, *7* (12), 8214–8227. https://doi.org/10.1021/acscatal.7b03020.

(10) Kwak, J. H.; Tonkyn, R. G.; Kim, D. H.; Szanyi, J.; Peden, C. H. F. Excellent Activity and Selectivity of Cu-SSZ-13 in the Selective Catalytic Reduction of NO_x with NH_3. *Journal of Catalysis* **2010**, *275* (2), 187–190. https://doi.org/10.1016/j.jcat.2010.07.031.

(11) Hu, W.; Gramigni, F.; Nasello, N. D.; Usberti, N.; Iacobone, U.; Liu, S.; Nova, I.; Gao, X.; Tronconi, E. Dynamic Binuclear Cu^{II} Sites in the Reduction Half-Cycle of Low-Temperature NH_3−SCR over Cu-CHA Catalysts. *ACS Catalysis* **2022**, *12* (9), 5263–5274. https://doi.org/10.1021/acscatal.2c01213.

(12) Villamaina, R.; Gramigni, F.; Iacobone, U.; Liu, S.; Nova, I.; Tronconi, E.; Ruggeri, M. P.; Collier, J.; York, A. P. E.; Thompsett, D.; Casapu, M.; Doronkin, D. E. The H_2O Effect on Cu Speciation in Cu-CHA-Catalysts for NH_3-SCR Probed by NH_3 Titration. *Catalysts* **2021**, *11* (7), 759. https://doi.org/10.3390/catal11070759.

(13) Dusselier, M.; Davis, M. E. Small-Pore Zeolites: Synthesis and Catalysis. *Chemical Reviews* **2018**, *118* (11), 5265–5329. https://doi.org/10.1021/ACS.CHEMREV.7B00738.
(14) Shih, A. J.; González, J. M.; Khurana, I.; Pérez Ramírez, L.; Peña, A.; Kumar, A.; Villa, A. L. Influence of ZCuOH, Z_2Cu, and Extraframework Cu_xO_y Species in Cu-SSZ-13 on N_2O Formation during the Selective Catalytic Reduction of NO_x with NH_3. *ACS Catalysis* **2021**, *11*, 10362–10376. https://doi.org/10.1021/acscatal.1c01871.
(15) Gao, F.; Szanyi, J. On the Hydrothermal Stability of Cu/SSZ-13 SCR Catalysts. *Applied Catalysis A: General* **2018**, *560*, 185–194. https://doi.org/10.1016/j.apcata.2018.04.040.
(16) Li, S.; Li, H.; Gounder, R.; Debellis, A.; Müller, I. B.; Prasad, S.; Moini, A.; Schneider, W. F. First-Principles Comparison of Proton and Divalent Copper Cation Exchange Energy Landscapes in SSZ-13 Zeolite. *The Journal of Physical Chemistry C* **2018**, *122* (41), 23564–23573. https://doi.org/10.1021/acs.jpcc.8b07213.
(17) Loewenstein, W. The Distribution of Aluminum in the Tetrahedra of Silicates and Aluminates. *American Mineralogist* **1954**, *39* (1–2), 92–96.
(18) Dědeček, J.; Kaucky, D.; Wichterlová, B.; Gonsiorová, O. Co^{2+} Ions as Probes of Al Distribution in the Framework of Zeolites. ZSM-5 Study. *PCCP* **2002**, *4*, 5406–5413. https://doi.org/10.1039/b203966b.
(19) Pashkova, V.; Klein, P.; Dedecek, J.; Tokarová, V.; Wichterlová, B. Incorporation of Al at ZSM-5 Hydrothermal Synthesis. Tuning of Al Pairs in the Framework. *Microporous and Mesoporous Materials* **2015**, *202*, 138–146. https://doi.org/10.1016/J.MICROMESO.2014.09.056.
(20) Chen, K.; Abdolrahmani, M.; Horstmeier, S.; Pham, T. N.; Nguyen, V. T.; Zeets, M.; Wang, B.; Crossley, S.; White, J. L. Brønsted–Brønsted Synergies between Framework and Noncrystalline Protons in Zeolite H-ZSM-5. *ACS Catalysis* **2019**, *9* (7), 6124–6136. https://doi.org/10.1021/ACSCATAL.9B01583.
(21) Mlekodaj, K.; Dedecek, J.; Pashkova, V.; Tabor, E.; Klein, P.; Urbanova, M.; Karcz, R.; Sazama, P.; Whittleton, S. R.; Thomas, H. M.; Fishchuk, A. V.; Sklenak, S. Al Organization in the SSZ-13 Zeolite. Al Distribution and Extraframework Sites of Divalent Cations. *The Journal of Physical Chemistry C* **2019**, *123* (13), 7968–7987. https://doi.org/10.1021/ACS.JPCC.8B07343.
(22) Nimlos, C. T.; Hoffman, A. J.; Hur, Y. G.; Lee, J.; Di Iorio, J. R.; Hibbitts, D. D.; Gounder, R. Experimental and Theoretical Assessments of Aluminum Proximity in MFI Zeolites and Its Alteration by Organic and Inorganic Structure-Directing Agents. *Chemistry of Materials* **2020**, *32* (21), 9277–9298. https://doi.org/10.1021/acs.chemmater.0c03154.
(23) Di Iorio, J. R.; Li, S.; Jones, C. B.; Nimlos, C. T.; Wang, Y.; Kunkes, E.; Vattipalli, V.; Prasad, S.; Moini, A.; Schneider, W. F.; Gounder, R. Cooperative and Competitive Occlusion of Organic and Inorganic Structure-Directing Agents within Chabazite Zeolites Influences Their Aluminum Arrangement. *Journal of the American Chemical Society* **2020**, *142* (10), 4807–4819. https://doi.org/10.1021/jacs.9b13817.
(24) Schwalbe-Koda, D.; Kwon, S.; Paris, C.; Bello-Jurado, E.; Jensen, Z.; Olivetti, E.; Willhammar, T.; Corma, A.; Román-Leshkov, Y.; Moliner, M.; Gómez-Bombarelli, R. A Priori Control of Zeolite Phase Competition and Intergrowth with High-Throughput Simulations. *Science* **2021**, *374* (6565), 308–315. https://doi.org/10.1126/science.abh3350.

(25) Pinar, A. B.; Rzepka, P.; Knorpp, A. J.; McCusker, L. B.; Baerlocher, C.; Huthwelker, T.; Bokhoven, J. A. van. Pinpointing and Quantifying the Aluminum Distribution in Zeolite Catalysts Using Anomalous Scattering at the Al Absorption Edge. *Journal of the American Chemical Society* **2021**, *143* (43), 17926–17930. https://doi.org/10.1021/JACS.1C06925.
(26) Shen, B.; Wang, H.; Xiong, H.; Chen, X.; Bosch, E. G. T.; Lazić, I.; Qian, W.; Wei, F.; Xiong, H. Atomic Imaging of Zeolite-Confined Single Molecules by Electron Microscopy. *Nature* **2022**, *607*, 703–707. https://doi.org/10.1038/s41586-022-04876-x.
(27) Chen, K.; Zornes, A.; Nguyen, V.; Wang, B.; Gan, Z.; Crossley, S. P.; White, J. L. ^{17}O Labeling Reveals Paired Active Sites in Zeolite Catalysts. *Journal of the American Chemical Society* **2022**, *144* (37), 16916–16929. https://doi.org/10.1021/jacs.2c05332.
(28) Martineau-Corcos, C.; Dědeček, J.; Taulelle, F. ^{27}Al-^{27}Al Double-Quantum Single-Quantum MAS NMR: Applications to the Structural Characterization of Microporous Materials. *Solid State Nuclear Magnetic Resonance* **2017**, *84*, 65–72. https://doi.org/10.1016/J.SSNMR.2016.12.013.
(29) Schroeder, C.; Zones, S. I.; Mück-Lichtenfeld, C.; Hansen, M. R.; Koller, H. High Aluminum Ordering in SSZ-59: Residual ^{1}H-^{27}Al Dipolar Coupling Effects in ^{1}H MAS NMR Spectra of Brønsted Acid Sites in Zeolites. *Journal of Physical Chemistry C* **2021**, *125*, 4869–4877. https://doi.org/10.1021/acs.jpcc.0c11379.
(30) Pugh, S. M.; Wright, P. A.; Law, D. J.; Thompson, N.; Ashbrook, S. E. Facile, Room-Temperature ^{17}O Enrichment of Zeolite Frameworks Revealed by Solid-State NMR Spectroscopy. *Journal of the American Chemical Society* **2020**, *142* (2), 900–906. https://doi.org/10.1021/JACS.9B10528.
(31) Berkson, Z. J.; Hsieh, M.; Smeets, S.; Gajan, D.; Lund, A.; Lesage, A.; Xie, D.; Zones, S. I.; McCusker, L. B.; Baerlocher, C.; Chmelka, B. F. Preferential Siting of Aluminum Heteroatoms in the Zeolite Catalyst Al-SSZ-70. *Angewandte Chemie International Edition* **2019**, *58* (19), 6255–6259. https://doi.org/10.1002/anie.201813533.
(32) Li, S.; Lafon, O.; Wang, W.; Wang, Q.; Wang, X.; Li, Y.; Xu, J.; Deng, F. Recent Advances of Solid-State NMR Spectroscopy for Microporous Materials. *Advanced Materials* **2020**, *32* (44), 2002879. https://doi.org/10.1002/adma.202002879.
(33) Kumar, M.; Berkson, Z. J.; Clark, R. J.; Shen, Y.; Prisco, N. A.; Zheng, Q.; Zeng, Z.; Zheng, H.; McCusker, L. B.; Palmer, J. C.; Chmelka, B. F.; Rimer, J. D. Crystallization of Mordenite Platelets Using Cooperative Organic Structure-Directing Agents. *Journal of the American Chemical Society* **2019**, *141* (51), 20155–20165. https://doi.org/10.1021/JACS.9B09697.
(34) Massiot, D.; Fayon, F.; Deschamps, M.; Cadars, S.; Florian, P.; Montouillout, V.; Pellerin, N.; Hiet, J.; Rakhmatullin, A.; Bessada, C. Detection and Use of Small J Couplings in Solid State NMR Experiments. *Comptes Rendus Chimie* **2010**, *13* (1–2), 117–129. https://doi.org/10.1016/J.CRCI.2009.05.001.
(35) Brouwer, D. H.; Cadars, S.; Eckert, J.; Liu, Z.; Terasaki, O.; Chmelka, B. F. A General Protocol for Determining the Structures of Molecularly Ordered but Noncrystalline Silicate Frameworks. *Journal of the American Chemical Society* **2013**, *135* (15), 5641–5655. https://doi.org/10.1021/JA311649M.
(36) Cadars, S.; Brouwer, D. H.; Chmelka, B. F. Probing Local Structures of Siliceous Zeolite Frameworks by Solid-State NMR and First-Principles Calculations of ^{29}Si–O–

^{29}Si Scalar Couplings. *Physical Chemistry Chemical Physics* **2009**, *11* (11), 1825–1837. https://doi.org/10.1039/B815361B.
(37) Di Iorio, J. R.; Nimlos, C. T.; Gounder, R. Introducing Catalytic Diversity into Single-Site Chabazite Zeolites of Fixed Composition via Synthetic Control of Active Site Proximity. *ACS Catalysis* **2017**, *7* (10), 6663–6674. https://doi.org/10.1021/acscatal.7b01273.
(38) Marsden, G.; Kostetskyy, P.; Sekiya, R. S.; Hoffman, A.; Lee, S.; Gounder, R.; Hibbitts, D.; Broadbelt, L. J. Quantifying Effects of Active Site Proximity on Rates of Methanol Dehydration to Dimethyl Ether over Chabazite Zeolites through Microkinetic Modeling. *ACS Materials Au* **2022**, *2* (2), 163–175. https://doi.org/10.1021/ACSMATERIALSAU.1C00057/.
(39) Hoffman, A. J.; Bates, J. S.; Di Iorio, J. R.; Nystrom, S. V.; Nimlos, C. T.; Gounder, R.; Hibbitts, D. Rigid Arrangements of Ionic Charge in Zeolite Frameworks Conferred by Specific Aluminum Distributions Preferentially Stabilize Alkanol Dehydration Transition States. *Angewandte Chemie International Edition* **2020**, *59* (42), 18686–18694. https://doi.org/10.1002/anie.202007790.
(40) Devos, J.; Bols, M. L.; Plessers, D.; Goethem, C. V.; Seo, J. W.; Hwang, S. J.; Sels, B. F.; Dusselier, M. Synthesis-Structure-Activity Relations in Fe-CHA for C-H Activation: Control of Al Distribution by Interzeolite Conversion. *Chemistry of Materials* **2020**, *32* (1), 273–285. https://doi.org/10.1021/ACS.CHEMMATER.9B03738.
(41) Di Iorio, J. R.; Gounder, R. Controlling the Isolation and Pairing of Aluminum in Chabazite Zeolites Using Mixtures of Organic and Inorganic Structure-Directing Agents. *Chemistry of Materials* **2016**, *28* (7), 2236–2247. https://doi.org/10.1021/acs.chemmater.6b00181.
(42) Robijns, S.; Devos, J.; Donckels, T.; de Oliveira-Silva, R.; De Witte, N.; Sakellariou, D.; Van Assche, T. R. C.; Dusselier, M. Steering Interzeolite Conversion with Alkali Metal Cations: Lithium Maximizes Al Proximity in SSZ-13 Zeolite Genesis. *Crystal Growth and Design* **2023**, *23* (1), 289–299. https://doi.org/10.1021/ACS.CGD.2C01009.
(43) Massiot, D.; Fayon, F.; Alonso, B.; Trebosc, J.; Amoureux, J. P. Chemical Bonding Differences Evidenced from J-Coupling in Solid State NMR Experiments Involving Quadrupolar Nuclei. *Journal of Magnetic Resonance* **2003**, *164* (1), 160–164. https://doi.org/10.1016/S1090-7807(03)00134-4.
(44) Lesage, A.; Bardet, M.; Emsley, L. Through-Bond Carbon-Carbon Connectivities in Disordered Solids by NMR. *Journal of the American Chemical Society* **1999**, *121* (47), 10987–10993. https://doi.org/10.1021/ja992272b.
(45) Fung, B. M.; Khitrin, A. K.; Ermolaev, K. An Improved Broadband Decoupling Sequence for Liquid Crystals and Solids. *Journal of Magnetic Resonance* **2000**, *142* (1), 97–101. https://doi.org/10.1006/JMRE.1999.1896.
(46) Jaeger, C.; Hemmann, F. EASY: A Simple Tool for Simultaneously Removing Background, Deadtime and Acoustic Ringing in Quantitative NMR Spectroscopy—Part I: Basic Principle and Applications. *Solid State Nuclear Magnetic Resonance* **2014**, *57–58*, 22–28. https://doi.org/10.1016/J.SSNMR.2013.11.002.
(47) Saalwächter, K.; Lange, F.; Matyjaszewski, K.; Huang, C. F.; Graf, R. BaBa-Xy16: Robust and Broadband Homonuclear DQ Recoupling for Applications in Rigid and Soft

Solids up to the Highest MAS Frequencies. *Journal of Magnetic Resonance* **2011**, *212* (1), 204–215. https://doi.org/10.1016/J.JMR.2011.07.001.
(48) Olsbye, U.; Svelle, S.; Bjørgen, M.; Beato, P.; Janssens, T. V. W.; Joensen, F.; Bordiga, S.; Lillerud, K. P. Conversion of Methanol to Hydrocarbons: How Zeolite Cavity and Pore Size Controls Product Selectivity. *Angewandte Chemie International Edition* **2012**, *51* (24), 5810–5831. https://doi.org/10.1002/anie.201103657.
(49) Massiot, D.; Fayon, F.; Capron, M.; King, I.; Le Calvé, S.; Alonso, B.; Durand, J.-O.; Bujoli, B.; Gan, Z.; Hoatson, G. Modelling One-and Two-Dimensional Solid-State NMR Spectra. *Magnetic Resonance in Chemistry* **2002**, *40*, 70–76. https://doi.org/10.1002/mrc.984.
(50) Carr, R. T.; Neurock, M.; Iglesia, E. Catalytic Consequences of Acid Strength in the Conversion of Methanol to Dimethyl Ether. *Journal of Catalysis* **2011**, *278* (1), 78–93. https://doi.org/10.1016/J.JCAT.2010.11.017.
(51) Iuga, D.; Schäfer, H.; Verhagen, R.; Kentgens, A. P. M. Population and Coherence Transfer Induced by Double Frequency Sweeps in Half-Integer Quadrupolar Spin Systems. *Journal of Magnetic Resonance* **2000**, *147* (2), 192–209. https://doi.org/10.1006/jmre.2000.2192.
(52) Hjorth Larsen, A.; Jørgen Mortensen, J.; Blomqvist, J.; Castelli, I. E.; Christensen, R.; Dułak, M.; Friis, J.; Groves, M. N.; Hammer, B.; Hargus, C.; Hermes, E. D.; Jennings, P. C.; Bjerre Jensen, P.; Kermode, J.; Kitchin, J. R.; Leonhard Kolsbjerg, E.; Kubal, J.; Kaasbjerg, K.; Lysgaard, S.; Bergmann Maronsson, J.; Maxson, T.; Olsen, T.; Pastewka, L.; Peterson, A.; Rostgaard, C.; Schiøtz, J.; Schütt, O.; Strange, M.; Thygesen, K. S.; Vegge, T.; Vilhelmsen, L.; Walter, M.; Zeng, Z.; Jacobsen, K. W. The Atomic Simulation Environment—a Python Library for Working with Atoms. *Journal of Physics: Condensed Matter* **2017**, *29* (27), 273002. https://doi.org/10.1088/1361-648X/AA680E.
(53) Antonio, D. D.; Guo, J.; Holton, S. J.; Kulkarni, A. R. Simplifying Computational Workflows with the Multiscale Atomic Zeolite Simulation Environment (MAZE). *SoftwareX* **2021**, *16*, 100797. https://doi.org/10.1016/J.SOFTX.2021.100797.
(54) Palamara, J.; Seidel, K.; Moini, A.; Prasad, S. Ion Distribution in Copper Exchanged Zeolites by Using Si-29 Spin Lattice Relaxation Analysis. *Journal of Magnetic Resonance* **2016**, *267*, 9–14. https://doi.org/10.1016/J.JMR.2016.03.009.

Chapter 3

Understanding distributions of copper and aluminum species in an aged copper chabazite deNO_x catalyst

This chapter is adapted from the manuscript: Schmithorst, M.B.; Ikonnikova, E.; Cruz Delgado, B.; Stoev, A.; McNarney, A.; Zeng, L.; Vattipalli, V.; Prasad, S.; Moini, A.; Willhammar, T.; Zou, X.; Gounder, R.; Olsson, E.; Chmelka, B.F. Understanding distributions of copper and aluminum species in an aged copper chabazite deNO_x catalyst. *For submission to the Journal of the American Chemical Society*. I conceived of the experimental plan, performed experiments, and wrote the manuscript. A. Stoev helped perform STEM experiments and analyses. A. McNarney assisted with basic characterization and analysis. L. Zeng assisted with the STEM analyses and manuscript preparation. E. Ikonnikova and B. Cruz Delgado performed additional electron diffraction analyses and kinetic testing that are included in the manuscript but not this thesis chapter.

Abstract

Cu-exchanged chabazite zeolites are used industrially as catalysts for NO_x abatement from diesel engines. While the freshly prepared Cu-CHA catalyst performs very well for NO_x reduction to N_2, exposure to high-temperature hydrothermal environments during normal deployment conditions results in an irreversible loss of activity for the catalyst over time. This is due to a combination of dealumination of the zeolite framework and conversion of single-atom Cu species into larger agglomerates with poor catalytic activity. However, the types of Cu species that are most susceptible to deactivation by hydrothermal treatment and how the distributions of Cu in a Cu-CHA material evolve with time are not understood. Here, we combine state-of-the-art electron microscopy and nuclear magnetic resonance spectroscopy

techniques to better understand the evolution of Cu cation and zeolite framework species resulting from hydrothermal treatment of Cu-CHA. Scanning transmission electron microscopy measurements reveal the formation of nanoscale zeolite clusters upon hydrothermal treatment. Solid state 1D ^{15}N and 2D ^{27}Al-^{29}Si NMR analyses of Cu-CHA materials after simulation of the reduction half-cycle of the NO_x reaction pathway reveal changes in the types and distributions of framework species and adsorbates as a result of hydrothermal treatment. In addition, ^{15}N exchange NMR analyses reveal differences in exchange kinetics of adsorbates in the catalyst as a result of aging that may provide indirect information on the mobility of active species under reaction conditions. These results are anticipated to aid with the intelligent design of next-generation Cu-CHA catalysts for NO_x reduction.

Introduction

In recent years, single-atom metal catalysts on heterogeneous supports have received a great deal of attention due to their potential for providing relatively uniform catalytic environments and effective use of expensive precious metal species.[1] In particular, understanding the complicated interactions between single-atom metal catalysts, support materials, and adsorbates have been shown to be crucial for enhancing the activity and stability of single-atom metal species.[2,3] One class of heterogeneous support that has gained considerable interest is zeolites, a class aluminosilicates with nominally crystalline frameworks that provide uniform channels and cages with sub-nanometer dimensions and high specific surface areas. Zeolites are appealing as catalyst supports due both to (i) electrostatic interactions localized near four-coordinate aluminum atoms in the aluminosilicate framework and also (ii) confinement effects on both metal and reactant intermediate species in the sub-

nanoscale zeolite pores.[4–6] These effects have been leveraged in many hydrocarbon chemistries. For example, zeolite-supported precious metals have long been used as hydrocracking catalysts, due to the bifunctional reaction properties that result from the nanoscale proximities of the metal species, which catalyze hydrogenation and dehydrogenation reactions, and Bronsted acid sites that are associated with charge-balancing H^+ cations near framework aluminum atoms, which promote catalytic cracking reactions.[7] Rh, Mo, Cu, and Fe dispersed on zeolites have all been used to convert methane to useful chemical precursors.[8–11] In these catalysts, the zeolite support crucially stabilizes active metal species under reaction conditions.

One reaction chemistry over single-atom-metal species on zeolites that has been extensively studied over the past decade is the selective catalytic reduction (SCR) of nitric oxides (NO_x) by ammonia (NH_3) over copper-exchanged chabazite (Cu-CHA).[12,13] The Cu-CHA catalyst has been commercialized as a deNO_x catalyst in catalytic converters for diesel engines.[14] Nitric oxide species are thought to be primarily converted to N_2 over single atom Cu(II) species by the standard SCR reaction, though other reaction pathways exist:[15,16]

$$4NO + 4NH_3 + O_2 \rightarrow 4N_2 + 6H_2O$$

The active Cu(II) species in Cu-CHA catalysts are thought to be present as cations that charge-balance local negative framework charges imparted by four-coordinate Al^{IV} atoms in either paired framework configurations (Z_2Cu^{2+}) or at isolated framework sites with a charge-compensating hydroxyl group ($ZCuOH$).[17–20] Under reaction conditions, these Cu(II) species are coordinated to adsorbed NH_3 ligands, and Cu species in different framework coordination environments have been posited to have different activities.[21–25] Thus, understanding and

controlling the interactions between framework aluminum atoms and catalytically active copper species in Cu-CHA are crucial for controlling reaction properties.

Under low-temperature SCR conditions (<523 K), evidence has shown that the dominant mechanism for the SCR reaction over Cu-CHA involves the formation of dimeric Cu(I) species as part of a Cu redox cycle between Cu(I) and Cu(II) electronic states.[26–28] Under these conditions, reduced $[Cu(NH_3)_2]^+$ species are able to delocalize from charge-balancing framework aluminum and migrate to proximate framework aluminum sites, even diffusing to adjacent chabazite cages.[29–31] Kinetic evidence and simulations indicate that the rate of Cu dimer formation and oxidation to Cu(II) are enhanced by utilizing Cu-CHA with a high aluminum content, and that the 3D pore structure chabazite is important for Cu ligands to diffuse and for reduction half cycle to proceed efficiently at low temperatures.[32,33] Thus, the distributions of framework aluminum in Cu-CHA play a role not only in charge-balancing Cu cations, but also in the kinetics of the SCR process.

The distributions of Cu and Al in commercial Cu-CHA catalysts are complicated by the degradation of the catalyst during regular use in a catalytic converter. In a diesel system, the Cu-CHA catalyst is intermittently subjected to water vapor at temperatures of 750 ºC or more.[34] Under these conditions, aluminum atoms in the zeolite framework can be irreversibly removed from the framework and single-atom Cu cations can sinter to form CuO clusters.[35,36] While Cu-CHA has empirically been observed to be more resistant to deactivation by high-temperature hydrothermal treatment than larger-pore zeolite framework types, this deactivation pathway is nevertheless an issue for the catalyst.[37,38] In particular, the hydrothermal stability of Cu-CHA tends to decrease with increasing framework aluminum content, causing challenges for designing catalysts with high low-temperature SCR activity.[39] While studies

have identified apparent differences in stability to high-temperature hydrothermal treatment of Cu species in different cation exchange environments, the distributions of Cu and Al species active for the SCR process in heavily steam-aged Cu-CHA catalysts are not well understood.[40–43] Given the relationships between Cu and Al distributions on Cu-CHA SCR activity, particularly under low-temperature SCR conditions, understanding the distributions of these species after high-temperature hydrothermal treatment is important for the design of Cu-CHA catalysts with long lifetimes.

In this work, a series of advanced characterization techniques were applied to a Cu-CHA catalyst before hydrothermal treatment and after progressive amounts of high-temperature hydrothermal treatment to understand the evolution of the distributions of Cu and Al species as a result of the hydrothermal treatment. It is demonstrated that, after hydrothermal treatment, deactivated Cu species form nanoscale Cu agglomerates, likely at defects in the Cu-CHA lattice. In addition, the types of active Cu species in Cu-CHA are investigated by simulation of the reduction half-cycle of the SCR process over the catalyst. Interestingly, while the quantity of reducible species in the Cu-CHA catalyst was significantly lowered as a result of high-temperature hydrothermal treatment, the types of reduced Cu species present in the aged catalyst are similar to those of the fresh catalyst. However, the reducible Cu species in hydrothermally treated Cu-CHA are located preferentially near closely-paired framework aluminum species compared to the fresh Cu-CHA, indicating stabilization of these framework configurations during hydrothermal treatment. In addition, the adsorption dynamics of NH_3 ligands on the reduced Cu-CHA catalyst are investigated.

Results and Discussion

To investigate the influences of aging on Cu-CHA, a Cu-CHA catalysts (Si/Al = 11, Cu/Al = 0.21, see Table S1 for elemental analysis details) from industrial collaborators was steam-aged in 10% water vapor for both 4 h and 16 h at 750 ºC to simulate catalyst deterioration at different points in the lifetime of the SCR catalyst. After being subjected to both aging conditions, the Cu-CHA catalyst exhibits a powder X-ray diffraction pattern that is indexable crystalline chabazite (Figure S1), indicating that the long-range ordering of the aluminosilicate chabazite framework is preserved during steam-aging. However, local defects are formed in the chabazite framework during the steam-aging process and can be detected by nuclear magnetic resonance spectroscopy (NMR). Figure 1A shows solid-state 1D direct-excitation ^{29}Si MAS NMR spectra of fresh, 4-h-aged, and 16-h-aged Cu-CHA. Two regions of ^{29}Si NMR signal intensity are observed. The ^{29}Si NMR signals at –111 and –105 ppm are attributed to Q^4(0Al) and Q^4(1Al) moieties, respectively, where the Q^m(nAl) notation denotes a four-coordinate ^{29}Si with 4-m silanol groups and m bridging oxygen bonds to neighboring tetrahedra, of which n are Al atoms. Two notable trends are observed going from the fresh to the 16-h-aged Cu-CHA. The Q^4(1Al) ^{29}Si NMR signal at –105 ppm becomes less intense relative to the Q^4(0Al) ^{29}Si NMR signal as steam-aging progresses, indicating removal of aluminum from the framework. In addition, the Q^4(0Al) signal at –111 ppm narrows and is displaced slightly to higher frequency after steam-aging, likely due to the framework dealumination. The removal of aluminum from the chabazite framework can be quantified by integrating the Q^4(0Al) and Q^4(1Al) ^{29}Si NMR signals, and indicates that the framework Si/Al increases from 10 to 32 from the fresh material to the 16-h-aged Cu-CHA.[44] After 4 hours of aging, the framework Si/Al has increased to 24, indicating that a substantial amount of

framework dealumination occurs after relatively brief exposure to high-temperature steam. These dealumination observations are supported by NH_3 temperature-programmed desorption, which shows that high temperature desorption features associated with NH_3 adsorbed on framework Bronsted acid sites are heavily depleted in 4-h-aged Cu-CHA relative to fresh Cu-CHA (Figure S2), and also by thermogravimetric analysis, which shows less water adsorbed on the catalyst after aging (Table S2).[45] However, the pore volume of Cu-CHA stays largely constant after aging, suggesting loss of acid sites does not lead to substantial framework collapse (Figure S3).

The aluminum chemical environments in Cu-CHA also change as a result of aging. Solid-state 1D direct-excitation ^{27}Al MAS NMR spectra for fresh, 4-h-aged, and 16-h-aged Cu-CHA are shown in Figure 1B. The ^{27}Al NMR spectrum of fresh Cu-CHA exhibits a single signal at 59 ppm that is assigned to Al^{IV} species in the chabazite framework. In comparison, the ^{27}Al NMR spectra of 4-h-aged and 16-h-aged Cu-CHA exhibit three regions of signal at 59 ppm, 33 ppm, and 1 ppm, attributed to Al^{IV}, Al^{V}, and Al^{VI} species. Compared to the fresh Cu-CHA, the $^{27}Al^{IV}$ NMR signal of the steam-aged materials is broader, likely indicating an increase in local disorder of the zeolite framework. The ^{27}Al NMR signals attributed to Al^{V} and Al^{VI} are likely extraframework Al species resulting from dealumination of the framework, though the exact chemical identity of these species is debated in the literature.[46] Solid-state 1D ^{27}Al spin-counting NMR analyses indicate that the amount of aluminum detected by ^{27}Al NMR relative to the total amount in the material decreases from 33% in the fresh material to 12% and 7% for the 4-h-aged and 16-h-aged Cu-CHA, respectively (Figure S4, Table S3). Proximity to paramagnetic Cu^{2+} species results in broadening of ^{27}Al NMR signals beyond detection. In the fresh material, the low amount of visible aluminum is likely due to the high aluminum and

copper content of the material, where most Al species either are charge balanced by Cu^{2+} or have Cu^{2+} in sub-nanoscale proximity. The observed decrease in visible aluminum is consistent with the changes in framework Si/Al calculated from direct-excitation ^{29}Si NMR, suggesting that the majority of extraframework aluminum species produced by high-temperature hydrothermal treatment are NMR-invisible. For the high magnetic field (18.8 T) conditions at which the measurements were performed, this also indicates that extraframework Al species are located in close proximity to Cu(II) species, which are paramagnetic and broaden ^{27}Al NMR signals from proximate nuclei, often beyond detection. These NMR-invisible species may perhaps be present as copper- and aluminum-rich clusters, as has been previously suggested.[38]

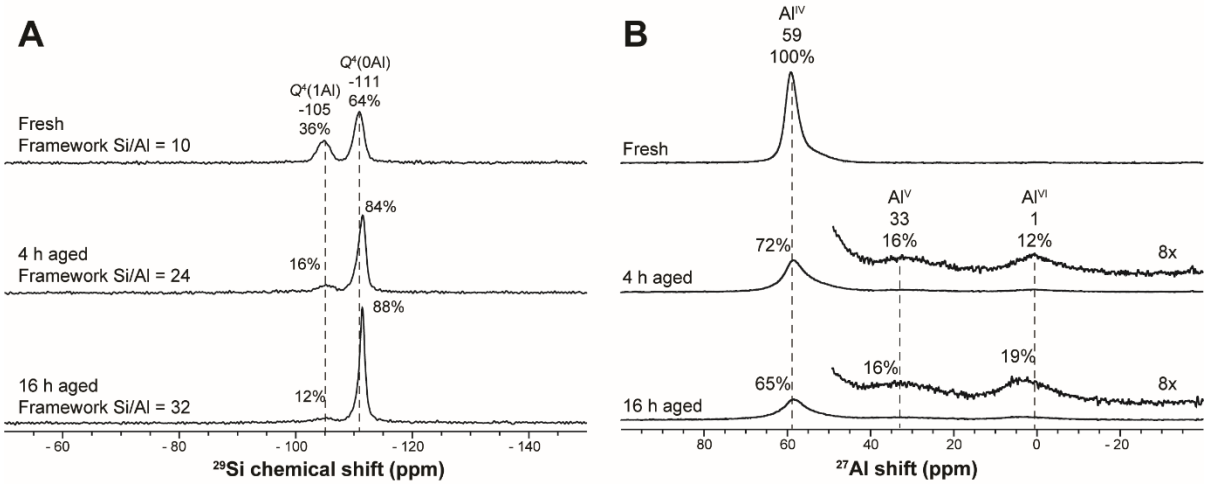

Figure 1. Solid-state 1D direct-excitation (A) ^{29}Si and (B) ^{27}Al MAS NMR spectra of Cu-CHA fresh and after different aging treatments. The framework Si/Al ratios in (A) were calculated based on the integrated intensities of the ^{29}Si NMR signals at –105 ppm and –111 ppm from Q^4(1Al) and Q^4(0Al) species, respectively. Inset ^{27}Al spectra in (B) show weak Al^V and Al^{VI} ^{27}Al NMR signals after aging of Cu-CHA for 4 h and 16 h. The ^{29}Si NMR spectra in (A) were acquired at 11.7 T, 12.5 kHz MAS, and room temperature. The ^{27}Al NMR spectra in (B) were acquired at 18.8 T, 20 kHz MAS, and room temperature.

As a result of considerable framework dealumination, Cu^{2+} cations charge-balancing framework aluminum in fresh Cu-CHA must occupy different chemical environments in the

hydrothermally treated Cu-CHA materials. To investigate the distributions of Cu species before and after hydrothermal treatment, high-angle annular dark field scanning transmission electron microscopy (HAADF-STEM) was performed on the Cu-CHA catalysts. HAADF-STEM has been used previously to detect metal clusters in zeolite pore systems and other catalyst materials.[47–50] HAADF-STEM images show *Z*-contrast, and thus regions of the catalyst with high concentrations of Cu species will appear more intense than surrounding regions in the images.[51] A representative HAADF-STEM image of fresh Cu-CHA is shown in Figure 2A. The image shows single-crystalline lattices with a spacing consistent with the chabazite framework. The homogeneous image contrast indicates that there are no nanoscale Cu clusters or particles in the fresh crystals, in line with the structure model in which individual Cu^{2+} cations are dispersed among chabazite cages. Though the atomic scale structure of chabazite framework is visible in HAADF-STEM images (Figure S5), these measurements are not able to detect single-atom Cu^{2+} species due to the relatively low local Cu concentration and the sensitivity of Cu-CHA structure to electron beam irradiation. Representative images of 4-h-aged Cu-CHA (Figure 2B) and 16-h-aged Cu-CHA (Figure 2C) also show a periodic lattice spacing consistent with the chabazite structure (additional images in Figure S6-S19). However, in contrast to fresh Cu-CHA these images exhibit nanoscale regions with high image intensity, suggesting the formation of Cu nanoparticles. To support the identification of these spots as Cu clusters, STEM - energy dispersive X-ray spectroscopy (EDS) mapping of 16-h-aged Cu-CHA was performed (Figure S20). When compared to the same region imaged simultaneously by HAADF-STEM, it is apparent that the high intensity regions observed in HAADF-STEM are rich with Cu. Electron paramagnetic resonance spectroscopy, sensitive to the lone electron on Cu(II), confirms that the types of single-atom Cu(II) species present in Cu-CHA evolve

upon aging, consistent with loss of ordered single-atom Cu(II) cations (Figure S21, Table S6-S8).

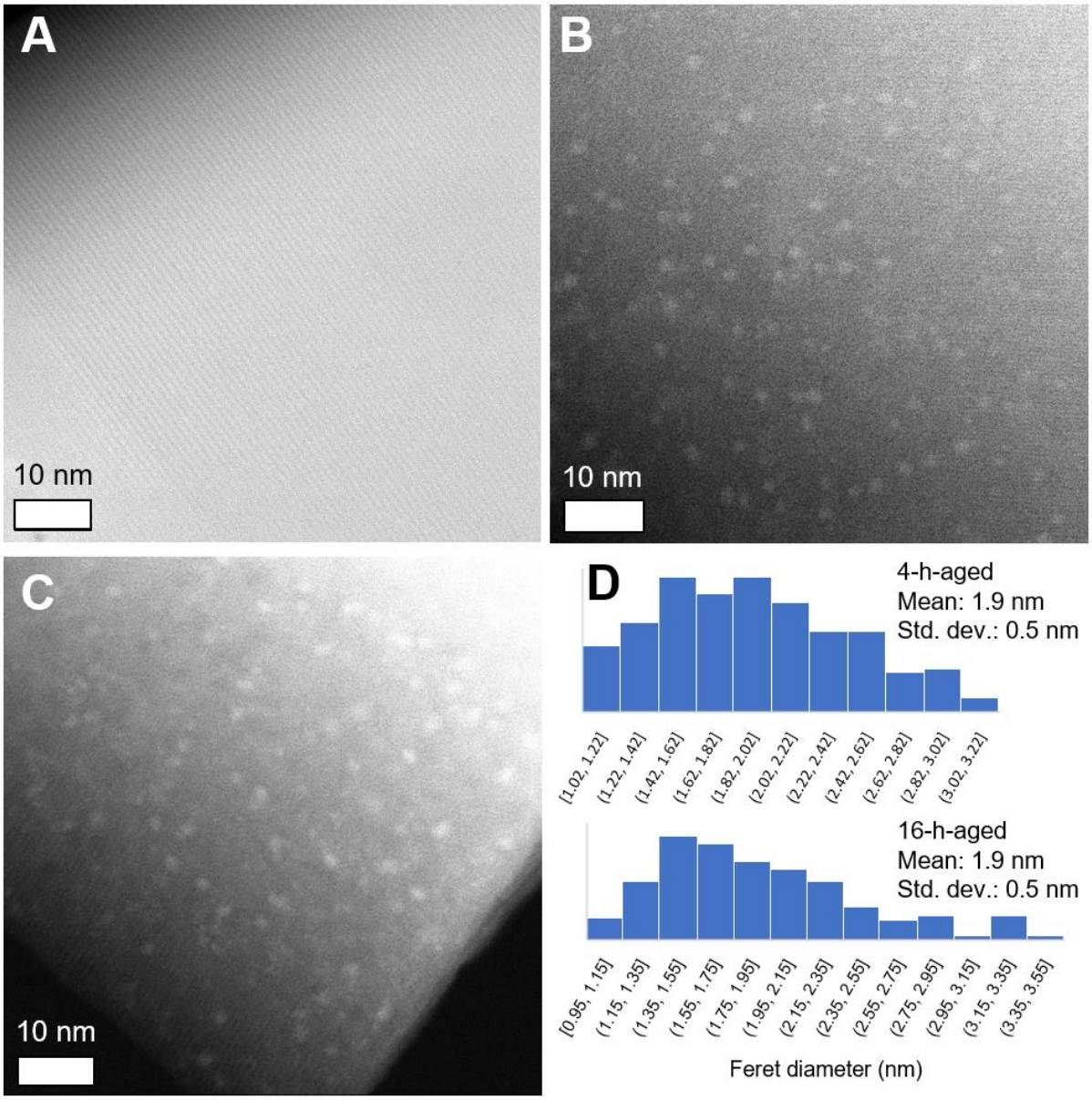

Figure 2. Representative HAADF STEM images of (A) fresh Cu-CHA, and after aging Cu-CHA for (B) 4 h, (and C) 16 h-. The insets show crystal structures determined by 3D electron diffraction. (D) Histograms of the size of bright spots in HAADF STEM images that are attributed to Cu-rich clusters for the 4-h-aged and 16-h-aged Cu-CHA materials. All images used to calculate the size distributions are shown in Figures S6-19.

To better understand the evolution of Cu-rich clusters at different extents of steam-aging, the size distributions of Cu clusters in 4-h-aged and 16-h-aged Cu-CHA were quantified

across several imaged regions of the material (Figure 2D). The average longest dimension of Cu clusters in both the 4-h-aged and 16-h-aged Cu-CHA was 1.9 nm with a standard deviation of 0.5 nm. The statistics for the individual images used in these analyses can be found in the SI (Figures S6-19, Tables S4-S5). The consistency in copper cluster size between the 4-h-aged and 16-h-aged Cu-CHA despite increasing disorder in the material after 16 hours of high-temperature hydrothermal treatment may indicate that Cu clusters are forming in confined environments. Interestingly, the reported diameters are too large to be attributed to cluster formation in a chabazite cage, which may indicate that clusters form at local zeolite framework defects that result in nanoscale voids in the chabazite lattice. Similar metal cluster size distributions have been observed in systems where metals are encapsulated in the zeolite during initial synthesis.[52]

While significant framework dealumination and Cu cluster formation are observed in 4-h-aged and 16-h-aged Cu-CHA, both catalysts are still active for the SCR reaction. To understand how the local environments of Cu species active for the SCR reaction evolve as a result of hydrothermal treatment, the Cu-CHA catalysts were exposed to a treatment of $^{15}NH_3$ and ^{15}NO intended to perform the reduction half-cycle of the SCR process. Cu(II) species are paramagnetic, whereas Cu(I) species are not. Reducing active Cu species renders ^{15}N moieties adsorbed on or near SCR-active Cu species NMR-visible, while adsorbates near non-active Cu species are not observable by NMR. Solid-state NMR is well-suited to characterization of these environments, as it is nucleus-specific and sensitive to both ordered and disordered regions of the aged Cu-CHA catalyst. After initial exposure to $^{15}NH_3$ at 120 ^{o}C, no ^{15}N NMR signal could be observed from fresh Cu-CHA. However, upon reduction in ^{15}NO at 300 ^{o}C, narrow signals are observed in the ^{15}N NMR spectra of the NO-reduced Cu-CHA both before and after steam

aging. Solid-state 1D direct-excitation ^{15}N MAS NMR spectra of fresh, 4-h-aged, and 16-h-aged Cu-CHA are shown in Figure 4. Three regions of ^{15}N NMR signal intensity are observed at 17, –18, and –24 ppm and are assigned to NH_4^+, $[Cu(NH_3)_2]^+$, and $[CuNH_3]^+$ based on previous literature.[53] Notably, the line width of the ^{15}N MAS NMR signals is substantially broader for 4-h-aged and 16-h-aged Cu-CHA compared to fresh Cu-CHA, indicating more varied ^{15}N chemical environments after steam-aging. ^{15}N spin-counting NMR analyses were undertaken to quantify the loss of $^{15}NH_3$ adsorption sites upon steam treatment.

The percentages of total detected ^{15}N from this analysis are shown in Figure 3, with associated spin-counting ^{15}N NMR spectra and analysis are shown in Figure S22 and Table S9. The percentages assume that each cation observed corresponds to one framework aluminum atom. Consistent with the framework Si/Al ratios calculated from Figure 1, the percentage of total detected aluminum declines substantially from 93% to 20% going from the fresh Cu-CHA to the 4-h-aged Cu-CHA, and then declines further to 12% for 16-h-aged Cu-CHA. The relative proportions of $[Cu(NH_3)_2]^+$ and $[Cu(NH_3)]^+$ are approximately the same in all materials, suggesting that these proportions may be a result of the pretreatment temperatures, not Cu distributions in Cu-CHA.[25] Interestingly, the relative proportion of ^{15}N NMR signal intensity attributed to NH_4^+ adsorption sites decreases as a result of steam-aging, suggesting that residual Bronsted acid environments in Cu-CHA are more susceptible to framework dealumination. This is consistent with previous observations that zeolites exchanged with Cu^{2+} are more resistant to dealumination by hydrothermal treatment than those in the H^+ form. This loss of excess Bronsted acid sites can be quantified as a change in the observed Cu/Al ratio, where each $[Cu(NH_3)_2]^+$ or $[Cu(NH_3)]^+$ corresponds to one Cu and each positive charge observed corresponds to one observed framework Al. The observed Cu/Al ratio of the fresh

Cu-CHA is 0.29. This is higher than the ratio observed by elemental analysis, likely due to some framework Al being inaccessible for adsorbates. After high-temperature hydrothermal treatment, a detected Cu/Al ratio of 0.34 is observed for the 4-h-aged Cu-CHA, and a detected Cu/Al ratio of 0.50 is observed for the 16-h-aged Cu-CHA.

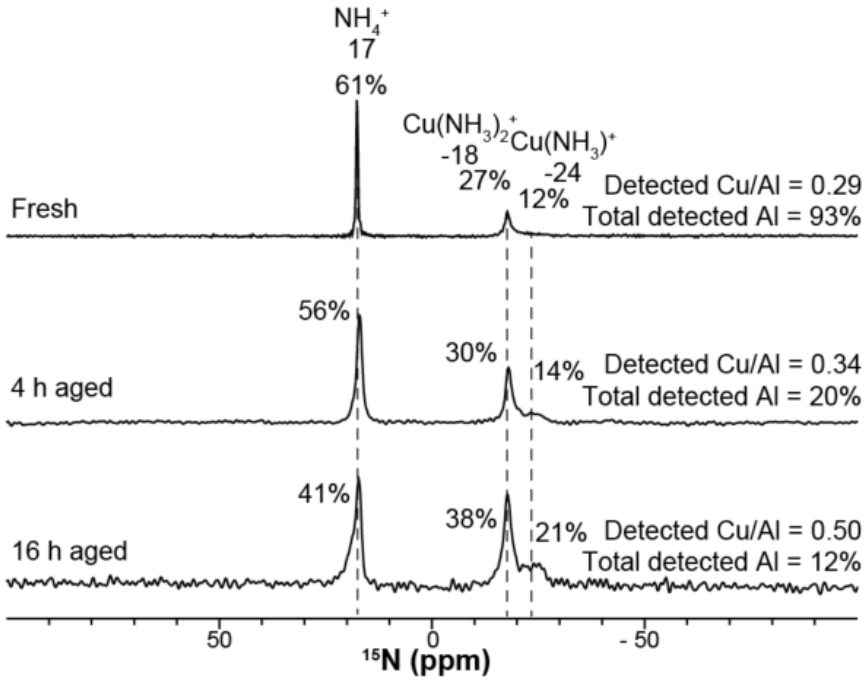

Figure 3. Solid-state 1D direct-excitation ^{15}N MAS NMR spectra of Cu-CHA catalyst materials after exposure to $^{15}NH_3$ at 120 ºC and reduction in ^{15}NO at 300 ºC. Spectra are normalized to the same absolute intensity. The total detected Al percentages are determined from the relative intensity of the 17 ppm ^{15}NMR signal as a function of total Al content based on ^{15}N spin counting (details in Figure SXX). The ^{15}N NMR spectra were acquired at 9.4 T, 10 kHz MAS, and room temperature.

Assessing changes in aluminum and silicon distributions in the Cu-CHA framework as a result of steam-aging is challenging due to the disorder created by framework dealumination and Cu nanoparticle formation. Solid-state NMR analyses are well-suited to identifying Si and Al framework connectivity through a combination of ^{27}Al and ^{29}Si NMR experiments.[54–57] However, proximity to paramagnetic Cu(II) cations result in rapid relaxation of excited nuclei in NMR, resulting in some ambiguity in the observed distributions of ^{29}Si and ^{27}Al chemical

shifts in Cu-containing zeolites.[58] Here, the effect of paramagnetic ions on NMR signal lifetimes is leveraged on Cu-CHA exposed to a simulated reduction-half-cycle of the SCR process to examine framework chemical environments of only framework ^{27}Al and ^{29}Si species located near reduced Cu(I) species, not deactivated Cu(II) species that do not undergo a reduction half cycle. This facilitates the observation of the types of framework species associated with active regions of the catalyst after high-temperature hydrothermal treatment, as compared to those same environments in the fresh catalyst.

Interestingly, the fresh Cu-CHA catalyst and hydrothermally-treated Cu-CHA catalyst exhibit significant differences in the nanoscale proximities of framework aluminum moieties. Solid-state 2D ^{27}Al-^{29}Si dipolar-mediated NMR heteronuclear correlation analyses reveal through-space associations between ^{27}Al and ^{29}Si species in sub-nanometer proximity,[59] and thus can be utilized to assess differences in populations of relatively dilute closely-paired framework aluminum configurations between zeolites.[55] Specifically, these analyses reveal differences in dilute populations of Q^4(2Al) ^{29}Si moieties, which correspond to ^{27}Al–O–^{29}Si–O–^{27}Al paired aluminum configurations. These paired aluminum configurations have previously been shown to effectively stabilize bare, divalent Cu^{2+} upon initial ion exchange.[60] Figure 4A,B shows solid-state 2D ^{27}Al-^{29}Si dipolar-mediated NMR heteronuclear correlation spectra for NO-reduced fresh Cu-CHA and 4-h-aged Cu-CHA. Figure 4A shows three well-resolved regions of correlated intensity for fresh Cu-CHA at 56 ppm in the ^{27}Al dimension, corresponding to four-coordinate framework Al atoms, correlated to ^{29}Si NMR signals at –111, –105, and –99 ppm, from Q^4(0Al), Q^4(1Al), and Q^4(2Al) moieties, respectively. The assignment of the relatively weak ^{29}Si NMR signal at –99 ppm to Q^4(2Al) moieties was confirmed by a solid-state 2D ^{27}Al-^{29}Si *J*-mediated NMR correlation spectrum of NO-reduced

fresh Cu-CHA, which shows correlated intensities only from *J*-coupled ^{27}Al and ^{29}Si nuclei which are separated by a single ^{27}Al–O–^{29}Si bond (Figure S23).[61] This experiment was not performed for the 4-h-aged or 16-h-aged Cu-CHA due to an infeasible experiment time as a result of dealumination.

In contrast to Figure 4A, Figure 4B shows the analogous spectrum of 4-h-aged Cu-CHA. This spectrum exhibits the same three regions of correlated signal intensity as observed in the spectrum of fresh Cu-CHA. However, the relative intensity of the correlated signal region assigned to Q^4(2Al) ^{29}Si moieties relative to the region corresponding to Q^4(1Al) ^{29}Si moieties is substantially higher for the spectrum of the 4-h-aged Cu-CHA than that of the fresh Cu-CHA, indicating that closely-paired framework Al species charge-balanced by divalent Cu(II) species are more resistant to high-temperature hydrothermal treatment than more isolated framework Al species. A solid-state 2D ^{27}Al-^{29}Si dipolar-mediated NMR heteronuclear correlation spectra of NO-reduced 16-h-aged Cu-CHA acquired under the same conditions is shown in Figure S24. The signal-to-noise of this spectrum is poor due to the low amount of framework Al remaining after the long hydrothermal treatment. However, all three regions of correlated NMR signals observed for fresh and 4-h-aged Cu-CHA are observed in the spectrum of this material, indicating the preservation of closely-paired framework Al species even after extreme hydrothermal treatment. ^{29}Si projections from solid-state 2D ^{27}Al–^{29}Si dipolar-mediated NMR heteronuclear correlation spectra are shown in Figure S25 and clearly show the differences in Q^4(2Al) signal intensity. There is a notable lack of defect Q^3 species detected in the ^{27}Al–^{29}Si correlation spectra of the hydrothermally-aged Cu-CHA catalysts despite the high amount of framework dealumination that has occurred in these materials (framework Si/Al = 24, 32 for 4-h-aged and 16-h-aged, relative to Si/Al = 10 for fresh, from Figure 1). This

is likely due to deactivated Cu(II) species that do not respond to the simulated reduction half-cycle of the SCR process being preferentially located near defects in the chabazite framework lattice, rendering these regions invisible to these 2D NMR analyses.

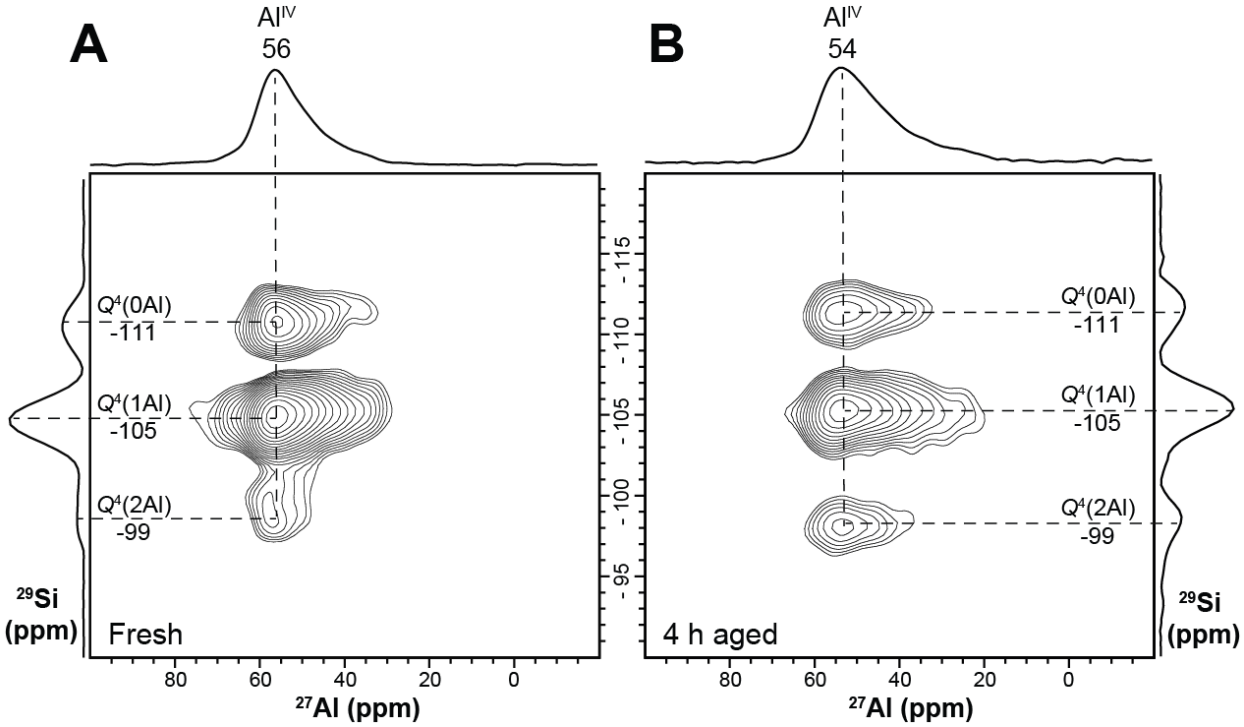

Figure 4. Solid-state 2D ^{27}Al–^{29}Si dipolar-mediated heteronuclear correlation NMR spectra of NO-reduced (A) fresh and (B) 4-h-aged Cu-CHA. A solid-state 2D ^{27}Al–^{29}Si dipolar-mediated heteronuclear correlation NMR spectrum of 16-h-aged Cu-CHA is shown in Figure S24. The 1D spectra shown across the top and sides are ^{27}Al and ^{29}Si projections of the 2D spectra, respectively. All spectra were acquired at 9.4 T, 100 K and 8 kHz MAS.

The preferential stabilization of closely paired framework aluminum species in Cu-CHA is unexpected from the perspective of framework stability. It has long been observed that the removal of framework Al from a zeolite framework resulted in a ^{29}Si NMR spectrum analogous to that of a fresh material synthesized with the resulting Si/Al ratio, suggesting closely paired framework Al species were preferentially lost.[62,63] In addition, recent work has indicated that closely-paired aluminum species are more susceptible to hydrolysis from the framework than unpaired aluminum atoms.[57] However, the observation of stabilized paired

framework aluminum species by Cu is consistent with reports of changes in distributions of EPR-active Cu cation species upon high-temperature hydrothermal treatment. It has been observed by EPR that Z_2Cu species appear more stable to hydrothermal treatment than ZCuOH species, which sinter to form CuO.[35] It has even been suggested that ZCuOH species may transform into Z_2Cu species as a result of hydrothermal treatment.[42] From these observations, it necessarily follows that multiple negative charges must be located in close proximity to charge balance the Cu^{2+} cation. These 2D NMR measurements unambiguously show that the charge-balancing species are closely-paired aluminum species in the zeolite framework. Thus, bare divalent Cu^{2+} cations preferentially protect closely paired aluminum species against high-temperature hydrothermal treatment.

The $[Cu(NH_3)_2]^+$ complex has been posited to be an important intermediate in the low-temperature SCR process due to its relative mobility. The ability of $[Cu(NH_3)_2]^+$ complexes to hop to neighboring residual Bronsted acid sites to form pairs and dimerize has been demonstrated to be a rate-limiting step in some reaction regimes.[32] Understanding the influences of catalyst aging on these processes is challenging due to the complicated distributions of Cu and Al species produced by high-temperature hydrothermal treatment. However, the relationships between proximate adsorbed species can be examined.

Solid-state NMR is sensitive to the proximities and relationships between local chemical environments. Specifically, exchange NMR analyses are sensitive to the transformation of NMR-active nuclear spins from one chemical environment to another. This can be due conformational changes, such as isomer switching or conformation changes of molecules in confined environments.[64,65] In addition, exchange NMR analyses are sensitive to the site hopping of adsorbed species between disparate adsorption environments.[66,67] Thus,

these analyses can be used to examine the exchange of NH_3 species between NH_4^+ and $[Cu(NH_3)_2]^+$ complexes, as shown in Figure 5A. While not a direct measure of Cu mobility, these analyses provide information on the proximity of $[Cu(NH_3)_2]^+$ complexes to nearby residual Bronsted acid sites.

Solid-state 2D exchange NMR analyses were performed on fresh, 4-h-aged, and 16-h-aged Cu-CHA after exposure to $^{15}NH_3$ at 120 ºC and reduction in ^{15}NO at 300 ºC. In the 2D ^{15}N exchange NMR experiment, the chemical shifts of ^{15}N nuclei are initially measured and compared to those at a later time (after the so-called mixing time), during which some species can undergo chemical exchange that results in different chemical shifts of the ^{15}N nuclei, such that the chemical shift of the ^{15}N nuclei before and after the mixing time can be correlated. Solid-state 2D ^{15}N exchange NMR spectra of fresh Cu-CHA obtained at 326 K at three different mixing times are shown in Figure 5B-D. Solid-state 2D ^{15}N exchange NMR spectra acquired at different temperatures and mixing times for fresh, 4-h-aged and 16-h-aged Cu-CHA can be found in the SI (Figure S26-S70). The ^{15}N NMR signals shown along the vertical axis represent the ^{15}N chemical environments observed prior to the mixing time, and the ^{15}N NMR signals shown along the horizontal axis represent the ^{15}N chemical environments observed after the mixing time. Regions of intensity in the 2D contour map represent correlations between ^{15}N chemical environments before and after the mixing time. Two ^{15}N NMR signals are observed on both the horizontal and vertical axes at 17 ppm and –18 ppm corresponding to ^{15}N nuclei in NH_4^+ and $[Cu(NH_3)_2]^+$ complexes charge-balancing aluminum in the zeolite framework, respectively. The ^{15}N NMR signal at –24 ppm assigned to ^{15}N in $[Cu(NH_3)]^+$ complexes was consistently not observed above the noise level in the 2D ^{15}N exchange NMR spectra observed, and thus is excluded from the exchange NMR analyses. Four

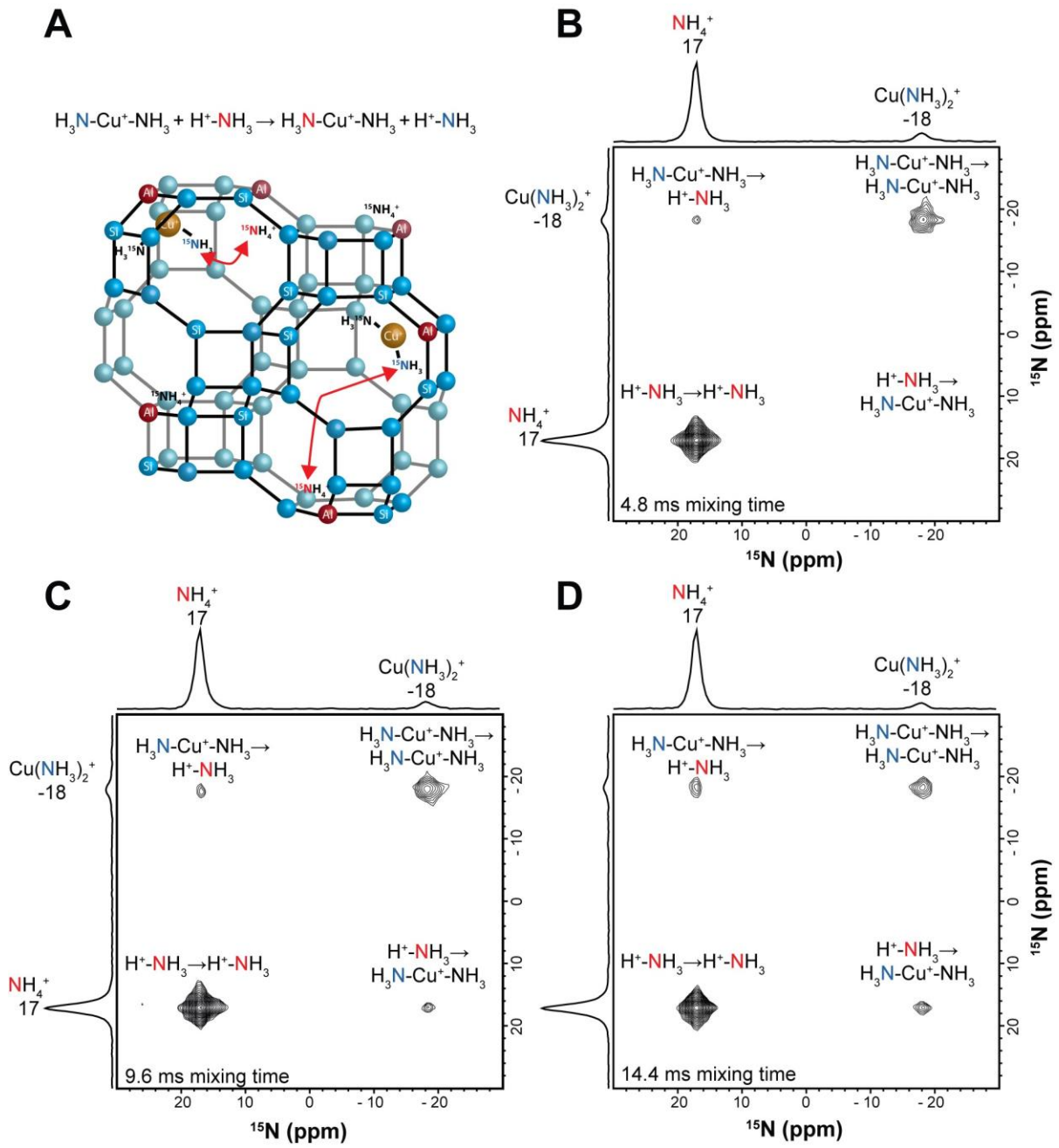

Figure 5. (A) Schematic diagram depicting exchange of $^{15}NH_3$ species between NH_4^+ and $[Cu(NH_3)_2]^+$ species in Cu-CHA. Framework Si and Al atoms are shown in blue and red, respectively, and Cu cations are shown in gold. Arrows show possible exchange pairs in the Cu-CHA pores. (B–D) Solid-state 2D ^{15}N EXSY NMR spectra of fresh Cu-CHA after $^{15}NH_3$ exposure at 120 °C and subsequent reduction in ^{15}NO at 300 °C. The spectra were acquired with mixing times of (B) 4.8 ms, (C) 9.6 ms, and (D) 14.4 ms at 326 K, 11.7 T, and 12.5 kHz MAS. Additional 2D ^{15}N EXSY NMR spectra acquired of fresh Cu-CHA at different mixing times and temperatures, along with 2D ^{15}N EXSY NMR spectra of 4-h-aged Cu-CHA and 16-h-aged Cu-CHA, are shown in Figures S26-S70.

regions of correlated intensity are observed in the 2D exchange NMR spectra. The region of correlated intensity at 17 ppm in both the horizontal and vertical dimensions represents ^{15}N nuclei in NH_4^+ chemical environments before and after the mixing period. Similarly, the region of correlated intensity at –18 ppm in both the horizontal and vertical dimensions represents ^{15}N nuclei in $[Cu(NH_3)_2]^+$ complexes before and after the mixing period. These correlated signals represent nuclei that have not changed chemical environments. In comparison, regions of correlated intensity at (i) 17 ppm in the vertical dimension and –18 ppm in the horizontal dimension and (ii) –18 ppm in the vertical dimension and 17 ppm in the horizontal dimension represent ^{15}N nuclei that have exchanged (i) from NH_4^+ to $[Cu(NH_3)_2]^+$ chemical environments and (ii) from $[Cu(NH_3)_2]^+$ chemical environments during the mixing time, respectively. Notably, these cross signals grow more intense relative to the on-diagonal signals (those with the same ppm ^{15}N chemical shift in the vertical and horizontal dimension) as mixing time increases from Figure 5B to Figure 5D. This suggests a kinetic process driving the exchange of NH_4^+ and NH_3 ligands on $[Cu(NH_3)_2]^+$ complexes.

The exchange of $^{15}NH_3$ ligands between proximate NH_4^+ and $[Cu(NH_3)_2]^+$ can be modeled as a first-order, reversible exchange process given by the chemical reaction:

$$H^+\text{-}NH_3^A + [H_3NCu\text{-}NH_3^B]^+ \leftrightarrow H^+\text{-}NH_3^B + [H_3NCu\text{-}NH_3^A]^+$$

The kinetics of this exchange process can be obtained from solid-state 2D ^{15}N exchange NMR by comparing the intensity of the on-diagonal signals and cross peaks following analyses from Ernst Bodenhausen, and Wokaun.[68] These signals were integrated for solid-state 2D ^{15}N exchange NMR spectra obtained at 5 different mixing times. These data could then be fit by Equation 1:

$$I_{kl}(\tau_m) = [exp\{\boldsymbol{L}\tau_{\boldsymbol{m}}\}]_{kl} * x_l * M_0$$

where I is the intensity of a region of signal intensity, τ_m is the mixing time, x_l is the fraction of overall magnetization represented by chemical environment l, M_0 is the overall magnetization in the system, and $\boldsymbol{L}$ is the matrix given by Equation 2:

$$\boldsymbol{L} = \begin{pmatrix} -k_{BA} - R_1^A & k_{AB} - R_{AB} \\ k_{BA} - R_{BA} & -k_{AB} - R_1^B \end{pmatrix}$$

In Equation 2, k_{BA} and k_{AB} represent apparent rate coefficients for the exchange to B from A and A from B, respectively, where A corresponds to NH_4^+ chemical environments and B corresponds to $[Cu(NH_3)_2]^+$ chemical environments. R_1^A and R_1^B are spin-lattice relaxation coefficients for ^{15}N nuclei in NH_4^+ and $[Cu(NH_3)_2]^+$ chemical environments and were calculated from ^{15}N saturation recovery NMR analyses (values detailed in Table S10). R_{AB} and R_{BA} are cross-relaxation parameters related to magnetic dipole couplings between ^{15}N spins in NH_4^+ and $[Cu(NH_3)_2]^+$ chemical environments. Due to the low gyromagnetic ratio of ^{15}N and anticipated mobility of $^{15}NH_3$ species, these terms were assumed to have negligible effects on the data and were set to 0. The full treatment of fitting the solid-state 2D ^{15}N exchange NMR spectra with this model is described in the SI.

Integrated intensities from solid-state 2D ^{15}N exchange NMR spectra for fresh Cu-CHA A at 314, 326, and 339 K along with kinetic model fits are shown in Figure 6A-C. As mixing time increases, the intensity observed from ^{15}N NMR signals representing chemical exchange increases, and the intensity observed from ^{15}N NMR signals representing species staying in the same chemical environment correspondingly decreases. As measurement temperature increases from 314 K to 339 K going from Figure 6A to 6C, the intensity of the signals corresponding to exchange between NH_4^+ and $[Cu(NH_3)_2]^+$ increases. Apparent rate coefficients k_{AB} and k_{BA} extracted from these fits can be found in Table S11.

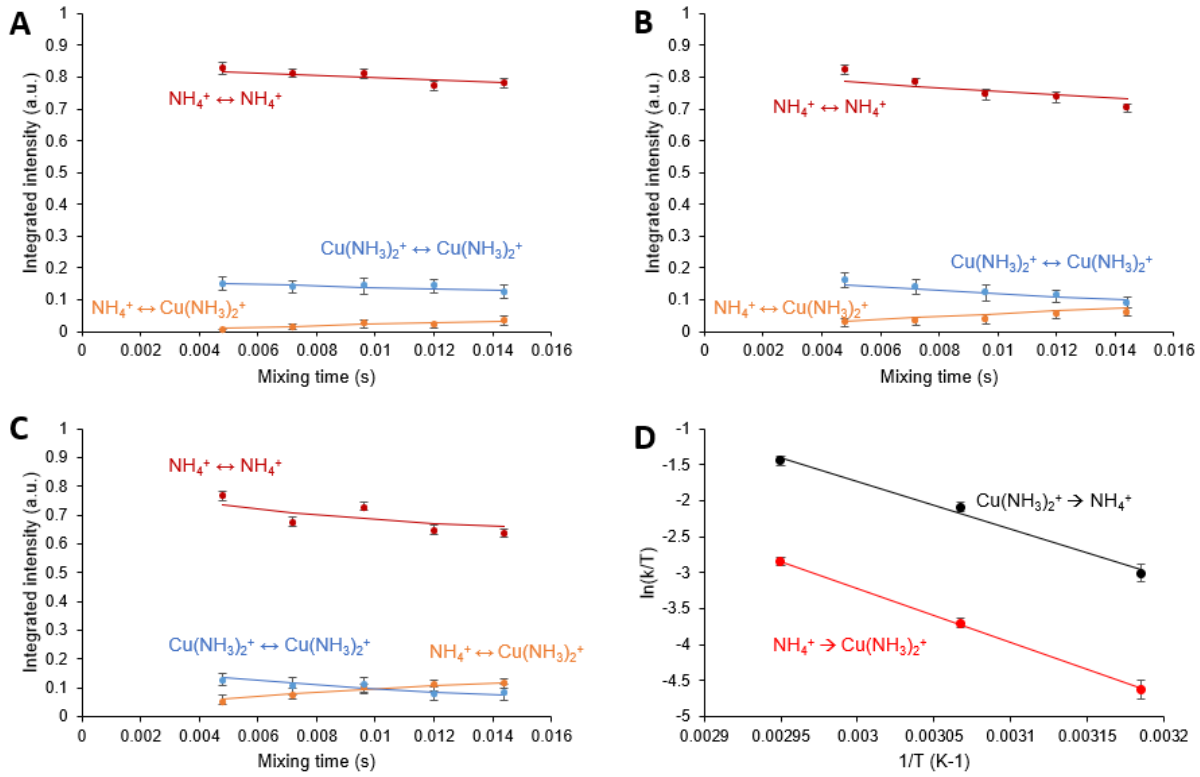

Figure 6. (A,B,C) Evolution of on-diagonal and off-diagonal 2D ^{15}N exchange NMR signal intensity at different mixing times for experiments performed at (A) 314 K, (B) 326 K, and (C) 339 K on fresh Cu-CHA after $^{15}NH_3$ adsorption at 120 ºC and subsequent reduction in ^{15}NO at 300 ºC. Measurement temperatures are based on an external calibration with lead nitrate. The fitted lines model the exchange process between NH_3 adsorbed as NH_4^+ on the zeolite framework and as part of a $[Cu(NH_3)_2]^+$ complex. (D) Eyring plot of the temperature-dependent exchange rate coefficients extracted from the models in A,B, and C. Similar analyses are shown for data collected on 4-h-aged Cu-CHA and 16-h-aged Cu-CHA in Figures S71-S72.

To better understand the differences in $^{15}NH_3$ chemical exchange between the fresh Cu-CHA and steam-aged Cu-CHA, the apparent rate coefficients extracted from analyses of the solid-state 2D ^{15}N exchange NMR spectra, the Eyring equation, given as Equation 3, was fit to the apparent rate coefficients for exchange as a function of temperature.[69]

$$k = \frac{\kappa k_B T}{h} e^{\Delta S^{\ddagger}/R} e^{-\Delta H^{\ddagger}/RT}$$

In Equation 3, $\Delta H^{\ddagger}$ and $\Delta S^{\ddagger}$ are the changes in enthalpy and entropy of activation, R is the ideal gas constant, k_B is Boltzmann's constant, h is the Planck constant, and κ is the transmission coefficient (assumed to be 1). A fit of the linearized Eyring equation to the apparent rate constants fit to the solid-state 2D ^{15}N exchange NMR spectra obtained for fresh Cu-CHA is shown in Figure 6D (analogous fits for the apparent rate constants fit to the solid-state 2D ^{15}N exchange NMR spectra of 4-h-aged Cu-CHA and 16-h-aged Cu-CHA are shown in Figure S71-72).

The values of $\Delta H^{\ddagger}$ and $\Delta S^{\ddagger}$ found from fitting the Eyring equation are summarized in Table 1. Given the assumption of an exchange process, the $\Delta H^{\ddagger}$ and $\Delta S^{\ddagger}$ values for exchange from NH_4^+ to $[Cu(NH_3)_2]^+$ and $[Cu(NH_3)_2]^+$ to NH_4^+ should be the same for a given set of measurements, and are well within the uncertainties of each other for all three Cu-CHA. Going from fresh Cu-CHA to 16-h-aged Cu-CHA, $\Delta H_{Cu \rightarrow H}^{\ddagger}$ decreases from 56 kJ/mol to 42 kJ/mol. This difference is on the edge of statistical significance ($p = 0.07$ for the above comparison). The similarity of these values indicates that, despite heavy dealumination from steam treatment, the types and proximities of $^{15}NH_3$ adsorption environments present in the steam-aged Cu-CHA catalyst do not drastically differ from those in the fresh catalyst. The minor decrease in activation enthalpy upon steam treatment could indicate either than, on average, the observed NH_3 adsorption environments are weaker after steam treatment or that the distances between proximate $^{15}NH_3$ adsorption environments have decreased. A decrease in distance with increasing hydrothermal treatment would be consistent with observations above about the preferential stabilization of closely-paired aluminum species against high-temperature hydrothermal treatment, as Z_2Cu species can form a $[Cu(NH_3)_2]^+$ and NH_4^+ pair charge-balancing the two framework sites after exposure to NH_3.[25] These exchange pairs

would be in closer proximity than some of the longer range pairs present in the fresh catalyst but lost upon high-temperature hydrothermal treatment. Interestingly, the trend in activation enthalpy with dealumination and corresponding apparent increase in the active Cu/Al ratio is consistent with observations made by impedance spectroscopy on the effect of Cu/Al ratio on the activation energy of ion conduction in NH_3-solvated Cu-CHA.[70]

The activation entropy associated with the NH_3 exchange process are negative, indicating that the transition state associated with this process is more constrained than the individual adsorption environments. Along with the trend in activation enthalpy with increased steam-aging, there is a corresponding decrease in the activation entropy with steam aging due to the compensation effect (Figure S73), which has been reported previously for adsorption of small molecules in other zeolite systems.[71–73] While examples of deviations from this trend in heterogeneous catalysis are rare,[74] the physical phenomena explaining the trend difficult to ascertain. Perhaps the loss of residual Bronsted acid sites results in a weaker stabilization of the transition state for the NH_3 exchange, resulting in a more distorted transition environment.

Table 1. NH_3-exchange Eyring equation parameters for NO-reduced Cu-CHA materials*

	$\Delta H_{Cu\rightarrow H}^{\ddagger}$ (kJ/mol)	$\Delta H_{H\rightarrow Cu}^{\ddagger}$ (kJ/mol)	$\Delta S_{Cu\rightarrow H}^{\ddagger}$ (J/mol*K)	$\Delta S_{H\rightarrow Cu}^{\ddagger}$ (J/mol*K)
Fresh	56(5)	63(5)	–45(16)	–35(15)
4-h-aged	47(8)	53(8)	–72(25)	–59(25)
16-h-aged	42(6)	46(6)	–90(18)	–82(18)

*Uncertainties shown in parentheses represent standard deviations of parameters based on a Monte Carlo-based error propagation from the uncertainties in the 2D ^{15}N EXSY NMR results.

Conclusions

A combination of molecular-level characterization techniques are demonstrated to reveal the evolution of copper and aluminum species as a result of high-temperature hydrothermal treatment of a Cu-CHA SCR catalyst. As a result of the hydrothermal treatment, a significant fraction of the aluminum in the chabazite framework is converted to

extraframework aluminum, which appears to complex with copper species. After hydrothermal treatment, single-atom Cu cations located near double-six-member-ring structures in the chabazite framework agglomerate into 1–2 nm size clusters, which appear to be located at internal defects in the chabazite crystal structure. The types of Cu NH_3 adsorption environments present in the hydrothermally-treated catalyst remain similar to fresh Cu-CHA, though reduced in intensity. 2D ^{27}Al-^{29}Si NMR correlation analyses reveal that closely-paired aluminum species are preferentially preserved during high-temperature hydrothermal treatment. 2D exchange NMR analyses reveal that the activation enthalpy related to NH_3 chemical exchange in Cu-CHA decreases slightly upon steam-treatment, perhaps reflecting changes in adsorption energies as a result of the hydrothermal treatment process. These results provide useful new details on the changes in local chemical environments induced in Cu-CHA by high-temperature hydrothermal treatment. These observations are likely to also be useful for understanding a variety of metal-exchanged zeolites used for different reaction chemistries.

Supporting Information

Materials and Methods

Materials. Fresh Cu-CHA, 4-h-aged Cu-CHA, and 16-h-aged Cu-CHA were obtained from BASF (Iselin New Jersey, USA). Aged samples were exposed to 10% steam in flowing air at 750 ºC for either 4 h or 16 h.

Preparation of NO-reduced Cu-CHA. To simulate the reduction half cycle of the selective catalytic reduction of NO_x by NH_3 (SCR) process, approximately 80 mg of a Cu-CHA sample were placed in a flow reactor. The sample was dehydrated by heating the material to 500 ºC under vacuum at a ramp rate of 2 ºC/min and held under vacuum for 12 h to ensure that no water was present on the catalyst prior to the reduction half-cycle. The sample was then exposed to flowing dry air (Airgas, Ultra Zero grade) at 100 SCCM for 1 h at 500 ºC to oxidize species to Cu(II) that may have been auto-reduced during the dehydration process.[75] The reactor was purged by vacuum-cycling with pure argon gas (Airgas, ultra-high purity grade) to remove oxygen and then cooled to 120 ºC under vacuum. The vacuum line was equipped with a liquid-nitrogen-cooled cold trap to ensure no back diffusion of water vapor into the reactor vessel. At 120 ºC, the sample was exposed to 1 kPa of ^{15}N-enriched NH_3 (Sigma-Aldrich, pure gas, 98 atom% ^{15}N) for 30 min to allow adsorption, after which a vacuum of 0.01 kPa was pulled for 30 min to remove weakly adsorbed species and then the reactor was vacuum-cycled with pure argon gas to remove excess $^{15}NH_3$ gas. The sample was then exposed to 10 kPa of ^{15}N-enriched NO (Cambridge Isotope Laboratories, pure gas, 98% ^{15}NO) at 120 ºC. The temperature was ramped to 300 ºC at a rate of 5 ºC/min and held at 300 ºC for 2 h. After 2 h, at 300 ºC the reactor was vacuum cycled with pure argon gas to remove reactant and product gas species. The reactor was then sealed under vacuum and cooled to room temperature, after

which it was transferred to an argon glovebox to prepare samples for characterization without exposure to oxygen or water vapor.

Solid-state ^{27}Al and ^{29}Si NMR. Solid-state 1D direct-excitation ^{27}Al and ^{29}Si MAS NMR spectra were acquired on hydrated Cu-CHA samples. To ensure consistent hydration across measured samples, the samples were stored for at least 24 h in a sealed container containing a saturated solution of potassium chloride to maintain a relative humidity of 85% and ensure full hydration of the zeolite materials. Solid-state 1D direct-excitation ^{27}Al MAS NMR spectra were acquired at 18.8 T under ambient temperature conditions on a 800 MHz Bruker Avance NMR spectrometer using a 3.2 mm zirconia rotor at a magic-angle-spinning (MAS) frequency of 20 kHz. A 0.5 μs radiofrequency (r.f.) excitation pulse corresponding to a 5-degree flip angle for ^{27}Al spins in solution was applied to ^{27}Al nuclei. 8192 scans were acquired on each sample with a recycle delay of 0.2 s, which was found to be sufficient for complete relaxation of ^{27}Al spins between scans. The ^{27}Al NMR spectra were referenced to a 0.5 M aqueous solution of $Al(NO_3)_3$ at 0 ppm. Solid-state 1D direct-excitation ^{29}Si MAS NMR spectra were acquired at 11.7 T under ambient temperature conditions on a 500 MHz Bruker Avance NMR spectrometer using a 4 mm zirconia rotor at a MAS frequency of 12.5 kHz. 256 scans were acquired with a 90^{o} 50 kHz r.f. excitation pulse applied to ^{29}Si nuclei. Recycle delays of 1 s, 2 s, and 3 s were used for fresh, 4-h-aged, and 16-h-aged Cu-CHA, respectively, to maintain a recycle delay of at least 5*T_1 for each material, as measured by a ^{29}Si saturation recovery experiment, and ensure full relaxation between scans. During ^{29}Si NMR signal acquisition, SPINAL-64 heteronuclear decoupling was applied to ^{1}H nuclei.[76] The ^{29}Si NMR spectra were referenced to tetramethylsilane (TMS) at 0 ppm by using tetrakis(trimethylsilyl)silane (TKS) as a

secondary standard at –9.84 ppm. Deconvolutions and integrations of direct-excitation ^{29}Si MAS NMR spectra were performed using the DMFit software.[77]

Solid-state ^{27}Al spin-counting NMR experiments on hydrated Cu-CHA samples were acquired at 18.8 T under ambient temperature conditions on a 800 MHz Bruker Avance NMR spectrometer using a 3.2 mm zirconia rotor spinning at 20 kHz. Aluminum nitride was used as a spin-counting reference. The rotor was packed with a small plug of Teflon tape, followed by a known mass of AlN, followed by another plug of Teflon tape, followed by a known mass of Cu-CHA sample. A 0.5 μs radiofrequency (r.f.) excitation pulse corresponding to a 5-degree flip angle for ^{27}Al spins in solution was applied to ^{27}Al nuclei. 128 scans were acquired on each sample with a recycle delay of 16 s. This recycle delay was found to be sufficient for full relaxation of slow-relaxing ^{27}Al nuclear spins in AlN at the shallow flip angle used, and 128 scans was sufficient to integrate the Al^{IV} signal for each sample, providing information on the fraction of visible aluminum. Deconvolutions and integrations were performed using the DMFit software.

Elemental analysis. Elemental analysis of the fresh Cu-CHA catalyst to obtain Cu, Al, and Si contents was performed by X-ray fluorescence spectroscopy using a Rigaku ZXS Primus IV wavelength-dispersive X-ray fluorescence spectrometer. Approximately 50 mg of the fresh Cu-CHA were mixed with X-ray mix powder (Chemplex, catalog number: 600) and compressed into a pellet, which was used for the elemental analysis. The Cu, Al, and Si contents were measured three times to provide information on the precision of the measurement.

X-ray diffraction characterization. Powder X-ray diffraction patterns were acquired on a Panalytical Empyrean Powder Diffractometer with a Cu-Kα radiation source. For measurements, samples were dispersed in ethanol solution and deposited on a zero-background

plate (MTI Corporation) to produce a thin layer of sample. Diffraction patterns were measured from 5° to 50° with a scan rate of 0.00005 ° s^{-1} and step size of 0.007 °; a background was subtracted from the datasets.

NH_3 temperature-programmed desorption (TPD). TPD experiments were performed with a Micromeritics AutoChem II 2920 Chemisorption analyzer and outlet gas was monitored using a thermal conductivity detector (TCD). Powder catalyst samples (50mg) were loaded in a quartz reactor tube supported between two quartz wool plugs. Prior to the TPD experiment samples were dehydrated in UHP helium, 99.999%, (Airgas) at 450 °C for 2 hours followed by an oxidation at 450 °C for 1 hour in UHP oxygen, 99.999%, (Airgas). The samples were then cooled in UHP helium, 99.999%, (Airgas) to 120 °C and held for 15 minutes before exposing the sample to 10% NH_3 in helium (Airgas) for 2 hours. The system was purged with UHP helium, 99.999%, (Airgas) for 2 hours at 120 °C before starting the TPD measurement from 120 °C to 700 °C with a ramp rate of 10 °C/minute. NH_3 desorption rate was derived from TCD calibration curve of 10% NH_3 in Helium (Airgas).

N_2 physisorption. N_2 adsorption isotherms at 77 K were acquired for fresh, 4-h-aged, and 16-h-aged Cu-CHA on a Micrometrics 3Flex Porosimeter. For each measurement, approximately 100 mg of hydrated CHA material were loaded into the instrument. Prior to the N_2 physisorption measurements, samples were pretreated by dehydrating for 10 h at 300 °C under vacuum with a temperature ramp of 1 °C/min. This dehydration was found to be sufficient to remove the majority of the adsorbed water from the hydrated CHA material. After dehydration, the sample was submerged in liquid nitrogen and dosed with N_2 gas.

Thermogravimetric analysis. Thermogravimetric analysis (TGA) was performed on fresh, 4-h-aged, and 16-h-aged Cu-CHA to calculate the fraction of sample mass from water in each material. Prior to measurement, samples were stored for at least 24 h in a sealed container containing a saturated solution to maintain a relative humidity of 85% and ensure full hydration of the zeolite materials. Approximately 5 mg of hydrated sample was loaded into the sample pan of a Discovery TGA 5500. Under 25 SCCM flowing argon, the furnace temperature was ramped from room temperature to 450 ºC at a rate of 10 ºC/min, and then held at 450 ºC for 1 h. The mass of the sample was tracked throughout the temperature program, and the difference between the mass at the start and end of the temperature program was assumed to be entirely due to water loss.

Scanning Transmission Electron Microscopy. Zeolite samples for microscopy were dispersed in ethanol and deposited on lacey carbon gold transmission electron microscopy grids (Ted Pella). The atomic resolution high angle annular dark field (HAADF) scanning transmission electron microscopy (STEM) images were obtained using a FEI Titan 80-300 transmission electron microscope (TEM), which is equipped with a Schottky field emission gun, a Wien-type monochromator, a CEOS probe C_s corrector, a Fischione STEM HAADF detector, as well as Gatan STEM detectors and Gatan Image Filter (GIF) Tridium. The HAADF STEM images were acquired with an electron beam energy of 300 kV, a beam current of ~ 50 pA, a beam convergence half-angle of ~ 19 mrad, and an inner collection half-angle of ~ 55 mrad. Single-frame HAADF STEM images used for measuring the sizes of Cu-rich clusters were acquired with a dwell time of 16 µs, a pixel number of 1024x1024, a pixel size of 97.5 pm, and at a magnification of 1.3M. The atomic scale structure of the zeolite was imaged by integrating around 10 consecutive HAADF STEM images acquired at 3.6M magnification and

with a pixel number of 512x512, a pixel size of 47.7 pm, and a dwell time of 8 μs. Fourier filtering was also applied to the raw images to better reveal the atomic scale structure of the chabazite crystals.

STEM energy dispersive X-ray spectroscopy (EDS) measurements were carried out using a JEOL monochromated ARM200F equipped with a Schottky field emission gun, a double-Wien type monochromator, CEOS probe and image C_s correctors, a double silicon drift detector (SDD) for EDS, and a Gatan GIF Continuum for electron energy loss spectroscopy. The microscope was operated at 200 kV and the electron beam current was set to ~ 80 pA for STEM EDS measurements.

Continuous-wave EPR. Continuous-wave (cw) EPR spectra were acquired for dehydrated, oxidized samples. To dehydrate the zeolite samples, the samples were held under vacuum at 500 ºC for 12 h with a 2 ºC/min ramp rate. The samples were then exposed to 100 SCCM flowing dry air (Airgas, Ultra Zero grade) for 1 h at 500 ºC, after which the vessel was vacuum-cycled with pure argon gas (Airgas, ultra-high purity grade) to remove oxygen. The samples were sealed under vacuum, cooled to room temperature, and transferred to an argon glove box for sample preparation. Samples were packed in 4 mm quartz EPR tubes (Wilmad Labglass) and sealed with an epoxy resin in the glove box. Continuous-wave EPR spectra were obtained using a Bruker EMXplus X-band EPR Spectrometer cooled to a temperature of 100 K. For each sample, 16 scans were obtained with a field sweep from 125 to 525 mT. Fits to the experimental EPR spectra were performed using EASYSPIN.[78]

Solid-state ^{15}N NMR. Solid-state 1D ^{15}N direct-excitation MAS NMR spectra were acquired on NO-reduced Cu-CHA samples at 9.4 T on a 400 MHz Bruker Ascend NMR spectrometer using a 3.2 mm zirconia rotor spinning at 10 kHz under ambient temperature conditions. A 25

kHz 90° pulse was used for excitation of ^{15}N nuclei. 16384 scans were acquired were 4-h-aged and 16-h-aged Cu-CHA, while only 4096 scans were acquired for fresh Cu-CHA due to sufficient signal-to-noise. A 5 s recycle delay was used between scans to ensure full relaxation of all ^{15}N NMR signals. SPINAL64 heteronuclear decoupling was applied to ^{1}H nuclei during acquisition. ^{15}N chemical shifts were referenced to liquid NH_3 at 0 ppm using a secondary reference of powder ^{15}N-enriched NH_4Cl (Sigma Aldrich, >99% chemical purity, >98% ^{15}N) at 39.3 ppm.[79] The authors note that CH_3NO_2 is also commonly used as a 0 ppm reference for ^{15}N NMR chemical shifts.[53] To compare the ^{15}N chemical shifts reported here to those in literature using a CH_3NO_2 0 ppm reference, 380.6 should be subtracted from all ^{15}N chemical shifts in this manuscript.[79]

Solid-state ^{15}N spin-counting NMR experiments were conducted on NO-reduced Cu-CHA samples at 11.7 T on a 500 MHz Bruker Avance NMR spectrometer using a 4 mm zirconia rotor spinning at 12.5 kHz under ambient temperature conditions. ^{15}N-enriched NH_4Cl (Sigma Aldrich, >99% chemical purity, >98% ^{15}N) was used as a spin-counting reference. Rotors were packed with a plug of Teflon tape, followed by a known mass of $^{15}NH_4Cl$, followed by Teflon tape, followed by a known mass of NO-reduced Cu-CHA. A 22.7 kHz 90° r.f. pulse was used for excitation of ^{15}N nuclei. 256 scans were acquired for fresh Cu-CHA, and 2048 scans were acquired for 4-h-aged and 16-h-aged Cu-CHA. A recycle delay of 30 s was used in all experiments, which was found to be sufficient for full relaxation of ^{15}N nuclear spins in $^{15}NH_4Cl$. During acquisition, SPINAL-64 heteronuclear decoupling was applied to ^{1}H nuclei. Deconvolutions and integrations were performed using the DMFit software.

Solid-state 2D ^{27}Al–^{29}Si NMR correlation analyses. 2D dipolar-mediated ^{27}Al–^{29}Si D-HMQC were acquired for NO-reduced forms of each Cu-CHA sample, and a 2D *J*-mediated ^{27}Al–^{29}Si *J*-HMQC was acquired for the NO-reduced fresh Cu-CHA. These measurements were performed at 9.4 T at 100 K on a 400 MHz Bruker Ascend NMR spectrometer equipped with a triple-resonance Bruker NMR probehead using 3.2 mm zirconia rotors spinning at an MAS frequency of 8 kHz. Rotors were packed in an argon glove box. For the 2D ^{27}Al–^{29}Si D-HMQC experiments, 32 increments with a t_1 increment of 250 μs were acquired with a recycle delay of 1 s. For each increment, 128 scans were acquired for fresh Cu-CHA, 2048 scans were acquired for 4-h-aged Cu-CHA, and 4096 scans were acquired for 16-h-aged Cu-CHA in order to acquire spectra with sufficient signal-to-noise for each material. 25 kHz r.f. pulses were applied to ^{29}Si for the 90^{o} pulses in the experiment, and 15.6 kHz r.f. pulses were applied to ^{27}Al. SR4$^2_1$ recoupling at an r.f. field of 16 kHz was applied to recouple ^{27}Al and ^{29}Si nuclei through dipolar interactions with a total recoupling time of 9 ms.[59] A 1-ms double-frequency-sweep shaped pulse was applied to ^{27}Al nuclei at the start of the pulse sequence and swept between 100 kHz and 1 MHz relative to the carrier frequency.[80] Continuous-wave heteronuclear decoupling was applied to the ^{1}H channel during the ^{27}Al–^{29}Si recoupling blocks, and SPINAL64 heteronuclear decoupling was applied to the ^{1}H channel during t_1 evolution and acquisition. For the 2D ^{27}Al–^{29}Si *J*-HMQC spectrum acquired of fresh Cu-CHA, 32 increments of 256 scans were acquired with a t_1 increment of 250 μs and a recycle delay of 1 s. 25 kHz r.f. pulses were applied to ^{29}Si nuclei, and 15.6 kHz r.f. pulses were applied to ^{27}Al nuclei. A τ delay of 16 ms was used to allow ^{27}Al–^{29}Si *J*-couplings to evolve. A 1-ms double-frequency-sweep shaped pulse was applied to ^{27}Al nuclei at the start of the pulse sequence and swept between 100 kHz and 1 MHz relative to the carrier frequency.

Solid-state 2D ^{15}N exchange NMR analyses. 2D ^{15}N EXSY NMR spectra of NO-reduced Cu-CHA samples were acquired at 11.7 T on a 500 MHz Bruker Avance NMR spectrometer using a 4 mm zirconia rotor at a MAS frequency of 12.5 kHz. Samples were packed in rotors in an argon glove box. For spectra acquired on fresh Cu-CHA, 128 increments of 64 scans were acquired with a t_1 increment of 62.5 μs with a recycle delay of 1 s between scans. 20 kHz r.f. pulses were applied to ^{15}N nuclei. For spectra acquired on 4-h-aged Cu-CHA and 16-h-aged Cu-CHA, 48 increments of 256 scans were acquired with a t_1 increment of 62.5 μs with a recycle delay of 1 s between scans. 22.7 kHz r.f pulses were applied to ^{15}N nuclei. These differences in parameters for fresh and hydrothermal-treated Cu-CHA were necessary to acquire adequate signal-to-noise for all samples and to acquire sufficient t_1 increments for magnetization to meaningfully decay. For all samples, 2D spectra were acquired with mixing times of 4.8, 7.2, 9.6, 12.0, and 14.4 ms at temperatures of 314, 326, and 339 K. Sample temperatures were determined by a secondary temperature calibration to the ^{207}Pb chemical shift of solid $Pb(NO_3)_2$, which has a linear dependence on temperature change, measured under the same flow and heating conditions as the variable-temperature measurements, following standard methods.[81] Room temperature in the probe was calibrated by ^{1}H NMR of methanol following standard methods.[82] For all experiments, SPINAL64 heteronuclear decoupling was applied on the ^{1}H channel from initial excitation to the end of acquisition. For all spectra, it was necessary to apply a two-fold linear forward prediction to the indirect dimension of the processed data to obtain fully relaxed data for all acquired spectra. Truncation of the acquired data was necessary to make experiment times reasonable. Spectra were processed for kinetic

analysis by taking horizontal projections around the signals at 17 and –18 ppm, which were then integrated with constant lineshapes using DMFit.

Basic characterization

Bulk Cu, Al, and Si contents of the Cu-CHA material investigated were characterized by X-ray fluorescence spectroscopy and are shown in Table S1. Hydrothermal treatment does not result in loss of Si, Al, or Cu species, only their rearrangement, so these values were assumed to be consistent regardless of hydrothermal treatment conditions.

Table S1. Bulk atomic percentages and ratios as calculated by X-ray fluorescence spectroscopy*

Si	90.31(6)
Al	8.00(4)
Cu	1.69(2)
Si/Al	11.29(6)
Cu/Al	0.211(2)

*Numbers in parentheses correspond to last digit, and are sample standard deviations calculated by repeating the x-ray fluorescence spectroscopy measurement on three different sample regions.

To assess changes in the crystallinity of the Cu-CHA framework structure as a result of hydrothermal treatment, powder X-ray diffraction patterns were acquired for fresh, 4-h-aged, and 16-h-aged Cu-CHA (Figure S1). For all materials, sharp diffraction peaks are observed that are indexed to a chabazite framework structure (Space group $R\bar{3}m$). Notably, while there are minor decreases in the intensities of the sharp diffraction peaks because of hydrothermal treatment, there is no broad diffraction feature that could be attributed to formation of amorphous alumina-silica regions, indicating that the bulk of the material maintains a degree of crystallinity.

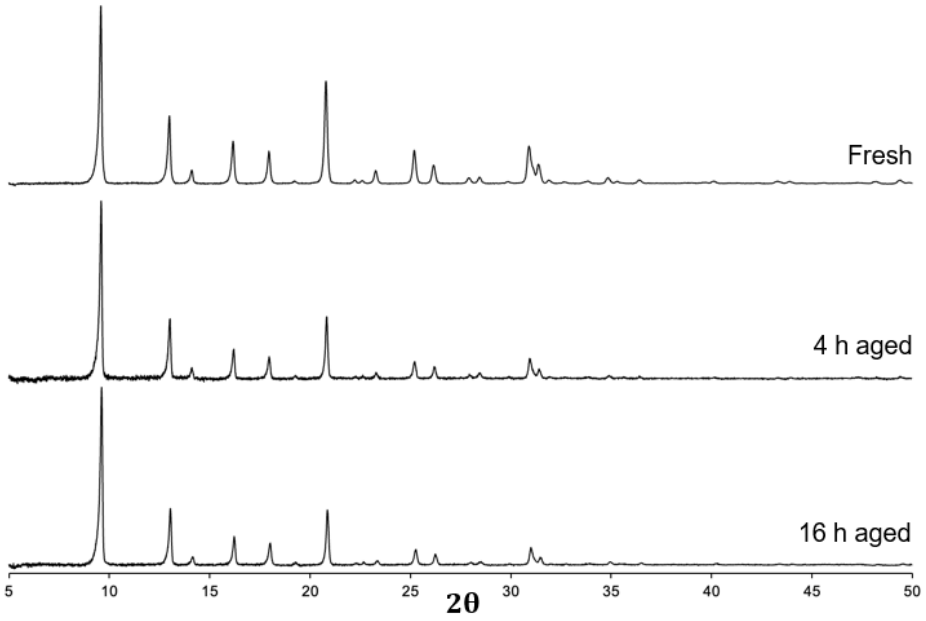

Figure S1. Powder X-ray diffraction patterns acquired for fresh, 4-h-aged, and 16-h-aged Cu-CHA. All three diffraction patterns exhibit sharp features indexable to a CHA framework (Space group $R\bar{3}m$) and no broad features indicative of significant formation of amorphous domains.

NH_3 temperature-programmed desorption (TPD) is commonly used to assess differences in amounts and strengths of adsorption environments in small-pore chabazite zeolites. NH_3 TPD desorption curves for fresh, 4-h-aged, and 16-h-aged Cu-CHA are shown in Figure S2. The NH_3 TPD desorption curve for fresh Cu-CHA exhibits three broad features at approximately 200 ºC, 325 ºC and 450 ºC which are assigned to weak adsorption environments, NH_3 on Cu, and NH_3 on framework Bronsted acid sites, respectively, based on the literature.[83] After high-temperature hydrothermal treatment, the NH_3 TPD curves of 4-h-aged and 16-h-aged Cu-CHA show a substantial depletion of the high temperature desorption environment, consistent with dealumination of the zeolite framework. In addition, the 325 ºC feature appears to be depleted, consistent with the formation of Cu clusters observed by STEM (Figure 3). The NH_3 TPD desorption curves for these hydrothermally-treated materials exhibit a new, broad desorption feature at approximately 250 ºC. Given the significant dealumination

that has occurred in these materials, this feature likely results from NH_3 adsorption on extraframework aluminum and sintered Cu species. Specific assignment is challenging due to the distribution of dealumination products created during hydrothermal treatment, and precise quantification of the individual desorption features is challenging due to the appearance of broad, overlapping features. However, these analyses are consistent with other discussed analyses on the loss of high-temperature NH_3 adsorption environments as a result of hydrothermal treatment.

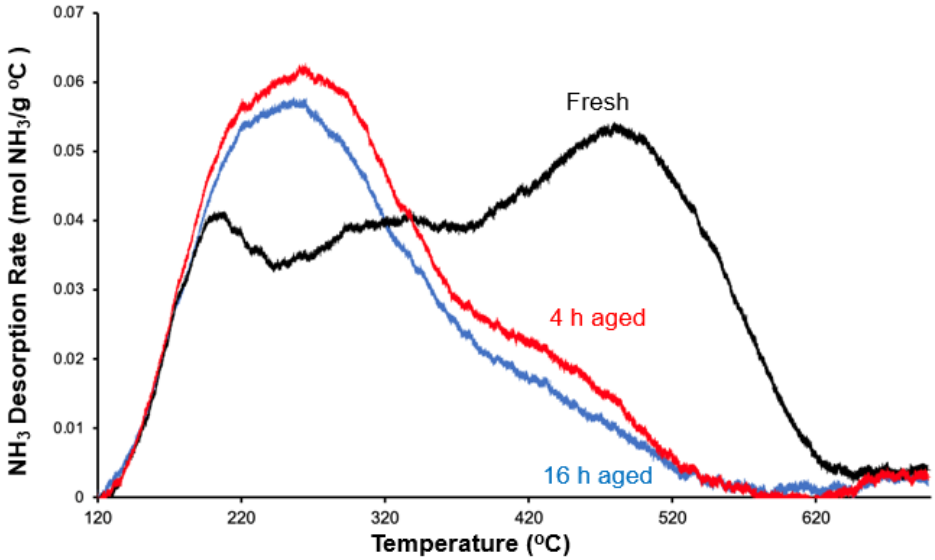

Figure S2. NH_3-temperature-programmed desorption curves for fresh (black), 4-h-aged (red), and 16-h-aged (blue) Cu-CHA. High-temperature desorption features attributed to NH_3 adsorbed on Bronsted acid sites are depleted as a result of high-temperature hydrothermal treatment. In comparison, the hydrothermally-treated materials exhibit a low temperature feature at ~250 °C likely corresponding to adsorption on extraframework aluminum species.

To assess changes in porosity that may have been induced by high-temperature hydrothermal treatment, N_2 adsorption isotherms were acquired at 77 K for fresh, 4-h-aged, and 16-h-aged Cu-CHA, and are shown in Figure S3. The three isotherms are all similar and are characteristic of a system with uniform micropores and no mesopores. This indicates that there are not significant amounts of large mesopores created by collapse of the zeolite

framework as a result of dealumination. The three micropore volumes, measured by the t-plot method,[84] range from 0.23 cm^3/g STP for fresh Cu-CHA to 0.25 cm^3/g STP for 4-h-aged and 16-h-aged Cu-CHA.

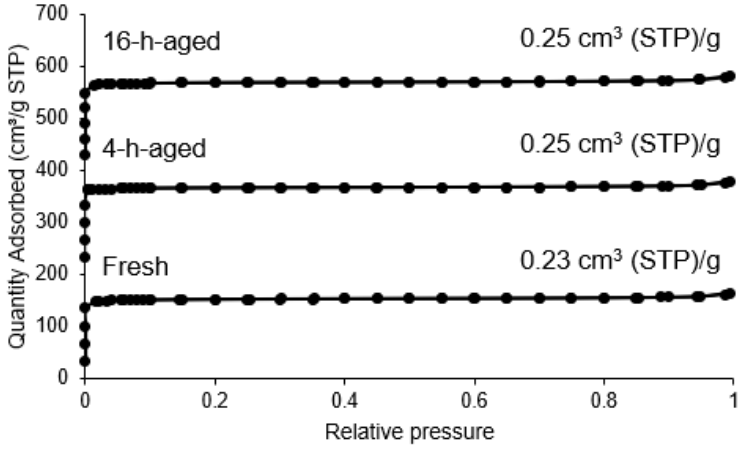

Figure S3. N_2 physisorption isotherms at 77 K for fresh, 4-h-aged, and 16-h-aged Cu-CHA. The isotherms for each material are offset by 200 cm^3/g STP for clarity. T-plot micropore volumes are listed for each material.

Zeolites adsorb substantial amounts of water. To accurately report per mass measurements on hydrated zeolites, thermogravimetric analysis (TGA) was used to measure the amount of water on the zeolite samples. The mass of water per mass of hydrated zeolite for fresh, 4-h-aged, and 16-h-aged Cu-CHA is shown in Table S2. The water mass decreases from 0.17 g water/g hydrated zeolite to 0.10 g water/g hydrated zeolite going from fresh Cu-CHA to 16-h-aged Cu-CHA, consistent with a loss of framework aluminum in the material due to high-temperature hydrothermal treatment. This difference is important for correcting calculations involving the mass of hydrated zeolites, such as those for the ^{27}Al spin counting NMR analyses discussed below.

Table S2. Water mass in Cu-CHA as characterized by thermogravimetric analysis

Sample	g water/g hydrated sample
Fresh	0.17
4-h-aged	0.14
16-h-aged	0.10

^{27}Al spin-counting NMR of hydrated Cu-CHA

Due to the presence of paramagnetic Cu(II) species in hydrated Cu-CHA, ^{27}Al NMR signals detected may not correspond to the total amount of aluminum in the material, due to paramagnetic broadening of ^{27}Al nuclear spins located in close proximity to Cu(II). To assess the amount of aluminum detected by ^{27}Al NMR and trends in this observed amount that result from hydrothermal treatment, ^{27}Al NMR spin counting experiments were performed on fresh, 4-h-aged, and 16-h-aged Cu-CHA by obtaining ^{27}Al NMR spectra of rotors packed with a combination of known masses of Cu-CHA sample and aluminum nitride. The resulting direct-excitation ^{27}Al MAS NMR spectra are shown in Figure S4 and consist of signals 114 and 59 ppm assigned to aluminum nitride and framework Al^{IV} in Cu-CHA, respectively. In addition, a wide spinning sideband manifold is observed for the AlN ^{27}Al NMR signal. Given the known masses of AlN and Cu-CHA sample in a rotor, the ^{27}Al NMR signals can be integrated and used to calculate the amount of aluminum detected by ^{27}Al NMR as a fraction of total aluminum in the sample by elemental analysis (Table S1), under the assumption that a ^{27}Al nuclear spin in AlN or the Cu-CHA zeolite framework yield the same amount of ^{27}Al NMR signal and correcting for the mass of water in the sample as calculated by TGA. The total aluminum content detected by ^{27}Al NMR can be calculated for each sample by accounting for the Al^{V} and Al^{VI} environments observed in Figure 1B. Table S3 summarizes the masses and integrated intensities for the ^{27}Al NMR spin counting experiments on the different Cu-CHA materials, and also lists the percentage of aluminum detected. The percentage of aluminum

detected by ^{27}Al NMR decreases from 27% in fresh Cu-CHA to 10% and 6% in 4-h-aged and 16-h-aged Cu-CHA, indicating that dealumination ^{27}Al species are likely located in close proximity to Cu(II).

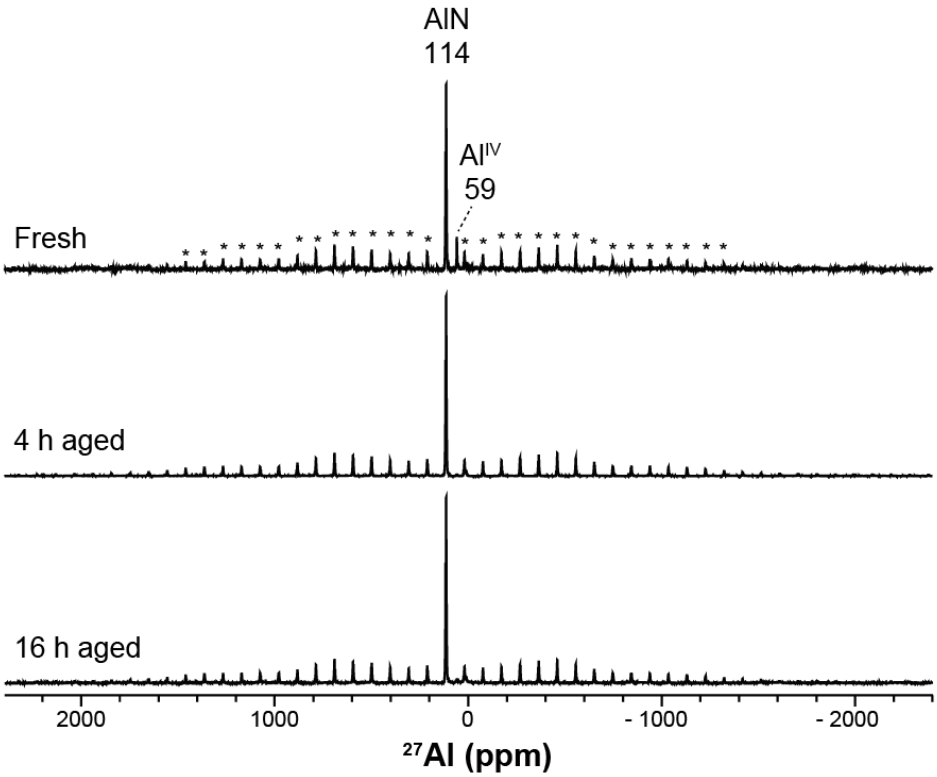

Figure S4. Direct-excitation ^{27}Al MAS NMR spectra of hydrated fresh, 4-h-aged, and 16-h-aged Cu-CHA used for ^{27}Al NMR spin counting analyses. A known amount of AlN was added to the rotor, such that the absolute amount of detected ^{27}Al spins in different chemical environments could be compared across samples. Asterisks (*) denote spinning sidebands for the AlN ^{27}Al NMR signal. The integrated percentages of AlN and zeolite framework Al^{IV} signal intensities are summarized in Table SX.

Table S3. Masses, integrated ^{27}Al NMR signal intensities and calculated values for ^{27}Al NMR spin counting analyses.

	Mass AlN (mg)	Mass hydrated sample (mg)	NH_4Cl ^{15}N NMR signal intensity	NH_4^+ ^{15}N NMR signal intensity	Percentage of total Al detected by NMR
Fresh	4.0	12.3	95.5%	4.5%	33%
4-h-aged	11.3	5.2	99.8%	0.2%	12%
16-h-aged	6.7	9.6	99.7%	0.3%	7%

Scanning transmission electron microscopy analyses

To verify the chabazite pore structure of 16-h-aged Cu-CHA, efforts were made to obtain a well-resolved image aligned with the zeolite micropores. Figure S5A shows a combination of six aligned images of 16-h-aged-Cu-CHA. The resulting image shows good resolution of the chabazite pore structure. Some faint increases in intensity on the order of 2–3 chabazite cages in a dimension or observable, consistent with the Cu clusters discussed in Figure 2. To obtain improved resolution of the pore structure, the image in Figure S5A was processed by applying a spot mask over bright spots observed after taking a Fourier transform of the image. This masking preserves only information from periodic features in the image. The resulting image in Figure S5B clearly shows the chabazite pore structure with some resolution of the Si or Al atomic columns.

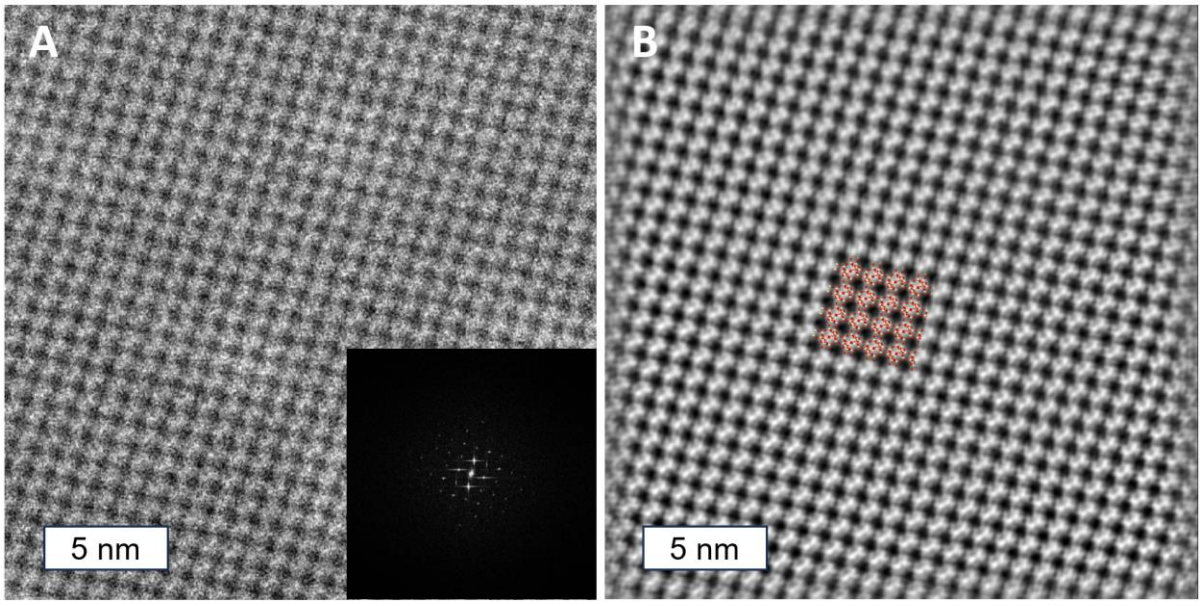

Figure S5. (A) Combination of six aligned HAADF-STEM images of 16-h-aged Cu-CHA showing the zeolite micropores. The inset shows a Fourier transform of the image in A. (B) Resulting image after performing an inverse Fourier transform of a spot-filtered version of the inset in (A), resulting in some resolution of the Si or Al atomic columns.

In order to compare the size distribution of Cu clusters in the 4-h-aged and 16-h-aged Cu-CHA materials, statistics on cluster size were acquired using a series of HAADF STEM images from each material, such that more than 300 total clusters were included in each histogram shown in Figure 2D. This corresponded to 6 images of 4-h-aged Cu-CHA and 8 images of 16-h-aged Cu-CHA. Given that the images are 2D projections and are taken of thin regions near edges of particles, no determination of cluster density can be given based on these images. However, the average cluster size can be compared. In order to not bias these analyses with human judgement on cluster size, an algorithm for detecting local differences in contrast from ImageJ was employed.[85] If necessary, images were cropped to remove regions of poor contrast or Cu-CHA particle edges. A background correction and Gaussian blur was then applied to the image to remove contrast across the image due to thickness variation or visible CHA lattice fringes. Contrast was adjusted to improve the contrast difference between clusters and the background, and intensity below the threshold of the clusters was removed. The inbuilt particle analysis in ImageJ was then used to calculate the Feret diameter, or longest dimension, of each cluster with an area greater than 0.5 nm^2. This lower bound was used to remove small intensity spots that appeared to be artifacts created during processing. The Feret diameter was used as a measure of cluster size as opposed to area to minimize uncertainty introduced by processing. Several outliers on the high end were observed, which based on an examination of the analyses appear to be primarily due to proximate clusters being combined into a single cluster in the analyses. Because of this, outliers at a threshold of 1.5 times the interquartile range above the upper quartile were excluded when calculated statistics on the Feret diameter.[86] Outliers were assessed based on the interquartile range as the data form a skewed distribution in Figure 2D. All images used, the resulting analyses, and histograms of the cluster sizes for

each image are shown in Figures S6-S19. The statistics for all images of 4-h-aged and 16-h-aged Cu-CHA are summarized in Tables S4 and S5, respectively.

This method of calculating cluster size enables consistent comparisons across different images and between images of different preparations of Cu-CHA. However, there are limitations to interpretations of these analyses. For one, excluding all detected features with an area < 0.5 nm^2 biases the average Feret diameter values to larger values, though we see little evidence of being able to detect clusters below this threshold. The image processing may remove low-intensity features, though it is likely these have a similar distribution to those that appear at higher intensity. For these reasons, the calculated Feret diameters reported here are valid for comparison between each other, but the absolute values could be biased slightly and should not be interpreted as an accurate distribution of the sizes of all Cu species present in these materials. In addition, as HAADF-STEM only provides a 2D projection of a 3D material, density of Cu clusters cannot be accurately assessed from these images.

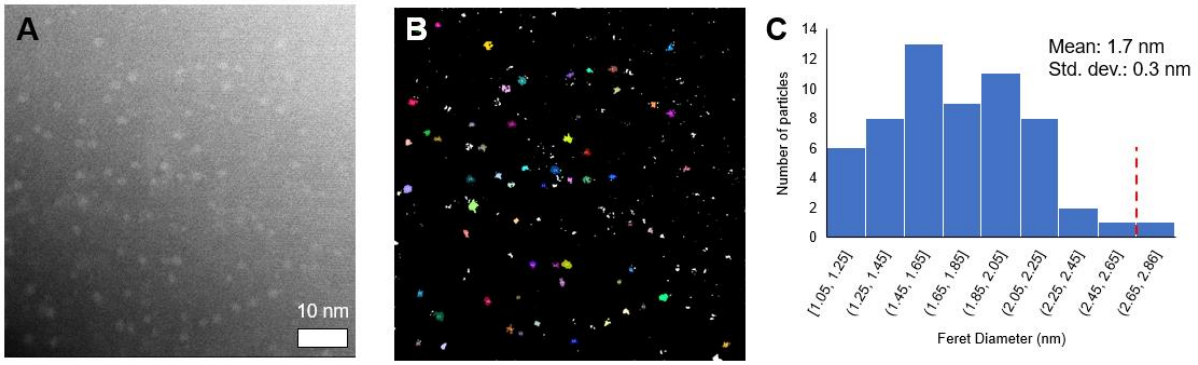

Figure S6. (A) HAADF-STEM Image 1 of 4-h-aged Cu-CHA. (B) Processed image data of Image 1 of 4-h-aged Cu-CHA showing clusters identified by automated analysis as different colors. (C) Histogram of the Feret diameters of clusters detected in (B). The red line denotes the cutoff for outliers, and the listed mean and standard deviation exclude these outliers.

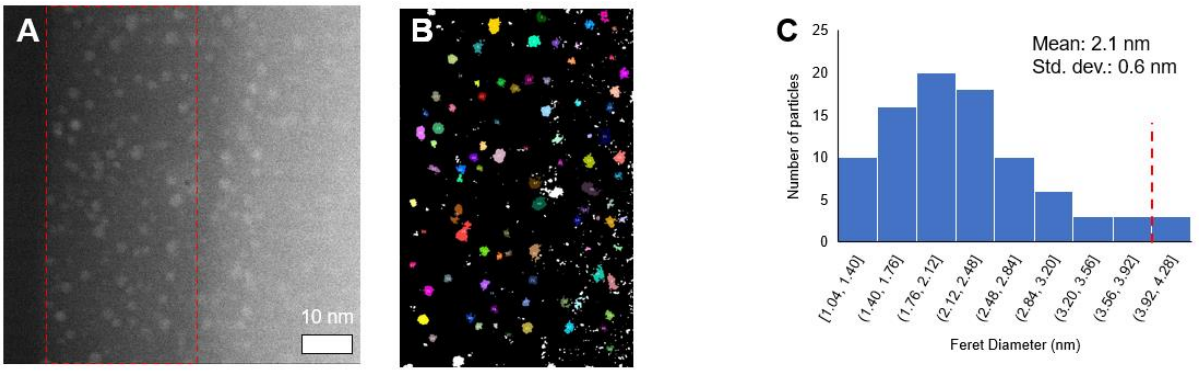

Figure S7. (A) HAADF-STEM Image 2 of 4-h-aged Cu-CHA. (B) Processed image data of Image 2 of 4-h-aged Cu-CHA showing clusters identified by automated analysis as different colors. (C) Histogram of the Feret diameters of clusters detected in (B). The red line denotes the cutoff for outliers, and the listed mean and standard deviation exclude these outliers.

Figure S8. (A) HAADF-STEM Image 3 of 4-h-aged Cu-CHA. (B) Processed image data of Image 3 of 4-h-aged Cu-CHA showing clusters identified by automated analysis as different colors. (C) Histogram of the Feret diameters of clusters detected in (B). No outliers were identified in this analysis.

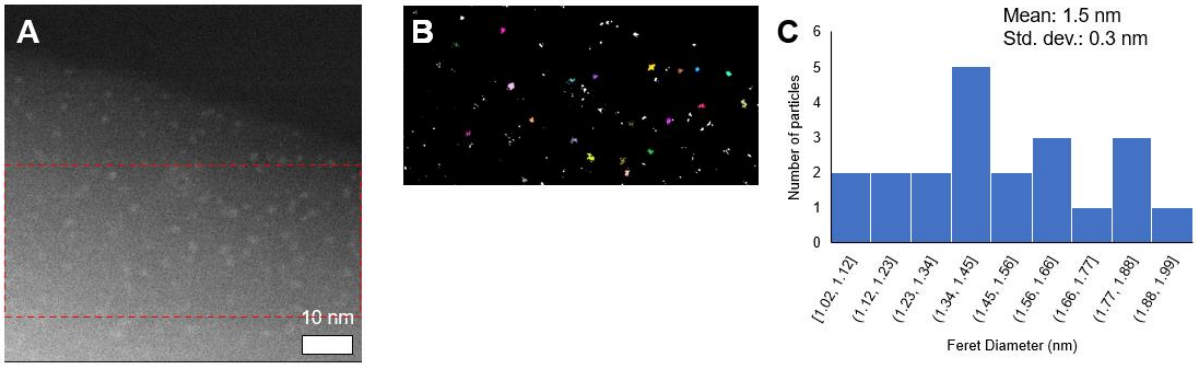

Figure S9. (A) HAADF-STEM Image 4 of 4-h-aged Cu-CHA. (B) Processed image data of Image 4 of 4-h-aged Cu-CHA showing clusters identified by automated analysis as different colors. (C) Histogram of the Feret diameters of clusters detected in (B). No outliers were identified in this analysis.

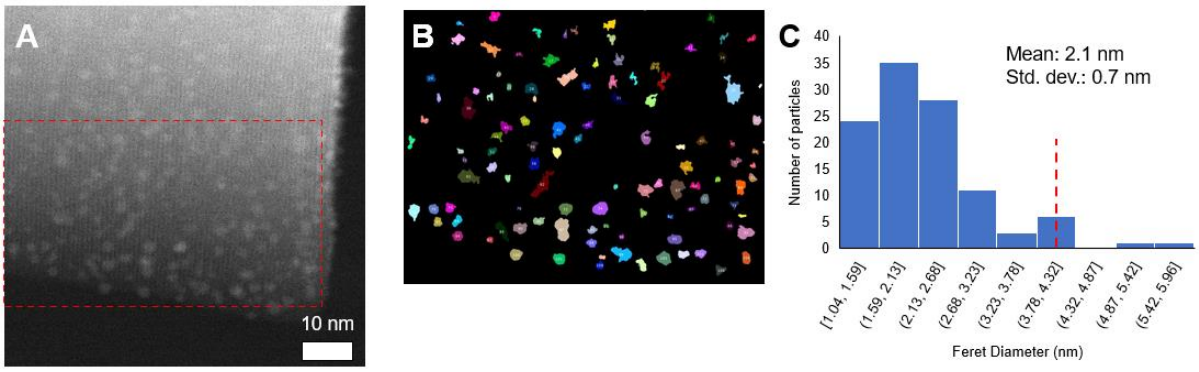

Figure S10. (A) HAADF-STEM Image 5 of 4-h-aged Cu-CHA. (B) Processed image data of Image 5 of 4-h-aged Cu-CHA showing clusters identified by automated analysis as different colors. (C) Histogram of the Feret diameters of clusters detected in (B). The red line denotes the cutoff for outliers, and the listed mean and standard deviation exclude these outliers.

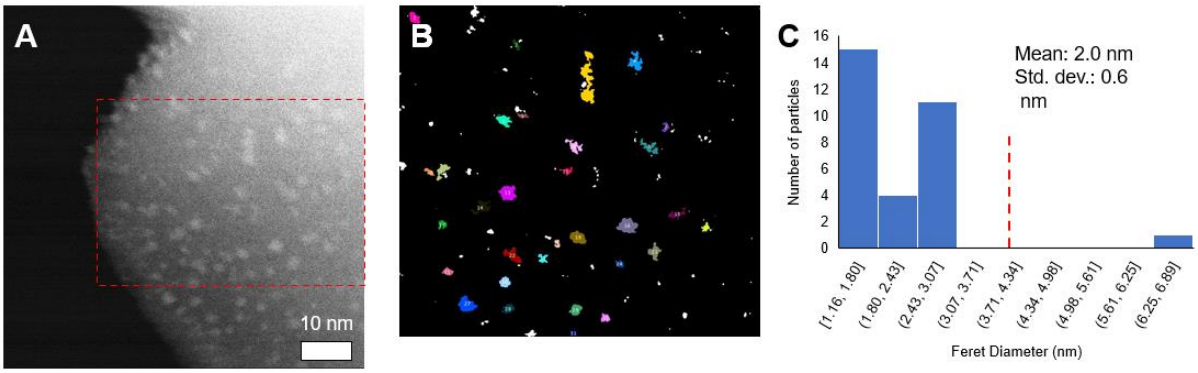

Figure S11. (A) HAADF-STEM Image 6 of 4-h-aged Cu-CHA. (B) Processed image data of Image 6 of 4-h-aged Cu-CHA showing clusters identified by automated analysis as different colors. (C) Histogram of the Feret diameters of clusters detected in (B). The red line denotes the cutoff for outliers, and the listed mean and standard deviation exclude these outliers.

Table S4. Summary of image analyses of HAADF-STEM images of 4-h-aged Cu-CHA

Image	Number of clusters	Detected outliers	Average Feret diameter (nm)*	Feret diameter standard deviation (nm)*
1	59	1	1.7	0.3
2	89	3	2.1	0.6
3	29	0	2.0	0.4
4	21	0	1.5	0.3
5	109	5	2.1	0.7
6	31	1	2.0	0.6
Overall**	338	21	1.9	0.5

*Average and sample standard deviation values calculated with outliers excluded.

**Outliers for overall distribution calculated from overall distribution, not by excluding outliers found for each individual dataset

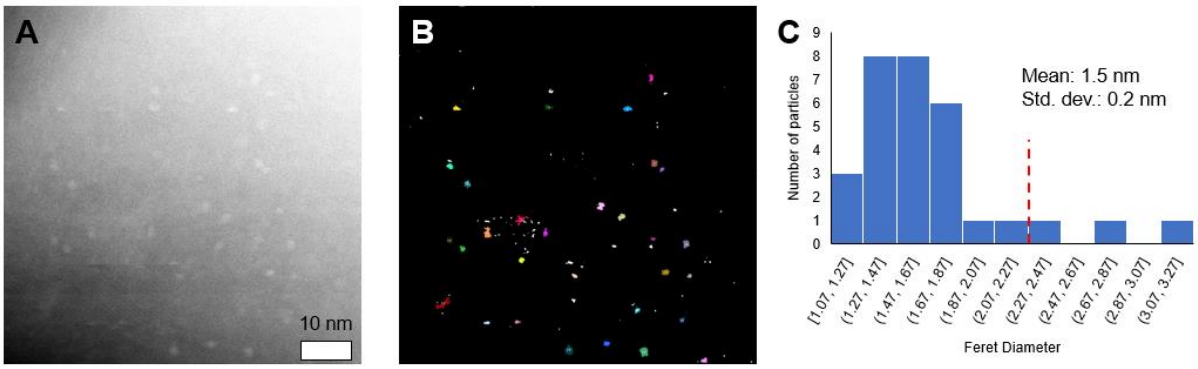

Figure S12. (A) HAADF-STEM Image 1 of 16-h-aged Cu-CHA. (B) Processed image data of Image 1 of 16-h-aged Cu-CHA showing clusters identified by automated analysis as different colors. (C) Histogram of the Feret diameters of clusters detected in (B). The red line denotes the cutoff for outliers, and the listed mean and standard deviation exclude these outliers.

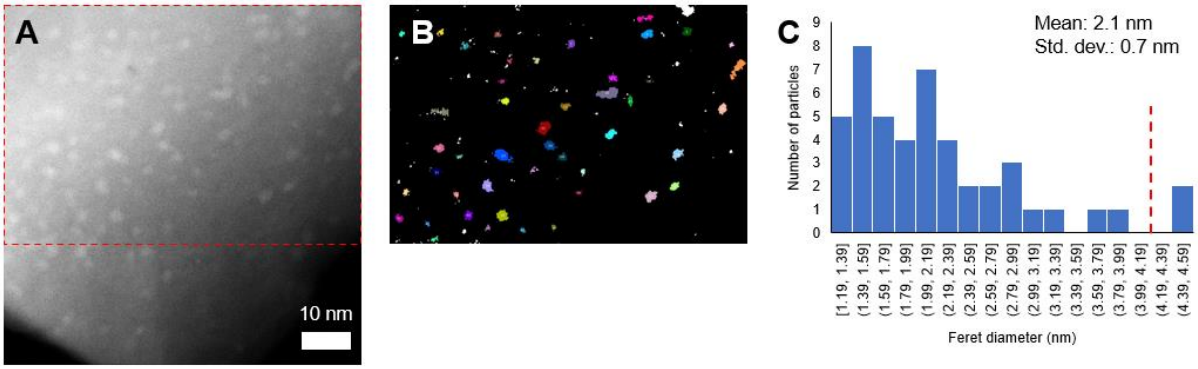

Figure S13. (A) HAADF-STEM Image 2 of 16-h-aged Cu-CHA. The red box denotes the region used for analyses. (B) Processed image data of Image 2 of 16-h-aged Cu-CHA showing clusters identified by automated analysis as different colors. (C) Histogram of the Feret diameters of clusters detected in (B). The red line denotes the cutoff for outliers, and the listed mean and standard deviation exclude these outliers.

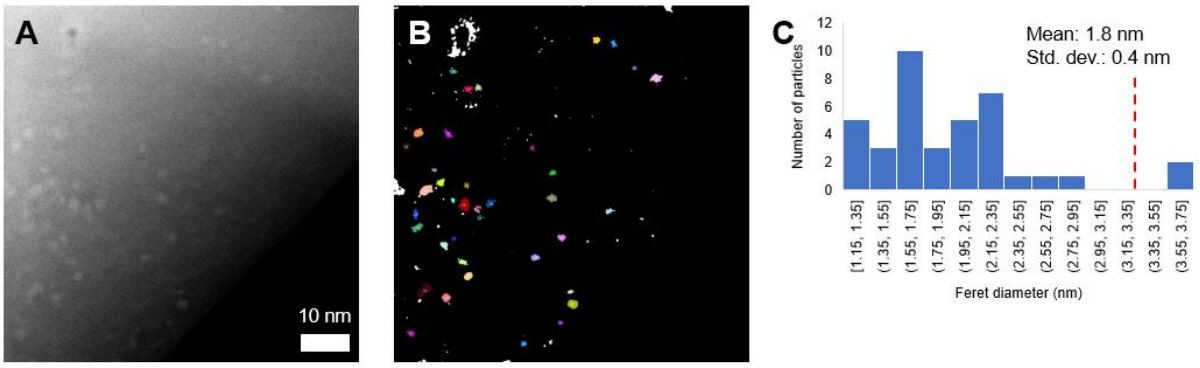

Figure S14. (A) HAADF-STEM Image 3 of 16-h-aged Cu-CHA. (B) Processed image data of Image 3 of 16-h-aged Cu-CHA showing clusters identified by automated analysis as different colors. (C) Histogram of the Feret diameters of clusters detected in (B). The red line denotes the cutoff for outliers, and the listed mean and standard deviation exclude these outliers.

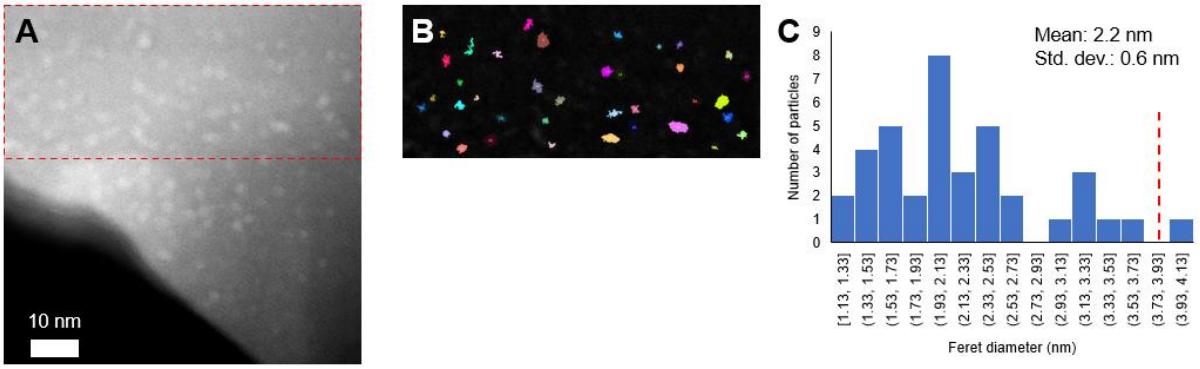

Figure S15. (A) HAADF-STEM Image 4 of 16-h-aged Cu-CHA. The red box denotes the region used for analyses. (B) Processed image data of Image 4 of 16-h-aged Cu-CHA showing clusters identified by automated analysis as different colors. (C) Histogram of the Feret diameters of clusters detected in (B). The red line denotes the cutoff for outliers, and the listed mean and standard deviation exclude these outliers.

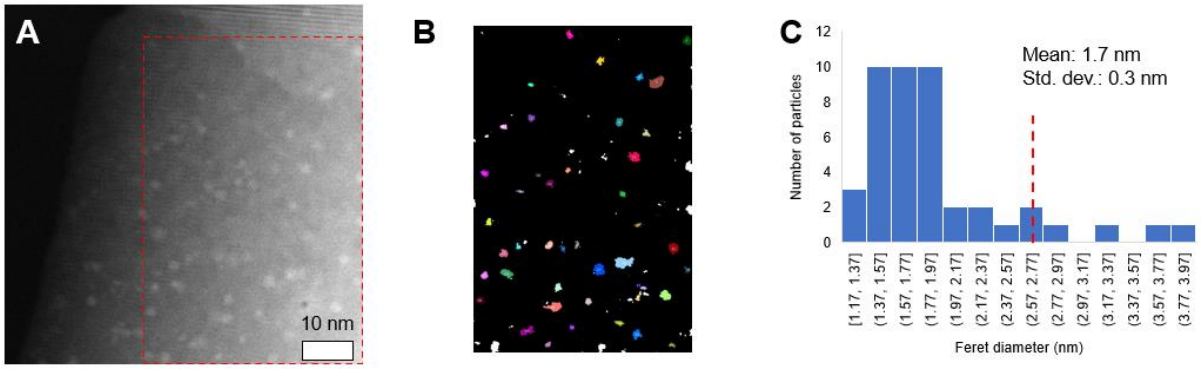

Figure S16. (A) HAADF-STEM Image 5 of 16-h-aged Cu-CHA. The red box denotes the region used for analyses. (B) Processed image data of Image 5 of 16-h-aged Cu-CHA showing clusters identified by automated analysis as different colors. (C) Histogram of the Feret diameters of clusters detected in (B). The red line denotes the cutoff for outliers, and the listed mean and standard deviation exclude these outliers.

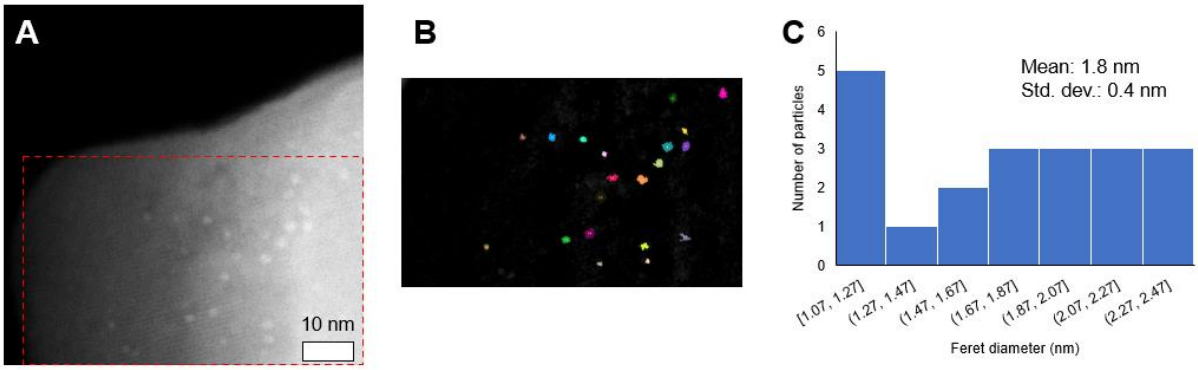

Figure S17. (A) HAADF-STEM Image 6 of 16-h-aged Cu-CHA. The red box denotes the region used for analyses. (B) Processed image data of Image 6 of 16-h-aged Cu-CHA showing clusters identified by automated analysis as different colors. (C) Histogram of the Feret diameters of clusters detected in (B). The red line denotes the cutoff for outliers, and the listed mean and standard deviation exclude these outliers.

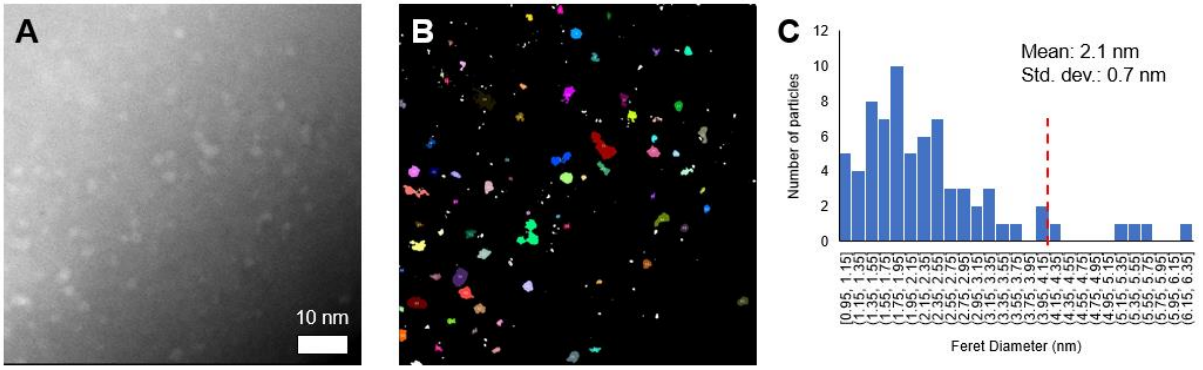

Figure S18. (A) HAADF-STEM Image 7 of 16-h-aged Cu-CHA. (B) Processed image data of Image 7 of 16-h-aged Cu-CHA showing clusters identified by automated analysis as different colors. (C) Histogram of the Feret diameters of clusters detected in (B). The red line denotes the cutoff for outliers, and the listed mean and standard deviation exclude these outliers.

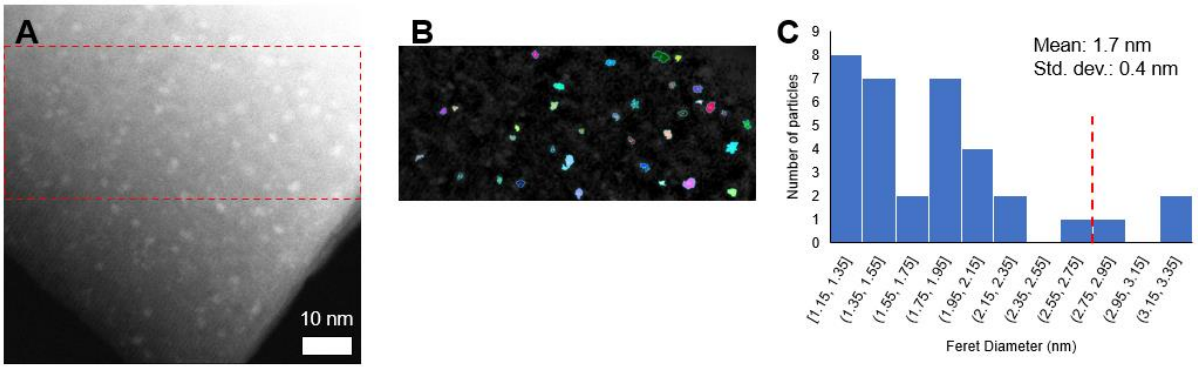

Figure S19. (A) HAADF-STEM Image 8 of 16-h-aged Cu-CHA. The red box denotes the region used for analyses. (B) Processed image data of Image 8 of 16-h-aged Cu-CHA showing clusters identified by automated analysis as different colors. (C) Histogram of the Feret diameters of clusters detected in (B). The red line denotes the cutoff for outliers, and the listed mean and standard deviation exclude these outliers.

Table S5. Summary of image analyses of HAADF-STEM images of 16-h-aged Cu-CHA

Image	Number of clusters	Detected outliers	Average Feret diameter (nm)*	Feret diameter standard deviation (nm)*
1	30	3	1.5	0.2
2	46	2	2.1	0.7
3	38	2	1.8	0.4
4	38	1	2.2	0.6
5	44	6	1.7	0.3
6	20	0	1.8	0.4
7	72	5	2.1	0.7
8	34	3	1.7	0.4
Overall**	322	18	1.9	0.5

*Average and sample standard deviation values calculated with outliers excluded.
**Outliers for overall distribution calculated from overall distribution, not by excluding outliers found for each individual dataset

To better characterize the bright spots observed in 4-h-aged and 16-h-aged Cu-CHA, energy-dispersive X-ray spectroscopy (EDS) mapping was performed on 16-h-aged Cu-CHA. By measuring scattered X-rays simultaneous to acquiring a HAADF-STEM image, maps of element-specific X-ray intensity can be compared to contrast patterns in the HAADF-STEM image. Due to the high electron beam sensitivity of zeolites, this technique is challenging to perform at high magnification on these materials. Nevertheless, sufficient Cu EDS signal was acquired in these measurements to make EDS mapping at a nanoscale possible. Figure S20 shows copper, silicon, and aluminum EDS maps for two regions of 16-h-aged Cu-CHA. In both characterized regions, Cu intensity maps well onto high-contrast spots in the HAADF-STEM image, confirming that these spots are rich in copper. The silicon EDS maps for both regions exhibit intensity consistent with the overall background intensity of the HAADF-

STEM images, indicating that beam damage was not causing significant local variation in sample thickness during measurement. The aluminum distribution is non-homogenous and suggestive of high aluminum EDS signal intensity associated with high copper EDS signal intensity. However, the contrast in the aluminum EDS map is too weak to draw conclusions due to the ubiquitous high aluminum background throughout the high-aluminum chabazite material.

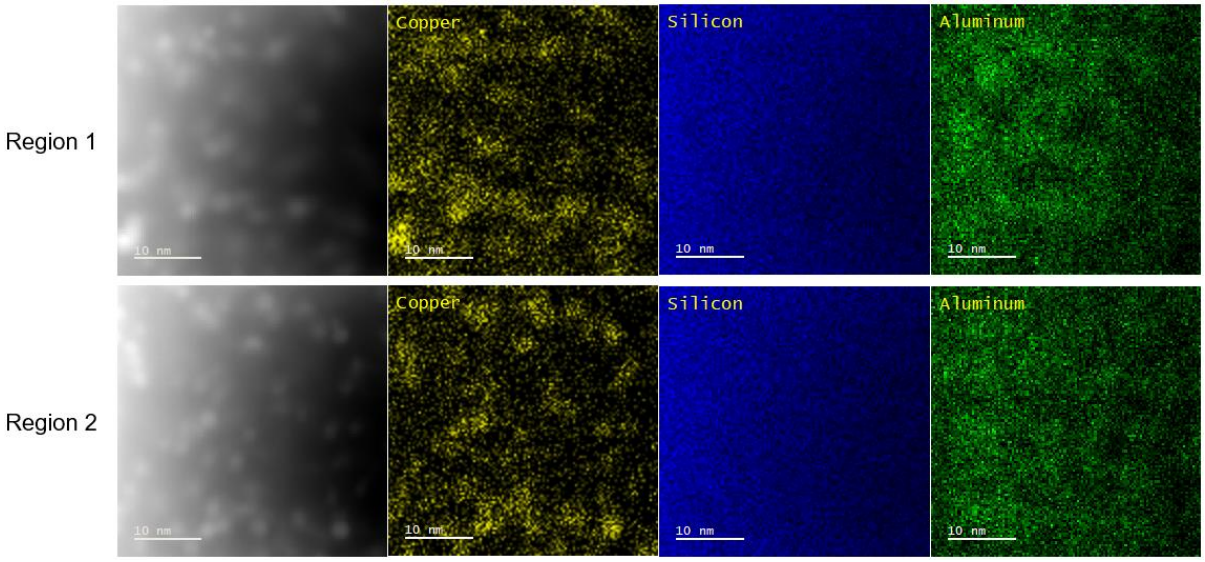

Figure S20. HAADF-STEM images (left) and corresponding EDS maps for copper (yellow), silicon (blue), and aluminum (green) from two regions of 16-h-aged Cu-CHA crystallites.

Electron paramagnetic resonance analyses

Electron paramagnetic resonance (EPR) is a commonly used technique to characterize the local environment of Cu^{2+} cations in Cu-CHA zeolites due to Cu(II) being paramagnetic, and thus EPR-sensitive.[18,20,23,42,53] Through a combination of experimental EPR and computational studies to determine EPR parameters, expected EPR parameters of Z_2Cu and ZCuOH have been reported in the literature.[18,23] To compare the Cu distributions found by

electron diffraction to more well-established techniques from literature, continuous-wave EPR spectra of fresh, 4-h-aged, and 16-h-aged Cu-CHA after dehydration and activation in O_2 were acquired and are shown in Figure S21, and deconvolutions of the lineshapes were performed. The fit parameters for the EPR spectra of fresh, 4-h-aged, and 16-h-aged Cu-CHA are shown in Tables S6-8. The EPR spectrum of fresh Cu-CHA in Figure S21A was fit with three lineshapes consistent with previous literature reports of EPR of Cu-CHA. Line 1 is consistent with literature reports of Z_2Cu, and line 2 is consistent with literature reports of ZCuOH. Line 3 has previously been attributed to more disordered single-atom Cu^{2+} species. The deconvolution of the EPR spectrum indicates that 49% of Cu^{2+} species are present as Z_2Cu, 38% of the Cu^{2+} species are present as ZCuOH, and 13% of the Cu^{2+} species are in more disordered environments. In comparison, the identified Cu location in fresh Cu-CHA by electron diffraction only shows a position, not a chemical environment. It is possible the locations of these different Cu species in the chabazite structure are similar enough to be detected as the same by electron diffraction.

In contrast to the EPR spectrum of fresh Cu-CHA, the EPR spectra of 4-h-aged and 16-h-aged Cu-CHA necessitated four lineshapes to fully fit the spectrum, as shown in Figure S21B-C. The four lineshapes used were similar for the EPR spectra of the two materials. Lines 1 and 2 have parameters consistent with literature reports of Z_2Cu species. Line 2 is broader than Line 1, suggesting greater disorder of the Cu^{2+} species in this chemical environment. Line 4 is consistent with previous reports of single-atom Cu^{2+} species in poorly-defined environments. In contrast to the lineshapes reported for fresh Cu-CHA and Lines 1 and 2 for the aged Cu-CHA materials, this simulated EPR lineshape is rhombohedral. There are previous reports of EPR spectra of dealuminated Cu-zeolites with similar features, but the authors could

locate no literature reports assigning this feature to a specific moiety.[87] Identifying this moiety is beyond the scope of this manuscript, but given its presence only in the hydrothermally-treated materials, further work to identify this moiety would be beneficial. The weights of the different lineshapes to compose the experimental spectra of 4-h-aged Cu-CHA and 16-h-aged Cu-CHA are similar, with one notable difference. The proportion of signal assigned to well-ordered Z_2Cu species (Line 1) decreases from 32% to 20% going from 4-h-aged to 16-h-aged Cu-CHA. To compensate, the proportions of signal assigned to disordered Z_2Cu (Line 2) and Cu in poorly defined environments (Line 4) increase, consistent with greater disorder at longer extents of hydrothermal treatment. A caveat to these fits is that, due to the lack of literature reports, Line 3 had to be empirically fit without a good starting point for parameters in the spin Hamiltonian from literature. As such, it is possible that this fit is not unique and other explanations may exist for these linshapes. It should be noted that only Cu in well-defined Cu^{2+} complexes is anticipated to be detected under the experimental conditions used here, and thus the Cu species in clusters formed during hydrothermal treatment (detected by HAADF-STEM, Figure 2), are not detectable in these measurements.

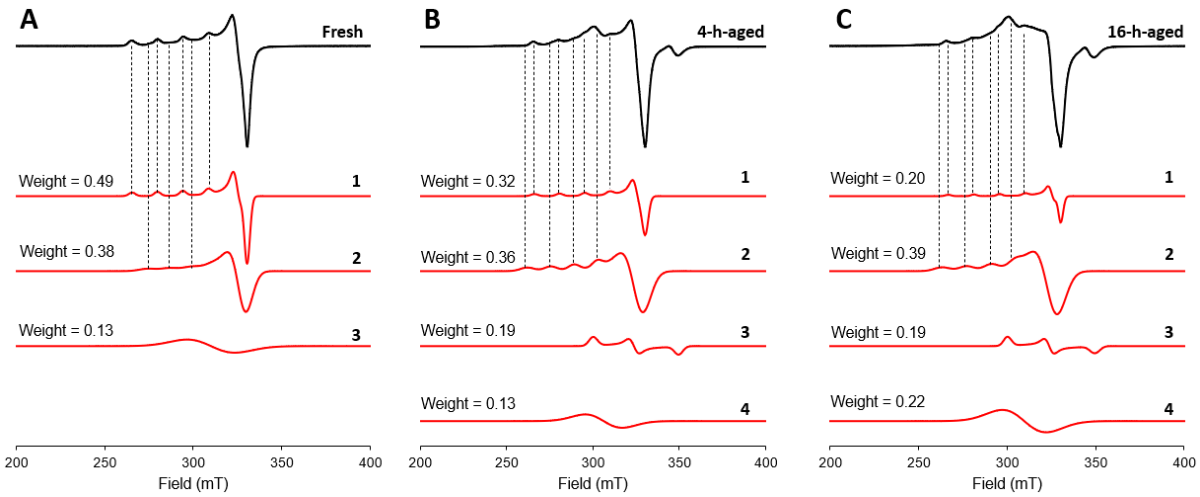

Figure S21. Continuous-wave EPR spectra (black) and spectral deconvolutions (red) of oxidized (A) fresh, (B) 4-h-aged, and (C) 16-h-aged Cu-CHA. Spectra were acquired on an X-

band EPR spectrometer at 100 K in EPR tubes sealed under argon in a glove box. The parameters for the individual fitted lines are listed in Tables SX-Y.

Table S6. EPR fitting parameters for spectrum acquired on fresh Cu-CHA

Site	Weight (%)	Spin Hamiltonian Parameters				Line broadening				
		g		A (MHz)		FWHM (mT)	g-strain		A-strain (MHz)	
		$g_\perp$	$g_\parallel$	$A_\perp$	$A_\parallel$		$g_\perp$	$g_\parallel$	$A_\perp$	$A_\parallel$
1	49	2.08	2.37	38	465	3	0.001	0.008	3	1
2	38	2.08	2.32	10	391	2	0.06	0.09	5	2
3	13	g_{iso} = 2.19, A_{iso} = 20 MHz, FWHM = 27 mT								

Table S7. EPR fitting parameters for spectrum acquired on 4-h-aged Cu-CHA

Site	Weight (%)	Spin Hamiltonian Parameters						Line broadening				
		g			A (MHz)			FWHM (mT)	g-strain		A-strain (MHz)	
		$g_\perp/g_x$	$g_\parallel/g_y$	g_z	$A_\perp/A_x$	$A_\parallel/A_y$	A_z		$g_\perp/g_x$	$g_\parallel/g_y$	$A_\perp/A_x$	$A_\parallel/A_y$
1	32	2.08	2.36	-	28	470	-	4	0.005	0.009	5	6
2	36	2.09	2.40	-	24	446	-	1	0.09	0.07	8	30
3	19	1.94	2.1	2.26	1	9	6	5	-	-	-	-
4	13	g_{iso} = 2.22, A_{iso} = 20 MHz, FWHM = 21 mT										

Table S8. EPR fitting parameters for spectrum acquired on 16-h-aged Cu-CHA

Site	Weight (%)	Spin Hamiltonian Parameters						Line broadening				
		g			A (MHz)			FWHM (mT)	g-strain		A-strain (MHz)	
		$g_\perp/g_x$	$g_\parallel/g_y$	g_z	$A_\perp/A_x$	$A_\parallel/A_y$	A_z		$g_\perp/g_x$	$g_\parallel/g_y$	$A_\perp/A_x$	$A_\parallel/A_y$
1	20	2.08	2.35	-	30	468	-	4	0.009	0.009	2	3
2	39	2.1	2.39	-	21	453	-	7	0.07	0.03	2	43
3	19	1.94	2.1	2.26	34	11	2	4	-	-	-	-
4	22	g_{iso} = 2.19, A_{iso} = 20 MHz, FWHM = 25 mT										

^{15}N spin-counting NMR

Based on the drastic differences in framework Si/Al ratio and NMR-visible ^{27}Al between the fresh Cu-CHA and aged Cu-CHA materials, it was anticipated that the observed

^{15}N NMR signals in Figure 5 represent significantly different amounts of adsorbed ^{15}N species. To investigate this, ^{15}N NMR spin counting experiments were performed on NO-reduced fresh, 4-h-aged, and 16-h-aged Cu-CHA by packing an NMR rotor with known masses of sample and $^{15}NH_4Cl$. The resulting direct-excitation ^{15}N MAS NMR spectra are shown in Figure S22, and show a prominent signal at 39 ppm assigned to a NH_4Cl chemical environment, along with signal at 17 and –18 ppm corresponding to $^{15}NH_3$ adsorbed in Cu-CHA as NH_4^+ and $[Cu(NH_3)_2]^+$, respectively. Masses and integrated signal intensities for the spin counting analysis are shown in Table S9. Given the masses of the NH_4Cl spin counting reference and Cu-CHA in the sample, the amount of $^{15}NH_4^+$ represented by the ^{15}N NMR signal could be easily calculated and compared to bulk aluminum content using the elemental analysis in Table S1. Compared to the bulk aluminum content of the Cu-CHA, which remains constant despite hydrothermal treatment, the amount of NH_4^+ detected by ^{15}N NMR decreases as a result of hydrothermal treatment, from an NH_4^+/Al of 0.66 for fresh Cu-CHA to 0.13 and 0.06 for 4-h-aged and 16-h-aged Cu-CHA, respectively. This is consistent with the observed decrease in framework Si/Al ratio. While ^{15}N NMR signals corresponding to $[Cu(NH_3)_2]^+$ and $[Cu(NH_3)]^+$ moieties were

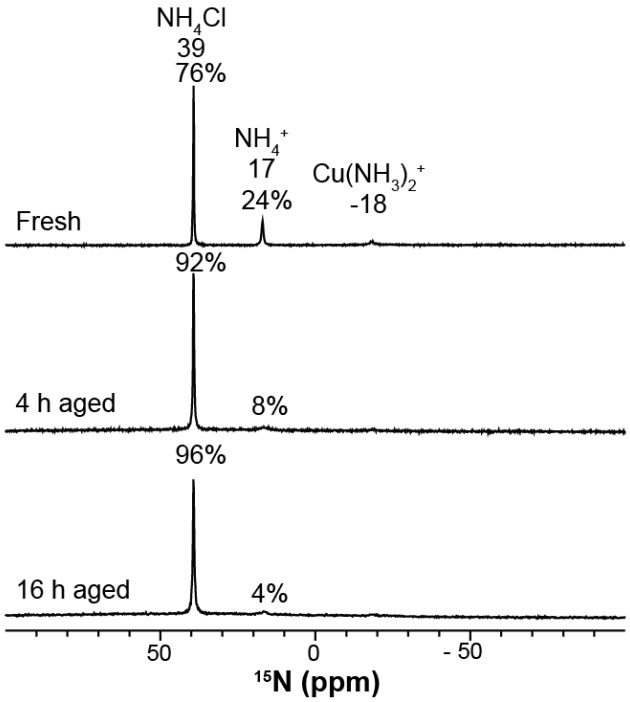

Figure S22. Direct-excitation ^{15}N MAS NMR spectra of NO-reduced fresh, 4-h-aged, and 16-h-aged Cu-CHA used for ^{15}N NMR spin counting analyses. A known amount of $^{15}NH_4Cl$ was added to the rotor, such that the absolute amount of detected ^{15}N spins in different chemical environments could be compared across samples. The percentages listed reflect the proportions of ^{15}N signal intensity attributed to NH_4Cl and NH_4^+ charge-balancing zeolite framework aluminum.

too weak to confidently integrate in the direct-excitation ^{15}N MAS NMR spectra shown in Figure S22, the relative ^{15}N NMR signal intensities from Figure 3 could be combined with the ^{15}N spin counting NMR analyses in Figure S22 to calculate the percentage of total aluminum in each material for which adsorbates were detected. For the fresh Cu-CHA, 93% of aluminum was detected indirectly by probing adsorbates through ^{15}N NMR. This number being slightly below 100% is likely due to some framework Al sites being inaccessible for adsorbates. An amount of adsorbates corresponding to 20% and 12% of total aluminum was detected for 4-h-aged and 16-h-aged Cu-CHA, respectively. These numbers are consistent with an observed loss of framework aluminum. The lack of additional ^{15}N NMR signals in the ^{15}N NMR spectra

of 4-h-aged and 16-h-aged Cu-CHA indicates that after the NO reduction pretreatment $^{15}NH_3$ is not adsorbed on aluminum species resulting from dealumination.

Table S9. Masses, integrated ^{15}N NMR signal intensities and calculated values for ^{15}N NMR spin counting analyses.

	Mass $^{15}NH_4Cl$ (mg)	Mass sample (mg)	NH_4Cl ^{15}N NMR signal intensity	NH_4^+ ^{15}N NMR signal intensity	NH_4^+/Al	Percentage of Al with adsorbates observed
Fresh	3.8	25.6	76%	24%	0.66	93%
4-h-aged	2.1	18.7	92%	8%	0.13	20%
16-h-aged	1.7	17.1	96%	4%	0.06	12%

Additional 2D ^{27}Al–^{29}Si NMR correlation analyses

While the 2D ^{27}Al–^{29}Si dipolar-mediated heteronuclear correlation NMR spectra of NO-reduced Cu-CHA materials shown in Figure 6 establish sub-nanoscale proximities of ^{29}Si and ^{27}Al nuclear spins, these analyses do not unambiguously establish the identities of framework ^{29}Si moieties. In particular, the assignment of the ^{29}Si NMR signal at –99 ppm to Q^4(2Al) moieties is complicated by the assumed presence of a ^{29}Si NMR signal at –101 ppm attributable to Q^3 silanol species, which would overlap with the Q^4(2Al)-attributed NMR signal.[55] To resolve this ambiguity, a solid-state 2D ^{27}Al–^{29}Si *J*-HMQC NMR spectrum was acquired for NO-reduced fresh Cu-CHA. In contrast to the dipolar-mediated experiment, which correlates proximate spins, the *J*-mediated experiment shows correlated ^{29}Si and ^{27}Al intensity only from nuclear spins connected through ^{27}Al–O–^{29}Si covalent bonds. As such, the *J*-mediated experiment can be used to unambiguously assign the –99 ppm ^{29}Si NMR signal. The solid-state 2D ^{27}Al–^{29}Si *J*-HMQC NMR spectrum of NO-reduced fresh Cu-CHA is shown in Figure S23. In contrast to the solid-state 2D ^{27}Al-^{29}Si dipolar-mediated NMR heteronuclear correlation spectrum of NO-reduced fresh Cu-CHA shown in Figure 4A, only two regions of correlated intensity are present at 56 ppm in the ^{27}Al dimension, corresponding to four-

coordinate framework Al atoms, and –105 and –99 ppm in the ^{29}Si dimension, from Q^4(1Al) and Q^4(2Al) moieties, respectively. The ^{29}Si NMR signal at –111 ppm observed in the dipolar-mediated spectrum in Figure 4A is not observed in the *J*-mediated spectrum, as Q^4(0Al) moieties have no bonds to aluminum. This spectrum unambiguously establishes the –99 ppm ^{29}Si NMR signal as Q^4(2Al) moieties. Interestingly, intensity at around –101 ppm observed in the spectrum in Figure 4A is not observed in the spectrum in Figure S23, suggesting that there may be some through-space correlated intensity from framework ^{27}Al species and Q^3 silanol ^{29}Si species in the spectrum in Figure 6A.

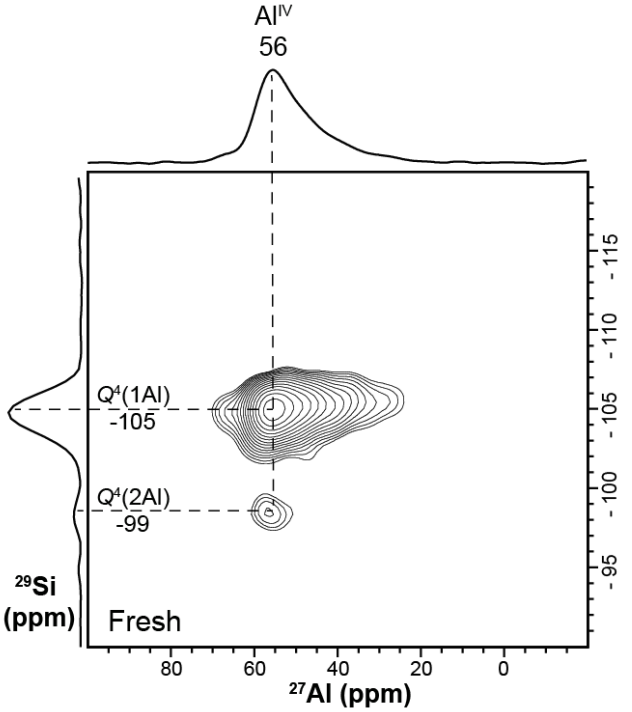

Figure S23. Solid-state 2D ^{27}Al–^{29}Si *J*-HMQC NMR spectrum of NO-reduced fresh Cu-CHA. The 1D spectra shown across the top and side are ^{27}Al and ^{29}Si projections of the 2D spectrum, respectively. The spectrum was acquired at 9.4 T, 100 K and 8 kHz MAS.

Along with the NO-reduced fresh and 4-h-aged Cu-CHA, a solid state 2D ^{27}Al-^{29}Si dipolar-mediated heteronuclear correlation NMR spectrum of 16-h-aged Cu-CHA was acquired and is shown in Figure S24. Due to the lower amount of reducible copper species in

16-h-aged Cu-CHA, the signal-to-noise of the spectrum in Figure S24 is poor compared to the spectra in Figure 4. Nevertheless, the solid state 2D ^{27}Al–^{29}Si dipolar-mediated heteronuclear correlation NMR spectrum of 16-h-aged Cu-CHA reveals three resolved regions of correlated ^{27}Al and ^{29}Si NMR signals at 54 ppm in the ^{27}Al dimension, assigned to framework four-coordinate aluminum species, and –111, –105, and –99 ppm in the ^{29}Si dimension assigned to Q^4(0Al), Q^4(1Al), and Q^4(2Al) moieties, respectively. This is consistent with the same analyses performed on fresh and 4-h-aged Cu-CHA. Given the calculated framework Si/Al ratio of 32 for the 16-h-aged Cu-CHA (Figure 1A), the detection of framework Q^4(2Al) moieties corresponding to closely paired framework aluminum species is unexpected, and further supports the assertion that Cu^{2+} species must be preferentially stabilizing these configurations during high-temperature hydrothermal treatment.

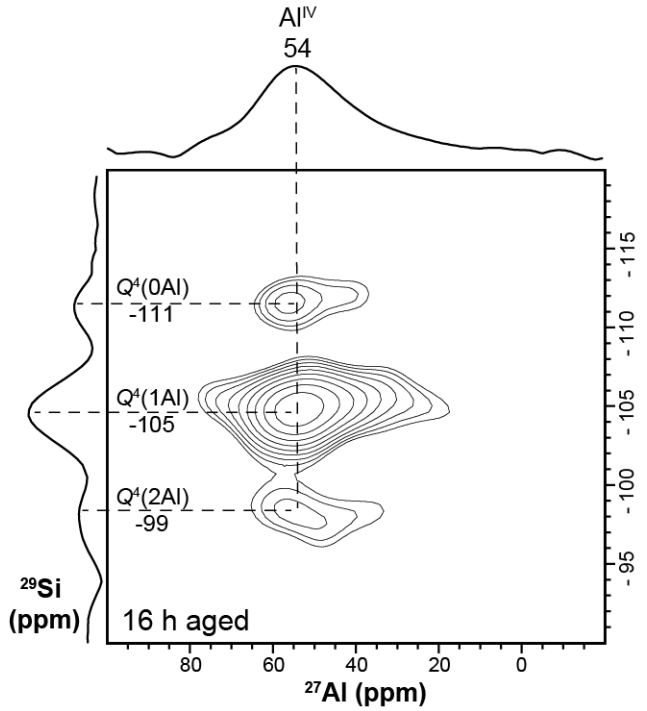

Figure S24. Solid-state 2D ^{27}Al–^{29}Si D-HMQC NMR spectrum of NO-reduced 16-h-aged Cu-CHA. The 1D spectra shown across the top and side are ^{27}Al and ^{29}Si projections of the 2D spectrum, respectively. The spectrum was acquired at 9.4 T, 100 K and 8 kHz MAS.

To better analyze the differences in Q^4(1Al) and Q^4(2Al) signal proportions for the solid-state 2D ^{27}Al–^{29}Si D-HMQC NMR spectra of the different NO-reduced Cu-CHA materials, ^{29}Si projections were obtained from the 2D spectra of all materials and are shown in Figure S25. The integrated intensities of the Q^4(0Al), Q^4(1Al), and Q^4(2Al) NMR signals from these projections were calculated. Though these integrated signal intensities from the ^{29}Si projections are not absolutely quantitative, they can be used to compare relative intensities between samples, since the spectra were acquired under the same conditions. For fresh Cu-CHA, the Q^4(0Al), Q^4(1Al), and Q^4(2Al) ^{29}Si NMR signals are 20%, 73%, and 7% of the integrated intensity in the ^{29}Si projection, respectively. This corresponds to a Q^4(1Al)/Q^4(2Al) ratio of 10.4. For 4-h-aged Cu-CHA, the Q^4(0Al), Q^4(1Al), and Q^4(2Al) ^{29}Si NMR signals are 22%, 61%, and 17% of the integrated intensity of the ^{29}Si projection, respectively, corresponding to a Q^4(1Al)/Q^4(2Al) intensity ratio of 3.6. Since significant framework dealumination occurs going from the fresh to 4-h-aged Cu-CHA, this indicates that closely paired aluminum species corresponding to Q^4(2Al) moieties are preferentially preserved over isolated framework aluminum species upon high-temperature hydrothermal treatment. For 16-h-aged Cu-CHA, the Q^4(0Al), Q^4(1Al), and Q^4(2Al) ^{29}Si NMR signals are 14%, 73%, and 13% of the integrated intensity, respectively, corresponding to a Q^4(1Al)/Q^4(2Al) intensity ratio of 5.6. This is significantly lower than the ratio observed for fresh Cu-CHA, but higher than the ratio observed for 4-h-aged Cu-CHA. Interpretation of the precise ratio for the 16-h-aged Cu-CHA should be cautious due to the significantly lower signal-to-noise of this spectrum compared to fresh and 4-h-aged Cu-CHA. However, this suggests that closely-paired aluminum species are still preserved, even after intense high-temperature hydrothermal treatment subjecting the Cu-CHA material to severe framework dealumination.

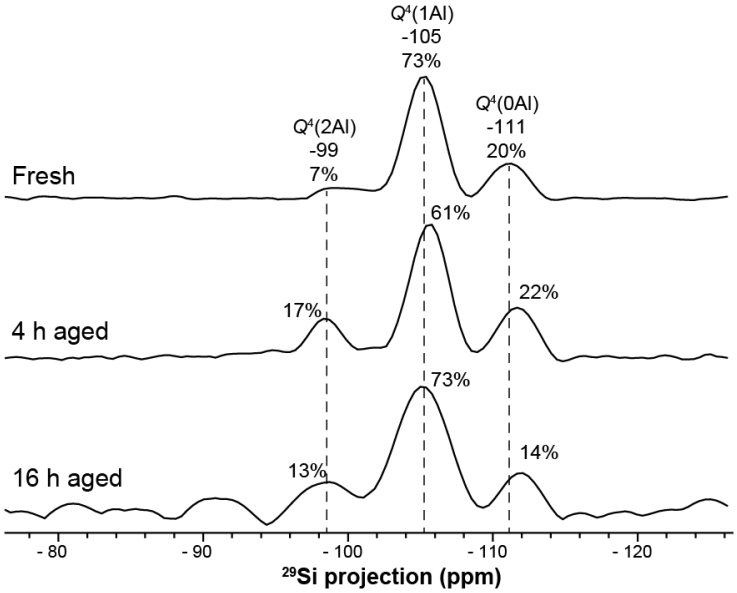

Figure S25. ^{29}Si projections from solid-state 2D ^{27}Al–^{29}Si D-HMQC NMR spectra of NO-reduced fresh, 4-h-aged, and 16-h-aged Cu-CHA. These projections were obtained by summing the intensity in the ^{29}Si dimension between ^{27}Al chemical shifts of 0 and 90 ppm, to ensure all positive signal was integrated while minimizing integration of signal-free regions. Deconvolutions and integrations were performed in DMFit.

2D ^{15}N exchange NMR analyses

In order to perform the kinetic analyses of the 2D ^{15}N exchange NMR spectra as discussed in Figures 7 and 8, 2D ^{15}N exchange NMR spectra of NO-reduced fresh, 4-h-aged, and 16-h-aged Cu-CHA were acquired at 314, 326, and 339 K with mixing times of 4.8, 7.2, 9.6, 12.0, and 14.4 ms, for a total of 45 2D NMR spectra. In order to analyze the integrated intensities of 2D signal regions corresponding to exchanged and non-exchanged species, horizontal projections were taken around the 17 ppm and –18 ppm regions of the vertical dimension corresponding to species that had occupied NH_4^+ or $[Cu(NH_3)_2]^+$ ^{15}N chemical environments prior to the mixing period, respectively. The same integration region for the projections was used on all spectrum for a single Cu-CHA material. Integration of the 1D projections was performed using DMFit, with signal regions fit with Gaussian lineshapes. The

line width and position were kept consistent within each dataset for a material at a given temperature. For the curious reader, all 45 solid-state 2D ^{15}N exchange NMR spectra and corresponding 1D horizontal projections used for the ^{15}N exchange kinetic analyses are shown in Figure S26-S70. In all 2D spectra, four signal regions are observed correlated ^{15}N NMR signals at 17 ppm and –18 ppm assigned to ^{15}N nuclei in NH_4^+ and $[Cu(NH_3)_2]^+$ complexes. Signal regions with the same ppm chemical shift on the vertical and horizontal axes correspond to species which occupy the same chemical environment before and after the mixing period, while NMR signal regions with different ppm chemical shifts on the horizontal and vertical axes represent species that have undergone chemical exchange during the mixing period. Broadly, signal regions corresponding to chemical exchange become more intense with increasing mixing time and increasing temperature.

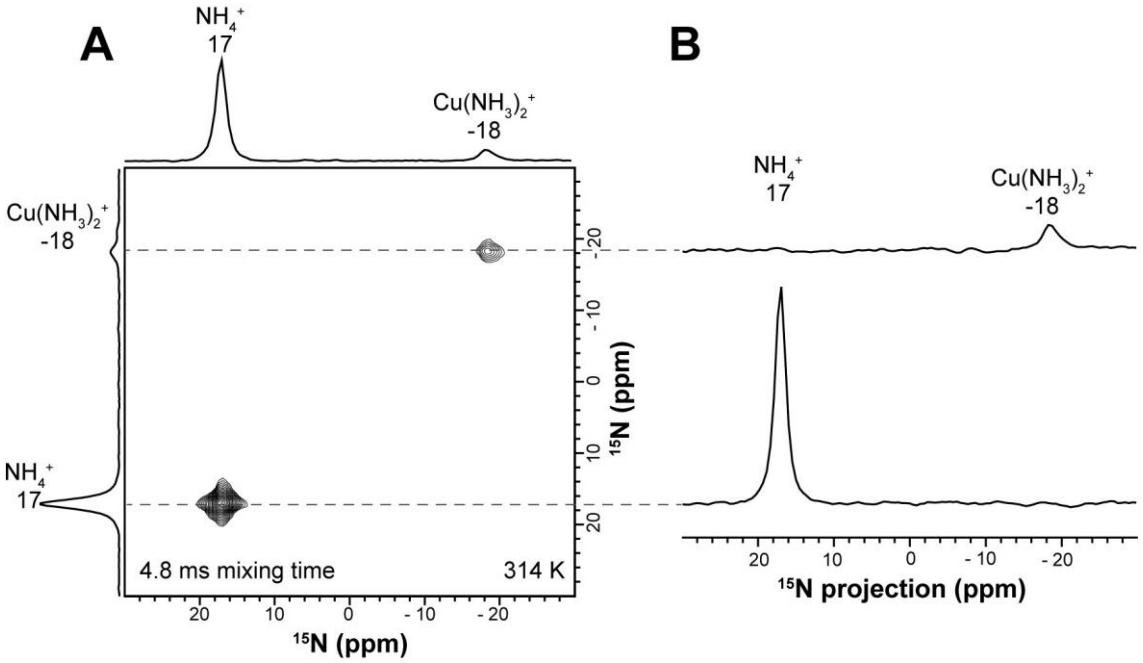

Figure S26. (a) Solid-state 2D ^{15}N EXSY NMR spectrum of fresh Cu-CHA (Cu/Al = 0.21). The spectrum was acquired at 11.7 T, 314 K, and 12.5 kHz MAS, with a mixing time of 4.8 ms and a recycle delay of 1.0 s. (b) Horizontal projections along the ω_1 axis of the 2D spectrum at –18 ppm (top) and 17 ppm (bottom); the integrated signal intensities were used in the kinetic analyses described in the manuscript.

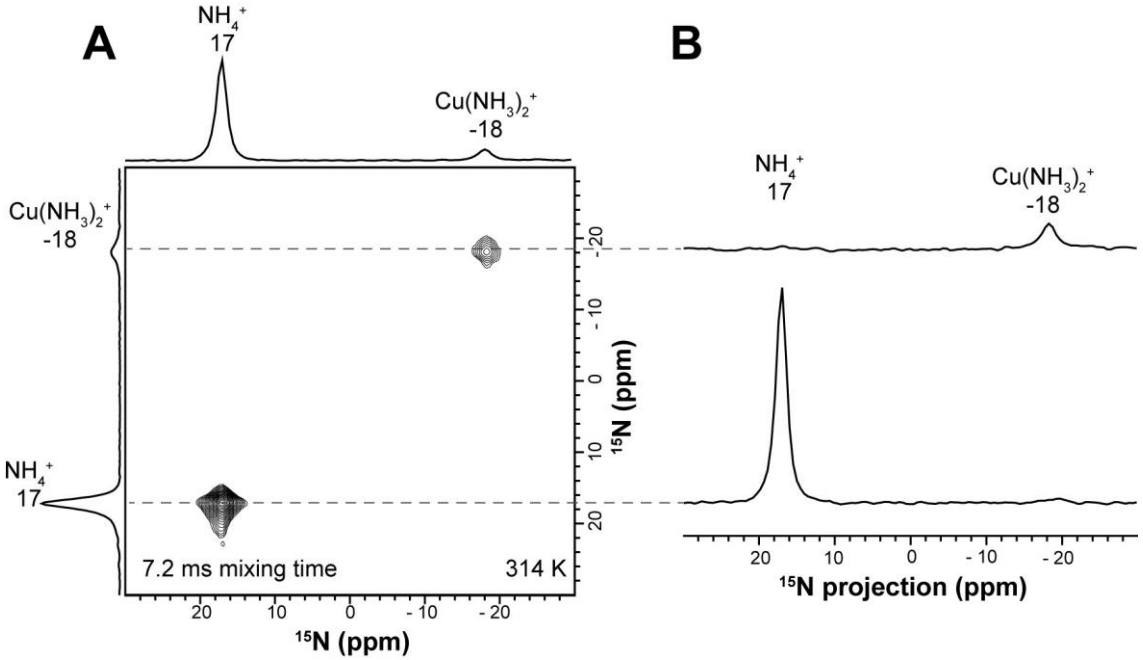

Figure S27. (a) Solid-state 2D ^{15}N EXSY NMR spectrum of fresh Cu-CHA (Cu/Al = 0.21). The spectrum was acquired at 11.7 T, 314 K, and 12.5 kHz MAS, with a mixing time of 7.2 ms and a recycle delay of 1.0 s. (b) Horizontal projections along the ω_1 axis of the 2D spectrum at –18 ppm (top) and 17 ppm (bottom); the integrated signal intensities were used in the kinetic analyses described in the manuscript.

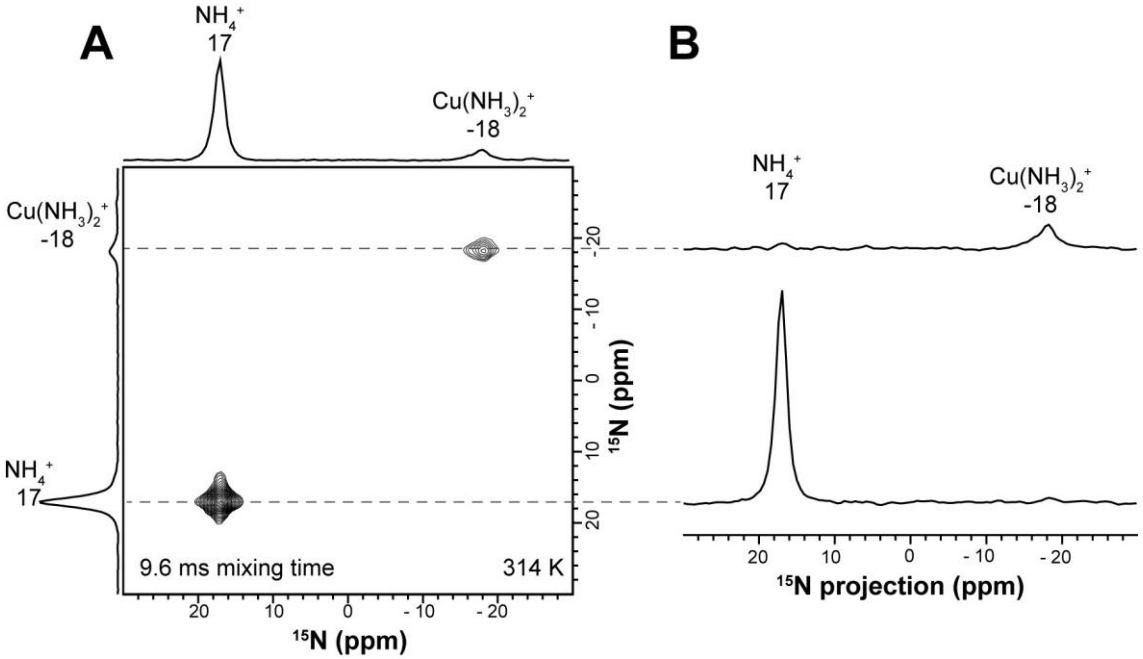

Figure S28. (a) Solid-state 2D ^{15}N EXSY NMR spectrum of fresh Cu-CHA (Cu/Al = 0.21). The spectrum was acquired at 11.7 T, 314 K, and 12.5 kHz MAS, with a mixing time of 9.6 ms and a recycle delay of 1.0 s. (b) Horizontal projections along the ω_1 axis of the 2D spectrum at –18 ppm (top) and 17 ppm (bottom); the integrated signal intensities were used in the kinetic analyses described in the manuscript.

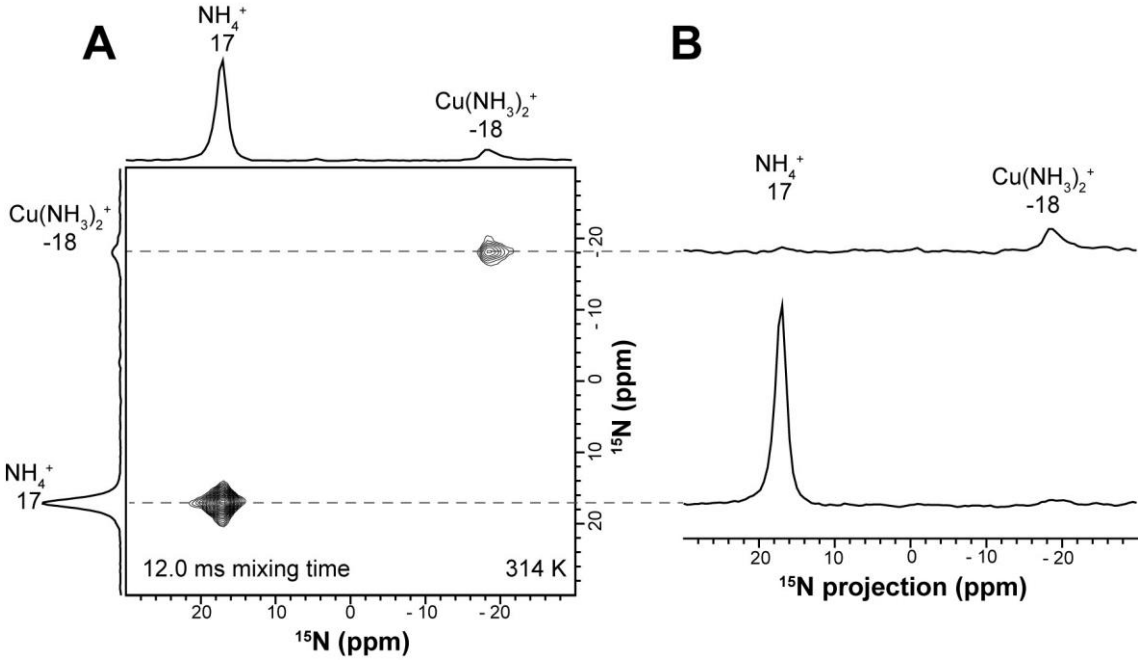

Figure S29. (a) Solid-state 2D ^{15}N EXSY NMR spectrum of fresh Cu-CHA (Cu/Al = 0.21). The spectrum was acquired at 11.7 T, 314 K, and 12.5 kHz MAS, with a mixing time of 12.0 ms and a recycle delay of 1.0 s. (b) Horizontal projections along the ω_1 axis of the 2D spectrum at –18 ppm (top) and 17 ppm (bottom); the integrated signal intensities were used in the kinetic analyses described in the manuscript.

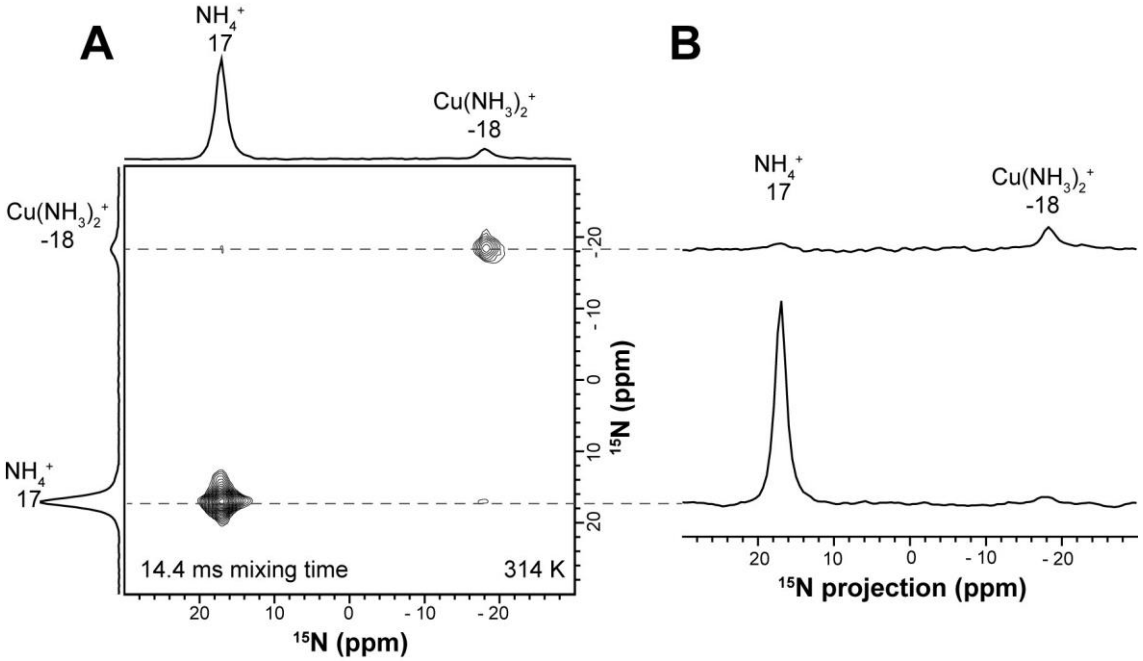

Figure S30. (a) Solid-state 2D ^{15}N EXSY NMR spectrum of fresh Cu-CHA (Cu/Al = 0.21). The spectrum was acquired at 11.7 T, 314 K, and 12.5 kHz MAS, with a mixing time of 14.4 ms and a recycle delay of 1.0 s. (b) Horizontal projections along the ω_1 axis of the 2D spectrum at –18 ppm (top) and 17 ppm (bottom); the integrated signal intensities were used in the kinetic analyses described in the manuscript.

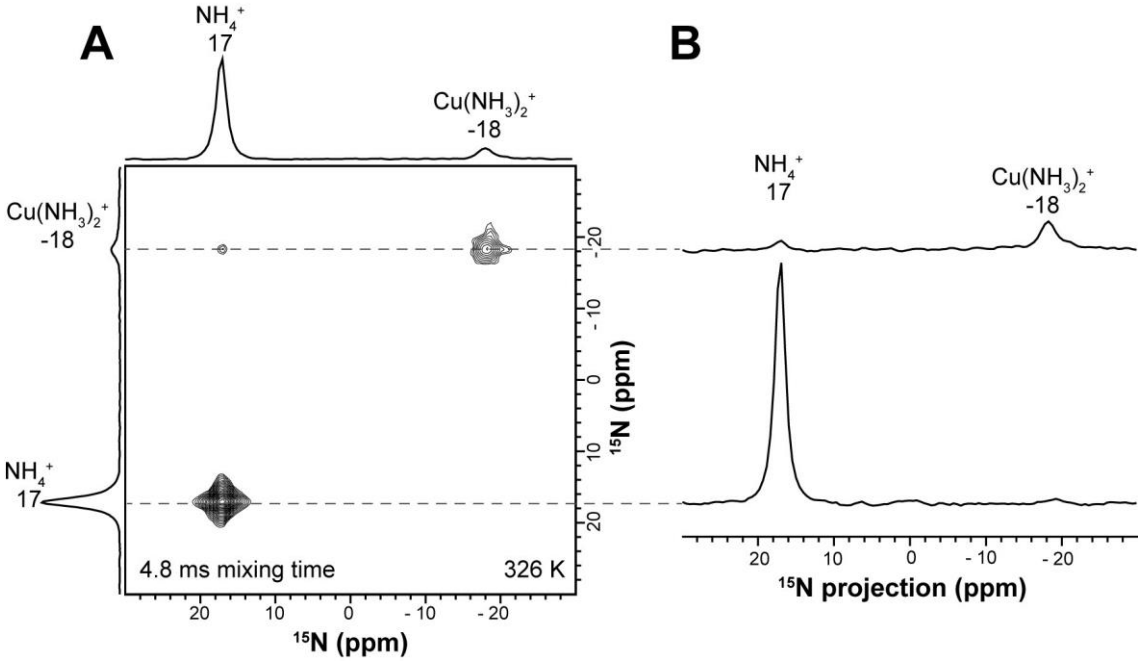

Figure S31. (a) Solid-state 2D ^{15}N EXSY NMR spectrum of fresh Cu-CHA (Cu/Al = 0.21). The spectrum was acquired at 11.7 T, 326 K, and 12.5 kHz MAS, with a mixing time of 4.8 ms and a recycle delay of 1.0 s. (b) Horizontal projections along the ω_1 axis of the 2D spectrum at –18 ppm (top) and 17 ppm (bottom); the integrated signal intensities were used in the kinetic analyses described in the manuscript.

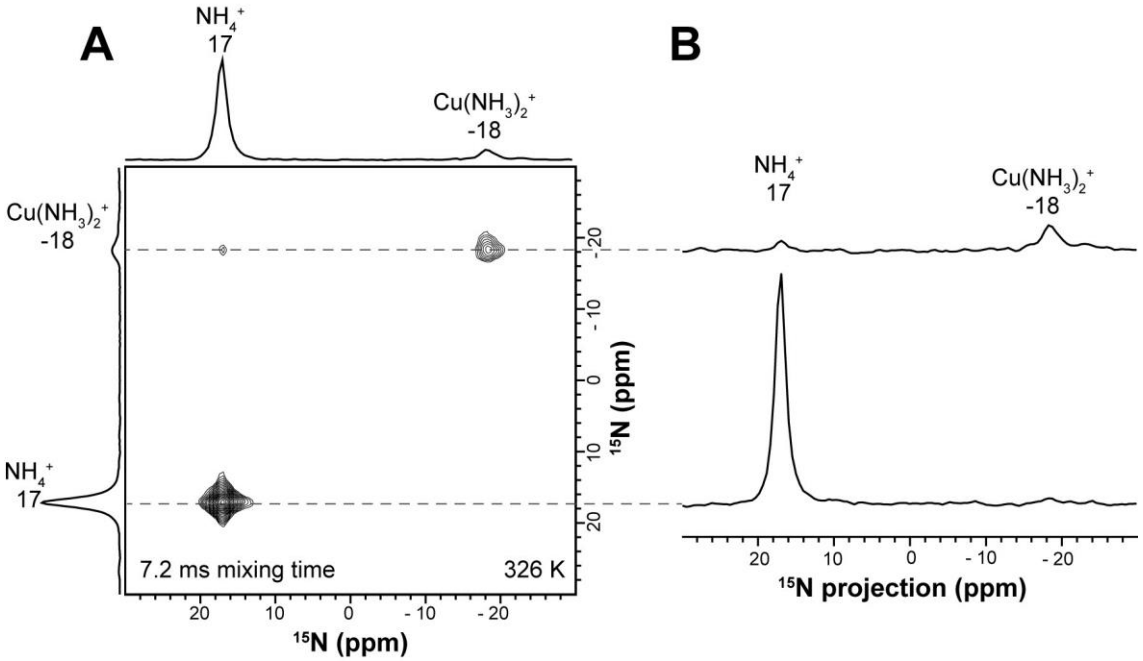

Figure S32. (a) Solid-state 2D ^{15}N EXSY NMR spectrum of fresh Cu-CHA (Cu/Al = 0.21). The spectrum was acquired at 11.7 T, 326 K, and 12.5 kHz MAS, with a mixing time of 7.2 ms and a recycle delay of 1.0 s. (b) Horizontal projections along the ω_1 axis of the 2D spectrum at –18 ppm (top) and 17 ppm (bottom); the integrated signal intensities were used in the kinetic analyses described in the manuscript.

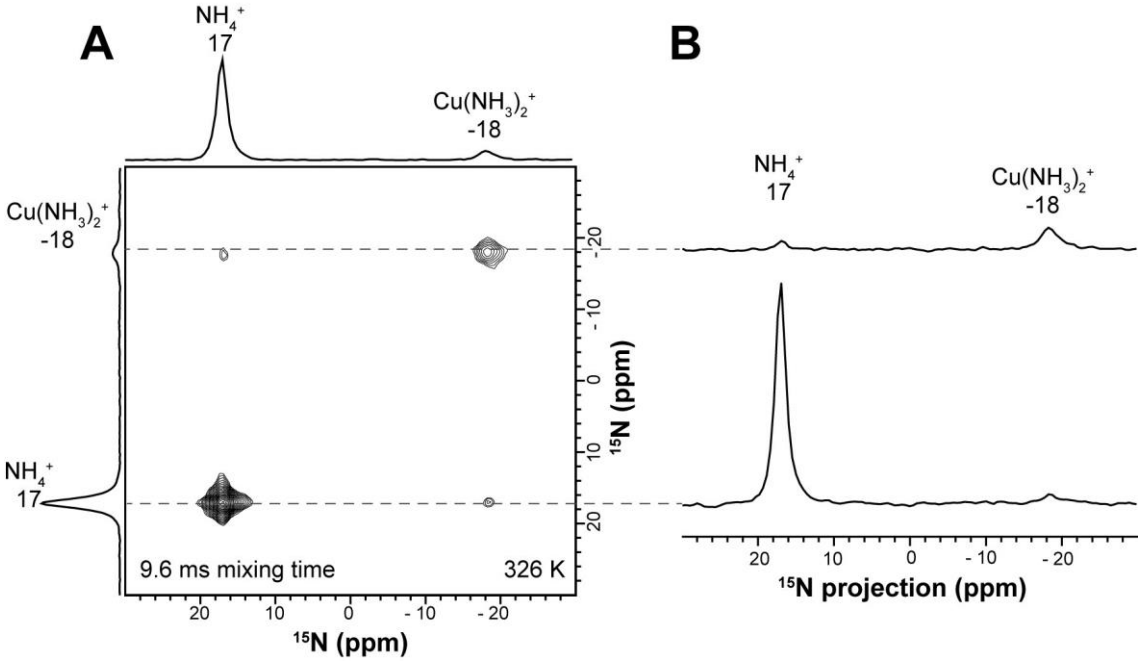

Figure S33. (a) Solid-state 2D ^{15}N EXSY NMR spectrum of fresh Cu-CHA (Cu/Al = 0.21). The spectrum was acquired at 11.7 T, 326 K, and 12.5 kHz MAS, with a mixing time of 9.6 ms and a recycle delay of 1.0 s. (b) Horizontal projections along the ω_1 axis of the 2D spectrum at –18 ppm (top) and 17 ppm (bottom); the integrated signal intensities were used in the kinetic analyses described in the manuscript.

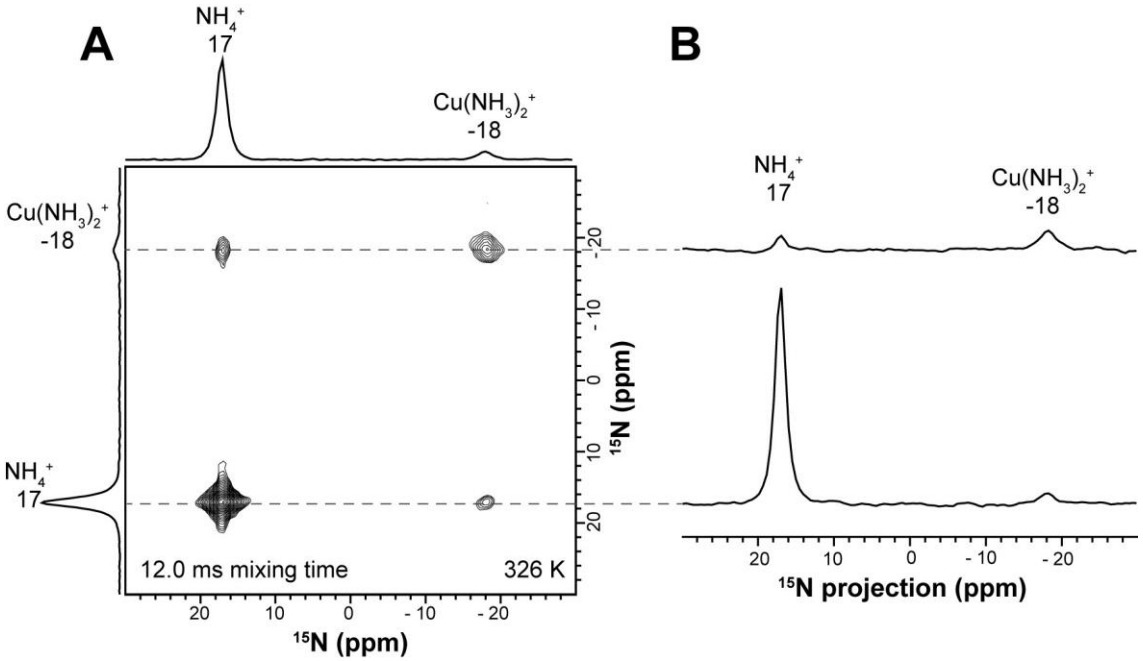

Figure S34. (a) Solid-state 2D ^{15}N EXSY NMR spectrum of fresh Cu-CHA (Cu/Al = 0.21). The spectrum was acquired at 11.7 T, 326 K, and 12.5 kHz MAS, with a mixing time of 12.0 ms and a recycle delay of 1.0 s. (b) Horizontal projections along the ω_1 axis of the 2D spectrum at –18 ppm (top) and 17 ppm (bottom); the integrated signal intensities were used in the kinetic analyses described in the manuscript.

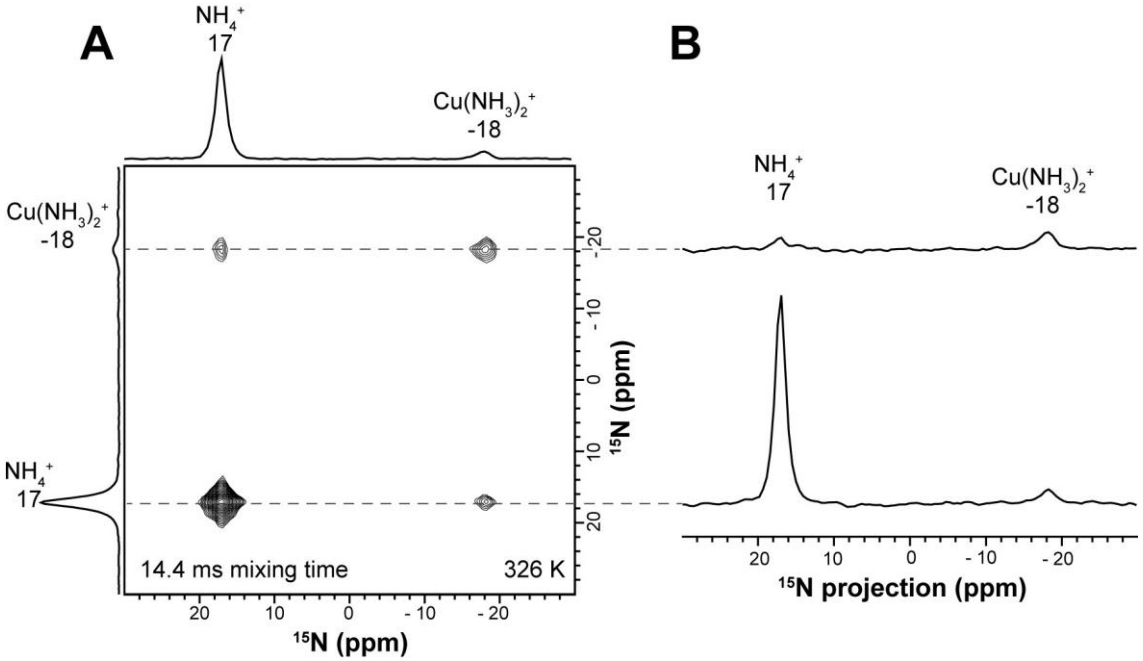

Figure S35. (a) Solid-state 2D ^{15}N EXSY NMR spectrum of fresh Cu-CHA (Cu/Al = 0.21). The spectrum was acquired at 11.7 T, 326 K, and 12.5 kHz MAS, with a mixing time of 14.4 ms and a recycle delay of 1.0 s. (b) Horizontal projections along the ω_1 axis of the 2D spectrum at –18 ppm (top) and 17 ppm (bottom); the integrated signal intensities were used in the kinetic analyses described in the manuscript.

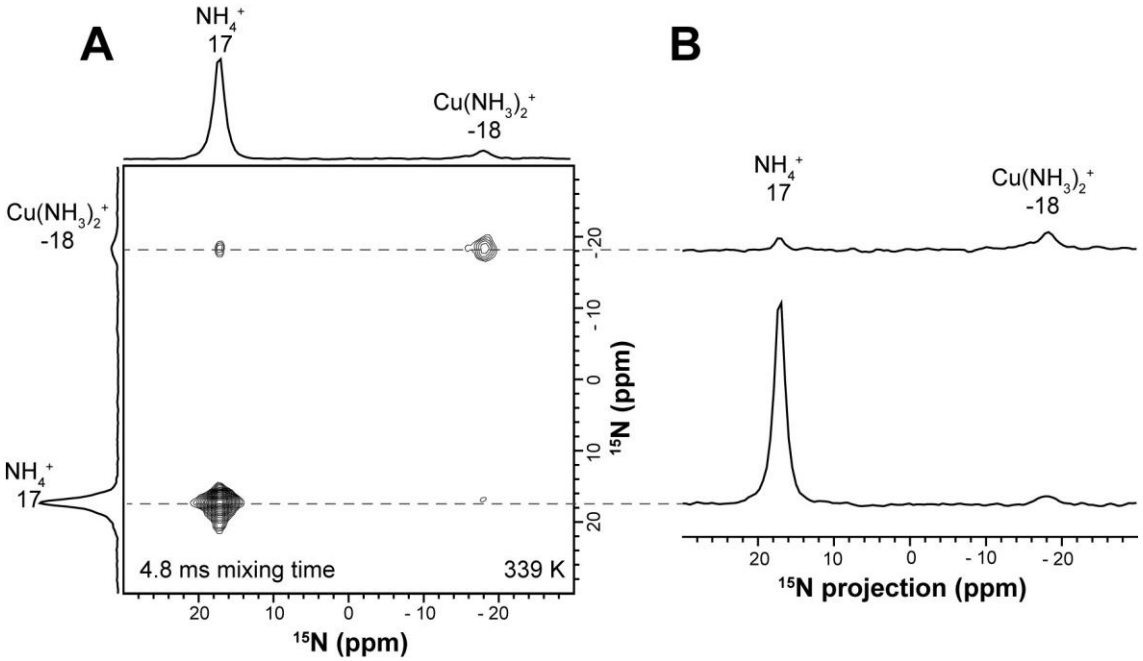

Figure S36. (a) Solid-state 2D ^{15}N EXSY NMR spectrum of fresh Cu-CHA (Cu/Al = 0.21). The spectrum was acquired at 11.7 T, 339 K, and 12.5 kHz MAS, with a mixing time of 4.8 ms and a recycle delay of 1.0 s. (b) Horizontal projections along the ω_1 axis of the 2D spectrum at –18 ppm (top) and 17 ppm (bottom); the integrated signal intensities were used in the kinetic analyses described in the manuscript.

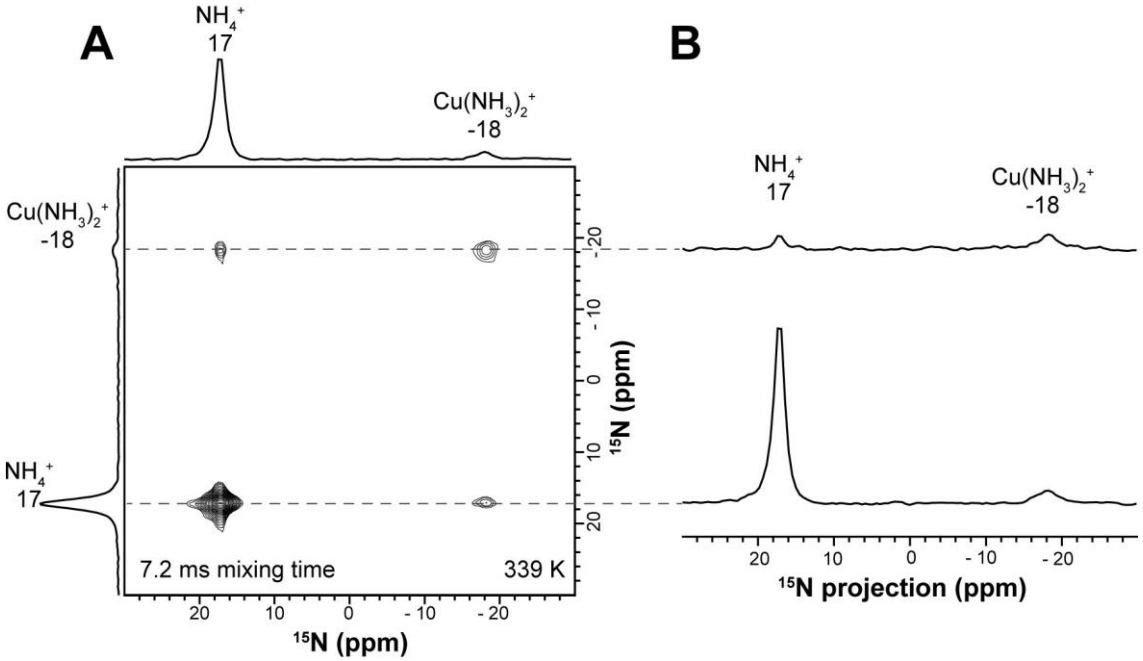

Figure S37. (a) Solid-state 2D ^{15}N EXSY NMR spectrum of fresh Cu-CHA (Cu/Al = 0.21). The spectrum was acquired at 11.7 T, 339 K, and 12.5 kHz MAS, with a mixing time of 7.2 ms and a recycle delay of 1.0 s. (b) Horizontal projections along the ω_1 axis of the 2D spectrum at –18 ppm (top) and 17 ppm (bottom); the integrated signal intensities were used in the kinetic analyses described in the manuscript.

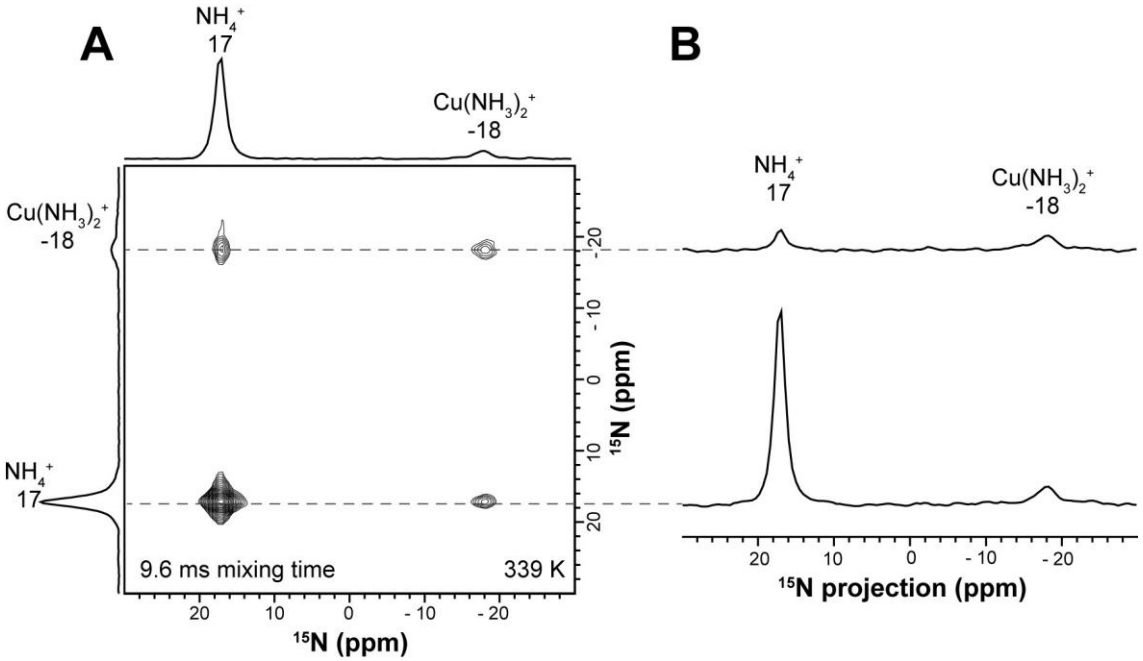

Figure S38. (a) Solid-state 2D ^{15}N EXSY NMR spectrum of fresh Cu-CHA (Cu/Al = 0.21). The spectrum was acquired at 11.7 T, 339 K, and 12.5 kHz MAS, with a mixing time of 9.6 ms and a recycle delay of 1.0 s. (b) Horizontal projections along the ω_1 axis of the 2D spectrum at –18 ppm (top) and 17 ppm (bottom); the integrated signal intensities were used in the kinetic analyses described in the manuscript.

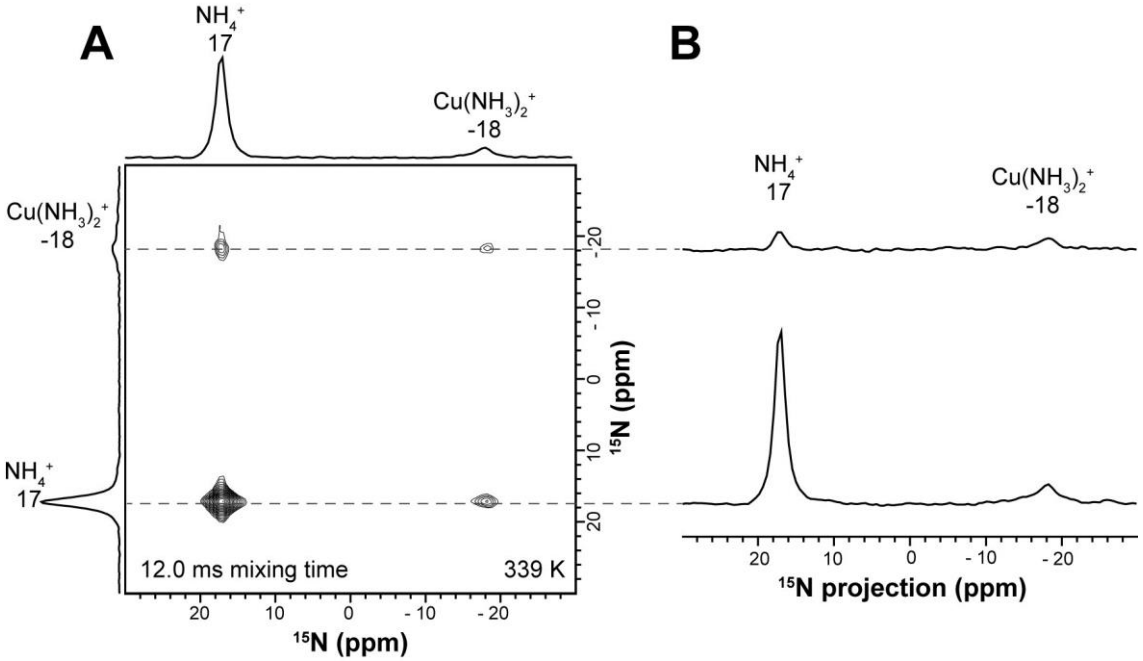

Figure S39. (a) Solid-state 2D ^{15}N EXSY NMR spectrum of fresh Cu-CHA (Cu/Al = 0.21). The spectrum was acquired at 11.7 T, 339 K, and 12.5 kHz MAS, with a mixing time of 12.0 ms and a recycle delay of 1.0 s. (b) Horizontal projections along the ω_1 axis of the 2D spectrum at –18 ppm (top) and 17 ppm (bottom); the integrated signal intensities were used in the kinetic analyses described in the manuscript.

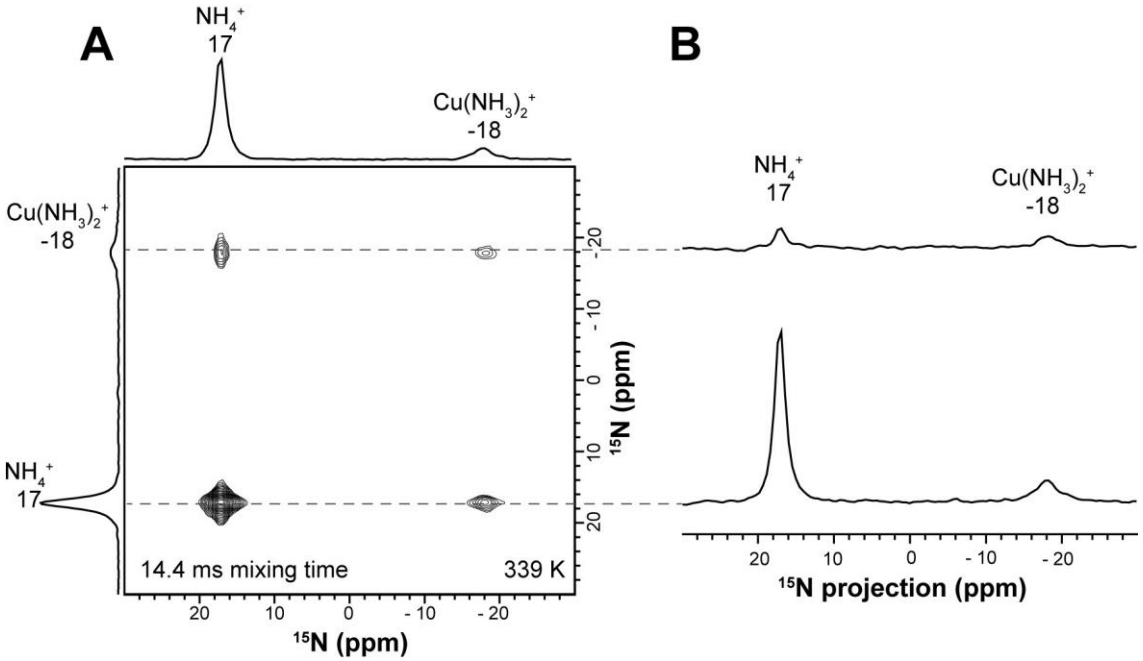

Figure S40. (a) Solid-state 2D ^{15}N EXSY NMR spectrum of fresh Cu-CHA (Cu/Al = 0.21). The spectrum was acquired at 11.7 T, 339 K, and 12.5 kHz MAS, with a mixing time of 14.4 ms and a recycle delay of 1.0 s. (b) Horizontal projections along the ω_1 axis of the 2D spectrum at –18 ppm (top) and 17 ppm (bottom); the integrated signal intensities were used in the kinetic analyses described in the manuscript.

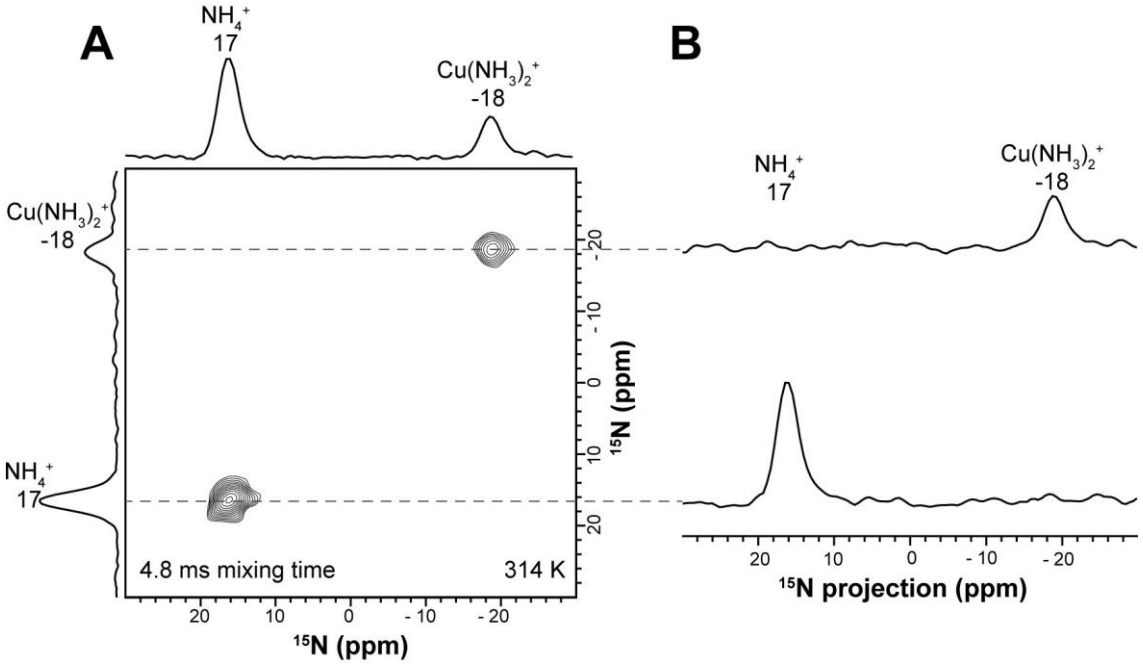

Figure S41. (a) Solid-state 2D ^{15}N EXSY NMR spectrum of 4-h-aged Cu-CHA (Cu/Al = 0.21). The spectrum was acquired at 11.7 T, 314 K, and 12.5 kHz MAS, with a mixing time of 4.8 ms and a recycle delay of 1.0 s. (b) Horizontal projections along the ω_1 axis of the 2D spectrum at –18 ppm (top) and 17 ppm (bottom); the integrated signal intensities were used in the kinetic analyses described in the manuscript.

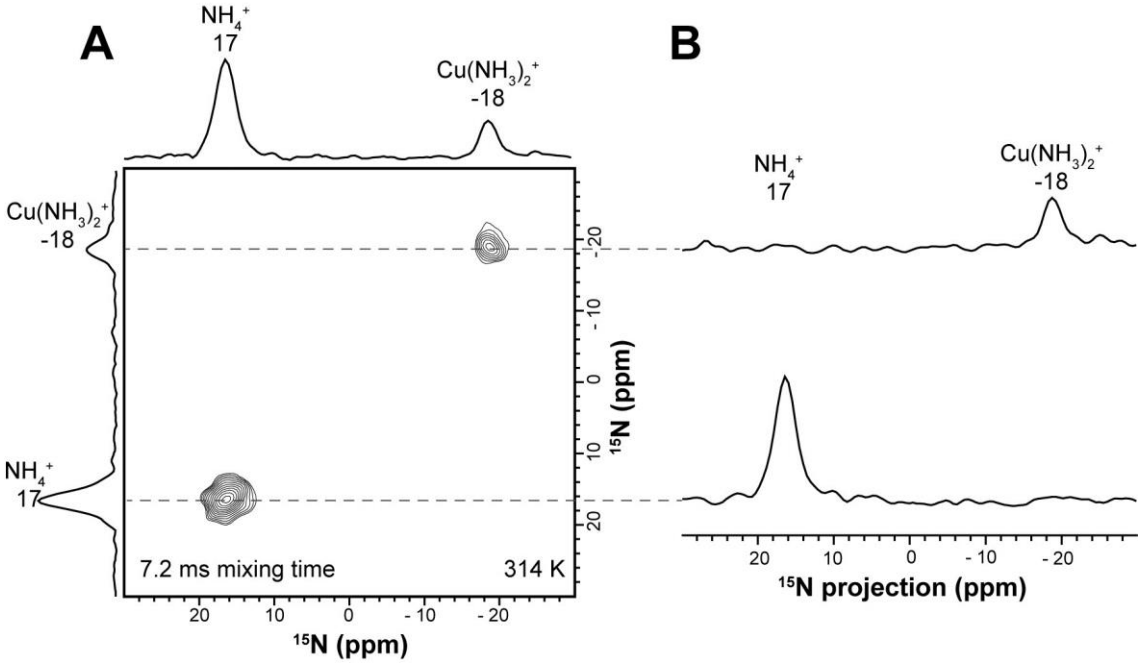

Figure S42. (a) Solid-state 2D ^{15}N EXSY NMR spectrum of 4-h-aged Cu-CHA (Cu/Al = 0.21). The spectrum was acquired at 11.7 T, 314 K, and 12.5 kHz MAS, with a mixing time of 7.2 ms and a recycle delay of 1.0 s. (b) Horizontal projections along the ω_1 axis of the 2D spectrum at –18 ppm (top) and 17 ppm (bottom); the integrated signal intensities were used in the kinetic analyses described in the manuscript.

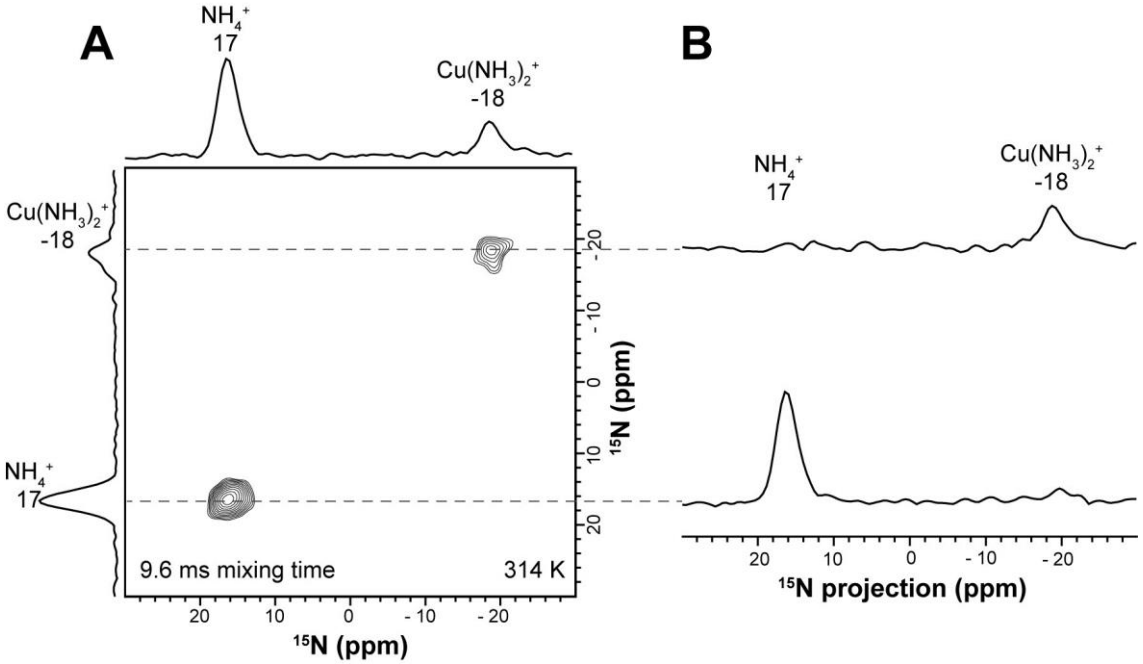

Figure S43. (a) Solid-state 2D ^{15}N EXSY NMR spectrum of 4-h-aged Cu-CHA (Cu/Al = 0.21). The spectrum was acquired at 11.7 T, 314 K, and 12.5 kHz MAS, with a mixing time of 9.6 ms and a recycle delay of 1.0 s. (b) Horizontal projections along the ω_1 axis of the 2D spectrum at –18 ppm (top) and 17 ppm (bottom); the integrated signal intensities were used in the kinetic analyses described in the manuscript.

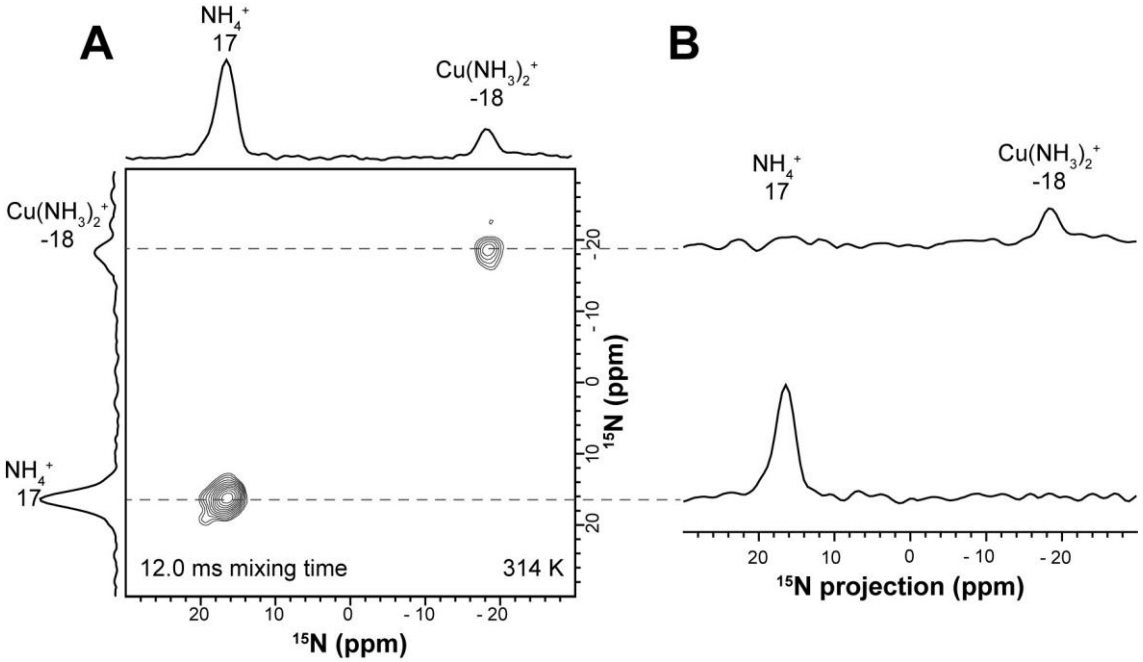

Figure S44. (a) Solid-state 2D ^{15}N EXSY NMR spectrum of 4-h-aged Cu-CHA (Cu/Al = 0.21). The spectrum was acquired at 11.7 T, 314 K, and 12.5 kHz MAS, with a mixing time of 12.0 ms and a recycle delay of 1.0 s. (b) Horizontal projections along the ω_1 axis of the 2D spectrum at –18 ppm (top) and 17 ppm (bottom); the integrated signal intensities were used in the kinetic analyses described in the manuscript.

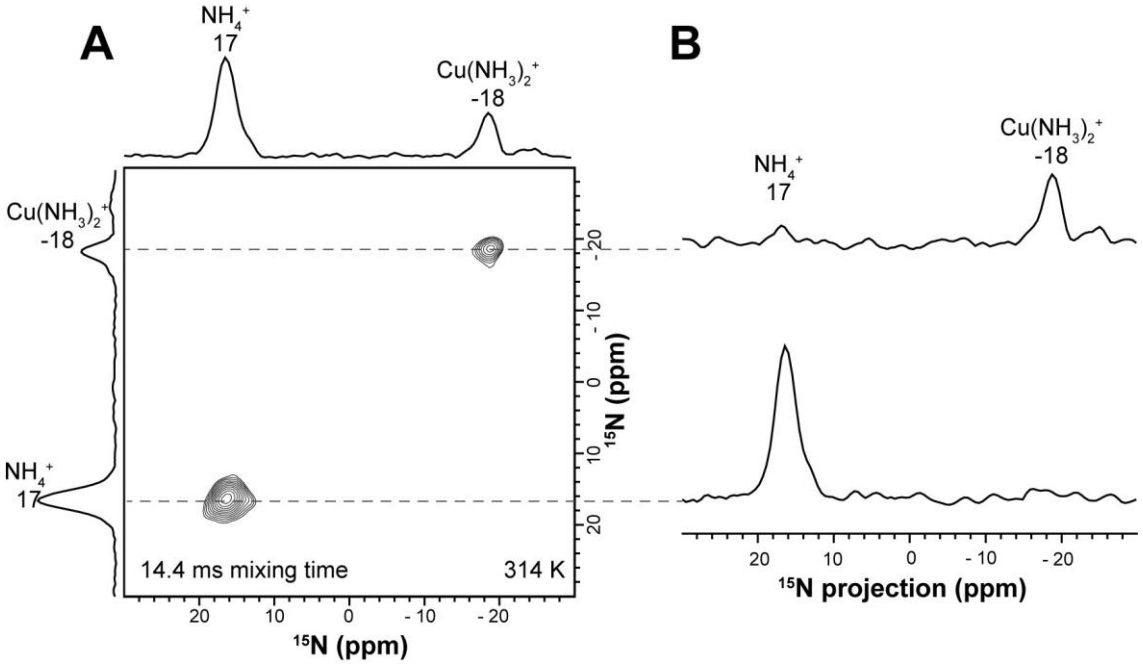

Figure S45. (a) Solid-state 2D ^{15}N EXSY NMR spectrum of 4-h-aged Cu-CHA (Cu/Al = 0.21). The spectrum was acquired at 11.7 T, 314 K, and 12.5 kHz MAS, with a mixing time of 14.4 ms and a recycle delay of 1.0 s. (b) Horizontal projections along the ω_1 axis of the 2D spectrum at –18 ppm (top) and 17 ppm (bottom); the integrated signal intensities were used in the kinetic analyses described in the manuscript.

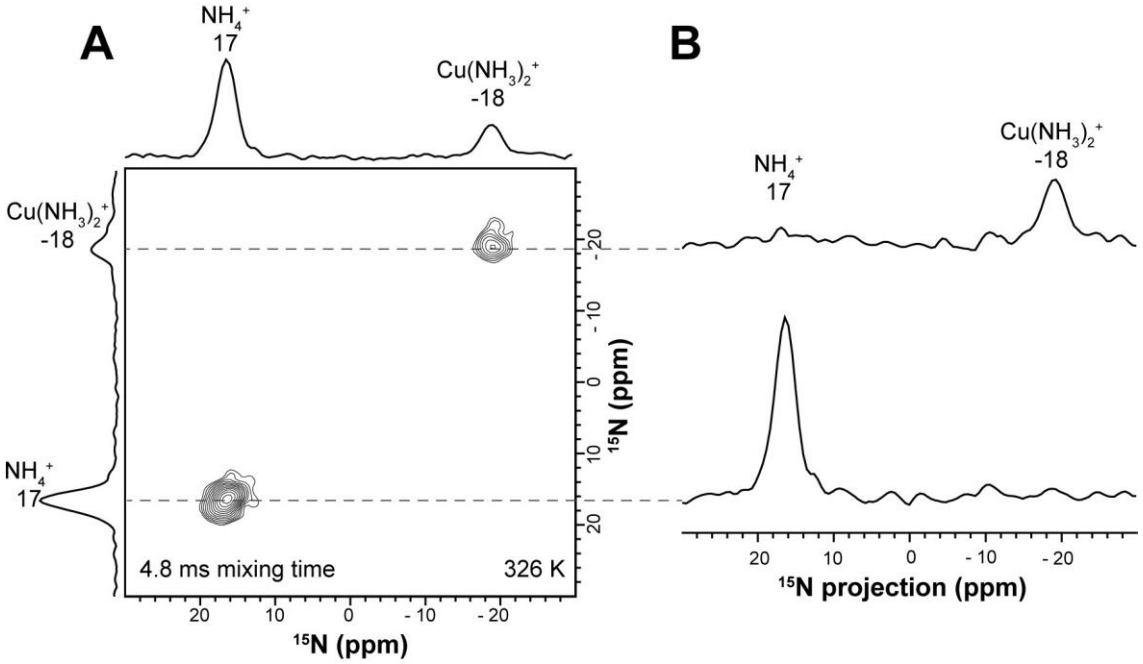

Figure S46. (a) Solid-state 2D ^{15}N EXSY NMR spectrum of 4-h-aged Cu-CHA (Cu/Al = 0.21). The spectrum was acquired at 11.7 T, 326 K, and 12.5 kHz MAS, with a mixing time of 4.8 ms and a recycle delay of 1.0 s. (b) Horizontal projections along the ω_1 axis of the 2D spectrum at –18 ppm (top) and 17 ppm (bottom); the integrated signal intensities were used in the kinetic analyses described in the manuscript.

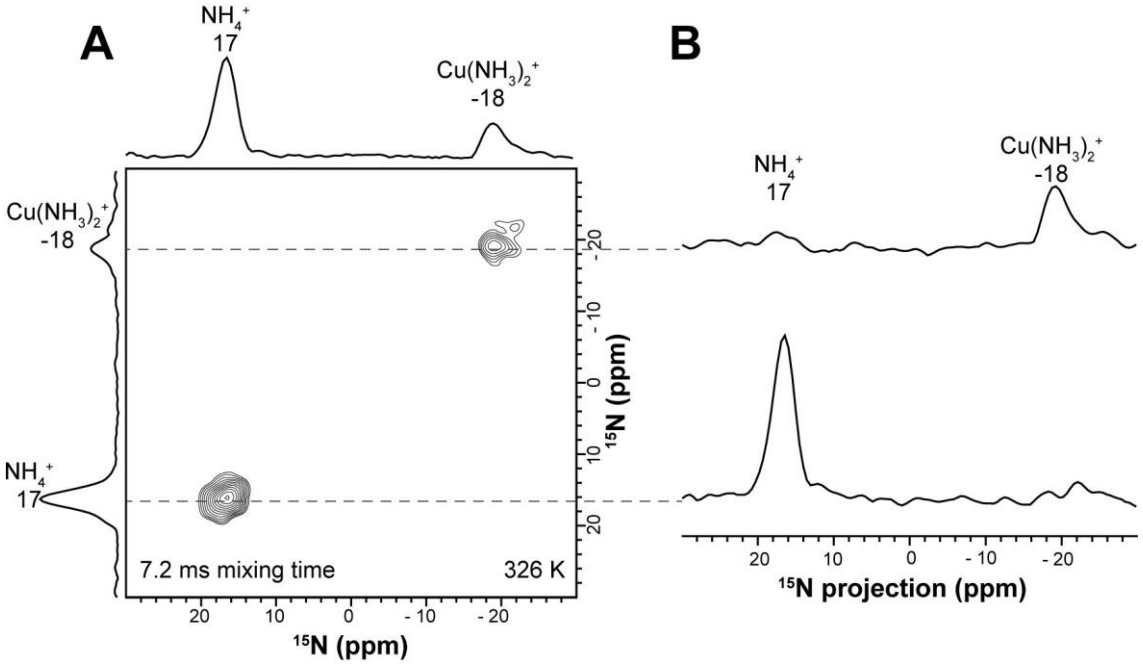

Figure S47. (a) Solid-state 2D ^{15}N EXSY NMR spectrum of 4-h-aged Cu-CHA (Cu/Al = 0.21). The spectrum was acquired at 11.7 T, 326 K, and 12.5 kHz MAS, with a mixing time of 7.2 ms and a recycle delay of 1.0 s. (b) Horizontal projections along the ω_1 axis of the 2D spectrum at –18 ppm (top) and 17 ppm (bottom); the integrated signal intensities were used in the kinetic analyses described in the manuscript.

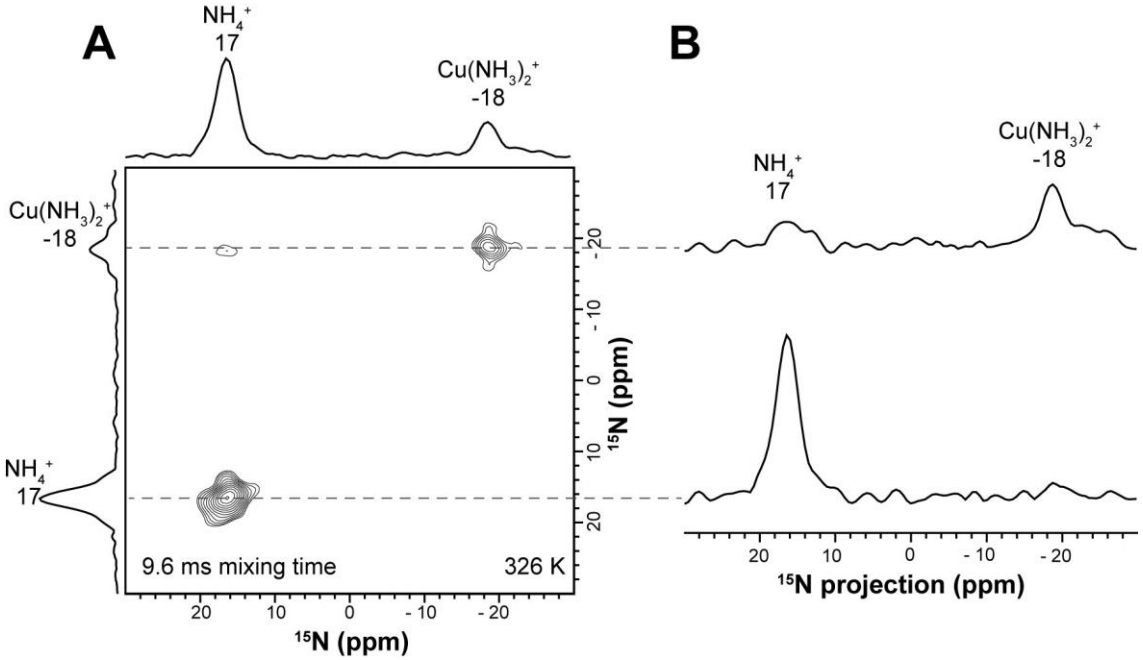

Figure S48. (a) Solid-state 2D ^{15}N EXSY NMR spectrum of 4-h-aged Cu-CHA (Cu/Al = 0.21). The spectrum was acquired at 11.7 T, 326 K, and 12.5 kHz MAS, with a mixing time of 9.6 ms and a recycle delay of 1.0 s. (b) Horizontal projections along the ω_1 axis of the 2D spectrum at –18 ppm (top) and 17 ppm (bottom); the integrated signal intensities were used in the kinetic analyses described in the manuscript.

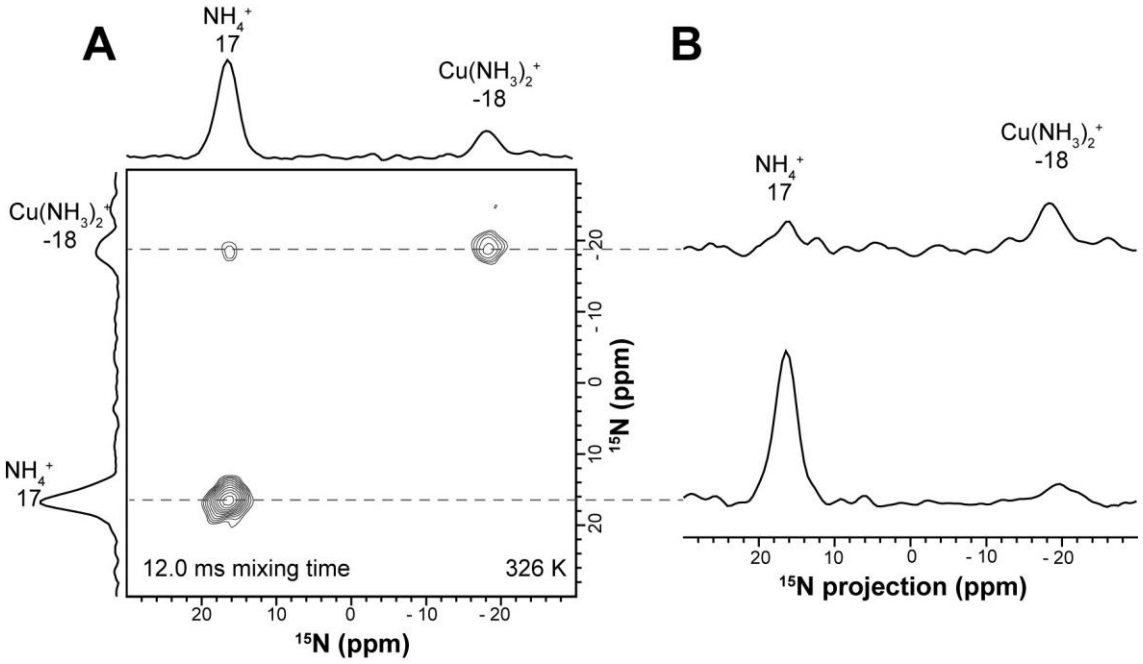

Figure S49. (a) Solid-state 2D ^{15}N EXSY NMR spectrum of 4-h-aged Cu-CHA (Cu/Al = 0.21). The spectrum was acquired at 11.7 T, 326 K, and 12.5 kHz MAS, with a mixing time of 12.0 ms and a recycle delay of 1.0 s. (b) Horizontal projections along the ω_1 axis of the 2D spectrum at –18 ppm (top) and 17 ppm (bottom); the integrated signal intensities were used in the kinetic analyses described in the manuscript.

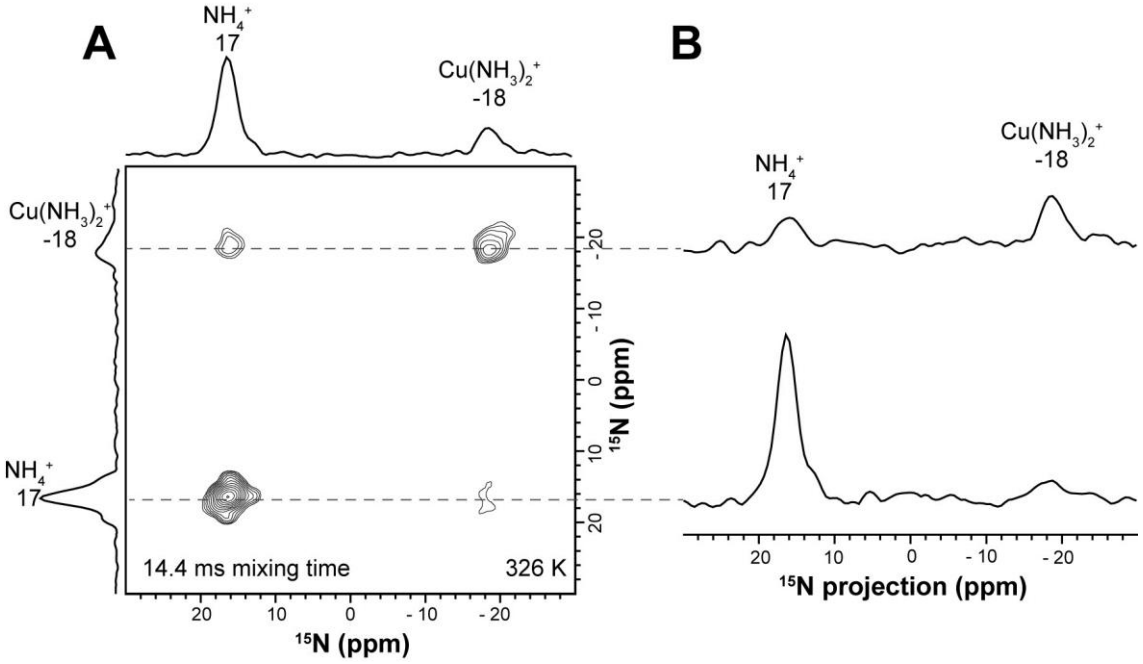

Figure S50. (a) Solid-state 2D ^{15}N EXSY NMR spectrum of 4-h-aged Cu-CHA (Cu/Al = 0.21). The spectrum was acquired at 11.7 T, 326 K, and 12.5 kHz MAS, with a mixing time of 14.4 ms and a recycle delay of 1.0 s. (b) Horizontal projections along the ω_1 axis of the 2D spectrum at –18 ppm (top) and 17 ppm (bottom); the integrated signal intensities were used in the kinetic analyses described in the manuscript.

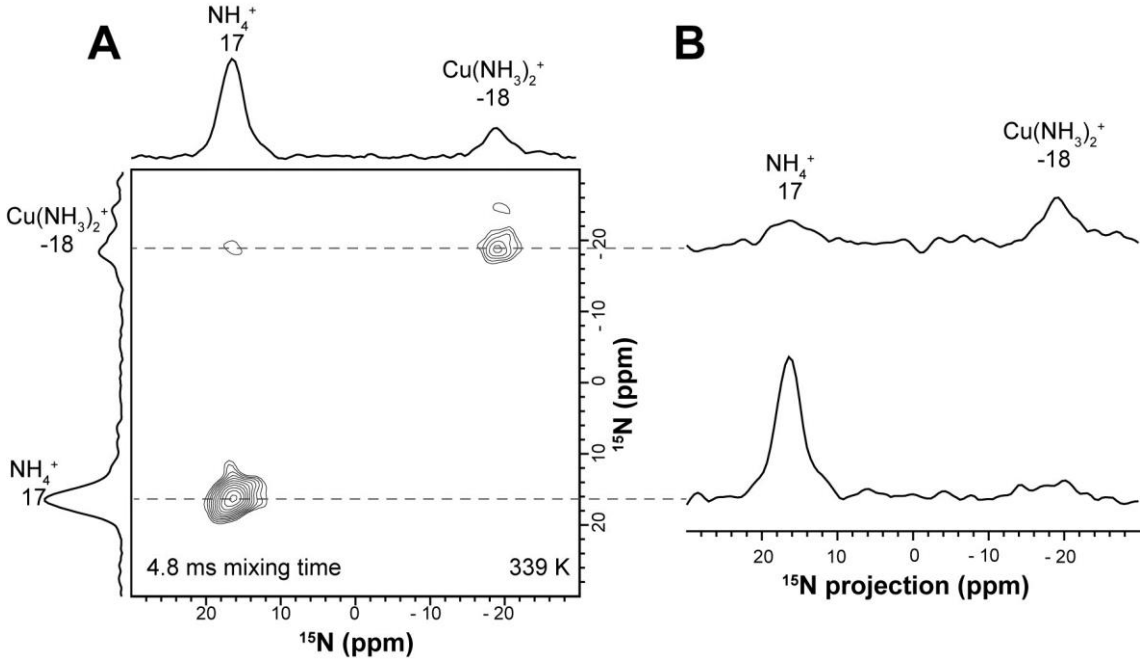

Figure S51. (a) Solid-state 2D ^{15}N EXSY NMR spectrum of 4-h-aged Cu-CHA (Cu/Al = 0.21). The spectrum was acquired at 11.7 T, 339 K, and 12.5 kHz MAS, with a mixing time of 4.8 ms and a recycle delay of 1.0 s. (b) Horizontal projections along the ω_1 axis of the 2D spectrum at –18 ppm (top) and 17 ppm (bottom); the integrated signal intensities were used in the kinetic analyses described in the manuscript.

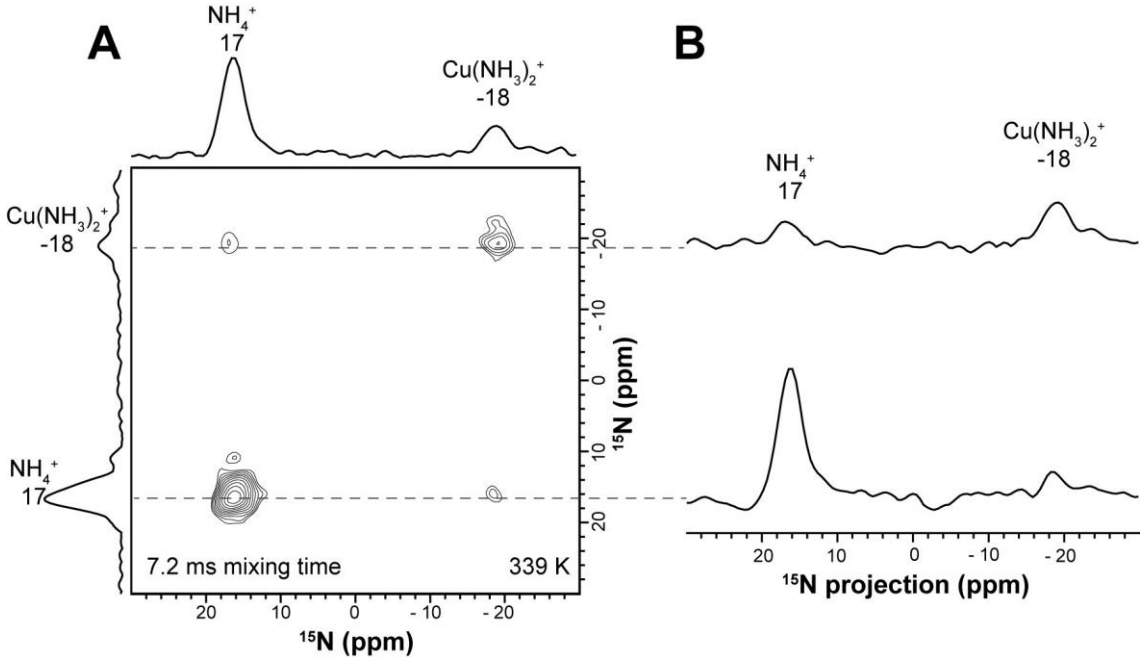

Figure S52. (a) Solid-state 2D ^{15}N EXSY NMR spectrum of 4-h-aged Cu-CHA (Cu/Al = 0.21). The spectrum was acquired at 11.7 T, 339 K, and 12.5 kHz MAS, with a mixing time of 7.2 ms and a recycle delay of 1.0 s. (b) Horizontal projections along the ω_1 axis of the 2D spectrum at –18 ppm (top) and 17 ppm (bottom); the integrated signal intensities were used in the kinetic analyses described in the manuscript.

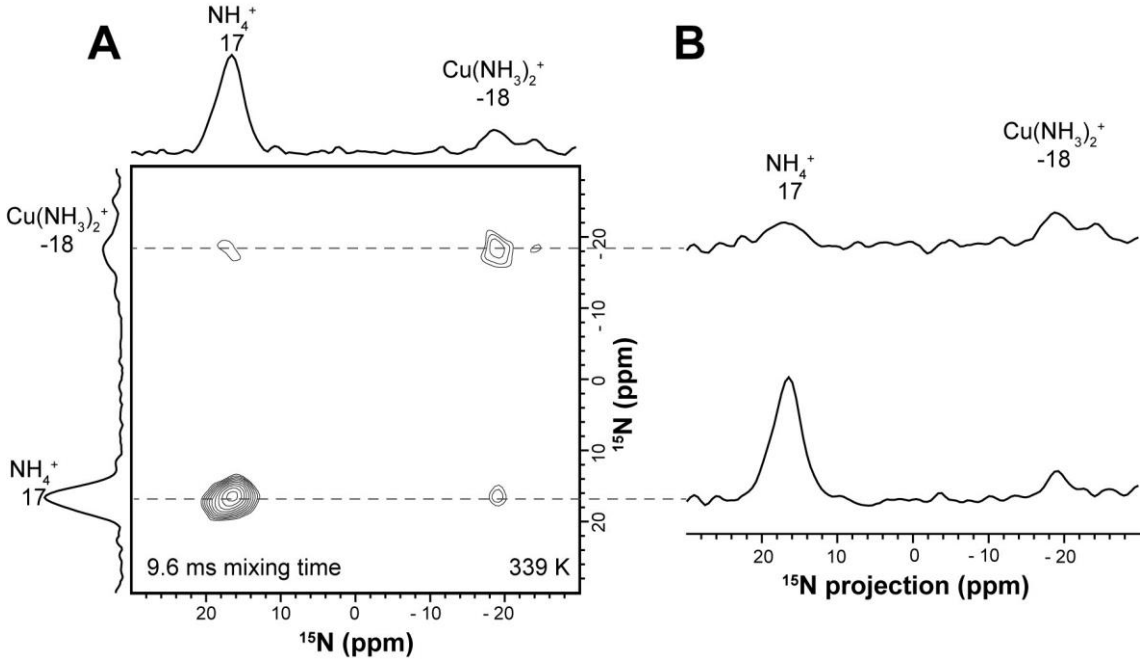

Figure S53. (a) Solid-state 2D ^{15}N EXSY NMR spectrum of 4-h-aged Cu-CHA (Cu/Al = 0.21). The spectrum was acquired at 11.7 T, 339 K, and 12.5 kHz MAS, with a mixing time of 9.6 ms and a recycle delay of 1.0 s. (b) Horizontal projections along the ω_1 axis of the 2D spectrum at –18 ppm (top) and 17 ppm (bottom); the integrated signal intensities were used in the kinetic analyses described in the manuscript.

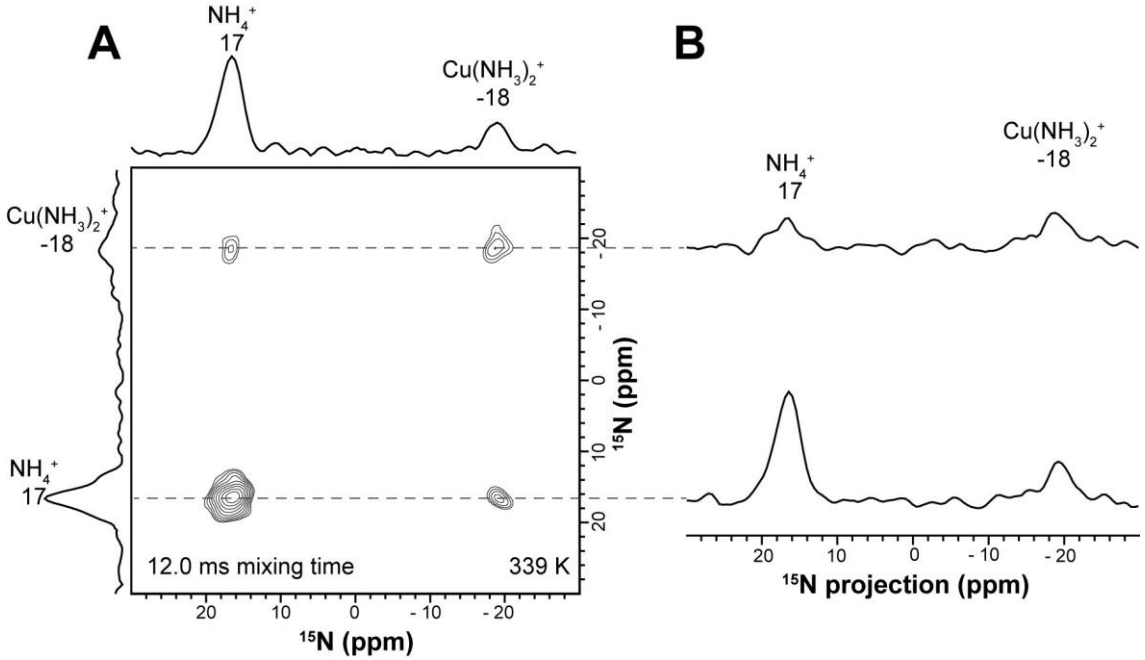

Figure S54. (a) Solid-state 2D ^{15}N EXSY NMR spectrum of 4-h-aged Cu-CHA (Cu/Al = 0.21). The spectrum was acquired at 11.7 T, 339 K, and 12.5 kHz MAS, with a mixing time of 12.0 ms and a recycle delay of 1.0 s. (b) Horizontal projections along the ω_1 axis of the 2D spectrum at –18 ppm (top) and 17 ppm (bottom); the integrated signal intensities were used in the kinetic analyses described in the manuscript.

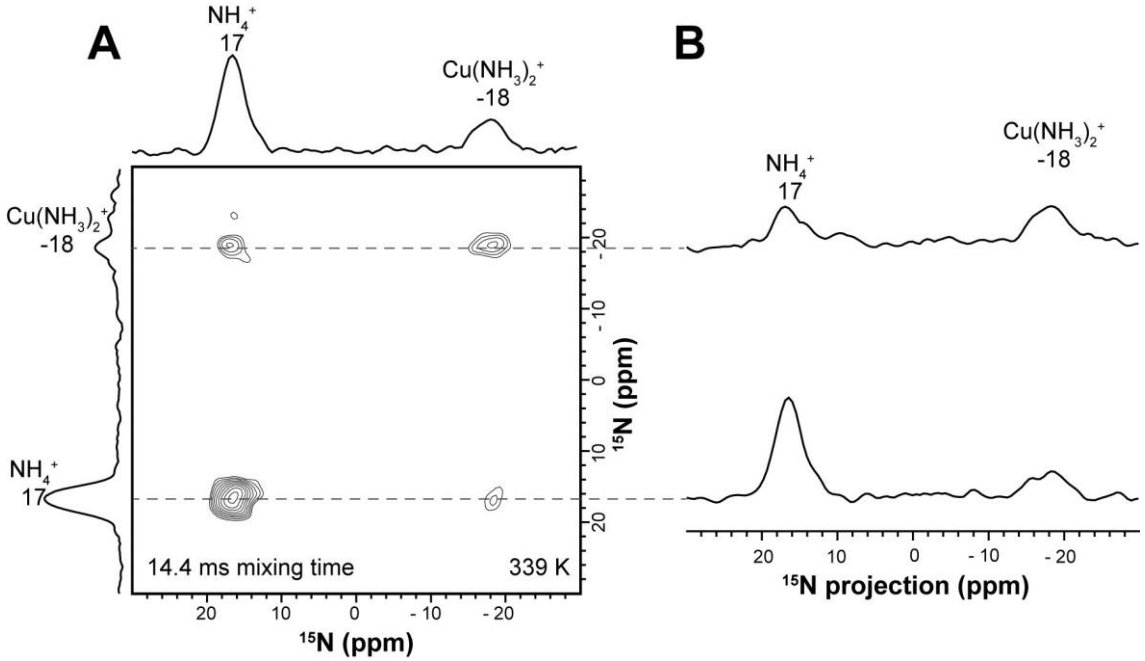

Figure S55. (a) Solid-state 2D ^{15}N EXSY NMR spectrum of 4-h-aged Cu-CHA (Cu/Al = 0.21). The spectrum was acquired at 11.7 T, 339 K, and 12.5 kHz MAS, with a mixing time of 14.4 ms and a recycle delay of 1.0 s. (b) Horizontal projections along the ω_1 axis of the 2D spectrum at –18 ppm (top) and 17 ppm (bottom); the integrated signal intensities were used in the kinetic analyses described in the manuscript.

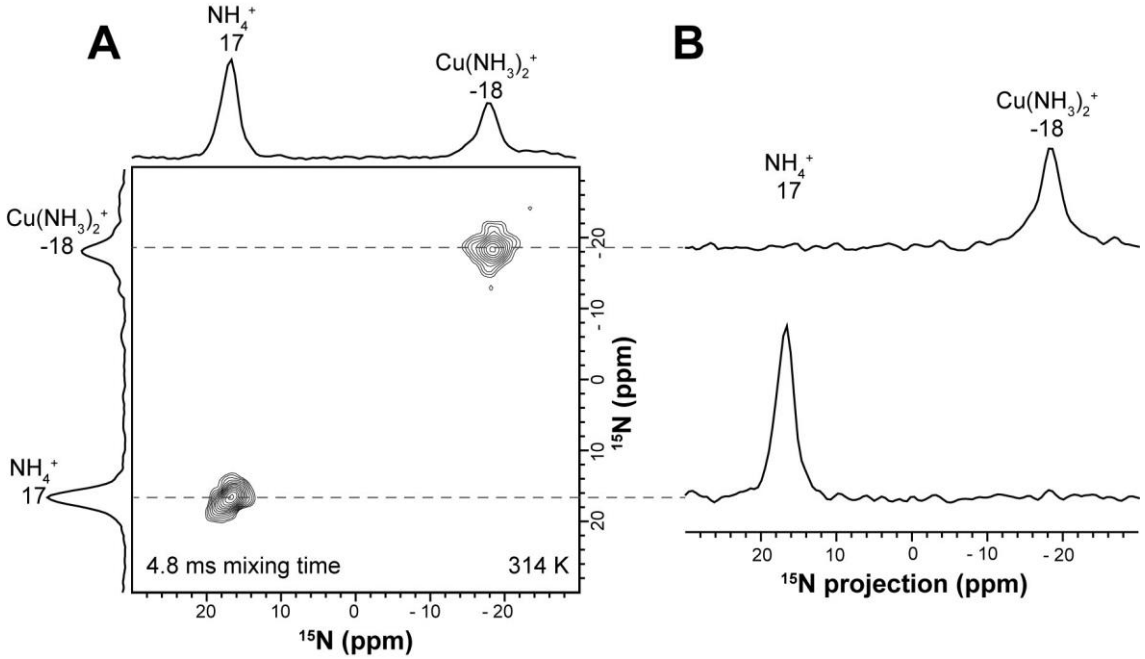

Figure S56. (a) Solid-state 2D ^{15}N EXSY NMR spectrum of 16-h-aged Cu-CHA (Cu/Al = 0.21). The spectrum was acquired at 11.7 T, 314 K, and 12.5 kHz MAS, with a mixing time of 4.8 ms and a recycle delay of 1.0 s. (b) Horizontal projections along the ω_1 axis of the 2D spectrum at –18 ppm (top) and 17 ppm (bottom); the integrated signal intensities were used in the kinetic analyses described in the manuscript.

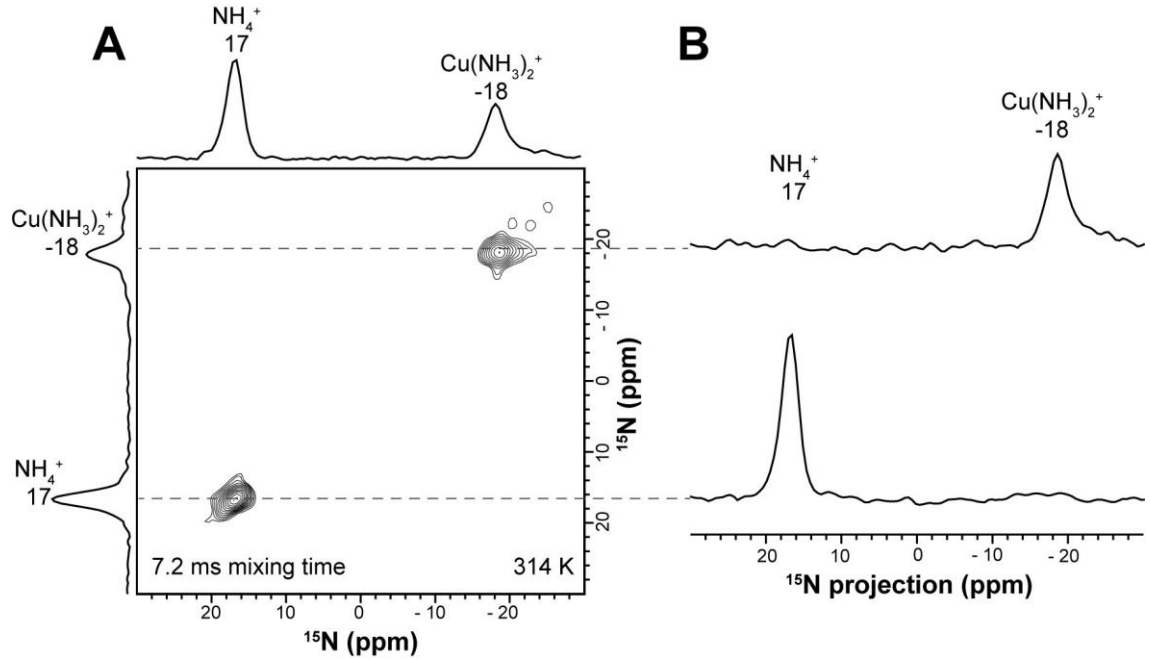

Figure S57. (a) Solid-state 2D ^{15}N EXSY NMR spectrum of 16-h-aged Cu-CHA (Cu/Al = 0.21). The spectrum was acquired at 11.7 T, 314 K, and 12.5 kHz MAS, with a mixing time of 7.2 ms and a recycle delay of 1.0 s. (b) Horizontal projections along the ω_1 axis of the 2D spectrum at –18 ppm (top) and 17 ppm (bottom); the integrated signal intensities were used in the kinetic analyses described in the manuscript.

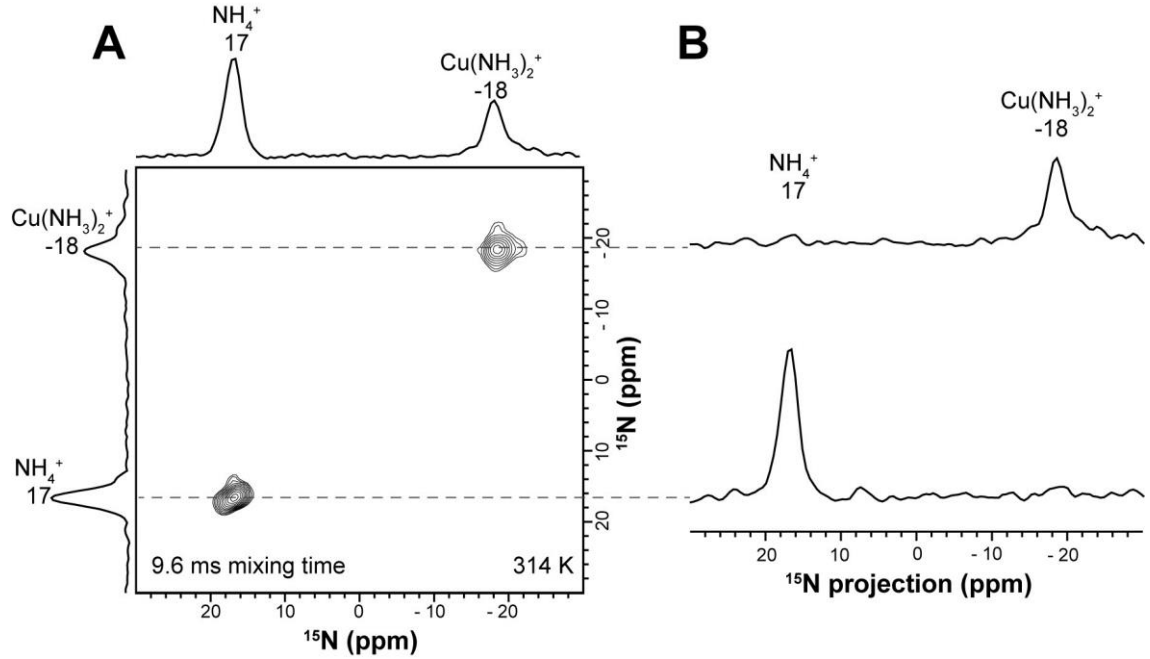

Figure S58. (a) Solid-state 2D ^{15}N EXSY NMR spectrum of 16-h-aged Cu-CHA (Cu/Al = 0.21). The spectrum was acquired at 11.7 T, 314 K, and 12.5 kHz MAS, with a mixing time of 9.6 ms and a recycle delay of 1.0 s. (b) Horizontal projections along the ω_1 axis of the 2D spectrum at –18 ppm (top) and 17 ppm (bottom); the integrated signal intensities were used in the kinetic analyses described in the manuscript.

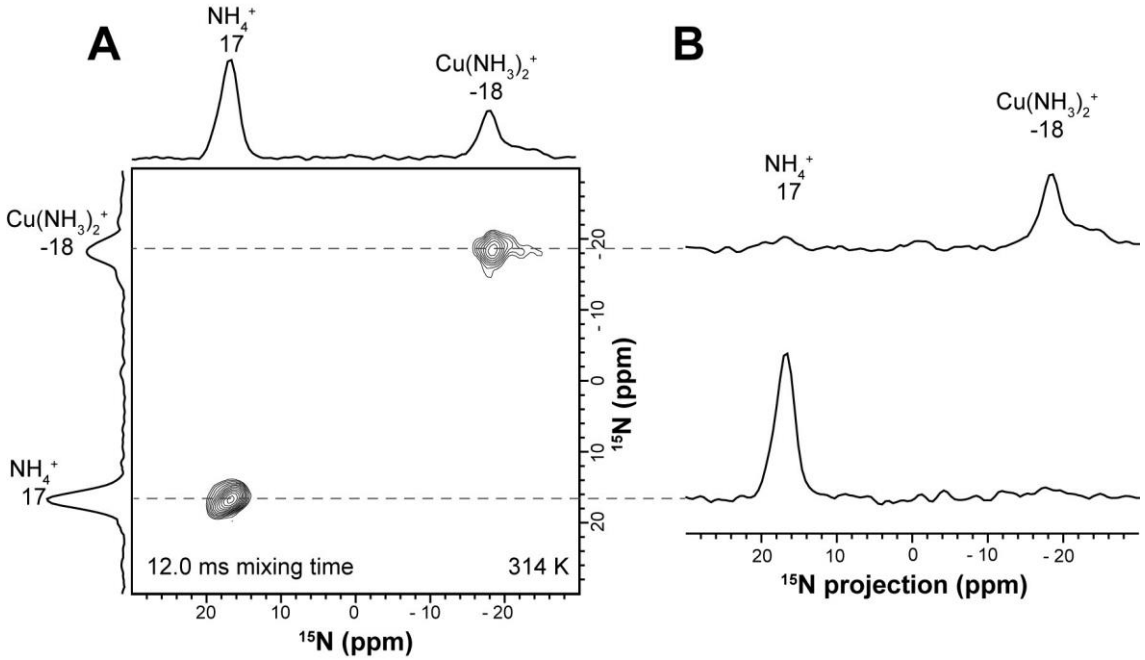

Figure S59. (a) Solid-state 2D ^{15}N EXSY NMR spectrum of 16-h-aged Cu-CHA (Cu/Al = 0.21). The spectrum was acquired at 11.7 T, 314 K, and 12.5 kHz MAS, with a mixing time of 12.0 ms and a recycle delay of 1.0 s. (b) Horizontal projections along the ω_1 axis of the 2D spectrum at –18 ppm (top) and 17 ppm (bottom); the integrated signal intensities were used in the kinetic analyses described in the manuscript.

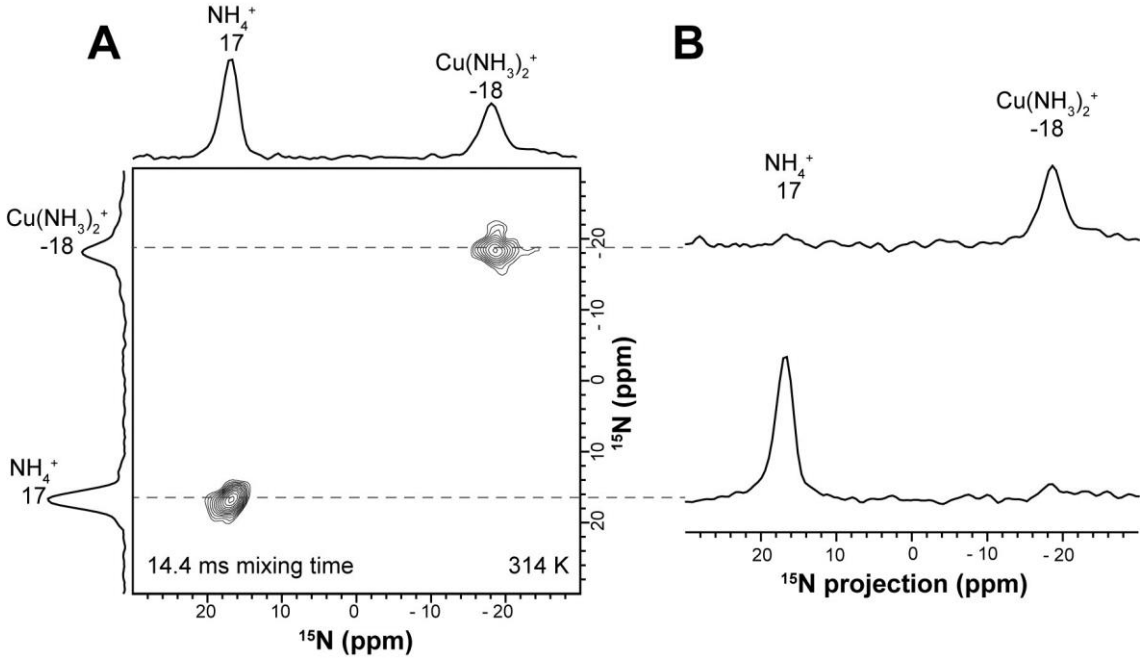

Figure S60. (a) Solid-state 2D ^{15}N EXSY NMR spectrum of 16-h-aged Cu-CHA (Cu/Al = 0.21). The spectrum was acquired at 11.7 T, 314 K, and 12.5 kHz MAS, with a mixing time of 14.4 ms and a recycle delay of 1.0 s. (b) Horizontal projections along the ω_1 axis of the 2D spectrum at –18 ppm (top) and 17 ppm (bottom); the integrated signal intensities were used in the kinetic analyses described in the manuscript.

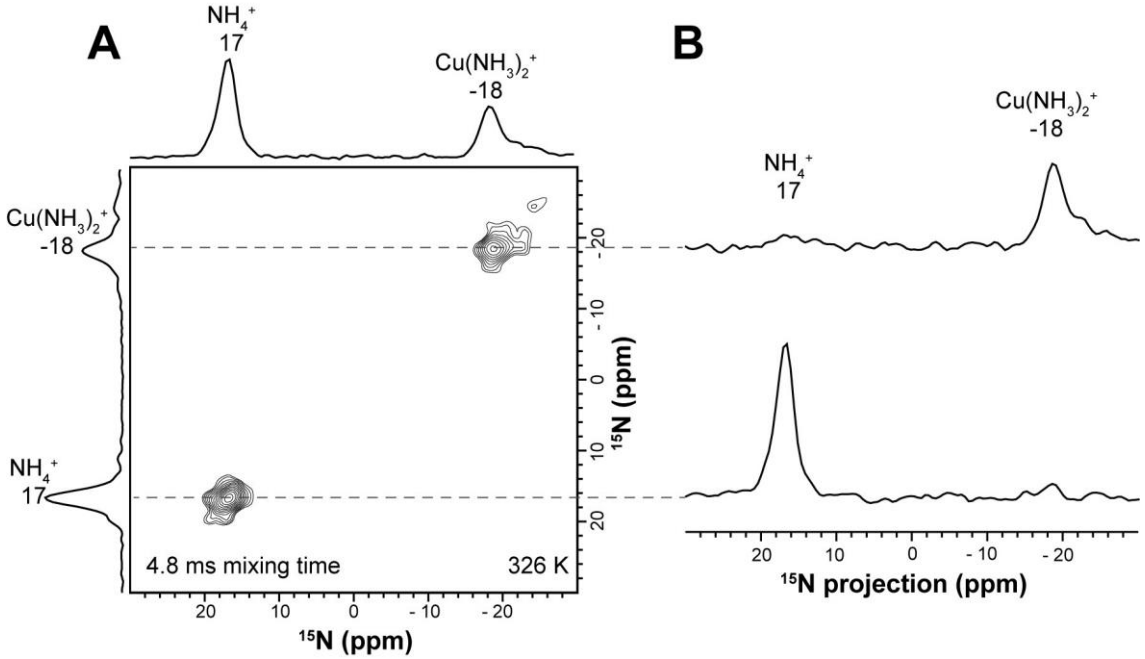

Figure S61. (a) Solid-state 2D ^{15}N EXSY NMR spectrum of 16-h-aged Cu-CHA (Cu/Al = 0.21). The spectrum was acquired at 11.7 T, 326 K, and 12.5 kHz MAS, with a mixing time of 4.8 ms and a recycle delay of 1.0 s. (b) Horizontal projections along the ω_1 axis of the 2D spectrum at –18 ppm (top) and 17 ppm (bottom); the integrated signal intensities were used in the kinetic analyses described in the manuscript.

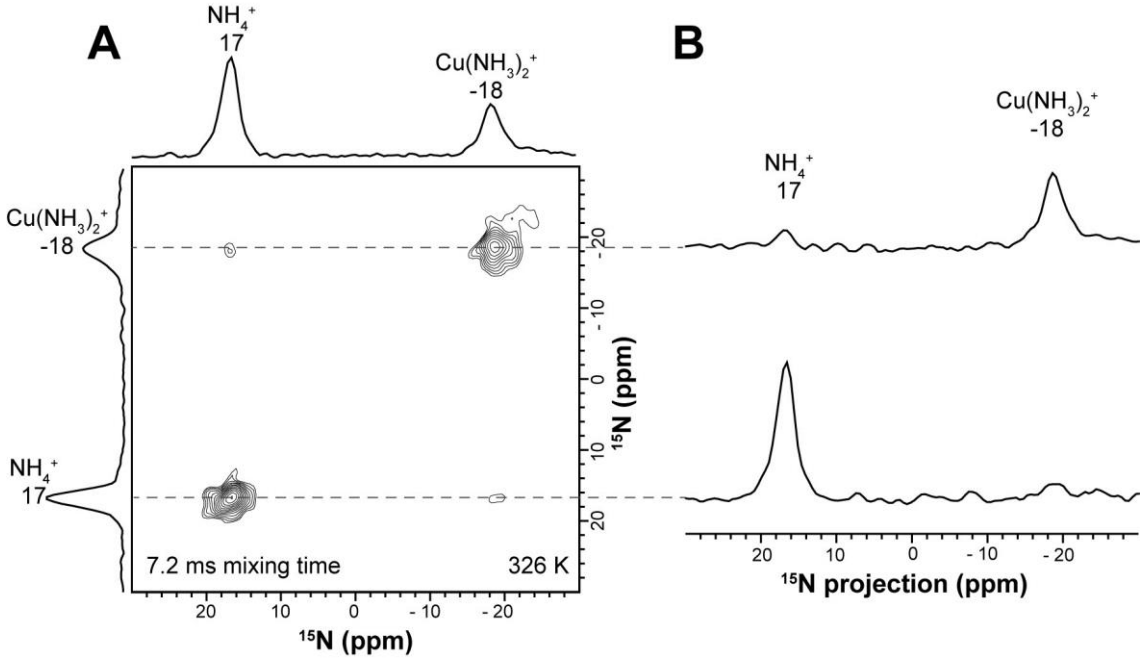

Figure S62. (a) Solid-state 2D ^{15}N EXSY NMR spectrum of 16-h-aged Cu-CHA (Cu/Al = 0.21). The spectrum was acquired at 11.7 T, 326 K, and 12.5 kHz MAS, with a mixing time of 7.2 ms and a recycle delay of 1.0 s. (b) Horizontal projections along the ω_1 axis of the 2D spectrum at –18 ppm (top) and 17 ppm (bottom); the integrated signal intensities were used in the kinetic analyses described in the manuscript.

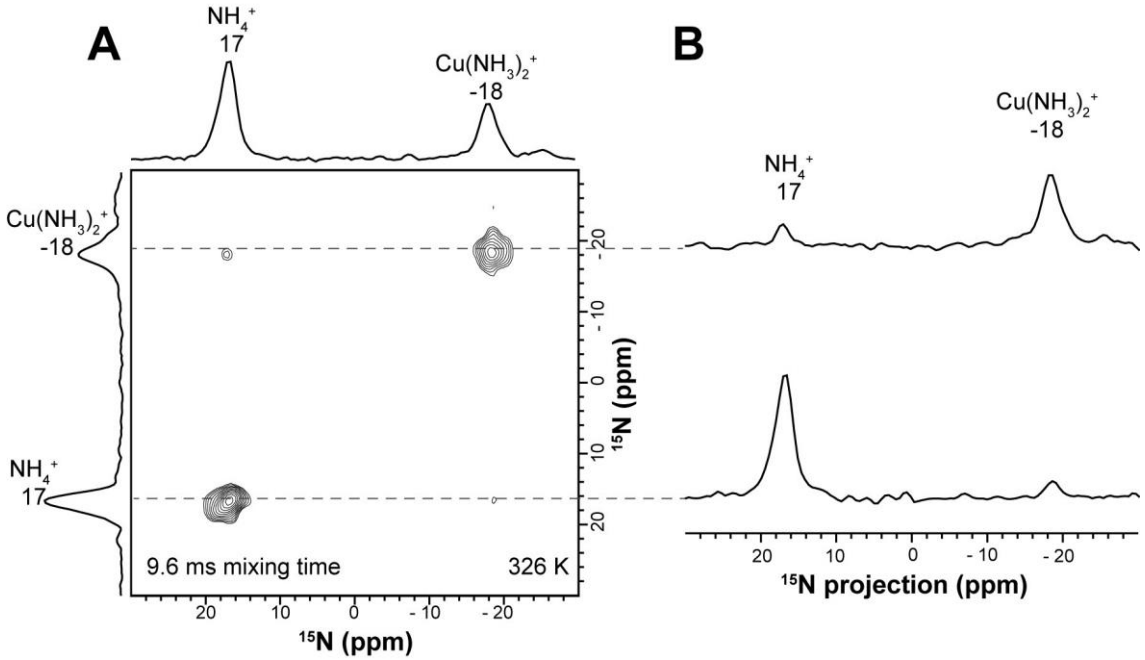

Figure S63. (a) Solid-state 2D ^{15}N EXSY NMR spectrum of 16-h-aged Cu-CHA (Cu/Al = 0.21). The spectrum was acquired at 11.7 T, 326 K, and 12.5 kHz MAS, with a mixing time of 9.6 ms and a recycle delay of 1.0 s. (b) Horizontal projections along the ω_1 axis of the 2D spectrum at –18 ppm (top) and 17 ppm (bottom); the integrated signal intensities were used in the kinetic analyses described in the manuscript.

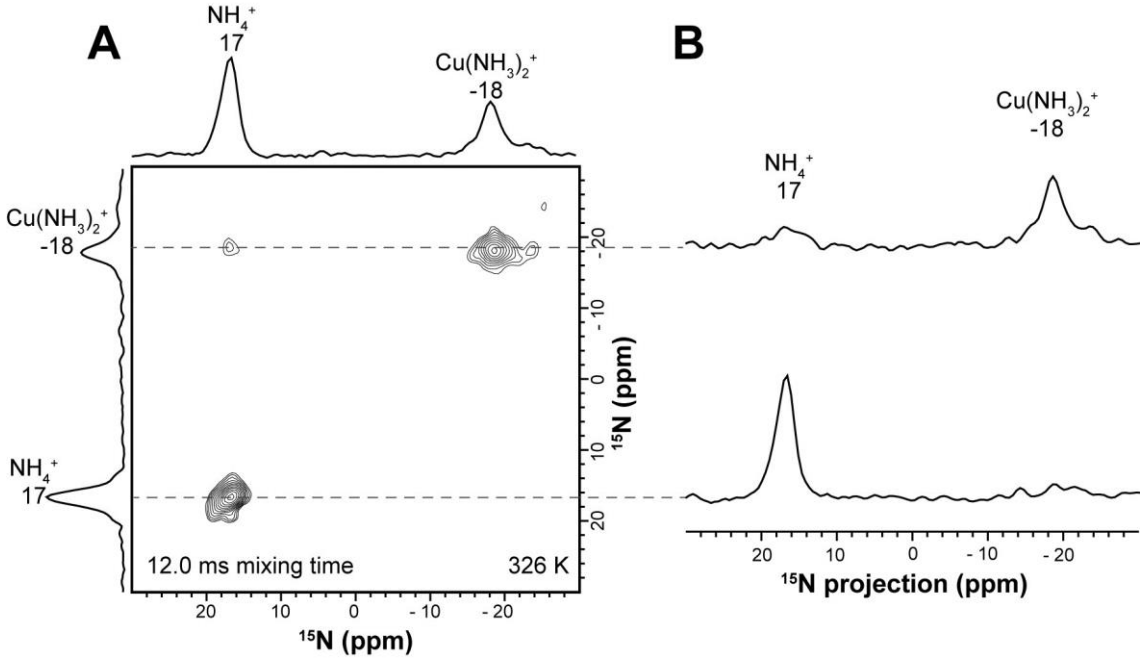

Figure S64. (a) Solid-state 2D ^{15}N EXSY NMR spectrum of 16-h-aged Cu-CHA (Cu/Al = 0.21). The spectrum was acquired at 11.7 T, 326 K, and 12.5 kHz MAS, with a mixing time of 12.0 ms and a recycle delay of 1.0 s. (b) Horizontal projections along the ω_1 axis of the 2D spectrum at –18 ppm (top) and 17 ppm (bottom); the integrated signal intensities were used in the kinetic analyses described in the manuscript.

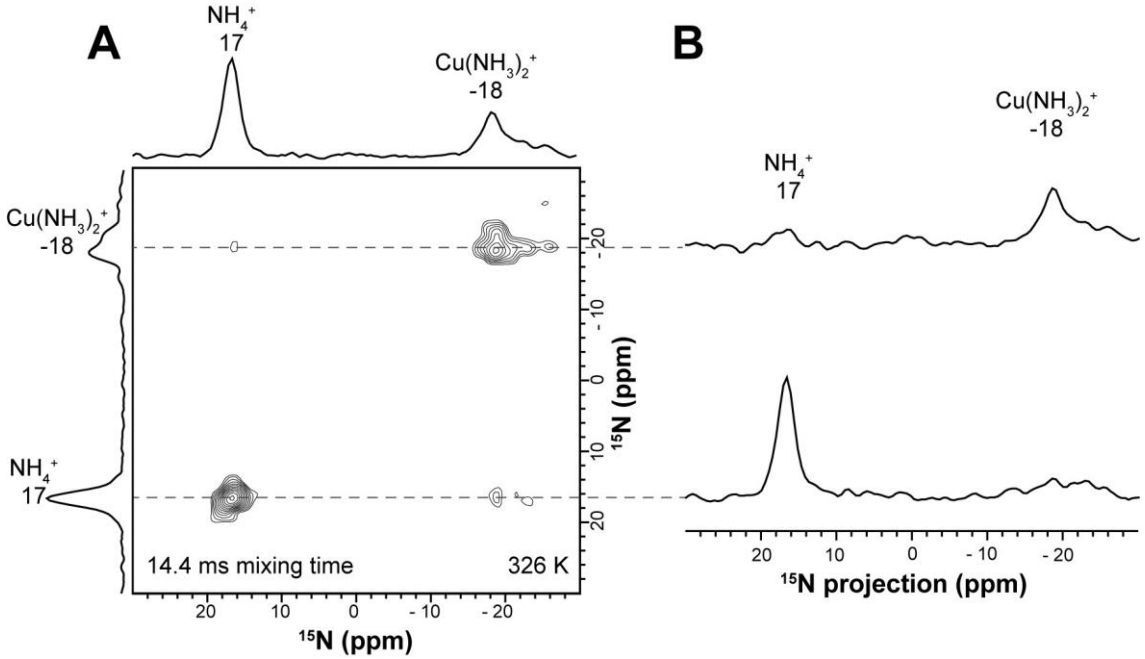

Figure S65. (a) Solid-state 2D ^{15}N EXSY NMR spectrum of 16-h-aged Cu-CHA (Cu/Al = 0.21). The spectrum was acquired at 11.7 T, 326 K, and 12.5 kHz MAS, with a mixing time of 14.4 ms and a recycle delay of 1.0 s. (b) Horizontal projections along the ω_1 axis of the 2D spectrum at –18 ppm (top) and 17 ppm (bottom); the integrated signal intensities were used in the kinetic analyses described in the manuscript.

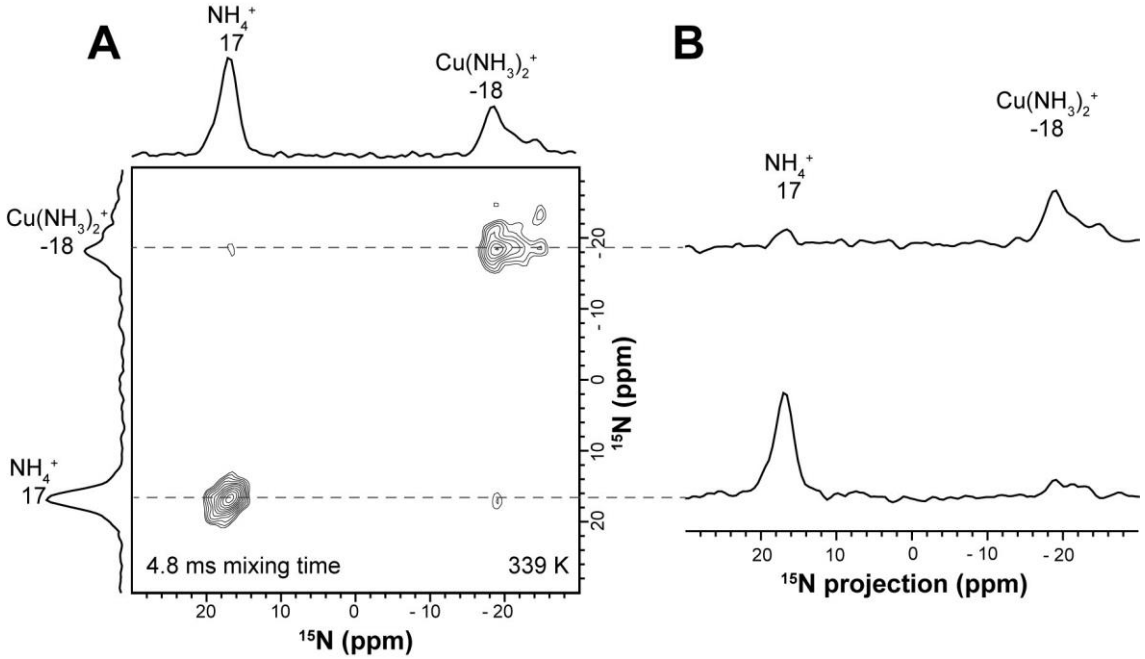

Figure S66. (a) Solid-state 2D ^{15}N EXSY NMR spectrum of 16-h-aged Cu-CHA (Cu/Al = 0.21). The spectrum was acquired at 11.7 T, 339 K, and 12.5 kHz MAS, with a mixing time of 4.8 ms and a recycle delay of 1.0 s. (b) Horizontal projections along the ω_1 axis of the 2D spectrum at –18 ppm (top) and 17 ppm (bottom); the integrated signal intensities were used in the kinetic analyses described in the manuscript.

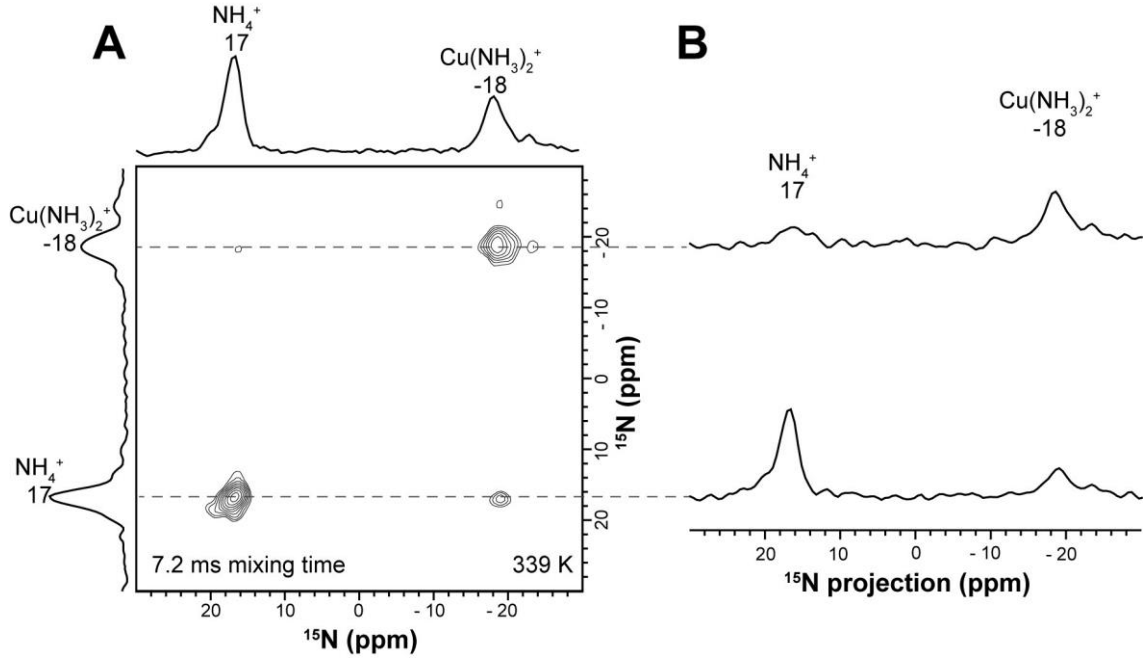

Figure S67. (a) Solid-state 2D ^{15}N EXSY NMR spectrum of 16-h-aged Cu-CHA (Cu/Al = 0.21). The spectrum was acquired at 11.7 T, 339 K, and 12.5 kHz MAS, with a mixing time of 7.2 ms and a recycle delay of 1.0 s. (b) Horizontal projections along the ω_1 axis of the 2D spectrum at –18 ppm (top) and 17 ppm (bottom); the integrated signal intensities were used in the kinetic analyses described in the manuscript.

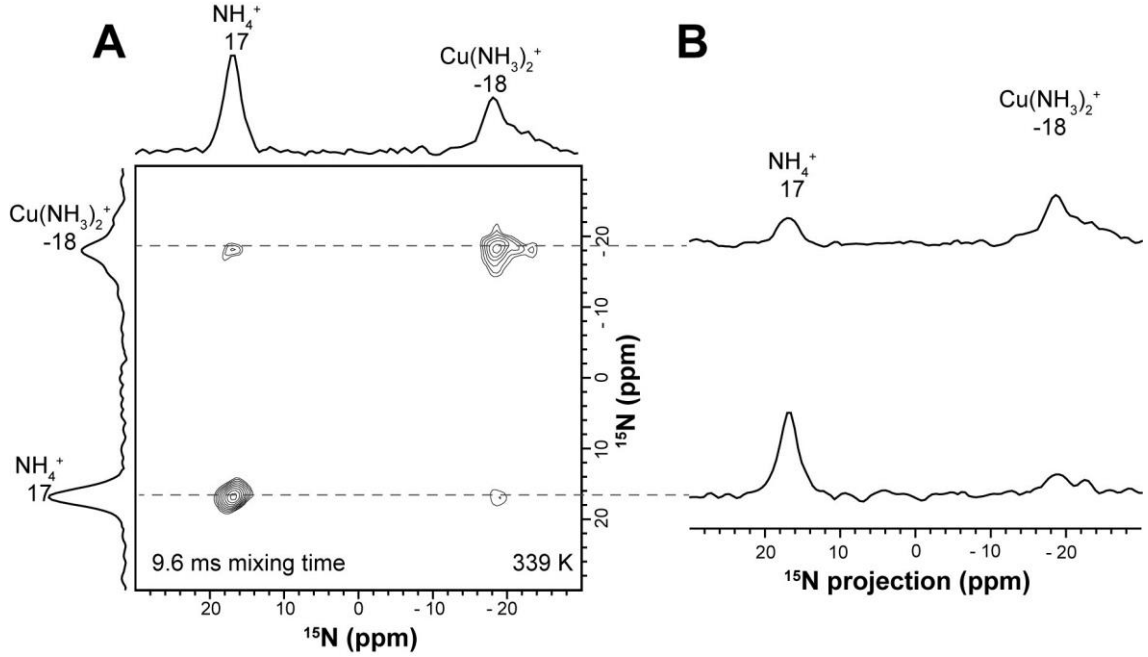

Figure S68. (a) Solid-state 2D ^{15}N EXSY NMR spectrum of 16-h-aged Cu-CHA (Cu/Al = 0.21). The spectrum was acquired at 11.7 T, 339 K, and 12.5 kHz MAS, with a mixing time of 9.6 ms and a recycle delay of 1.0 s. (b) Horizontal projections along the ω_1 axis of the 2D spectrum at –18 ppm (top) and 17 ppm (bottom); the integrated signal intensities were used in the kinetic analyses described in the manuscript.

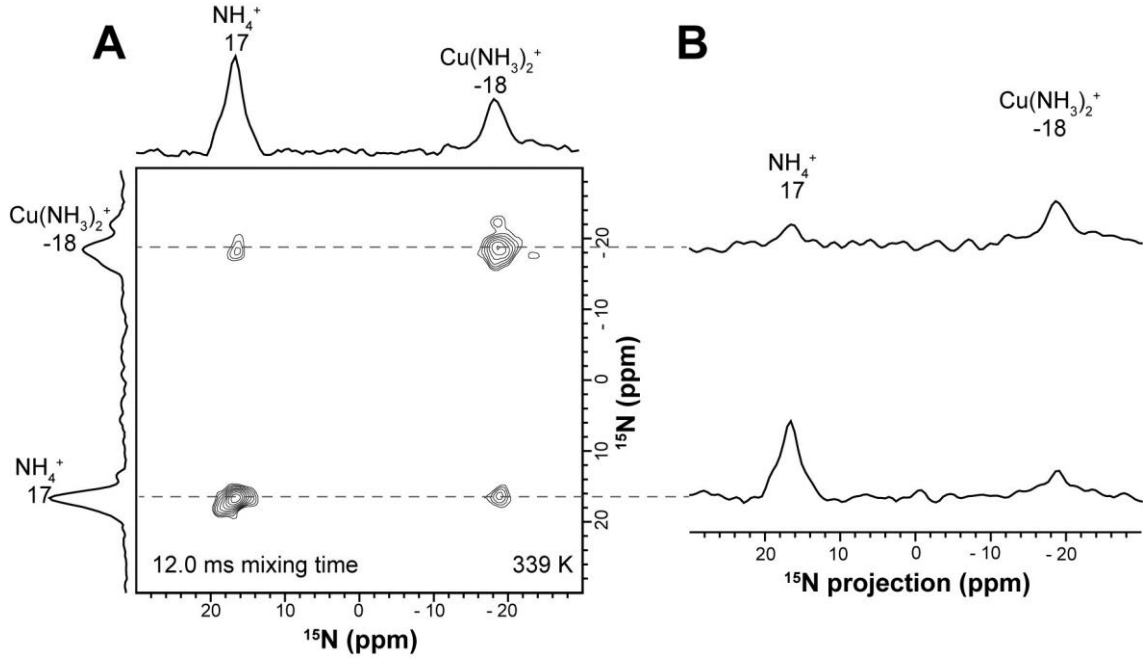

Figure S69. (a) Solid-state 2D ^{15}N EXSY NMR spectrum of 16-h-aged Cu-CHA (Cu/Al = 0.21). The spectrum was acquired at 11.7 T, 339 K, and 12.5 kHz MAS, with a mixing time of 12.0 ms and a recycle delay of 1.0 s. (b) Horizontal projections along the ω_1 axis of the 2D spectrum at –18 ppm (top) and 17 ppm (bottom); the integrated signal intensities were used in the kinetic analyses described in the manuscript.

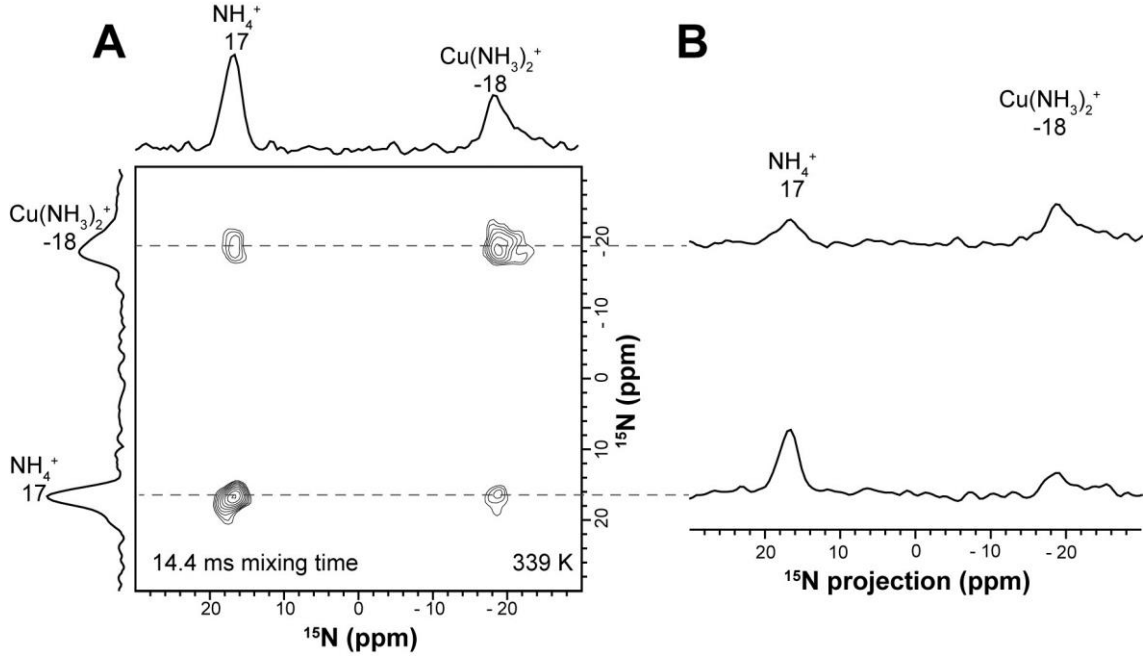

Figure S70. (a) Solid-state 2D ^{15}N EXSY NMR spectrum of 16-h-aged Cu-CHA (Cu/Al = 0.21). The spectrum was acquired at 11.7 T, 339 K, and 12.5 kHz MAS, with a mixing time of 14.4 ms and a recycle delay of 1.0 s. (b) Horizontal projections along the ω_1 axis of the 2D spectrum at –18 ppm (top) and 17 ppm (bottom); the integrated signal intensities were used in the kinetic analyses described in the manuscript.

The integrated intensities from the 1D projections of the 2D ^{15}N EXSY NMR spectra were fit to a site-exchange model following from analyses in Ernst, Bodenhausen, and Wokaun as described in the main text.[68] Specifically, for each set of five mixing times for a given Cu-CHA material and temperature, k_{AB}, k_{BA}, x_A, x_B, and M_0 were varied to minimize the residual between the experimental integrations of the 1D projections of the 2D ^{15}N EXSY NMR spectra and the intensity values produced by the following three equations:

$$I_{AA}(\tau_m) = \frac{1}{2}\left[\left(1 - \frac{\delta}{D}\right) + \left(1 + \frac{\delta}{D}\right)e^{-R_c\tau_m}\right]e^{-R_L\tau_m}M_{A0}$$

$$I_{AA}(\tau_m) = \frac{1}{2}\left[\left(1 + \frac{\delta}{D}\right) + \left(1 - \frac{\delta}{D}\right)e^{-R_c\tau_m}\right]e^{-R_L\tau_m}M_{B0}$$

$$I_{AB}(\tau_m) = I_{BA}(\tau_m) = \frac{1}{2}\left[1 - e^{-R_c\tau_m}\right]e^{-R_L\tau_m}\bar{M}$$

Given the following relationships:

$$R_c = 2D$$

$$R_D = \sigma - D$$

$$\bar{M} = M_{B0}\frac{k_{AB}}{D} = M_{A0}\frac{k_{BA}}{D}$$

$$M_{A0} = x_A M_0$$

$$M_{B0} = x_B M_0$$

$$\sigma = \frac{1}{2}(k_{BA} + k_{AB} + R_1^A + R_1^B)$$

$$\delta = \frac{1}{2}(k_{BA} - k_{AB} + R_1^A - R_1^B)$$

$$D = (\delta^2 + k_{BA}k_{AB})^{0.5}$$

In these equations, A is used as shorthand for ^{15}N in NH_4^+ chemical environments and B is used as shorthand for ^{15}N in $[Cu(NH_3)_2]^+$ environments. The variables k_{BA} and k_{AB} represent

apparent rate coefficients for the exchange to B from A and A from B, respectively, and x_A and x_B represent the proportion of magnetization in A and B chemical environments. R_1^A and R_1^B are spin-lattice relaxation coefficients for ^{15}N nuclei in NH_4^+ and $[Cu(NH_3)_2]^+$ chemical environments and were calculated from ^{15}N saturation recovery NMR analyses (Table S10). M_0 is the overall magnetization of the system. Given that this is a two-component system with the two magnetization populations at an observed equilibrium, the following two constraints can be added:

$$x_B = 1 - x_A$$

$$K_{eq} = \frac{k_{BA}}{k_{AB}} = \frac{x_B}{x_A}$$

Thus, only three variables x_A, k_{BA}, and M_0 are left to optimize to minimize the residuals between the model and 15 data points at a given temperature for a material. For the five mixing times measured, I_{AA}, I_{BB}, and I_{AB} were all be fit. Since $I_{AB} = I_{BA}$, the average of these two measured values was used for fitting. The magnitudes of I_{AB} and I_{BA} were generally similar, within the uncertainty of the measured results. These fits are shown in Figure 6 of the main text for fresh Cu-CHA, and as Figures S71 and S72 for 4-h-aged and 16-h-aged Cu-CHA. The values of k_{AB} and k_{BA} for all fits are shown in Table S11.

Table S10. Temperature-dependent measured ^{15}N T_1 values

	314 K		326 K		339 K	
	$^{15}NH_4^+$	$[Cu(^{15}NH_3)]^+$	$^{15}NH_4^+$	$[Cu(^{15}NH_3)]^+$	$^{15}NH_4^+$	$[Cu(^{15}NH_3)]^+$
Fresh	0.65 s	0.69 s	0.55 s	0.56 s	0.40 s	0.50 s
4-h-aged	1.05 s	0.98 s	0.67 s	0.75 s	0.38 s	0.33 s
16-h-aged	0.38 s	0.29 s	0.23 s	0.32 s	0.11 s	0.11 s

Table S11. Temperature-dependent apparent rate coefficients for ^{15}N exchange*

	314 K		326 K		339 K	
	k_{AB} (s^{-1})	k_{BA} (s^{-1})	k_{AB} (s^{-1})	k_{BA} (s^{-1})	k_{AB} (s^{-1})	k_{BA} (s^{-1})
Fresh	16(2)	3.1(4)	41(3)	8.0(5)	80(5)	20(1)
4-h-aged	15(3)	7(1)	33(5)	15(2)	62(7)	33(3)
16-h-aged	12(1)	9(1)	23(2)	17(1)	44(4)	35(3)

*Uncertainties shown in parentheses represent standard deviations of parameters based on a Monte Carlo-based error propagation from the uncertainties in the 2D ^{15}N EXSY NMR results.

The values of k_{AB} and k_{BA} for different temperatures for a given material can be easily fit to the linearized Eyring equation, given below, in order to extract activation enthalpies and entropies for the exchange process.[69]

$$\ln\left(\frac{k}{T}\right) = \frac{-\Delta H^{\ddagger}}{R}\frac{1}{T} + \ln\left(\frac{\kappa k_B}{h}\right) + \frac{\Delta S^{\ddagger}}{R}$$

In this equation, $\Delta H^{\ddagger}$ and $\Delta S^{\ddagger}$ are the changes in enthalpy and entropy of activation, R is the ideal gas constant, k_B is Boltzmann's constant, h is the Planck constant, and κ is the transmission coefficient (assumed to be 1). $\Delta H^{\ddagger}$ and $\Delta S^{\ddagger}$ were varied to minimize the residuals between the fitted linearized Eyring equation and the three k_{AB} or k_{BA} values calculated for each material. This fit is shown in Figure 6D for fresh Cu-CHA, and in Figures S71D and S72D for 4-h-aged and 16-h-aged Cu-CHA. All fits are linear, indicating that this procedure for calculating these parameters from the ^{15}N exchange NMR spectra is robust.

To propagate uncertainty through this system of equations, a Monte Carlo error analysis was performed. The uncertainty shown on plots in Figures 6A-C, S71A-C, and S72A-C are proportional to the inverse of the signal-to-noise of the ^{15}N NMR signals from the 1D projections of the 2D ^{15}N EXSY NMR experiments. While the inverse of the signal-to-noise is not a perfect measure of uncertainty, it is a decent proxy since the position and linewidth of all fitted lineshapes was kept constant within a dataset across different mixing times. To propagate these uncertainties through to values of k_{AB}, k_{BA}, $\Delta H^{\ddagger}$ and $\Delta S^{\ddagger}$, 1000 fits of the intensity data

were performed. In each fit, each intensity value was randomly perturbed by Gaussian noise, with the mean of the Gaussian distributions for each intensity data point being the observed value, and the standard deviation set as the uncertainty based on the signal-to-noise of the intensity data point. Thus, the influences of the uncertainties of each individual data point on the fitted parameters could be assessed. The values of k_{AB} and k_{BA} reported in Table S11 and the values of $\Delta H^{\ddagger}$ and $\Delta S^{\ddagger}$ reported in Table 1 are the mean values calculated from these Monte Carlo error analyses, and the uncertainties are the observed sample standard deviations from these Monte Carlo error analyses. This random perturbation method indicates that the fitted parameters are robust with relatively little uncertainty. While there are other sources of uncertainty not accounted for in these analyses—specifically the baseline of the fits and hardware variation over the course of and between experiments—these uncertainties are anticipated to be random and not bias the overall fits, and also to be smaller in magnitude than the uncertainty due to the noisiness of the acquired data.

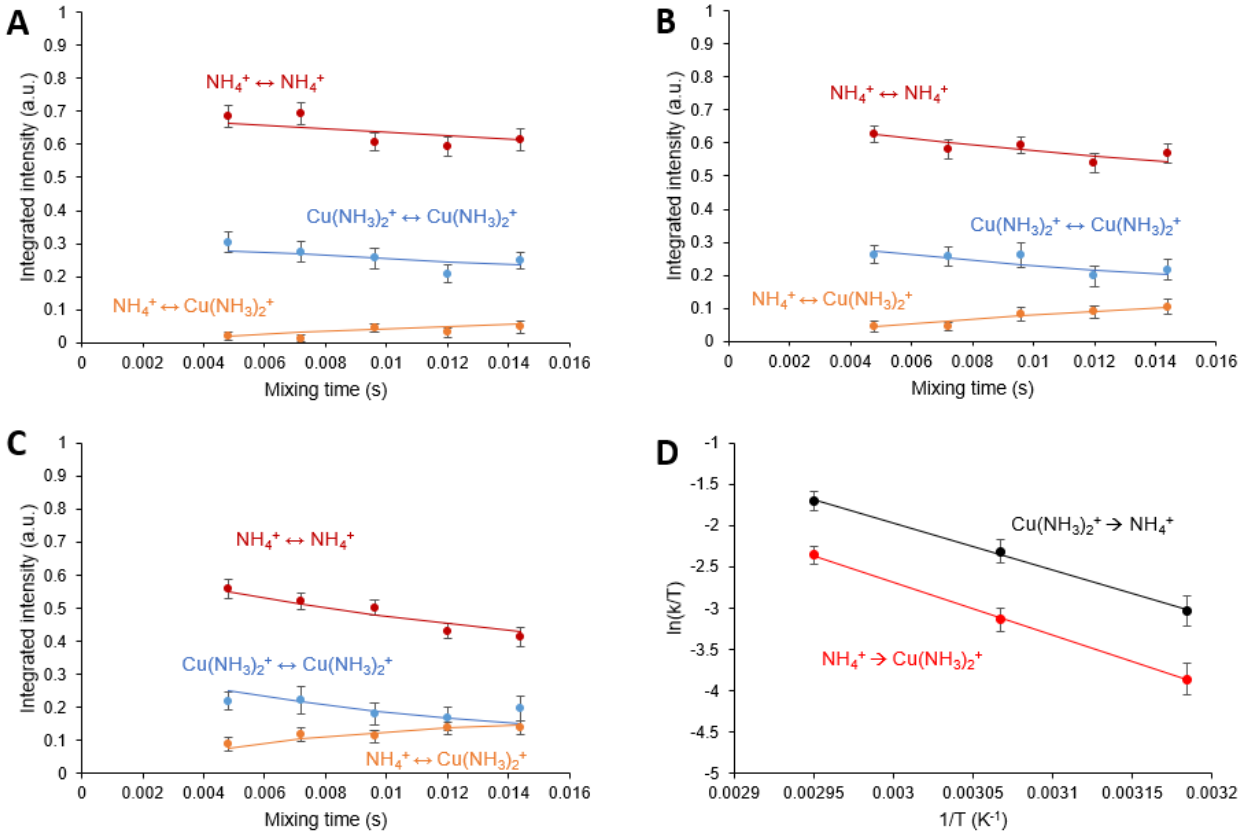

Figure S71. (A,B,C) Evolution of on-diagonal and off-diagonal 2D ^{15}N exchange NMR signal intensity at different mixing times for experiments performed at (A) 314 K, (B) 326 K, and (C) 339 K on 4-h-aged Cu-CHA after $^{15}NH_3$ adsorption at 120 ºC and subsequent reduction in ^{15}NO at 300 ºC. The fitted lines model the exchange process between NH_3 adsorbed as NH_4^+ on the zeolite framework and as part of a $[Cu(NH_3)_2]^+$ complex. (D) Eyring plot of the temperature-dependent exchange rate coefficients extracted from the models in A,B, and C. The error bars in A-C are proportional to the inverse of the signal-to-noise for each integrated signal. The error bars in D are standard deviations generated through a Monte Carlo error propagation procedure from the integrated intensities of the 1D projections of 2D ^{15}N EXSY NMR spectra.

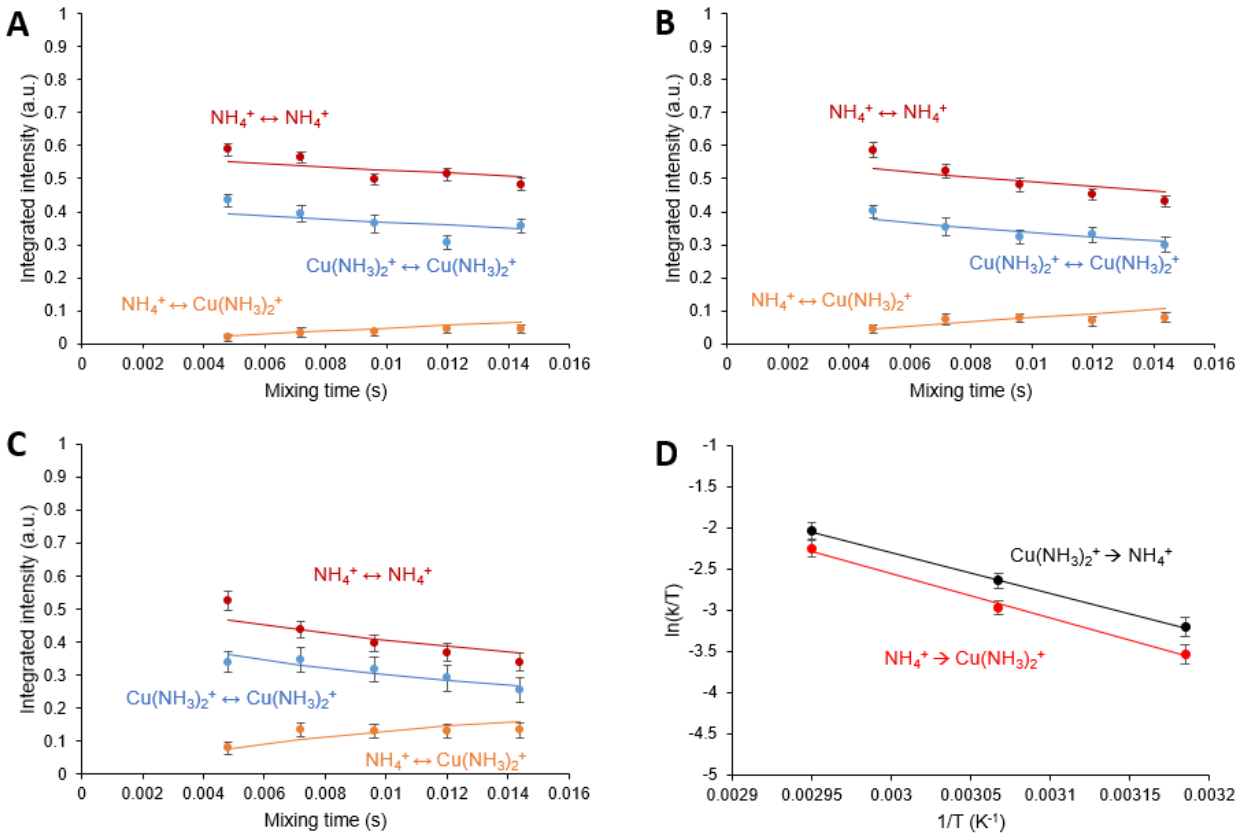

Figure S72. (A,B,C) Evolution of on-diagonal and off-diagonal 2D ^{15}N exchange NMR signal intensity at different mixing times for experiments performed at (A) 314 K, (B) 326 K, and (C) 339 K on 16-h-aged Cu-CHA after $^{15}NH_3$ adsorption at 120 °C and subsequent reduction in ^{15}NO at 300 °C. The fitted lines model the exchange process between NH_3 adsorbed as NH_4^+ on the zeolite framework and as part of a $[Cu(NH_3)_2]^+$ complex. (D) Eyring plot of the temperature-dependent exchange rate coefficients extracted from the models in A,B, and C. The error bars in A-C are proportional to the inverse of the signal-to-noise for each integrated signal. The error bars in D are standard deviations generated through a Monte Carlo error propagation procedure from the integrated intensities of the 1D projections of 2D ^{15}N EXSY NMR spectra.

Analyses of kinetic data for reactions in confined environments like zeolites commonly show a compensation effect between apparent activation enthalpies and activation entropies for reactions over similar catalysts, where a change in activation enthalpy is met with a proportional change in activation entropy.[88] To investigate this effect on the ^{15}N exchange reaction, calculated $\Delta H^{\ddagger}$ and $\Delta S^{\ddagger}$ values for all Cu-CHA materials are plotted in Figure S73. For both directions of the site exchange reaction, the ($\Delta H^{\ddagger}$, $\Delta S^{\ddagger}$) pairs are highly linear across

the different materials. This is consistent with a compensation effect and indicates that despite the changes in apparent activation parameters the mechanism by which the exchange reaction occurs is similar for all three samples, despite the significant dealumination in the high-temperature hydrothermally treated Cu-CHA. The uncertainty bars shown on all data points also visually demonstrate that the apparent activation enthalpies and entropies for fresh Cu-CHA and 16-h-aged Cu-CHA are significantly different beyond a high degree of uncertainty.

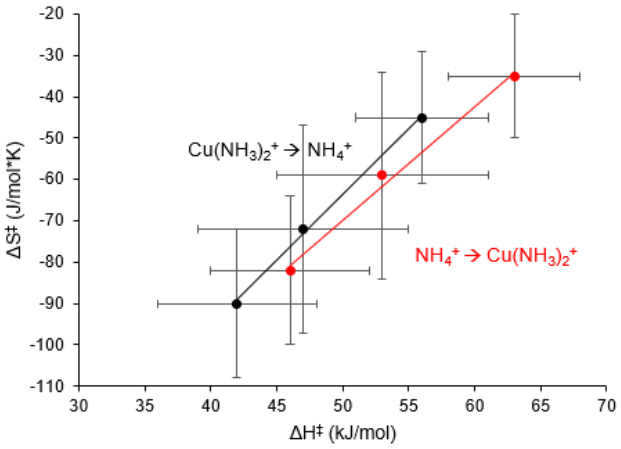

Figure S73. Calculated apparent activation enthalpies and activation entropies from kinetic analyses of 2D ^{15}N exchange NMR spectra for all samples. Lines represent linear fits of all ($\Delta H^{\ddagger}$, $\Delta S^{\ddagger}$) pairs for exchange from $[Cu(NH_3)_2]^+$ to NH_4^+ (black) or NH_4^+ to $[Cu(NH_3)_2]^+$ (red). Uncertainty bars are standard deviations for parameters calculated by Monte Carlo error propagation.

References

(1) Kaiser, S. K.; Chen, Z.; Faust Akl, D.; Mitchell, S.; Pérez-Ramírez, J. Single-Atom Catalysts across the Periodic Table. *Chemical Reviews* **2020**, *120* (21), 11703–11809. https://doi.org/10.1021/ACS.CHEMREV.0C00576.

(2) Qin, R.; Liu, K.; Wu, Q.; Zheng, N. Surface Coordination Chemistry of Atomically Dispersed Metal Catalysts. *Chemical Reviews* **2020**, *120* (21), 11810–11899. https://doi.org/10.1021/ACS.CHEMREV.0C00094.

(3) Xu, L.; Papanikolaou, K. G.; Lechner, B. A. J.; Je, L.; Somorjai, G. A.; Salmeron, M.; Mavrikakis, M. Formation of Active Sites on Transition Metals through Reaction-Driven Migration of Surface Atoms. *Science* **2023**, *380* (6640), 70–76. https://doi.org/10.1126/science.add0089.

(4) Babucci, M.; Guntida, A.; Gates, B. C. Atomically Dispersed Metals on Well-Defined Supports Including Zeolites and Metal-Organic Frameworks: Structure, Bonding, Reactivity, and Catalysis. *Chemical Reviews* **2020**, *120* (21), 11956–11985. https://doi.org/10.1021/ACS.CHEMREV.0C00864.

(5) Liu, L.; Corma, A. Confining Isolated Atoms and Clusters in Crystalline Porous Materials for Catalysis. *Nature Reviews Materials* **2021**, *6*, 244-263. https://doi.org/10.1038/s41578-020-00250-3.

(6) Wang, H.; Wang, L.; Xiao, F. S. Metal@zeolite Hybrid Materials for Catalysis. *ACS Central Science* **2020**, *6* (10), 1685–1697. https://doi.org/10.1021/ACSCENTSCI.0C01130.

(7) Weitkamp, J. Catalytic Hydrocracking—Mechanisms and Versatility of the Process. *ChemCatChem* **2012**, *4* (3), 292–306. https://doi.org/10.1002/CCTC.201100315.

(8) Ravi, M.; Sushkevich, V. L.; Knorpp, A. J.; Newton, M. A.; Palagin, D.; Pinar, A. B.; Ranocchiari, M.; van Bokhoven, J. A. Misconceptions and Challenges in Methane-to-Methanol over Transition-Metal-Exchanged Zeolites. *Nat. Catal.* **2019**, *2* (6), 485–494. https://doi.org/10.1038/s41929-019-0273-z.

(9) Ding, W.; Li, S.; Meitzner, G. D.; Iglesia, E. Methane Conversion to Aromatics on Mo/H-ZSM5: Structure of Molybdenum Species in Working Catalysts. *J. Phys. Chem. B* **2001**, *105* (2), 506–513. https://doi.org/10.1021/jp0030692.

(10) Tomkins, P.; Ranocchiari, M.; van Bokhoven, J. A. Direct Conversion of Methane to Methanol under Mild Conditions over Cu-Zeolites and Beyond. *Acc. Chem. Res.* **2017**, *50* (2), 418–425. https://doi.org/10.1021/acs.accounts.6b00534.

(11) R. Ismagilov, Z.; V. Matus, E.; T. Tsikoza, L. Direct Conversion of Methane on Mo /ZSM-5 Catalysts to Produce Benzene and Hydrogen : Achievements and Perspectives. *Energy & Environmental Science* **2008**, *1* (5), 526–541. https://doi.org/10.1039/B810981H.

(12) Kwak, J. H.; Tonkyn, R. G.; Kim, D. H.; Szanyi, J.; Peden, C. H. F. Excellent Activity and Selectivity of Cu-SSZ-13 in the Selective Catalytic Reduction of NO_x with NH_3. *Journal of Catalysis* **2010**, *275* (2), 187–190. https://doi.org/10.1016/j.jcat.2010.07.031.

(13) Fickel, D. W.; D'Addio, E.; Lauterbach, J. A.; Lobo, R. F. The Ammonia Selective Catalytic Reduction Activity of Copper-Exchanged Small-Pore Zeolites. *Applied Catalysis B: Environmental* **2011**, *102* (3–4), 441–448. https://doi.org/10.1016/j.apcatb.2010.12.022.
(14) Bull, I.; Xue, W.-M.; Burk, P.; Boorse, S.; Jaglowski, W. M.; Koermer, G. S.; Moini, A.; Patchett, J. A.; Dettling, J. C.; Caudle, M. T. Copper CHA Zeolite Catalysts. US7601662B2, 2009.
(15) Gao, F.; Kwak, J. H.; Szanyi, J.; Peden, C. H. F. Current Understanding of Cu-Exchanged Chabazite Molecular Sieves for Use as Commercial Diesel Engine $DeNO_x$ Catalysts. *Topics in Catalysis* **2013**, *56*, 1441–1459. https://doi.org/10.1007/s11244-013-0145-8.
(16) Bates, S. A.; Verma, A. A.; Paolucci, C.; Parekh, A. A.; Anggara, T.; Yezerets, A.; Schneider, W. F.; Miller, J. T.; Delgass, W. N.; Ribeiro, F. H. Identification of the Active Cu Site in Standard Selective Catalytic Reduction with Ammonia on Cu-SSZ-13. *Journal of Catalysis* **2014**, *312*, 87–97. https://doi.org/10.1016/j.jcat.2014.01.004.
(17) Kwak, J. H.; Zhu, H.; Lee, J. H.; Peden, C. H. F.; Szanyi, J. Two Different Cationic Positions in Cu-SSZ-13? *Chemical Communications* **2012**, *48* (39), 4758–4760. https://doi.org/10.1039/c2cc31184d.
(18) Bruzzese, P. C.; Salvadori, E.; Civalleri, B.; Jäger, S.; Hartmann, M.; Pöppl, A.; Chiesa, M. The Structure of Monomeric Hydroxo-Cu^{II} Species in Cu-CHA. A Quantitative Assessment. *Journal of the American Chemical Society* **2022**, *144* (29), 13079–13083. https://doi.org/10.1021/JACS.2C06037.
(19) Fickel, D. W.; Lobo, R. F. Copper Coordination in Cu-SSZ-13 and Cu-SSZ-16 Investigated by Variable-Temperature XRD. *Journal of Physical Chemistry C* **2010**, *114* (3), 1633–1640. https://doi.org/10.1021/jp9105025.
(20) Godiksen, A.; Stappen, F. N.; Vennestrøm, P. N. R.; Giordanino, F.; Rasmussen, S. B.; Lundegaard, L. F.; Mossin, S. Coordination Environment of Copper Sites in Cu-CHA Zeolite Investigated by Electron Paramagnetic Resonance. *Journal of Physical Chemistry C* **2014**, *118* (40), 23126–23138. https://doi.org/10.1021/jp5065616.
(21) Shih, A. J.; González, J. M.; Khurana, I.; Pérez Ramírez, L.; Peña, A.; Kumar, A.; Villa, A. L. Influence of ZCuOH, Z_2Cu, and Extraframework Cu_xO_y Species in Cu-SSZ-13 on N_2O Formation during the Selective Catalytic Reduction of NO_x with NH_3. *ACS Catalysis* **2021**, *11*, 10362–10376. https://doi.org/10.1021/acscatal.1c01871.
(22) Li, H.; Paolucci, C.; Khurana, I.; Wilcox, L. N.; Albarracin-Caballero, J. D.; Shih, A. J.; Ribeiro, F. H.; Gounder, R.; Schneider, W. F. Consequences of Exchange-Site Heterogeneity and Dynamics on the UV-Visible Spectrum of Cu-Exchanged SSZ-13. **2019**. https://doi.org/10.1039/c8sc05056b.
(23) Godiksen, A.; Isaksen, O. L.; Rasmussen, S. B.; Vennestrøm, P. N. R.; Ossin, S. Site-Specific Reactivity of Copper Chabazite Zeolites with Nitric Oxide, Ammonia, and

Oxygen. *ChemCatChem* **2017**, *10* (2), 366–370. https://doi.org/10.1002/cctc.201701357.

(24) Gao, F.; Walter, E. D.; Karp, E. M.; Luo, J.; Tonkyn, R. G.; Kwak, J. H.; Szanyi, J.; Peden, C. H. F. Structure-Activity Relationships in NH3-SCR over Cu-SSZ-13 as Probed by Reaction Kinetics and EPR Studies. *Journal of Catalysis* **2013**, *300*, 20–29. https://doi.org/10.1016/j.jcat.2012.12.020.

(25) Paolucci, C.; Parekh, A. A.; Khurana, I.; Di Iorio, J. R.; Li, H.; Albarracin Caballero, J. D.; Shih, A. J.; Anggara, T.; Delgass, W. N.; Miller, J. T.; Ribeiro, F. H.; Gounder, R.; Schneider, W. F. Catalysis in a Cage: Condition-Dependent Speciation and Dynamics of Exchanged Cu Cations in SSZ-13 Zeolites. *Journal of the American Chemical Society* **2016**, *138* (18), 6028–6048. https://doi.org/10.1021/JACS.6B02651.

(26) Gao, F.; Mei, D.; Wang, Y.; Szanyi, J.; Peden, C. H. F. Selective Catalytic Reduction over Cu/SSZ-13: Linking Homo- and Heterogeneous Catalysis. *Journal of the American Chemical Society* **2017**, *139* (13), 4935–4942. https://doi.org/10.1021/JACS.7B01128.

(27) Chen, L.; Janssens, T. V. W.; Vennestrøm, P. N. R.; Jansson, J.; Skoglundh, M.; Grönbeck, H. A Complete Multisite Reaction Mechanism for Low-Temperature NH_3-SCR over Cu-CHA. *ACS Catalysis* **2020**, *10* (10), 5646–5656. https://doi.org/10.1021/ACSCATAL.0C00440.

(28) Paolucci, C.; Di Iorio, J. R.; Schneider, W. F.; Gounder, R. Solvation and Mobilization of Copper Active Sites in Zeolites by Ammonia: Consequences for the Catalytic Reduction of Nitrogen Oxides. *Acc. Chem. Res* **2020**, *2020*, 50. https://doi.org/10.1021/acs.accounts.0c00328.

(29) Paolucci, C.; Khurana, I.; Parekh, A. A.; Li, S.; Shih, A. J.; Li, H.; Di Iorio, J. R.; Albarracin-Caballero, J. D.; Yezerets, A.; Miller, J. T.; Delgass, W. N.; Ribeiro, F. H.; Schneider, W. F.; Gounder, R. Dynamic Multinuclear Sites Formed by Mobilized Copper Ions in NO_x Selective Catalytic Reduction. *Science* **2017**, *357* (6354), 898–903. https://doi.org/10.1126/science.aan5630.

(30) Millan, R.; Cnudde, P.; Van Speybroeck, V.; Boronat, M. Mobility and Reactivity of Cu^+ Species in Cu-CHA Catalysts under NH_3-SCR-NO_x Reaction Conditions: Insights from AIMD Simulations. *JACS Au* **2021**, *1* (10), 1778–1787. https://doi.org/10.1021/JACSAU.1C00337.

(31) Millan, R.; Cnudde, P.; Hoffman, A. E. J.; Lopes, C. W.; Concepción, P.; Van Speybroeck, V.; Boronat, M. Theoretical and Spectroscopic Evidence of the Dynamic Nature of Copper Active Sites in Cu-CHA Catalysts under Selective Catalytic Reduction (NH_3-SCR-NO_x) Conditions. *Journal of Physical Chemistry Letters* **2020**, *11* (23), 10060–10066. https://doi.org/10.1021/ACS.JPCLETT.0C03020.

(32) Krishna, S. H.; Goswami, A.; Wang, Y.; Jones, C. B.; Dean, D. P.; Miller, J. T.; Schneider, W. F.; Gounder, R.; Davidson, C. D. Influence of Framework Al Density in Chabazite Zeolites on Copper Ion Mobility and Reactivity during NO_x Selective

Catalytic Reduction with NH_3. *Nature Catalysis 2023 6:3* **2023**, *6* (3), 276–285. https://doi.org/10.1038/s41929-023-00932-5.

(33) DeLuca, M.; Jones, C. B.; Krishna, S. H.; Goswami, A.; Saxena, R.; Li, S.; Prasad, S.; Moini, A.; Schneider, W. F.; Gounder, R. Effects of Zeolite Framework Topology on Cu(I) Oxidation and Cu(II) Reduction Kinetics of NO_x Selective Catalytic Reduction with NH_3. *Chem Catalysis* **2023**, 100726. https://doi.org/10.1016/j.checat.2023.100726.

(34) Kwak, J. H.; Tran, D.; Burton, S. D.; Szanyi, J.; Lee, J. H.; Peden, C. H. F. Effects of Hydrothermal Aging on NH_3-SCR Reaction over Cu/Zeolites. *Journal of Catalysis* **2012**, *287*, 203–209. https://doi.org/10.1016/j.jcat.2011.12.025.

(35) Song, J.; Wang, Y.; Walter, E. D.; Washton, N. M.; Mei, D.; Kovarik, L.; Engelhard, M. H.; Prodinger, S.; Wang, Y.; Peden, C. H. F.; Gao, F. Toward Rational Design of Cu/SSZ-13 Selective Catalytic Reduction Catalysts: Implications from Atomic-Level Understanding of Hydrothermal Stability. *ACS Catalysis* **2017**, *7* (12), 8214–8227. https://doi.org/10.1021/acscatal.7b03020.

(36) Uchisawa, J.; Obuchi, A.; Yamamoto, A.; Suzuki, S.; Mizushima, N.; Hayashi, S. Effect of Water Vapor on the Accelerated Deterioration Treatment of Cu-SSZ-13 as Catalysts for Selective Catalytic Reduction. *Industrial and Engineering Chemistry Research* **2021**, *60* (43), 15454–15463. https://doi.org/10.1021/ACS.IECR.1C02599/.

(37) Blakeman, P. G.; Burkholder, E. M.; Chen, H. Y.; Collier, J. E.; Fedeyko, J. M.; Jobson, H.; Rajaram, R. R. The Role of Pore Size on the Thermal Stability of Zeolite Supported Cu SCR Catalysts. *Catalysis Today* **2014**, *231*, 56–63. https://doi.org/10.1016/J.CATTOD.2013.10.047.

(38) Schmidt, J. E.; Oord, R.; Guo, W.; Poplawsky, J. D.; Weckhuysen, B. M. Nanoscale Tomography Reveals the Deactivation of Automotive Copper-Exchanged Zeolite Catalysts. *Nat. Commun.* **2017**, *8* (1), 1666. https://doi.org/10.1038/s41467-017-01765-0.

(39) Fan, C.; Chen, Z.; Pang, L.; Ming, S.; Zhang, X.; Albert, K. B.; Liu, P.; Chen, H.; Li, T. The Influence of Si/Al Ratio on the Catalytic Property and Hydrothermal Stability of Cu-SSZ-13 Catalysts for NH_3-SCR. *Applied Catalysis A: General* **2018**, *550*, 256–265. https://doi.org/10.1016/J.APCATA.2017.11.021.

(40) Luo, J.; Wang, D.; Kumar, A.; Li, J.; Kamasamudram, K.; Currier, N.; Yezerets, A. Identification of Two Types of Cu Sites in Cu/SSZ-13 and Their Unique Responses to Hydrothermal Aging and Sulfur Poisoning. *Catalysis Today* **2016**, *267*, 3–9. https://doi.org/10.1016/J.CATTOD.2015.12.002.

(41) Gao, F.; Szanyi, J. On the Hydrothermal Stability of Cu/SSZ-13 SCR Catalysts. *Applied Catalysis A: General* **2018**, *560*, 185–194. https://doi.org/10.1016/j.apcata.2018.04.040.

(42) Zhang, Y.; Peng, Y.; Li, J.; Groden, K.; McEwen, J. S.; Walter, E. D.; Chen, Y.; Wang, Y.; Gao, F. Probing Active-Site Relocation in Cu/SSZ-13 SCR Catalysts during Hydrothermal Aging by in Situ EPR Spectroscopy, Kinetics Studies, and DFT

Calculations. *ACS Catalysis* **2020**, *10* (16), 9410–9419. https://doi.org/10.1021/ACSCATAL.0C01590.
(43) Usui, T.; Liu, Z.; Igarashi, H.; Sasaki, Y.; Shiramata, Y.; Yamada, H.; Ohara, K.; Kusamoto, T.; Wakihara, T. Identifying the Factors Governing the Early-Stage Degradation of Cu-Chabazite Zeolite for NH_3-SCR. *ACS Omega* **2019**, *4* (2), 3653–3659. https://doi.org/10.1021/ACSOMEGA.8B03409.
(44) Engelhardt, G.; Lohse, U.; Samoson, A.; Mägi, M.; Tarmak, M.; Lippmaa, E. High Resolution ^{29}Si N.M.R. of Dealuminated and Ultrastable Y-Zeolites. *Zeolites* **1982**, *2* (1), 59–62. https://doi.org/10.1016/S0144-2449(82)80042-0.
(45) Kester, P. M.; Miller, J. T.; Gounder, R. Ammonia Titration Methods To Quantify Brønsted Acid Sites in Zeolites Substituted with Aluminum and Boron Heteroatoms. *Ind. Eng. Chem. Res.* **2018**, *57* (19), 6673–6683. https://doi.org/10.1021/acs.iecr.8b00933.
(46) Ravi, M.; Sushkevich, V. L.; van Bokhoven, J. A. Towards a Better Understanding of Lewis Acidic Aluminium in Zeolites. *Nat. Mater.* **2020**, *19* (10), 1047–1056. https://doi.org/10.1038/s41563-020-0751-3.
(47) Nilsson Pingel, T.; Jørgensen, M.; Yankovich, A. B.; Grönbeck, H.; Olsson, E. Influence of Atomic Site-Specific Strain on Catalytic Activity of Supported Nanoparticles. *Nat. Commun.* **2018**, *9* (1), 2722. https://doi.org/10.1038/s41467-018-05055-1.
(48) Nilsson Pingel, T.; Fouladvand, S.; Heggen, M.; Dunin-Borkowski, R. E.; Jäger, W.; Westenberger, P.; Phifer, D.; McNeil, J.; Skoglundh, M.; Grönbeck, H.; Olsson, E. Three-Dimensional Probing of Catalyst Ageing on Different Length Scales: A Case Study of Changes in Microstructure and Activity for CO Oxidation of a Pt-Pd/Al_2O_3 Catalyst. *ChemCatChem* **2017**, *9* (18), 3544–3553. https://doi.org/10.1002/cctc.201700479.
(49) Liu, L.; Lopez-Haro, M.; Calvino, J. J.; Corma, A. Tutorial: Structural Characterization of Isolated Metal Atoms and Subnanometric Metal Clusters in Zeolites. *Nature Protocols* **2020**, *16* (4), 1871–1906. https://doi.org/10.1038/s41596-020-0366-9.
(50) Liu, L.; Wang, N.; Zhu, C.; Liu, X.; Zhu, Y.; Guo, P.; Alfilfil, L.; Dong, X.; Zhang, D.; Han, Y. Direct Imaging of Atomically Dispersed Molybdenum That Enables Location of Aluminum in the Framework of Zeolite ZSM-5. *Angewandte Chemie* **2020**, *132* (2), 829–835. https://doi.org/10.1002/ange.201909834.
(51) Lin, Y.; Zhou, M.; Tai, X.; Li, H.; Han, X.; Yu, J. Analytical Transmission Electron Microscopy for Emerging Advanced Materials. *Matter* **2021**, *4* (7), 2309–2339. https://doi.org/10.1016/J.MATT.2021.05.005.
(52) Goel, S.; Wu, Z.; Zones, S. I.; Iglesia, E. Synthesis and Catalytic Properties of Metal Clusters Encapsulated within Small-Pore (SOD, GIS, ANA) Zeolites. *J. Am. Chem. Soc.* **2012**, *134* (42), 17688–17695. https://doi.org/10.1021/ja307370z.
(53) Moreno-González, M.; Hueso, B.; Boronat, M.; Blasco, T.; Corma, A. Ammonia-Containing Species Formed in Cu-Chabazite As Per In Situ EPR, Solid-State NMR, and

DFT Calculations. *Journal of Physical Chemistry Letters* **2015**, *6* (6), 1011–1017. https://doi.org/10.1021/ACS.JPCLETT.5B00069.

(54) Berkson, Z. J.; Hsieh, M.; Smeets, S.; Gajan, D.; Lund, A.; Lesage, A.; Xie, D.; Zones, S. I.; McCusker, L. B.; Baerlocher, C.; Chmelka, B. F. Preferential Siting of Aluminum Heteroatoms in the Zeolite Catalyst Al-SSZ-70. *Angewandte Chemie International Edition* **2019**, *58* (19), 6255–6259. https://doi.org/10.1002/anie.201813533.

(55) Schmithorst, M. B.; Prasad, S.; Moini, A.; Chmelka, B. F. Direct Detection of Paired Aluminum Heteroatoms in Chabazite Zeolite Catalysts and Their Significance for Methanol Dehydration Reactivity. *J. Am. Chem. Soc.* **2023**, *145* (33), 18215–18220. https://doi.org/10.1021/jacs.3c05708.

(56) Chen, K.; Gan, Z.; Horstmeier, S.; White, J. L. Distribution of Aluminum Species in Zeolite Catalysts: ^{27}Al NMR of Framework, Partially-Coordinated Framework, and Non-Framework Moieties. *Journal of the American Chemical Society* **2021**, *143* (17), 6669–6680. https://doi.org/10.1021/JACS.1C02361.

(57) Chen, K.; Zornes, A.; Nguyen, V.; Wang, B.; Gan, Z.; Crossley, S. P.; White, J. L. ^{17}O Labeling Reveals Paired Active Sites in Zeolite Catalysts. *Journal of the American Chemical Society* **2022**, *144* (37), 16916–16929. https://doi.org/10.1021/jacs.2c05332.

(58) Palamara, J.; Seidel, K.; Moini, A.; Prasad, S. Ion Distribution in Copper Exchanged Zeolites by Using Si-29 Spin Lattice Relaxation Analysis. *Journal of Magnetic Resonance* **2016**, *267*, 9–14. https://doi.org/10.1016/J.JMR.2016.03.009.

(59) Hu, B.; Trébosc, J.; Amoureux, J. P. Comparison of Several Hetero-Nuclear Dipolar Recoupling NMR Methods to Be Used in MAS HMQC/HSQC. *Journal of Magnetic Resonance* **2008**, *192* (1), 112–122. https://doi.org/10.1016/j.jmr.2008.02.004.

(60) Li, S.; Li, H.; Gounder, R.; Debellis, A.; Müller, I. B.; Prasad, S.; Moini, A.; Schneider, W. F. First-Principles Comparison of Proton and Divalent Copper Cation Exchange Energy Landscapes in SSZ-13 Zeolite. *The Journal of Physical Chemistry C* **2018**, *122* (41), 23564–23573. https://doi.org/10.1021/acs.jpcc.8b07213.

(61) Lesage, A.; Bardet, M.; Emsley, L. Through-Bond Carbon-Carbon Connectivities in Disordered Solids by NMR. *Journal of the American Chemical Society* **1999**, *121* (47), 10987–10993. https://doi.org/10.1021/ja992272b.

(62) Engelhardt, G.; Lohse, U.; Patzelová, V.; Mägi, M.; Lippmaa, E. High Resolution ^{29}Si N.M.R. of Dealuminated Y-Zeolites 1. The Dependence of the Extent of Dealumination on the Degree of Ammonium Exchange and the Temperature and Water Vapour Pressure of the Thermochemical Treatment. *Zeolites* **1983**, *3* (3), 233–238. https://doi.org/10.1016/0144-2449(83)90013-1.

(63) Engelhardt, G.; Lohse, U.; Patzelová, V.; Mägi, M.; Lippmaa, E. High Resolution ^{29}Si N.M.R. of Dealuminated Y-Zeolites. 2. Silicon, Aluminium Ordering in the Tetrahedral Zeolite Lattice. *Zeolites* **1983**, *3* (3), 239–243. https://doi.org/10.1016/0144-2449(83)90014-3.

(64) Jeener, J.; Meier, B. H.; Bachmann, P.; Ernst, R. R. Investigation of Exchange Processes by Two-dimensional NMR Spectroscopy. *The Journal of Chemical Physics* **1979**, *71* (11), 4546–4553. https://doi.org/10.1063/1.438208.
(65) Selter, P.; Schmithorst, M. B.; Chmelka, B. F. Hopping Dynamics and Diffusion of Atoms, Molecules, and Ions in Nanoporous Solids by Exchange NMR Spectroscopy. *Adsorption* **2021**, *27* (5), 857–874. https://doi.org/10.1007/s10450-021-00318-8.
(66) Schaefer, D. J.; Favre, D. E.; Wilhelm, M.; Weigel, S. J.; Chmelka, B. F. Site-Hopping Dynamics of Benzene Adsorbed on Ca-LSX Zeolite Studied by Solid-State Exchange ^{13}C NMR. *Journal of the American Chemical Society* **1997**, *119* (39), 9252–9267.
(67) Luzgin, M. V.; Freude, D.; Haase, J.; Stepanov, A. G. Methane Interaction with Zn^{2+}-Exchanged Zeolite H-ZSM-5: Study of Adsorption and Mobility by One- and Two-Dimensional Variable-Temperature ^{1}H Solid-State NMR. *J. Phys. Chem. C* **2015**, *119* (25), 14255–14261. https://doi.org/10.1021/acs.jpcc.5b04028.
(68) Ernst, R. R.; Bodenhausen, G.; Wokaun, A. *Principles of Nuclear Magnetic Resonance in One and Two Dimensions*, Repr.; The international series of monographs on chemistry; Clarendon Press: Oxford, 2004.
(69) Fogler, H. S. *Elements of Chemical Reaction Engineering*, Fifth edition.; Prentice Hall: Boston, 2016.
(70) Rizzotto, V.; Chen, P.; Simon, U. Mobility of NH3-Solvated Cu^{II} Ions in Cu-SSZ-13 and Cu-ZSM-5 NH_3-SCR Catalysts: A Comparative Impedance Spectroscopy Study. *Catalysts* **2018**, *8* (4), 162. https://doi.org/10.3390/catal8040162.
(71) Eder, F.; Lercher, J. A. Alkane Sorption in Molecular Sieves: The Contribution of Ordering, Intermolecular Interactions, and Sorption on Brønsted Acid Sites. *Zeolites* **1997**, *18* (1), 75–81. https://doi.org/10.1016/S0144-2449(96)00127-3.
(72) Eder, F.; Stockenhuber, M.; Lercher, J. A. Brønsted Acid Site and Pore Controlled Siting of Alkane Sorption in Acidic Molecular Sieves. *J. Phys. Chem. B* **1997**, *101* (27), 5414–5419. https://doi.org/10.1021/jp9706487.
(73) Bhan, A.; Gounder, R.; Macht, J.; Iglesia, E. Entropy Considerations in Monomolecular Cracking of Alkanes on Acidic Zeolites. *Journal of Catalysis* **2008**, *253* (1), 221–224. https://doi.org/10.1016/j.jcat.2007.11.003.
(74) Zakem, G.; Ro, I.; Finzel, J.; Christopher, P. Support Functionalization as an Approach for Modifying Activation Entropies of Catalytic Reactions on Atomically Dispersed Metal Sites. *Journal of Catalysis* **2021**, *404*, 883–896. https://doi.org/10.1016/J.JCAT.2021.07.030.
(75) Sushkevich, V. L.; Smirnov, A. V.; van Bokhoven, J. A. Autoreduction of Copper in Zeolites: Role of Topology, Si/Al Ratio, and Copper Loading. *J. Phys. Chem. C* **2019**, *123* (15), 9926–9934. https://doi.org/10.1021/acs.jpcc.9b00986.
(76) Fung, B. M.; Khitrin, A. K.; Ermolaev, K. An Improved Broadband Decoupling Sequence for Liquid Crystals and Solids. *Journal of Magnetic Resonance* **2000**, *142* (1), 97–101. https://doi.org/10.1006/JMRE.1999.1896.

(77) Massiot, D.; Fayon, F.; Capron, M.; King, I.; Le Calvé, S.; Alonso, B.; Durand, J.-O.; Bujoli, B.; Gan, Z.; Hoatson, G. Modelling One-and Two-Dimensional Solid-State NMR Spectra. *Magnetic Resonance in Chemistry* **2002**, *40*, 70–76. https://doi.org/10.1002/mrc.984.
(78) Stoll, S.; Schweiger, A. EasySpin, a Comprehensive Software Package for Spectral Simulation and Analysis in EPR. *Journal of Magnetic Resonance* **2006**, *178* (1), 42–55. https://doi.org/10.1016/j.jmr.2005.08.013.
(79) Bertani, P.; Raya, J.; Bechinger, B. ^{15}N Chemical Shift Referencing in Solid State NMR. *Solid State Nuclear Magnetic Resonance* **2014**, *61–62*, 15–18. https://doi.org/10.1016/J.SSNMR.2014.03.003.
(80) Iuga, D.; Schäfer, H.; Verhagen, R.; Kentgens, A. P. M. Population and Coherence Transfer Induced by Double Frequency Sweeps in Half-Integer Quadrupolar Spin Systems. *Journal of Magnetic Resonance* **2000**, *147* (2), 192–209. https://doi.org/10.1006/jmre.2000.2192.
(81) Bielecki, A.; Burum, D. P. Temperature Dependence of ^{207}Pb MAS Spectra of Solid Lead Nitrate. An Accurate, Sensitive Thermometer for Variable-Temperature MAS. *Journal of Magnetic Resonance, Series A* **1995**, *116* (2), 215–220. https://doi.org/10.1006/jmra.1995.0010.
(82) Raiford, D. S.; Fisk, C. L.; Becker, E. D. Calibration of Methanol and Ethylene Glycol Nuclear Magnetic Resonance Thermometers. *Anal. Chem.* **1979**, *51* (12), 2050–2051. https://doi.org/10.1021/ac50048a040.
(83) Luo, J.; Gao, F.; Kamasamudram, K.; Currier, N.; Peden, C. H. F.; Yezerets, A. New Insights into Cu/SSZ-13 SCR Catalyst Acidity. Part I: Nature of Acidic Sites Probed by NH_3 Titration. *Journal of Catalysis* **2017**, *348*, 291–299. https://doi.org/10.1016/j.jcat.2017.02.025.
(84) Galarneau, A.; Villemot, F.; Rodriguez, J.; Fajula, F.; Coasne, B. Validity of the T-Plot Method to Assess Microporosity in Hierarchical Micro/Mesoporous Materials. *Langmuir* **2014**, *30* (44), 13266–13274. https://doi.org/10.1021/la5026679.
(85) Schneider, C. A.; Rasband, W. S.; Eliceiri, K. W. NIH Image to ImageJ: 25 Years of Image Analysis. *Nat. Methods* **2012**, *9* (7), 671–675. https://doi.org/10.1038/nmeth.2089.
(86) Montgomery, D. C.; Runger, G. C. *Applied Statistics and Probability for Engineers*, 6. ed.; Wiley: Hoboken, NJ, 2014.
(87) Carl, P. J.; Larsen, S. C. EPR Study of Copper-Exchanged Zeolites: Effects of Correlated g- and A-Strain, Si/Al Ratio, and Parent Zeolite. *J. Phys. Chem. B* **2000**, *104* (28), 6568–6575. https://doi.org/10.1021/jp000015j.
(88) Gounder, R.; Iglesia, E. Catalytic Consequences of Spatial Constraints and Acid Site Location for Monomolecular Alkane Activation on Zeolites. *J. Am. Chem. Soc.* **2009**, *131* (5), 1958–1971. https://doi.org/10.1021/ja808292c.

Chapter 4

External-surface acid sites in a dealuminated zeolite and their role in coking

This chapter is adapted from the prepared manuscript: Schmithorst, M. B., McNarney, A., Stoev, A., Berkson, Z.J., and Chmelka, B.F. Detection of external surface defect acid sites in a dealuminated zeolite and their coke susceptibility. *For submission to Angewandte Chemie*. I conceived of and ran the majority of the experiments in the main text and SI and performed the data analysis. A. McNarney performed X-ray diffraction and NH_3 TPD measurements and analysis. A. Stoev assisted with reaction measurements and basic characterization measurements. Z.J. Berkson helped conceive of the project.

Abstract

Mesopores are frequently introduced into zeolite catalysts to improve mass transport of reactant species and to expose active sites to different pore environments. Due to the complex distributions of aluminosilicate framework structures present in these mesoporous zeolites, direct characterization of these moieties has been challenging. Here, we demonstrate advanced solid-state 2D ^{27}Al-^{29}Si NMR correlation analyses to identify mesoporous Si–O–Al defect sites in a commercial dealuminated Y. After organosilane deposition on the surface, spectroscopic features associated with these defects are reduced. The modified catalyst has a lower initial conversion in a hexane test reaction, but the conversions at long time on stream converge for the modified and unmodified catalyst due to increased coke formation and deactivation on the unmodified catalyst relative to the modified. Solid-state ^{1}H NMR measurements of the catalysts after different reaction times reveal differences in the types of aromatic species adsorbed on the two catalysts, with more polyaromatic species present on the unmodified catalyst. These bulky aromatic species are in sub-nanoscale proximity to aluminum

in the zeolite, indicating that they likely play a role in deactivation. These techniques are expected to be broadly useful for detecting defect acid sites in complex zeolite catalysts.

Introduction

Composition-structure-activity relationships of heterogeneous catalysts have long been sought to design next-generation catalysts through understanding of the important features in complex distributions of active sites. For example, nanoporous, crystalline aluminosilicate zeolites have long been utilized as acid catalysts for a wide variety of hydrocarbon conversion chemistries.[1,2] In zeolites, four-coordinate aluminum in the framework produces localized negative charges on the zeolite framework, which must be charge-balanced by electrostatic interactions with cations exchanged into the zeolite pores.[3] When these charge-balancing cations are H^+, these sites impart Bronsted acidity to the zeolite. The distributions of these Bronsted acid sites within a zeolite have effects on the reaction rates, selectivities, and deactivation rates for various acid-catalyzed reactions.[4–7] However, directly characterizing these distributions and understanding their influences on catalytic properties is challenging.

The introduction of hierarchical structures into zeolite crystallites to improve mass transport of reaction species has long been investigated. As an early example, the large-pore zeolite Y was dealuminated by steam treatment to form ultrastable Y, which was observed to have improved catalytic properties for catalytic cracking compared to pristine zeolite Y in part due to improved mass transport properties and site accessibility.[8] This ultrastable Y zeolite is used ubiquitously in fluidized catalytic cracking applications.[9] Both acid and base leaching have commonly been employed to introduce mesopores into zeolites post-synthetically.[10] More recent work has used more controlled synthesis approaches to introduce varied pore sizes into zeolites and increased external surface area to zeolites.[11] Recent examples include mesopore

templating with surfactants,[12–14] the synthesis of stable 2D zeolite structures,[15,16] and synthesis of zeolites with unusual particle morphology.[17] Along with improving mass transport properties, both synthetic and post-synthetic methods for introducing mesopores into zeolites can result in acid sites exposed to the external or mesopore surface.[12,18,19] However, external acidity is typically inferred by adsorption of bulky probe molecules, and direct characterization of the structures that give rise to mesopore acidity has been challenging.[20]

A major challenge associated with hydrocarbon conversion reactions over acidic zeolite catalysts is the formation of coke, bulky hydrocarbon species that do not desorb from active sites under reaction conditions, resulting in deactivation.[21] Bulky polyaromatic coke species form through a combination of oligomerization and hydrogen transfer reactions of adsorbed reactant hydrocarbons.[22,23] Under high temperature reaction conditions use for cracking reactions, the formation of coke species is thermodynamically favorable.[21] However, the pore structure of zeolites has been observed to constrain the growth of coke species, and zeolite mesopores can modify the rates of deactivation and types of coke species present.[24–27] Thus, a better understanding of the types of mesopore-accessible acid sites present in a zeolite could inform design of more effective catalysts.

Here, through advanced solid-state NMR techniques we identify framework associated aluminum species located near defects in the zeolite lattice. After performing well-established silylation procedures to deposit silica on the external surface of the zeolite,[28–32] spectroscopic features associated with the mesopore defect aluminum species are no longer observed, suggesting their passivation. A hexane cracking test reaction reveals that sites not passivated during the silylation procedure deactivate quickly on the unmodified catalyst, resulting in similar conversions at long times on stream for the unmodified and passivated catalyst under

the same flow conditions. It is observed that the unmodified catalyst has more coke present at long times on stream than the modified catalyst, and solid-state ^{1}H NMR reveals that the types of coke species evolve differently on the two catalysts. These types of analyses are expected to be broadly transferrable to other zeolite systems with complex distributions of micropore and mesopore acidity.

Results and Discussion

To investigate the role of external surface acid sites on cracking chemistry and coke formation, the external surface of a commercial dealuminated zeolite Y (deAl-Y, Si/Al = 15) was passivated by deposition of a bulky organosilane, ethoxytriphenylsilane (ETPS). Such an approach has previously been used to selectively modify the external surface of zeolites due to the phenyl groups making the molecule too large to easily enter zeolite micropores.[33] This deposition was performed at two different loadings, 0.5 ETPS/Al and 1.0 ETPS/Al. After calcination to remove organics, powder X-ray diffraction, solid-state ^{29}Si NMR, and solid-state ^{27}Al NMR reveal only minor differences in the zeolite structure (Figures S1–S3). N_2 physisorption reveals no significant change in surface area and micropore volume, and NH_3 temperature-programmed desorption reveal small decreases in total acid site density consistent with blockage of mesopore-accessible adsorption sites (Figures S4, S5, Table S1), indicating that the deposition primarily happens on the external or mesopore surface.

The effects of external surface passivation on cracking activity for the deAl-Y zeolite were assessed by performing hexane cracking over the catalysts in a flow reactor at 400 ºC with a flow of 4 kPa hexane at a WHSV of 2.5 h^{-1}. This relatively low temperature for cracking was chosen to slow the rate of coke formation over the catalysts in order to more easily analyze differences over time.[23] The hexane conversions observed over unmodified deAl-Y, 0.5-

ETPS/Al-deAl-Y, and 1.0-ETPS/Al-deAl-Y are shown in Figure 1A. The initial hexane conversion after five minutes on stream is 0.43 over the unmodified deAl-Y zeolite. In comparison, the initial conversion decreases to 0.30 and 0.26 for 0.5-ETPS/Al-deAl-Y and 1.0-ETPS/Al-deAl-Y, respectively. This is consistent with blocking of external surface and mesopore acid sites, which likely have high activity compared to internal micropore acid sites due to differences in diffusion limitations associated with the zeolite pore structure.[34] Over the first 12 h on stream, conversion decreases for all three catalysts, likely due to coking of the catalyst. For all three catalysts, there is an initial fast decrease in activity followed by a transition to slower deactivation after approximately 200 min on stream. Interestingly, after this initial period of deactivation, the measured hexane conversions over the three catalysts are more similar and by 730 min on stream, the hexane conversion over all three catalysts is approximately the same, ranging from 15–16% of hexane converted. This indicates that the active sites left over after ETPS deposition are the sites least susceptible to deactivation by coking.

Product distributions for the hexane cracking reactions over unmodified deAl-Y, 0.5-ETPS/Al-deAl-Y, and 1.0-ETPS/Al-deAl-Y as a function of time on stream are shown in Figure 1B-D. For all catalysts, the primary products observed were propane and propylene, along with minor amounts of methane, ethane, ethylene, butene, butylene, and pentane. No pentene was detected, likely due to the small amounts produced undergoing secondary reactions. Full product distributions at all measured time points are shown in Tables S2–S4. Based on the significantly higher production of propylene than propane, significant hydrogen was produced during the reactions. The implied H_2 conversion necessary to satisfy the carbon and hydrogen balances is shown in Tables S5–S7, and is consistent with previous reports of

hexane cracking over zeolite Y under similar conditions.[35] Interestingly, there is a slight increase in initial selectivity for propylene over propane for the 0.5-ETPS/Al-deAl-Y and 1.0-ETPS/Al compared to unmodified deAl-Y, which suggests that different hexane cracking reaction pathways are favored over internal and external or mesopore acid sites.

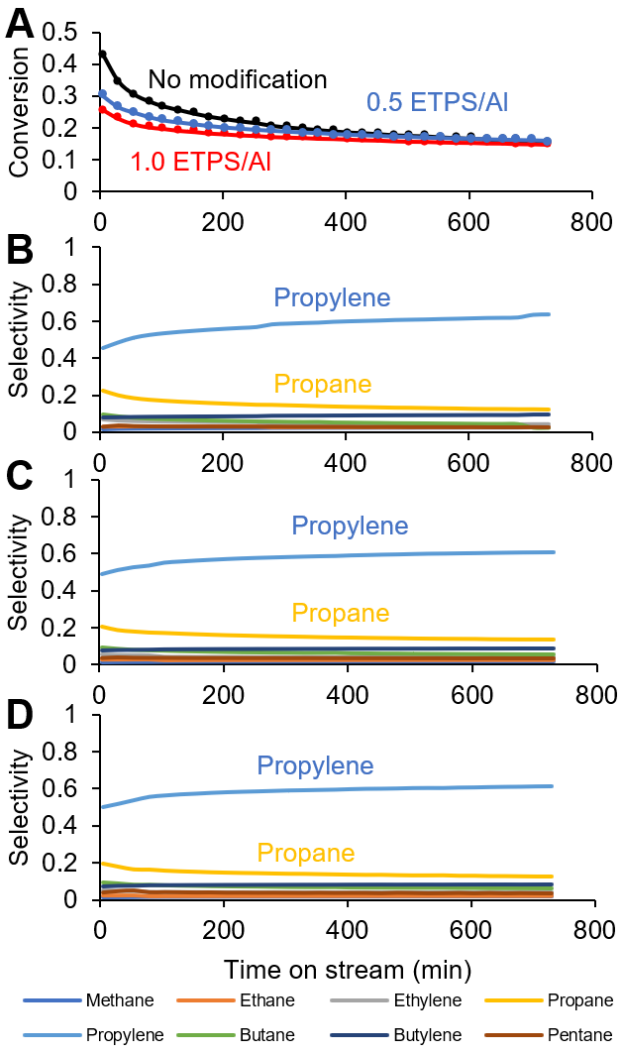

Figure 1. (A) Conversion as a function of time on stream for hexane cracking over unmodified deAl-Y (black), 0.5-ETPS/Al-deAl-Y (blue), and 1.0-ETPS/Al-deAlY (black). Reactions were performed in a packed bed at 400 ºC with 4 kPa hexane in the feed diluted with helium to atmospheric pressure at a WHSV of 2.5 h^{-1}. Data points were taken every 25 min after the first 5 min on stream using an online gas chromatograph equipped with a flame ionization detector. Selectivities denoted in terms of moles carbon/total moles carbon converted are shown for (B) unmodified deAl-Y, (C) 0.5-ETPS/Al-deAl-Y, and (D) 1.0-ETPS/Al-deAl-Y. Tables of these selectivities are shown in Tables SX–SY.

The distribution of acid sites in deAl-Y between mesopores and zeolite nanopores is complicated and is clearly altered by ETPS deposition based on these hexane cracking studies. To better understand these complex distributions and how they evolve upon ETPS deposition, solid-state 2D ^{27}Al-^{29}Si *J*-HMQC NMR spectra were acquired for unmodified deAl-Y and 1.0-ETPS/Al-deAl-Y. These spectra show correlated intensity only from ^{27}Al and ^{29}Si nuclei separated by a single ^{29}Si–O–^{27}Al bond, thus providing information on the types and local distributions of aluminum and Bronsted acid sites in zeolite frameworks.[36–38] Due to the low natural abundance of ^{29}Si (4.7%), these spectra are challenging to collect. However, by performing measurements under cryogenic conditions to increase the overall magnetization of nuclear spins in a static magnetic field, these spectra can be acquired in a reasonable amount of time (< 24 h). The solid-state 2D ^{27}Al-^{29}Si *J*-HMQC NMR spectrum of unmodified deAl-Y in Figure 2A shows a complex distribution of ^{27}Al–O–^{29}Si connectivity. A ^{27}Al NMR signal at 60 ppm assigned to zeolite Y framework ^{27}Al^{IV} is correlated with ^{29}Si NMR signals at –101 and –95 ppm. The ^{29}Si NMR signal at –101 ppm, highlighted in orange, is assigned to zeolite Y framework Q^4(1Al) moieties. Correlations are also observed between a ^{27}Al NMR signal at 57 ppm and a ^{29}Si NMR signal at –98 ppm, along with a ^{27}Al NMR signal at 52 ppm and a ^{29}Si NMR signal at –102 ppm. The ^{27}Al NMR signal at 52 ppm is assigned to alumina tetrahedra incorporated into an alumina-silica-like structure based on literature, and the associated ^{29}Si NMR signal at –102 ppm is assigned to adjacent Q^4(1Al) moieties.[39] The ^{29}Si NMR signals at –98 and –95 ppm, highlighted in blue, are assigned to ^{29}Si species in hydroxylated surface environments based off previous literature on ^{29}Si chemical shifts of species at silica-alumina interfaces.[40] Thus, deAl-Y contains acid sites not only associated with zeolite Y framework

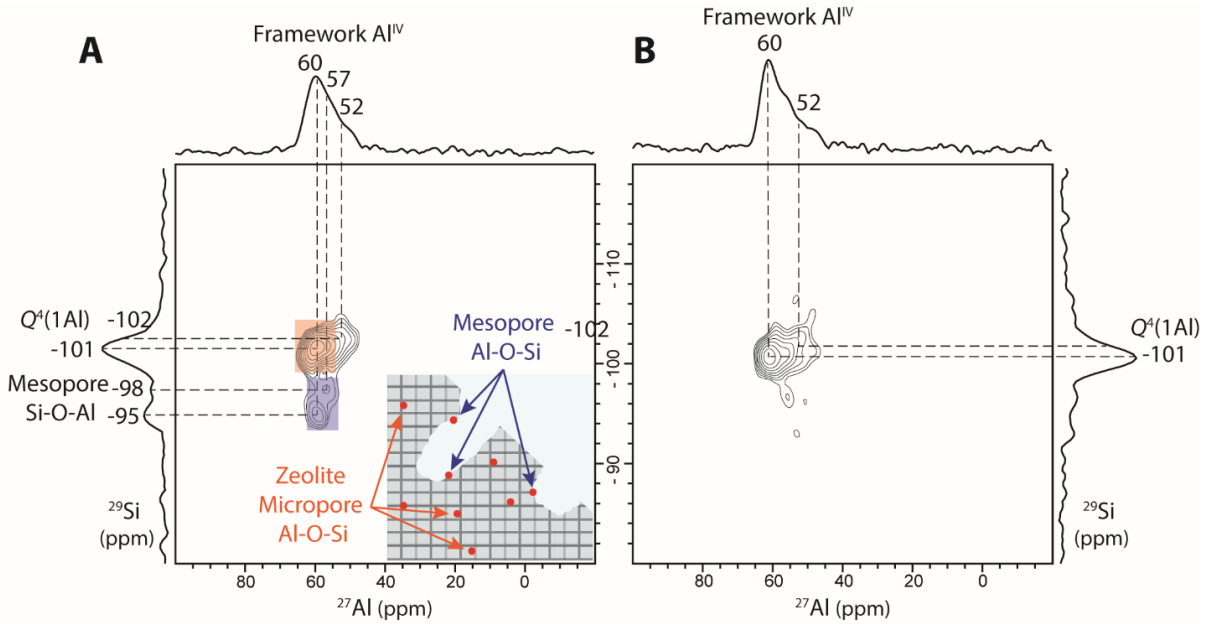

Figure 2. Solid-state 2D ^{27}Al–^{29}Si *J*-HMQC NMR spectra of hydrated (A) unmodified deAl-Y and (B) 1.0-ETPS/Al-deAl-Y acquired under the same conditions. Projections of the ^{27}Al and ^{29}Si intensity from the 2D spectra are shown on the top and side of each spectrum, respectively. Regions of correlated intensity assigned to faujasite Q^4(1Al) moieties are highlighted in orange, and regions of correlated intensity assigned to mesopore alumina-silica species are highlighted in blue. These regions are illustrated in the inset in (A), where the grid pattern represents the zeolite micropores and Al species are shown in red. Both spectra were acquired at 9.4 T, 100 K, and 8 kHz MAS.

aluminum, but also acid sites associated with hydroxylated mesopore surfaces and less-crystalline regions resulting from dealumination.

A solid-state 2D ^{27}Al-^{29}Si *J*-HMQC NMR spectrum of 1.0-ETPS/Al-deAl-Y is shown in Figure 2B and provides insight into the types of Al–O–Si moieties that are altered after ETPS deposition. The spectrum shows two notable regions of correlated intensity. A ^{27}Al NMR signal at 60 ppm assigned to zeolite Y framework ^{27}Al^{IV} is correlated with a ^{29}Si NMR signal at –101 ppm assigned to zeolite Y framework Q^4(1Al). In addition, a ^{27}Al NMR signal at 52 ppm assigned to an alumina tetrahedra incorporated into an alumina-silica-like structure is correlated with a ^{29}Si NMR signal at –102 ppm assigned to Q^4(1Al) moieties in environments distorted from zeolite Y resulting from dealumination. These correlations are consistent with

those observed for unmodified deAl-Y. Critically, clear ^{27}Al–^{29}Si correlated NMR signals in the region attributed to mesopore surface Si–O–Al are not observed in significant quantity above the noise level, indicating that these types of species are modified by ETPS deposition.

While these solid-state 2D ^{27}Al–^{29}Si *J*-HMQC NMR spectra show changes in the mesopore surface Si-O-Al moieties, they do not directly show evidence of ETPS deposition. To better identify the types of moieties the ETPS interacted with upon deposition, a solid-state 2D ^{29}Si{^{1}H} HETCOR NMR spectrum was acquired of 1.0-ETPS/Al-deAl-Y prior to calcination of the material to remove organic moieties from the ETPS, as shown in Figure 3A. The spectrum was acquired under cryogenic conditions to slow mobility of adsorbed species and provide a direct comparison to ^{29}Si NMR signals observed in solid-state 2D ^{27}Al–^{29}Si *J*-HMQC NMR spectra. This spectrum shows correlated intensity from ^{29}Si and ^{1}H nuclei in sub-nanoscale proximity with strong magnetic dipole-dipole couplings, and thus provides information on the types of ^{29}Si moieties located near the aromatic rings of ETPS. The spectrum shows three distinct regions of ^{29}Si NMR signal intensity centered at –107, –101, and –98 ppm, which are assigned to Q^4(0Al), Q^4(1Al), and mesopore surface Si–O-–Al moieties, respectively. Correlations are observed with three regions of ^{1}H NMR signal intensity at 3.4, 4.8, and 7.4 ppm. The signal at 3.4 ppm is assigned to adsorbed ethanol species originating from the ethoxy leaving groups of ETPS during deposition and is correlated to ^{29}Si NMR signals assigned to Q^4(0Al) and Q^4(1Al) moieties. Similarly, the signal at 4.8 ppm is assigned to adsorbed water species from the ambient atmosphere during drying of the material and preparation for NMR measurement and is correlated with ^{29}Si NMR signals assigned to Q^4(0Al) and Q^4(1Al) moieties. These correlated signals are consistent with ethanol and water adsorption within the zeolite micropores. Crucially, a ^{1}H NMR signal at 7.4 ppm assigned to

the phenyl rings of ETPS is correlated with ^{29}Si NMR signals assigned to Q^4(0Al), Q^4(1Al), and mesopore surface Si–O–Al moieties. Given the relatively dilute presence of the mesopore surface Si–O–Al moieties, the correlation to mesopore surface Si–O–Al species, highlighted in blue in the spectrum, is evidence of the ETPS being primarily deposited on the external mesopore surface. The correlations between NMR signals assigned to ETPS phenyl ^{1}H species and those assigned to Q^4(0Al) and Q^4(1Al) species results from through-space ^{1}H–^{29}Si dipole-dipole couplings between ETPS phenyl ^{1}H at the mesopore surface and ^{29}Si moieties located a few atomic layers below the mesopore surface, consistent with mesopore and external surface deposition.

A solid-state 2D ^{27}Al-^{29}Si *J*-HMQC NMR spectrum of the uncalcined 1.0-ETPS/Al-deAl-Y, measured after hydration to make direct comparison with other analogous spectra, is shown in Figure 3B. This spectrum shows three regions of correlated ^{27}Al and ^{29}Si signal intensity. A ^{27}Al NMR signal at 60 ppm assigned to zeolite framework ^{27}Al is correlated with a ^{29}Si NMR signal at –101 ppm assigned to Q^4(1Al) moieties in the zeolite framework. This correlation represents zeolite framework Al–O–Si moieties. A ^{27}Al NMR signal at 52 ppm is correlated with a ^{29}Si NMR signal at –102 ppm. As discussed above for the solid-state 2D ^{27}Al–^{29}Si *J*-HMQC NMR spectrum of unmodified deAl-Y, this correlation is assigned to framework Al and Si species in distorted tetrahedra near defect regions, likely mesopores. Notably, in comparison to this region of correlated signal in the spectrum of unmodified deAl-Y, the signal is broadened in the vertical ^{29}Si dimension in the spectrum of uncalcined 1.0-ETPS/Al-deAl-Y. This broadening, which is consistent with greater disorder, is likely due to the condensation of surface silanols on mesopore surface Si–O–Al moieties with ETPS molecules, resulting in a conversion of these ^{29}Si species to Q^4(1Al) moieties. These newly condensed species are

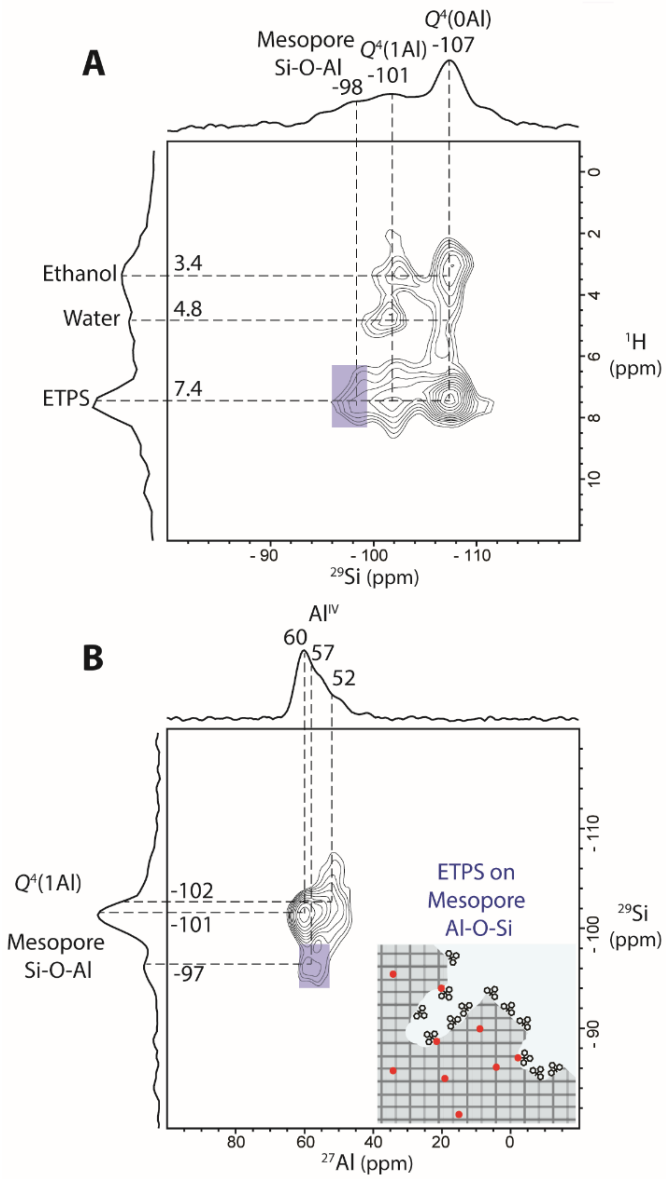

Figure 3. (A) Solid-state 2D ^{29}Si{^{1}H} HETCOR NMR spectrum and (B) solid-state 2D ^{27}Al–^{29}Si *J*-HMQC NMR spectrum of hydrated ETPS/Al-deAl-Y prior to calcination. Regions of correlated intensity associated with the mesopore surface are highlighted in blue. The inset in (B) shows the observed distribution of ETPS molecules deposited on the mesopores and external surface of the zeolite. Both spectra were acquired at 9.4 T, 100 K, and 8 kHz MAS.

likely to be poorly ordered, resulting in a broader distribution of ^{29}Si NMR signal. Additionally, a ^{27}Al NMR signal at 57 ppm is correlated with a ^{29}Si NMR signal at –97 ppm. As for the spectrum of unmodified deAl-Y, this correlation is assigned to ^{27}Al and ^{29}Si nuclei in mesopore surface Si–O–Al moieties. Interestingly, this signal appears with greater intensity than it does

in the analogous spectrum acquired after calcination (Figure 2B). This may indicate that further mesopore surface Si–O–Al moieties are lost to condensation with ETPS upon calcination to remove organic ligands. Overall, these spectra clearly establish that ETPS is deposited on mesopore surfaces, condensing with surface silanol groups.

Based on the differences in conversion trends observed during the hexane cracking reactions, the modification of deAl-Y with ETPS resulted in passivation of sites susceptible to deactivation. To better understand these differences, the hexane cracking reaction was halted after 0.5, 1, 2, 4, and 8 h on stream for the unmodified deAl-Y and 1.0-ETPS/Al-deAl-Y, and the catalyst was removed from the reactor tube under inert atmosphere for characterization of adsorbed species. To understand the differences in bulky carbonaceous species deposited on the two catalysts, thermogravimetric analysis was performed to measure the mass of adsorbed species that would not desorb at or below the reaction temperature but could be burned off following temperature programs similar to those found in literature.[27] The masses presented in Figure 4 represent the mass lost under oxygen flow during a temperature ramp from 450 to 750 ^{o}C compared to the catalyst mass remaining at 750 ^{o}C. This mass is considered to be coke. After 0.5 h on stream, both catalysts are measured to have approximately 0.01 g coke/g dry catalyst. This similarity is expected, as the activity of unmodified deAl-Y is much higher than the activity of 1.0-ETPS/Al-deAl-Y after this short time on stream, and the sites passivated by ETPS modification are not yet deactivated in unmodified deAl-Y. At longer times on stream, once the hexane conversions for the two catalysts have started to converge, the amount of coke deposited on the two catalysts is notably different. After 4 h on stream, 0.02 g coke/g dry catalyst are measured on the unmodified deAl-Y, while only 0.01 g coke/g dry catalyst are measured on the 1.0-ETPS/Al-deAl-Y. This is consistent with coke formation on mesopore

sites in unmodified deAl-Y resulting in deactivation of these sites over time. Two potential sources of the 0.01 g coke/g dry catalyst consistently present on 1.0-ETPS/Al-deAl-Y are highly-coke-susceptible sites that deactivate prior to five minutes on stream, or alternatively species adsorbed in the zeolite micropores that are too large to diffuse out of the pore structure, but do not readily crack to form smaller, more mobile species under reaction conditions. The overall trends observed indicate that sites responsible for high activity in unmodified deAl-Y are more susceptible to deactivation by coke formation than sites in the zeolite micropore structure.

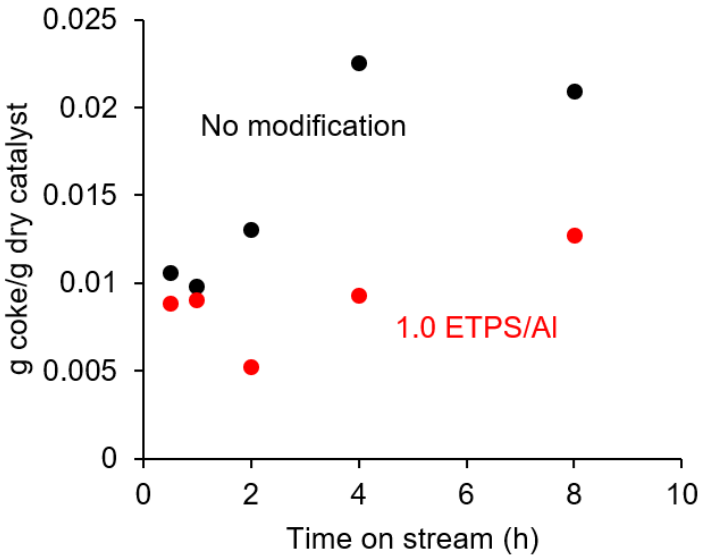

Figure 4. Specific mass of coke measured over unmodified-deAl-Y (black) and 1.0-ETPS/Al-deAl-Y (red) after quenching the hexane cracking reaction at 0.5, 1, 2, 4, and 8 h as quantified by thermogravimetric analysis after desorption of all species volatile below the reaction temperature.

The higher level of coke observed in unmodified deAl-Y compared to 1.0-ETPS/Al-deAl-Y is either due to a higher quantity of carbonaceous deactivation species or due to different types of carbonaceous deactivation species. To assess this difference, the catalysts removed from the reactor after 0.5, 1, 2, 4, and 8 h on stream were characterized by solid-state

direct-excitation ^{1}H MAS NMR, as shown in Figure 5. Samples for NMR were prepared in a glovebox to avoid exposure to water complicating the interpretation of the ^{1}H NMR spectra. The solid-state direct-excitation ^{1}H NMR spectra of the reacted unmodified deAl-Y taken at different time points shown in Figure 5A reveal a complex distribution of ^{1}H NMR signals attributed to zeolite framework features and adsorbed hydrocarbon species. ^{1}H NMR signals at 1.6, 2.5, and 4.4 ppm are assigned to zeolite framework species based on solid-state direct-excitation ^{1}H NMR spectra of the dehydrated zeolites (Figure S6). The ^{1}H NMR signal at 1.6 ppm is assigned to silanol species, while the signal at 2.5 is assigned to AlOH species. The ^{1}H signal at 4.4 ppm is assigned to Bronsted acid sites. In the literature, this ^{1}H NMR signal has been assigned to Bronsted acid ^{1}H species in the sodalite cages of zeolite Y, while Bronsted acid ^{1}H species are observed at 3.8 ppm, consistent with the ^{1}H NMR spectra in Figure S6.[41] The absence of a strong ^{1}H NMR signal at 3.8 ppm in these spectra is likely a result of these cations complexing with adsorbed hydrocarbon species. In contrast, the sodalite Bronsted acid sites are likely inaccessible to hexane reactants.

The remaining ^{1}H NMR signals observed in the solid-state direct-excitation ^{1}H NMR spectra of unmodified deAl-Y after different times on stream are assigned to hydrocarbon species. The ^{1}H NMR signal at 5.8 ppm is assigned to olefinic ^{1}H species, likely pentenes and hexenes adsorbed in the pores.[42] A broad distribution of ^{1}H NMR signal ranging from 8 to 11 ppm is observed, with partially resolved signals at 8.1, 8.7, 9.1, and 10.3 ppm. Signals in this region are assigned to aromatic and polyaromatic species and are consistent with literature reports of polycyclic aromatic compounds on zeolites.[43–45] Solid-state 2D ^{1}H-^{1}H single-quantum double-quantum NMR spectra reveal methyl groups with a ^{1}H NMR signal at around 3.0 ppm associated with these aromatic species (Figure S7). This signal is convoluted with the

signals assigned to AlOH species. Well resolved NMR signals ranging from –0.1 to 0.8 ppm are assigned to methyl groups on adsorbed species. Aliphatic CH_2 species are likely present but not resolved from the ^{1}H NMR signal at 1.6 ppm assigned to silanol species. Other broad underlying signal is also attributable to adsorbed hydrocarbon species but is difficult to assign due to poor resolution.

The distribution of ^{1}H NMR signal intensity assigned to adsorbed hydrocarbon species on unmodified deAl-Y in Figure 5A varies with time on stream. At 30 min on stream, the ^{1}H NMR signal at 5.8 ppm attributed to olefinic ^{1}H is observed as more intense than the region of signal attributed to aromatic ^{1}H species. Starting at 1 h, this feature is depleted relative to the aromatic signal region. Additionally, as time evolves from 30 min to 8 h, the aromatic ^{1}H NMR signal at 8.1 ppm is depleted. Correspondingly, the aromatic ^{1}H signal at 10.3 ppm grows more intense over time, particularly building up between 2 h and 4 h on stream. This loss of olefinic ^{1}H NMR signal and increase in intensity of aromatic ^{1}H NMR signals at higher ppm values at the expense of intensity from lower-frequency ^{1}H NMR signals is consistent with the formation of more polycyclic aromatic species as the reaction progresses over unmodified deAl-Y. A similar trend is observed in methyl ^{1}H chemical shifts, with small displacements in ^{1}H NMR signal occurring as a function of time on stream, likely similarly due to an evolution of the aromatic adsorbates.

Similar chemical species are identified in the solid-state direct-excitation ^{1}H MAS NMR spectra of 1.0-ETPS/Al-deAl-Y after different reaction times on stream, as shown in Figure 5B. ^{1}H NMR signals at 1.6 and 4.4 ppm are assigned to silanol and Bronsted acid ^{1}H species, respectively, while ^{1}H NMR signal at 2.5 ppm is assigned to AlOH. Similar broad distributions of olefinic and aromatic ^{1}H NMR signals are observed as those for unmodified

deAl-Y. Crucially, in contrast to the aromatic ^{1}H NMR signal region for the spectra of unmodified deAl-Y, the distribution of aromatic ^{1}H NMR signal observed from 1.0-ETPS/Al-deAl-Y remains relatively constant across the five ^{1}H NMR spectra measured after 0.5 h, 1 h, 2 h, 4 h, and 8 h on stream. This is consistent with adsorbed aromatic species not evolving to become more polyaromatic and block acid sites, as the evolution of aromatic ^{1}H NMR signals observed for unmodified deAl-Y suggests. This lack of growth is likely due to the acid sites on 1.0-ETPS/Al-deAl-Y primarily being in the micropores of the zeolite, constraining the growth of polyaromatic species. ^{1}H NMR signals at 0.8, 0.5, and –0.1 ppm are assigned to methyl groups. Similar to the ^{1}H spectra of unmodified deAl-Y, these ^{1}H NMR signals evolve as the reaction progresses, indicating variation in the types of adsorbed species.

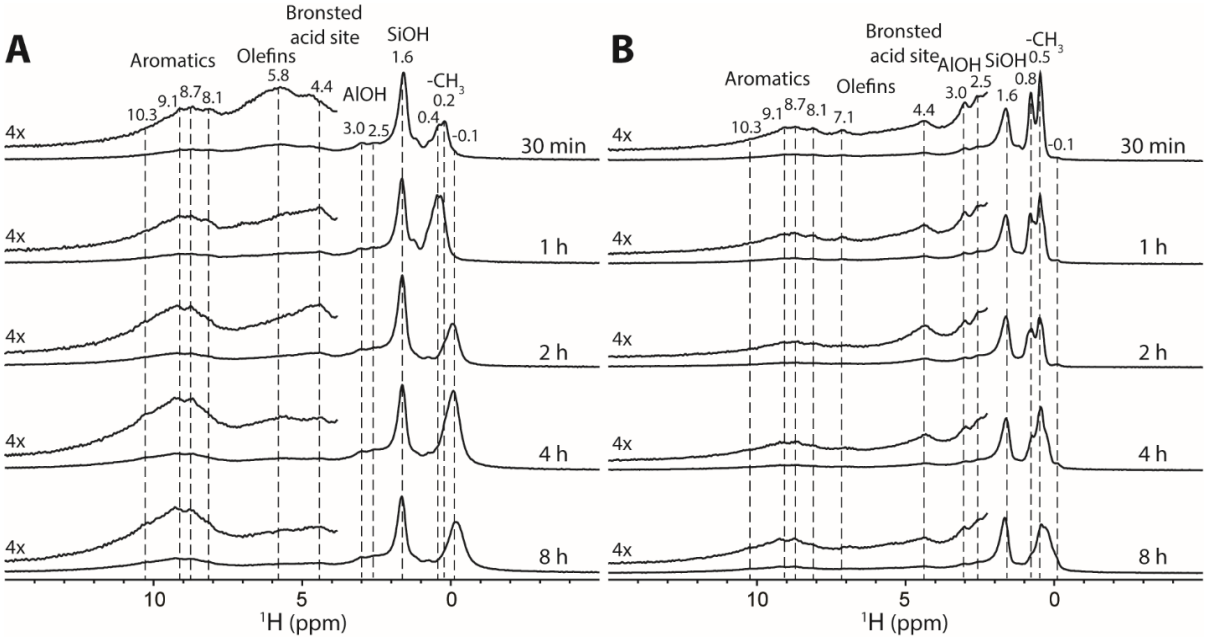

Figure 5. Solid-state direct-excitation ^{1}H NMR spectra of (A) unmodified-deAl-Y and (B) 1.0-ETPS/Al-deAl-Y after quenching the hexane cracking reaction at 0.5, 1, 2, 4, and 8 h. After quenching the reaction, the sealed reactor tube was transferred to an inert atmosphere and the zeolite was prepared for NMR without exposure to ambient air. Spectra were acquired at 11.7 T under 30 kHz MAS at room temperature.

While it is clear that the types of adsorbates on the unmodified deAl-Y and 1.0-ETPS/Al-deAl-Y evolve differently, solid-state direct-excitation ^{1}H NMR does not provide direct information on the types of species in close proximity to Bronsted acid sites. 2D correlative NMR techniques such as the solid-state 2D ^{27}Al–^{29}Si *J*-HMQC NMR spectra discussed above are challenging to acquire and interpret for dehydrated zeolites, as the ^{27}Al NMR signals broaden substantially in absence of water.[46] However, indirect detection NMR methods like S-RESPDOR can be used to analyze ^{1}H spectra of only species in close proximity to ^{27}Al.[47] These measurements have been used in the past to identify adsorbed species on heterogeneous catalysts.[48–50] In a ^{1}H-^{27}Al S-RESPDOR experiment, two NMR spectra are acquired, one of all ^{1}H nuclei in the sample (S_0), and one where NMR signals from ^{1}H species with strong through-space dipole-dipole couplings to ^{27}Al are depleted (S). Thus, a difference spectrum ($S_0 - S$) reveals only the ^{1}H NMR signals that have strong dipole-dipole couplings with ^{27}Al.

Solid-state 1D ^{1}H{^{27}Al} S-RESPDOR NMR difference spectra of unmodified deAl-Y and 1.0-ETPS/Al-deAl-Y after different times on stream are shown in Figure 6. Analyses of the S and S_0 spectra resulting in these difference spectra are shown in Figures S8 and S9 and are discussed in detail in the Supporting Information. The ^{1}H NMR difference spectra of unmodified deAl-Y after 0.5, 1, 2, 4, and 8 h on stream in Figure 6A show ^{1}H NMR signals at 1.6 ppm and 4.4 ppm which are assigned to silanol and Bronsted acid ^{1}H, respectively. In addition, signal at 2.5 ppm is assigned to AlOH species. More importantly, a ^{1}H NMR signal at 6.4 ppm is assigned to olefinic ^{1}H, and ^{1}H NMR signals at 8.7 and 10.3 ppm are assigned to aromatic ^{1}H. A minor signal at 0.8 ppm is assigned to methyl groups. Critically, the ^{1}H signal regions assigned to olefin and aromatic species evolve with increasing time on stream. After

30 min on stream, a strong, narrow ^{1}H NMR signal attributed at olefins at 6.4 ppm is observed. After 1 h on stream, this signal broadened, and is not easily distinguishable at longer times on stream. In contrast, an aromatic ^{1}H NMR signal at 10.3 ppm starts to build up after 2 h on stream and is prominent in both the 4 h and 8 h time-on-stream spectra. These spectra show that adsorbed species located on aluminum species become more polyaromatic with increased time on stream, consistent with deactivation by coke formation.

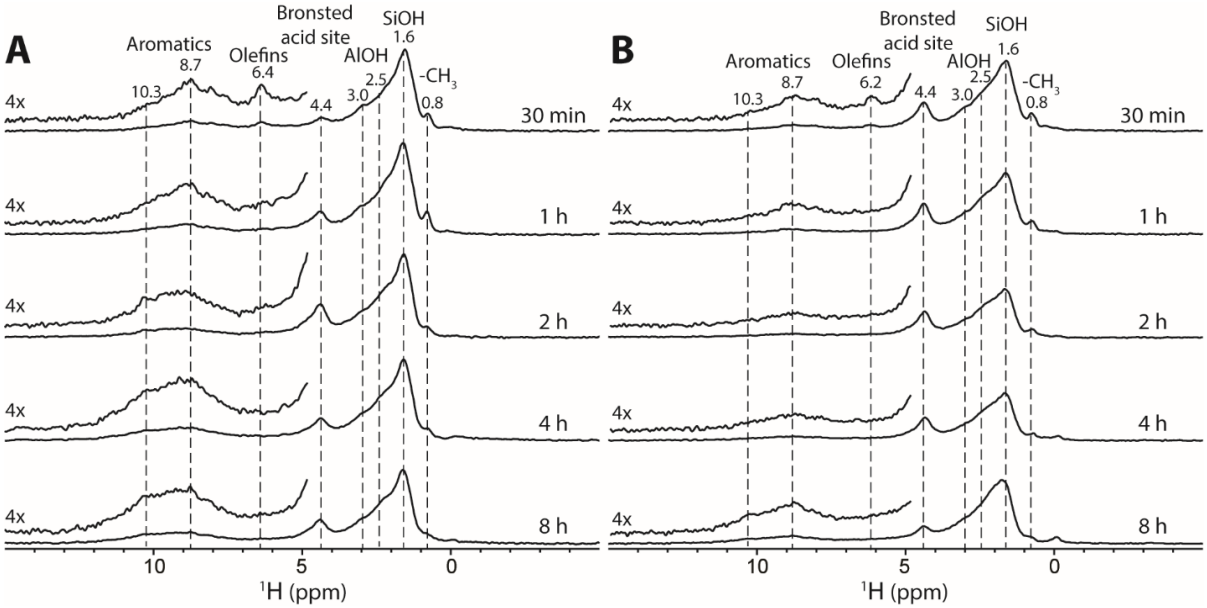

Figure 6. Solid-state 1D ^{1}H{^{27}Al} S-RESPDOR difference NMR spectra of (A) unmodified-deAl-Y and (B) 1.0-ETPS/Al-deAl-Y after quenching the hexane cracking reaction at 0.5, 1, 2, 4, and 8 h. After quenching the reaction, the sealed reactor tube was transferred to an inert atmosphere and the zeolite was prepared for NMR without exposure to ambient air. Spectra shown are obtained by taking the difference of a ^{1}H NMR spectrum (S_0), and a ^{1}H NMR spectrum acquired under the same conditions but with ^{1}H signals from species in sub-nanoscale proximity to ^{27}Al depleted (S). All S and S_0 spectra are shown in Figure SX-SY. Spectra were acquired at 11.7 T under 30 kHz MAS at room temperature.

The ^{1}H NMR difference spectra acquired of 1.0-ETPS/Al-deAl-Y after different times on stream in Figure 6B show similar signal distributions but different trends with respect to time on stream. Similar signals to those observed of unmodified deAl-Y at 1.6 ppm, 2.5 ppm, and 4.4 ppm are assigned to silanol, AlOH, and Bronsted acid ^{1}H moieties. A ^{1}H NMR signal

at 6.2 ppm is assigned to olefinic ^{1}H species, and ^{1}H NMR signals at 8.7 and 10.3 ppm are assigned to aromatic ^{1}H species. A ^{1}H NMR signal at 0.8 ppm is assigned to methyl groups. Similar to the spectra of unmodified deAl-Y, the ^{1}H signal region assigned to olefinic species depletes over time after being very well-defined after 30 min on stream. However, unlike for unmodified deAl-Y, a significant ^{1}H NMR signal in the aromatic region at 10.3 ppm does not start to clearly develop until after 8 h on stream, indicating that the growth of polyaromatic species closely associated with framework aluminum sites is not significant in the ETPS-modified catalyst. This suggests that these polyaromatic species are likely responsible for the observed rapid decrease in activity for the unmodified deAl-Y over the first 4 h on stream. Given that the primary structural difference between the unmodified and ETPS-modified catalyst is acid sites on the mesopore surface, this clearly shows that these sites are more susceptible to polyaromatic growth of coke species than acid sites in the zeolite micropores.

Conclusions

Dealuminated zeolites have a complex distributions of acid sites exposed to both internal zeolite micropores and external mesopores that are both active for hydrocarbon conversion reactions, including catalytic cracking. Here, we used a simple silylation with a bulky organosilane to modify the external and mesopore surfaces of a commercial deAl-Y zeolite catalyst. This modification of the external surface results in a passivation of active sites that are highly susceptible to deactivation during a hexane cracking reaction. Solid-state 2D ^{27}Al–^{29}Si *J*-HMQC NMR spectra reveal a complex distribution of Si–O–Al moieties assigned to the internal micropores or external and mesopore surfaces of the zeolite and show that the silylation procedure results in a modification of mesopore Si–O–Al moieties. Further advanced solid-state NMR measurements conclusively show that the bulky modifying organosilane is

located near these mesopore sites. Measurement of catalysts taken from the reactor after various hexane cracking reaction times reveal more significant buildup of coke species on the unmodified deAl-Y catalyst than the passivated deAl-Y catalyst. Solid-state ^{1}H NMR spectra of the catalyst after different hexane cracking reaction times reveal that adsorbed polyaromatic compounds develop more rapidly over the unmodified deAl-Y than the modified deAl-Y. Furthermore, these bulky polyaromatic species are located in sub-nanoscale proximity to aluminum atoms in the deAl-Y catalyst. Taken together, these measurements identify mesopore acid sites in dealuminated zeolite Y and show that these acid sites are associated with both high activity but rapid deactivation by coke formation. This workflow could be extended to better understand distributions of active sites in zeolites synthesized to have unusual morphologies or mesopores and helps to better inform design of zeolite catalysts for situation where deactivation by coke formation is undesirable.

Supporting Information

Materials and Methods

Materials. The parent material labeled ‘deAl-Y’ in this manuscript is a commercial zeolite Y, CBV-720, purchased from Zeolyst. According to the manufacturer, the material has a Si/Al = 15.

Post-synthetic modification with ethoxytriphenysilane (ETPS). DeAl-Y was dehydrated under vacuum to remove adsorbed water. Under vacuum, the powder sample was heated to 450 ºC at a rate of 2 ºC/min. The sample was held at 450 ºC for 2 h, after which the dehydration vessel was sealed and cooled to room temperature. Approximately 1 g of the dehydrated deAl-Y was then transferred to a round bottom flask containing 25 mL of hexane (Sigma Aldrich, ACS reagent grade). A suitable amount of ethoxytriphenysilane (TCI America) was added to the mixture to provide a molar ratio of either 0.5 ETPS/Al or 1.0 ETPS/Al in solution. The mixture was stirred under reflux conditions at 69 ºC for 16 h. The same batch of deAl-Y, hexane, and ETPS was used for all modifications to ensure observed differences were not due to batch-to-batch product variation. After 16 h, the mixture was cooled, vacuum filtered, and rinsed with excess hexane. After vacuum filtration, the solids were dried in air in an oven at 80 ºC for 2 h. The solids were then calcined in flowing dry air (Airgas, Ultra Zero grade). The solids were heated from room temperature to 560 ºC at a rate of 1 ºC/min in 1.0 SLM dry air and held at 560 ºC for 6 h under the same flow conditions. The resulting samples are assigned the names 0.5-ETPS/Al-deAl-Y and 1.0-ETPS/Al-deAl-Y.

X-ray diffraction. Powder X-ray diffraction analyses were conducted on a Panalytical Empyrean Powder Diffractometer with a Cu-Kα radiation source. Samples were dispersed on

a zero-background plate (MTI Corporation), and diffraction patterns were then measured from 2θ 5° to 50°. A background was subtracted from the data for clarity of presentation.

Solid-state ^{29}Si nuclear magnetic resonance (NMR) spectroscopy. Prior to measurement, samples were hydrated for at least 24 h in a closed vessel containing a saturated solution of potassium chloride to maintain a relative humidity of approximately 85%. Solid-state 1D direct-excitation ^{29}Si magic-angle-spinning (MAS) NMR spectra were acquired at 11.7 T at room temperature on a 500 MHz Bruker Avance NMR spectrometer using a 4 mm zirconia rotor at a MAS frequency of 12.5 kHz. 64 scans were acquired with a 90° 50 kHz radiofrequency (r.f.) excitation pulse applied to ^{29}Si nuclei. SPINAL-64 heteronuclear decoupling was applied to ^{1}H nuclei during acquisition.[51] A 300 s recycle delay was used between scans in order to ensure full T_1 relaxation of ^{29}Si spins. ^{29}Si NMR chemical shifts were referenced to tetramethylsilane at 0 ppm using a secondary reference of tetrakis(trimethylsilyl)silane as a secondary reference at –9.84 ppm. Spectra were deconvoluted using Dmfit.[52]

Solid-state ^{27}Al NMR spectroscopy. Prior to measurement, samples were hydrated for at least 24 h in a closed vessel containing a saturated solution of potassium chloride to maintain a relative humidity of approximately 85%. Solid-state 1D ^{27}Al spin-echo NMR spectra were acquired at 18.8 T at room temperature using a 800 MHz Bruker Avance NMR spectrometer with a 3.2 mm zirconia rotor spinning at a MAS frequency of 20 kHz. 83.3 kHz ^{27}Al r.f. pulses were used for the 90° and 180° pulses of the echo pulse sequence with a tau delay equivalent to one rotor period. 512 scans were acquired with a recycle delay of 0.5 s. ^{27}Al shifts were referenced to an aqueous solution of 0.5 M aluminum nitrate at 0 ppm. Spectra were deconvoluted using Dmfit.

N_2 physisorption. N_2 physisorption isotherms were acquired at 77 K on a Micrometrics 3Flex Porosimeter. Approximately 100 mg of hydrated zeolite was loaded into the instrument. The sample was then dehydrated *in situ* for 8 h at 300 ºC with a temperature ramp of 1 ºC/min. After dehydration and cooling to room temperature, the sample was submerged in liquid nitrogen and dosed with N_2 gas.

Ammonia temperature-programmed desorption (TPD). NH_3-TPD was performed on a Micrometrics AutoChem II 2920 Chemisorption analyzer equipped with a thermal conductivity detector (TCD) to monitor outlet gas. Approximately 50 mg of powder catalyst was loaded into the instrument. Samples were then dehydrated in flowing helium (Airgas, ultrahigh purity) at 450 ºC for 2 h with a temperature ramp rate of 2 ºC/min. Samples were then cooled to 120 ºC in flowing helium, at which point the sample was exposed to flowing 10% NH_3 in helium (Airgas) for 2 h. The system was then purged with flowing helium for 2 h at 120 ºC. A TPD measurement was then performed by tracking the desorption of NH_3 as the temperature was raised from 120 to 700 ºC with a ramp rate of 10 ºC/min in flowing helium. The NH_3 desorption rate was calculated using a TCD calibration curve obtained from 10% NH_3 in helium.

Hexane cracking reaction testing. For hexane cracking reactions, the zeolite catalyst was sieved with 30 mesh (0.6 mm) and 60 mesh (0.25 mm) sieves to control particle size. 50 mg of the middle fraction of sieved catalyst (ranging from 0.25 to 0.6 mm diameter) was suspended in a ¼''-inch stainless-steel tube between two plugs of quartz wool. The tube was placed into a home-built furnace and heated from room temperature to 400 ºC under flowing helium (Airgas, ultrahigh purity) at a rate of 2 ºC/min. The temperature was tracked by a thermocouple

in contact with the stainless-steel tube level with the plug of catalyst. Once the reactor temperature reached 400 ºC, a flow of 3 SCCM helium was bubbled through hexane (Sigma Aldrich, ACS reagent grade) at room temperature of approximately 20 ºC and diluted in a 12 SCCM flow of pure helium resulting in a reactant stream containing approximately 3 kPa hexane. Mixed hexanes were used as more coke buildup was expected with branched compounds than with pure n-hexane. The same batch of hexane was used for all measurements to eliminate differences caused by batch-to-batch variation. This reactant stream was fed into the heated catalyst bed. The resulting product distribution in the product stream was measured with a SRI Instruments 8610C Gas Chromatograph equipped with a flame ionization detector and a 6' alumina packed column. Starting at 5 min on stream, product distribution measurements were taken with the gas chromatograph every 25 min until 730 min on stream utilizing an autosampling valve. The resulting product distributions were calculated using calibrations made from mixtures of 1000 ppm C1-C6 paraffins in He (Sigma Aldrich) and 100 ppm C2-C6 olefins in He (Sigma Aldrich).

Catalysts intended for analysis of adsorbed species by thermogravimetric analysis and NMR were removed from the reactor at 0.5, 1, 2, 4, and 8 h on stream. The catalyst bed and reaction were prepared the same as described above, and the reaction proceeded under the same conditions. At the given time point, the ¼''-inch stainless-steel tube containing the catalyst was sealed off from the reactor at both ends. This tube was then cooled to room temperature and removed from the system. The tube was transferred into an argon-atmosphere glovebox, at which point the tube was opened and the catalyst was removed. The catalyst with adsorbed species was then stored in the glovebox at room temperature until needed for analysis.

Solid-state 2D ^{27}Al–^{29}Si *J*-HMQC NMR. Solid-state 2D ^{27}Al–^{29}Si *J*-HMQC NMR spectra were acquired on samples hydrated as described above. The measurements were performed at 9.4 T and 100 K on a 400 MHz Bruker Ascend NMR spectrometer equipped with a triple-resonance Bruker NMR probehead with a 3.2 mm zirconia rotor at an MAS frequency of 8 kHz. 32 indirect increments of 1024 scans were acquired with a t_1 increment of 250 μs and a recycle delay of 1 s. 25 kHz r.f. pulses were used for ^{29}Si excitation, and 15.6 kHz r.f. pulses were applied to ^{27}Al nuclei. A tau delay of 17.5 ms was used to allow *J*-couplings between ^{27}Al and ^{29}Si nuclei to evolve. High-powered heteronuclear continuous-wave decoupling was applied to ^{1}H nuclei during tau delays, and SPINAL-64 decoupling was applied to ^{1}H nuclei during t_1 evolution and acquisition. A 1 ms double-frequency-sweep shaped pulse with an offset of 100 kHz to 1 MHz was applied to ^{27}Al nuclei prior to excitation.[53] ^{27}Al and ^{29}Si chemical shifts were referenced at room temperature as described above.

Solid-state 2D ^{29}Si{^{1}H} HETCOR NMR. An uncalcined 1.0-ETPS/Al-deAl-Y sample was packed in a 3.2 mm zirconia MAS NMR rotor for solid-state 2D ^{29}Si{^{1}H} HETCOR NMR analysis. The spectrum was acquired at 9.4 T and 100 K on a 400 MHz Bruker Ascend NMR spectrometer at an MAS frequency of 8 kHz. 64 indirect dimension increments of 512 scans were acquired with a t_1 delay of 96 μs and a recycle delay of 1 s between scans. A 50 kHz r.f. pulse was used for initial excitation of ^{1}H nuclei, and a 1 ms cross-polarization contact pulse was used to transfer polarization from ^{1}H to ^{29}Si nuclei. To enhance resolution of the ^{1}H dimension, eDUMBO-1$_{22}$ homonuclear decoupling was applied to the ^{1}H nuclei.[54] SPINAL-64 heteronuclear decoupling was applied to ^{1}H nuclei during acquisition.

Thermogravimetric analysis (TGA). TGA was performed on post-reaction deAl-Y zeolites. Zeolite samples were taken from the glovebox and transferred in a sealed vial. Approximately 5 mg of sample was loaded into the sample pan of a Discovery TGA 5500, working quickly to minimize air exposure. Under 25 SCCM flowing argon, the furnace temperature was ramped from room temperature to 450 ºC. The temperature was held at 450 ºC for 15 min, during which time the mass of the sample remained constant. The sample was then ramped from 450 to 750 ºC in flowing dry air at 25 SCCM and held at 750 ºC for 15 min. The reported mass of coke in Figure 4 is the relative loss of mass from 450 ºC to 750 ºC compared to the remaining mass of catalyst at 750 ºC.

Solid-state ^{1}H NMR. Solid-state 1D direct-excitation ^{1}H MAS NMR spectra were acquired at 11.7 T at room temperature on a 500 MHz Bruker Avance NMR Spectrometer with a 2.5 mm zirconia rotor at an MAS frequency of 30 kHz. Post-reaction samples were packed in NMR rotors in an argon glovebox and were transferred quickly to the spectrometer, where they were spun with N_2 gas. 256 scans were acquired with a recycle delay of 10 s, which was found to be sufficient for full relaxation. A 50 kHz 90º r.f. pulse was used to excite ^{1}H nuclei. EASY background subtraction with a delay of 10 ms to remove a broad ^{1}H background from the probe.[55] ^{1}H NMR chemical shifts were referenced to tetramethylsilane at 0 ppm using tetrakis(trimethylsilyl)silane as a secondary reference at 0.25 ppm.

Solid-state 2D ^{1}H–^{1}H SQ-DQ NMR. Solid-state 2D ^{1}H-^{1}H single-quantum–double-quantum NMR spectra were acquired at 11.7 T at room temperature on a 500 MHz Bruker Avance NMR Spectrometer with a 2.5 mm zirconia rotor at an MAS frequency of 30 kHz. Post-reaction samples were packed in NMR rotors in an argon glovebox and were transferred quickly to the spectrometer, where they were spun with N_2 gas. 96 indirect dimension increments of 128

scans were acquired with a t_1 increment of 66.7 μs and a recycle delay of 1 s. 50 kHz r.f. pulses were used for ^{1}H excitation. A presaturation pulse train was used to ensure consistent ^{1}H magnetization at the start of each scan. The BaBa-xy16 homonuclear double-quantum recoupling pulse sequence was used to recouple proximate ^{1}H spins through homonuclear ^{1}H–^{1}H dipole-dipole couplings with a total recoupling time of 267 μs.[56] ^{1}H chemical shifts were referenced as described above.

Solid-state ^{1}H{^{27}Al} S-RESPDOR NMR. Solid-state ^{1}H{^{27}Al} S-RESPDOR NMR analyses were acquired at 11.7 T at room temperature on a 500 MHz Bruker Avance NMR Spectrometer with a 2.5 mm zirconia rotor at an MAS frequency of 30 kHz.[47] Post-reaction samples were packed in NMR rotors in an argon glovebox and were transferred quickly to the spectrometer, where they were spun with N_2 gas. 16384 scans were acquired for both the S and S_0 spectra, with alternating scans for the S and S_0 spectra. A recycle delay of 1 s was used, with a presaturation pulse train applied to ^{1}H nuclei prior to each scan to ensure consistent ^{1}H magnetization for each scan. 50 kHz r.f. pulses were used for ^{1}H pulses other than dipolar recoupling blocks. SR4$^2_1$ symmtery-based recoupling was used to couple proximate ^{1}H and ^{27}Al nuclei through ^{1}H–^{27}Al dipole-dipole couplings with a 60 kHz r.f. pulse and a total recoupling time of 2 ms.[57] For the S spectrum, a 50 μs high-powered saturation pulse was applied to ^{27}Al nuclei. ^{1}H chemical shifts were referenced as described above.

Basic characterization

Powder X-ray diffraction was performed on the parent deAl-Y material and also the modified materials after deposition of ETPS and calcination to remove the organic component. Figure S1 shows powder X-ray diffraction patterns for unmodified deAl-Y, 0.5-ETPS/Al-deAl-Y, and 1.0-ETPS/Al-deAl-Y. The diffraction pattern of each material consists of sharp

diffraction peaks that are indexed to the zeolite Y (faujasite) crystal structure. No broad features are observed that would be associated with significant amorphous regions of materials. Crucially, the observed diffraction pattern does not change as a result of modification with ETPS, indicating that the modification does not cause undesirable changes to the bulk crystal structure.

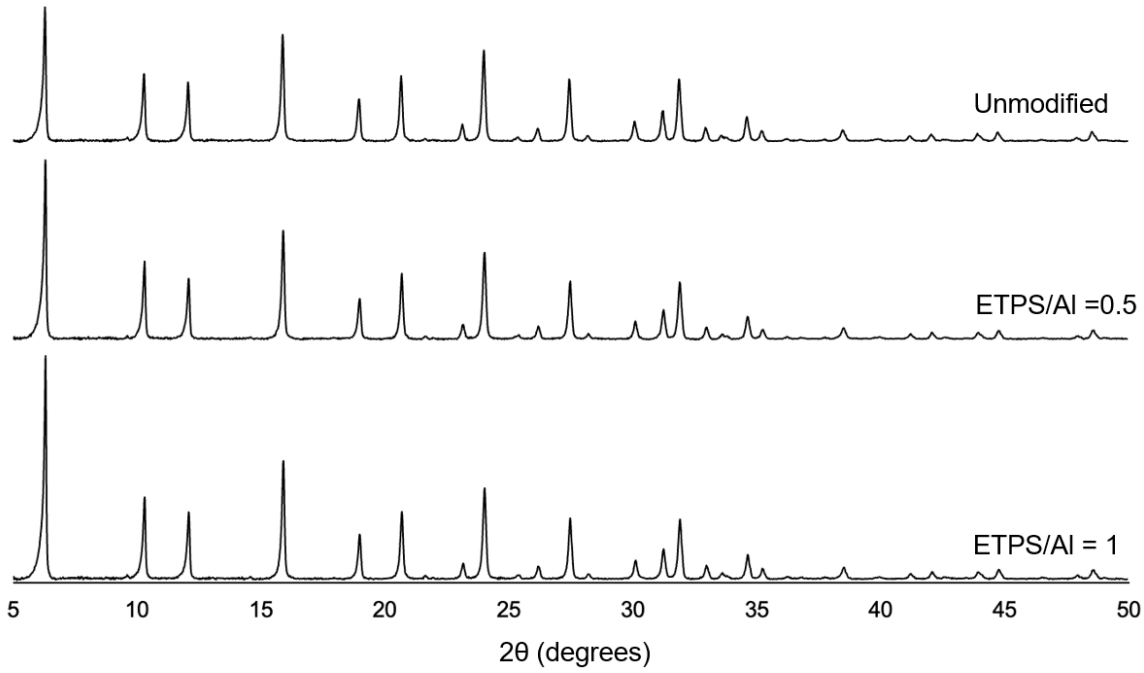

Figure S1. Powder X-ray diffraction patterns of unmodified deAl-Y, 0.5-ETPS/Al-deAl-Y and 1.0-ETPS/Al-deAl-Y.

Solid-state 1D direct-excitation ^{29}Si MAS NMR spectra were acquired of the unmodified deAl-Y, 0.5-ETPS/Al-deAl-Y, and 1.0-ETPS/Al-deAl-Y to assess if the local ^{29}Si chemical environments changed significantly because of ETPS deposition. For all three materials, three main signals are observed at –111, –107, and –101 ppm, which are attributed to disordered Q^4, zeolite Y Q^4(0Al), and zeolite Y Q^4(1Al) moieties, respectively.[58] There is also a weak shoulder from –90 to –100 ppm present in all materials that is likely a result of disordered surface species. The three signals integrated in Figure S2 indicate that there are not

significant changes in the relative distributions of ^{29}Si nuclei between these three chemical environments a result of the ETPS treatment, though there is broadening of signals associated with Q^4(1Al) and disordered Q^4 moieties in the ^{29}Si NMR spectrum of 1.0-ETPS/Al-deAl-Y that makes deconvolution more uncertain. Though ETPS is deposited on the material, even at full deposition for 1.0-ETPS/Al-deAl-Y this would only account for 6% of the total intensity of the ^{29}Si NMR spectrum, a difference that is difficult to detect with these broad signals.

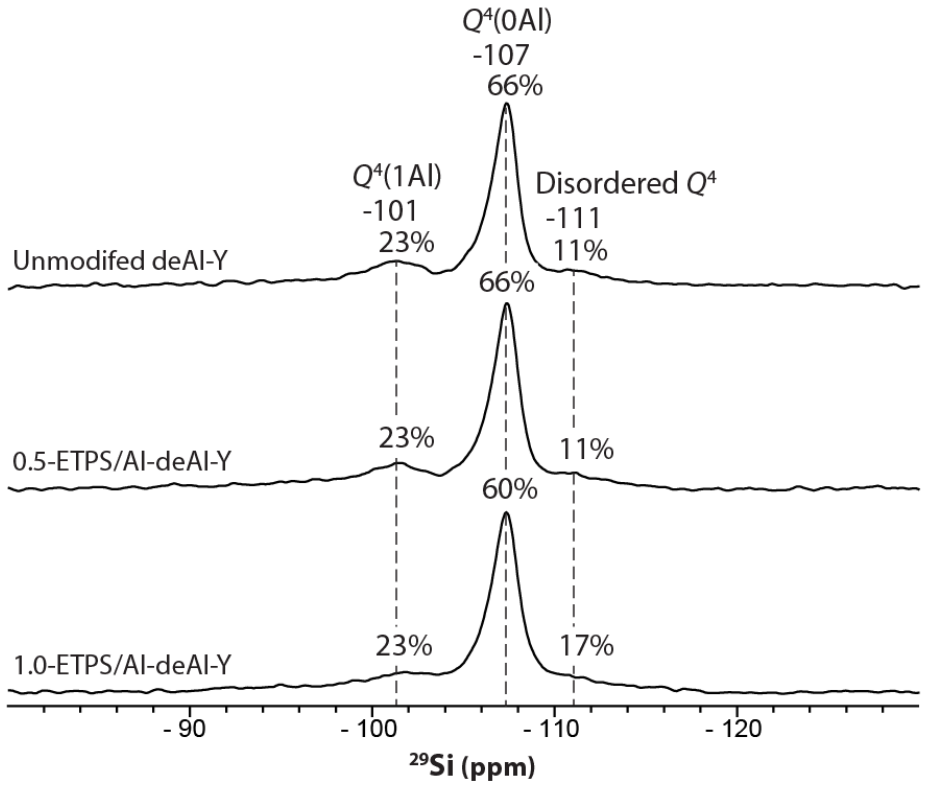

Figure S2. Solid-state 1D direct-excitation ^{29}Si MAS NMR spectra of hydrated unmodified deAl-Y, 0.5-ETPS/Al-deAl-Y, and 1.0-ETPS/Al-deAl-Y. The spectra were acquired at 11.7 T and 12.5 kHz MAS at room temperature.

Solid-state 1D ^{27}Al spin echo NMR spectra were acquired of the unmodified deAl-Y, 0.5-ETPS/Al-deAl-Y, and 1.0-ETPS/Al-deAl-Y to assess if the local chemical environments of aluminum species changed significantly as a result of ETPS deposition. Four ^{27}Al NMR signals are detected for each material at 61, 58, 0 and –2 ppm. The ^{27}Al NMR signals at 61

ppm and 58 ppm are assigned to four coordinate ^{27}Al species. The signal at 61 ppm is consistent with literature reports of pristine zeolite Y framework $^{27}Al^{IV}$, and the shoulder at 58 ppm is similar to previous observations of $^{27}Al^{IV}$ species that are in distorted environments as a result of zeolite steam treatment.[59] The two NMR signals at 0 and –2 ppm are assigned to Al^{VI} species resulting from steam-aging of the zeolite. The narrowness of the ^{27}Al NMR signal at 0 ppm is attributed to hydration.[60] While broadening of $^{27}Al^{IV}$ NMR signals is observed as a result of ETPS-modification, there are only minor differences in the distributions of ^{27}Al NMR signals observed of the different materials, indicating that the ETPS deposition does not have a side effect of dealuminating the zeolite framework in any significant quantities.

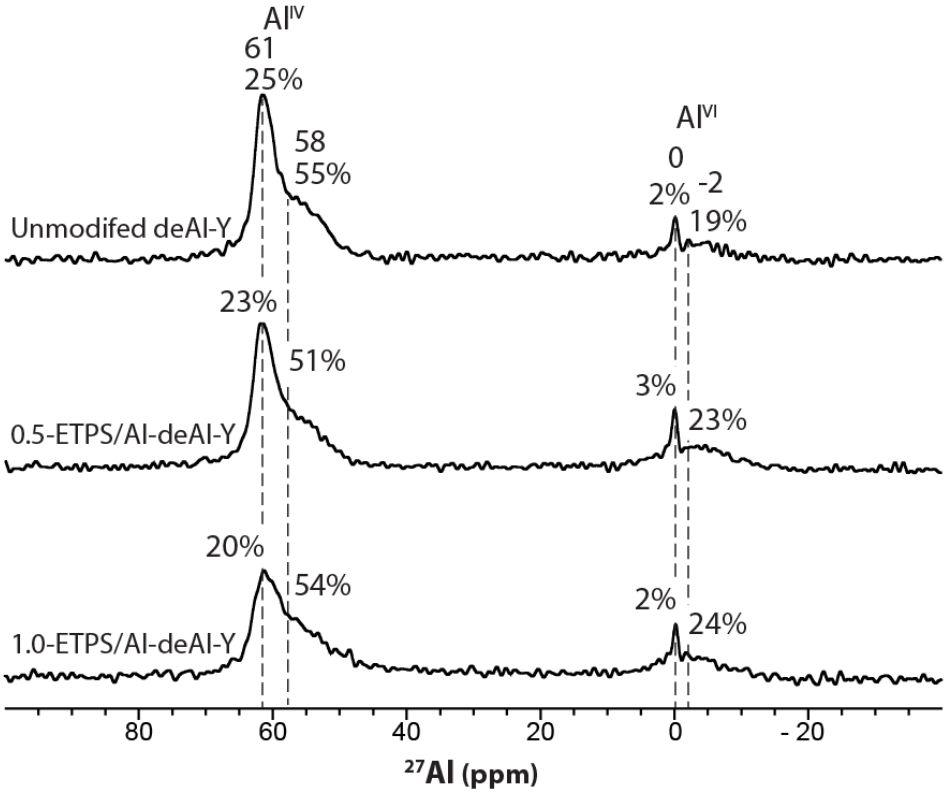

Figure S3. Solid-state 1D ^{27}Al spin-echo NMR spectra of hydrated unmodified deAl-Y, 0.5-ETPS/Al-deAl-Y, and 1.0-ETPS/Al-deAl-Y. The spectra were acquired at 18.8 T and 20 kHz MAS at room temperature.

N_2 physisorption isotherms at 77 K were obtained for the unmodified deAl-Y, 0.5-ETPS/Al-deAl-Y, and 1.0-ETPS/Al-deAl-Y to assess if ETPS deposition resulted in changes in the distributions of micropore and mesopores. These isotherms are shown in Figure S4. The micropore surface area, mesopore surface area, and micropore pore volume as determined by the t-plot method are shown in Table S1. The unmodified deAl-Y was measured to have a micropore surface area of 410 m^2/g, a mesopore surface area of 170 m^2/g, and a micropore volume of 0.20 cm^3/g. These values did not change for the ETPS-modified materials, indicating that there is not a significant blockage of pores resulting from the ETPS modification. It should be noted that the t-plot method has been shown to be inadequate in some situations for calculating micropore surface areas for hierarchical materials with both micro- and mesopores.[61] However, the values can still be compared across these similar samples to assess changes resulting from the modification.

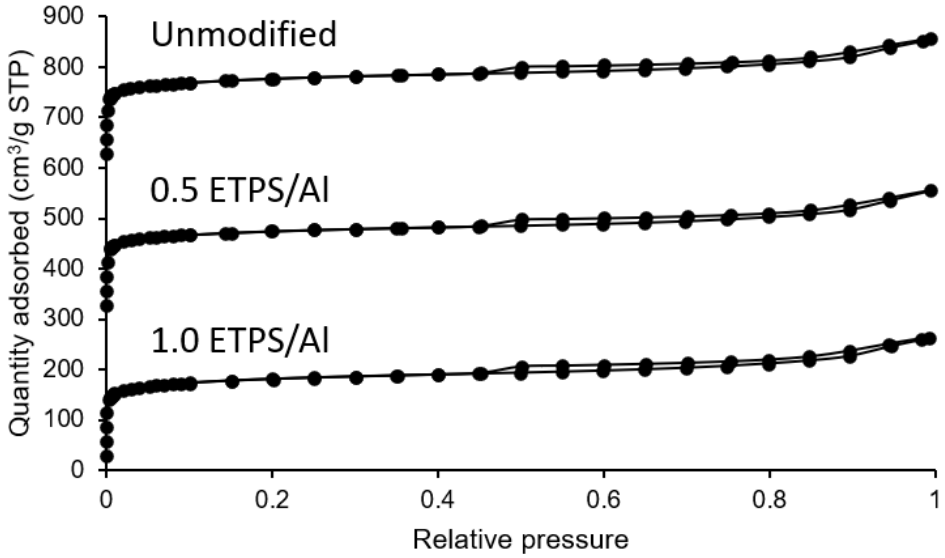

Figure S4. N_2 physisorption isotherms at 77 K for unmodified deAl-Y, 0.5-ETPS/Al-deAl-Y, and 1.0-ETPS/Al-deAl-Y. The isotherms are offset by 300 cm^3/g STP for each sample for clarity.

Table S1. Surface areas and pore volumes calculated from N_2 physisorption

	t-plot micropore surface area (m^2/g)	t-plot mesopore surface area (m^2/g)	t-plot micropore pore volume (cm^3/g)
No modification	410	170	0.20
0.5 ETPS/Al	410	160	0.20
1.0 ETPS/Al	430	170	0.21

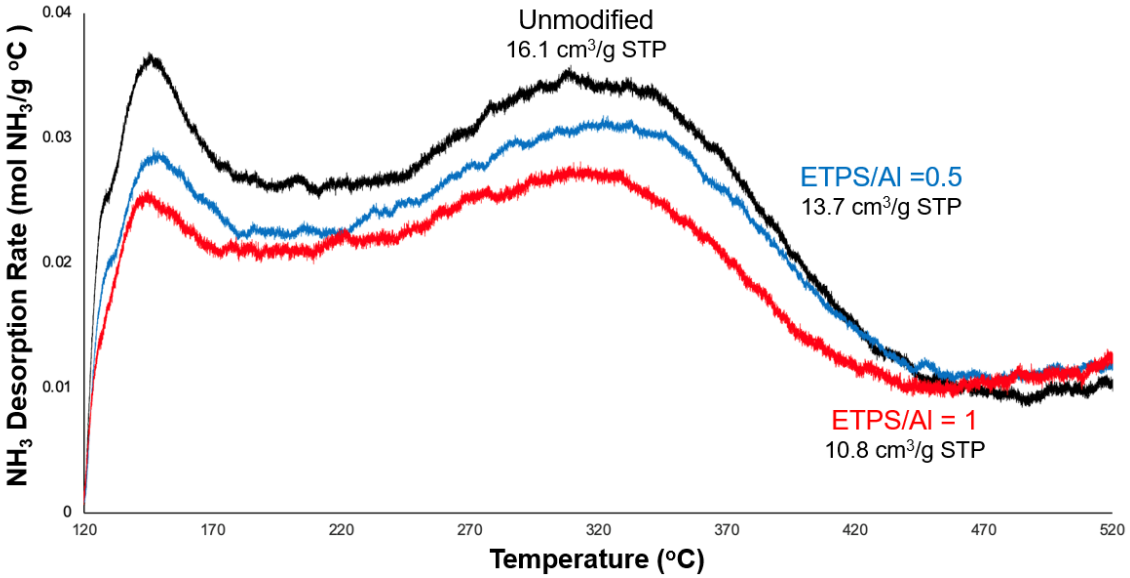

Figure S5. NH_3 temperature-programmed desorption curves of unmodified deAl-Y (black), 0.5-ETPS/Al-deAl-Y (blue), and 1.0-ETPS/Al-deAl-Y (red). Integrated quantities of desorbed NH_3 for each material are shown as labels.

To assess changes in accessibility of acid sites resulting from the ETPS modification, NH_3 temperature programmed desorption was performed on unmodified deAl-Y, 0.5-ETPS/Al-deAl-Y and 1.0-ETPS/Al-deAl-Y and is shown in Figure S5. The high-temperature feature centered at 320 °C is assigned to adsorption on Bronsted acid sites, and lower-temperature features are assigned to adsorption on extraframework aluminum based on previous literature.[62] The total amount of NH_3 desorbed from the unmodified deAl-Y was 16.1 cm^3/g. This value decreased to 13.7 cm^3/g and 10.8 cm^3/g for 0.5-ETPS/Al-deAl-Y and 1.0-ETPS/Al-deAl-Y, respectively, consistent with the blocking of a fraction of the acid sites in the catalyst

by ETPS deposition. Notably, ETPS modification appears to affect both weak and strong adsorption sites.

Hexane cracking reaction data

For clarity, the hexane cracking product selectivites shown in Figure 1B, C, and D are presented as Tables S2-S4. As these selectivities are calculated on a per carbon basis, the total selectivity adds up to 1. In addition, product selectivities presented as moles of product per mole of hexane reacted are shown in Tables S5-S7. These values provide clearer information on the reaction pathways present in the hexane cracking process. Notably, the propylene molar selectivity starts at approximately 1 for all catalysts and increases to above 1.2 for all catalysts at the end of the 12 h on stream measured. Taken with the relatively low selectivity for propane, this is consistent with propylene production requiring multiple reaction steps. Fore example, hexane could crack to form hexene and H_2, and then hexene could crack into two propylene molecules. As a flame ionization detector was used to analyze the product distribution resulting from hexane cracking reactions, H_2 selectivity could not be directly detected. However, H_2 selectivities necessary to close the C and H balances can be easily calculated from the distribution of carbon species detected. These H_2 selectivities are shown in Tables S5 and S7. As expected given the increase in olefin production over time on stream, the H_2 production also increases as a function of time on stream. These H_2 selectivites are consistent with literature reports of hexane cracking reactions performed under similar conditions.[35]

Table S2. Product selectivity of hexane cracking over unmodified deAl-Y on a carbon basis

Time on stream (min)	Selectivity (moles carbon of product/moles carbon reacted)							
	C_1	C_2-P	C_2-O	C_3-P	C_3-O	C_4-P	C_4-O	C_5-P
5	0.02	0.03	0.07	0.22	0.46	0.09	0.08	0.03
30	0.02	0.03	0.06	0.20	0.49	0.08	0.08	0.03
55	0.02	0.03	0.06	0.18	0.51	0.08	0.08	0.03
80	0.02	0.03	0.06	0.17	0.53	0.07	0.08	0.03
105	0.02	0.03	0.06	0.17	0.54	0.07	0.08	0.03
130	0.02	0.03	0.06	0.16	0.54	0.07	0.08	0.03
155	0.02	0.03	0.06	0.16	0.55	0.06	0.08	0.03
180	0.02	0.03	0.06	0.16	0.56	0.06	0.08	0.03
205	0.02	0.03	0.06	0.15	0.56	0.06	0.08	0.03
230	0.02	0.03	0.06	0.15	0.56	0.06	0.09	0.03
255	0.02	0.03	0.06	0.15	0.57	0.06	0.09	0.03
280	0.02	0.03	0.05	0.15	0.58	0.06	0.09	0.03
305	0.02	0.03	0.05	0.15	0.59	0.06	0.09	0.03
330	0.02	0.03	0.05	0.14	0.59	0.05	0.09	0.03
355	0.02	0.03	0.05	0.14	0.59	0.05	0.09	0.03
380	0.02	0.03	0.05	0.14	0.60	0.05	0.09	0.03
405	0.02	0.03	0.05	0.14	0.60	0.05	0.09	0.03
430	0.02	0.03	0.05	0.14	0.60	0.05	0.09	0.03
455	0.02	0.03	0.05	0.13	0.60	0.05	0.09	0.03
480	0.02	0.03	0.05	0.13	0.61	0.05	0.09	0.03
505	0.03	0.03	0.05	0.13	0.61	0.05	0.09	0.03
530	0.03	0.03	0.05	0.13	0.61	0.05	0.09	0.03
555	0.03	0.03	0.05	0.13	0.61	0.05	0.09	0.03
580	0.03	0.03	0.04	0.13	0.61	0.05	0.09	0.03
605	0.03	0.03	0.04	0.13	0.62	0.05	0.09	0.03
630	0.03	0.03	0.04	0.13	0.62	0.04	0.09	0.03
655	0.03	0.02	0.04	0.13	0.62	0.04	0.09	0.03
680	0.03	0.02	0.04	0.12	0.62	0.04	0.09	0.03
705	0.03	0.03	0.05	0.12	0.63	0.02	0.09	0.03
730	0.03	0.03	0.05	0.12	0.64	0.02	0.09	0.03

Table S3. Product selectivity of hexane cracking over 0.5-ETPS/Al-deAl-Y on a carbon basis

Time on stream (min)	Selectivity (moles carbon of product/moles carbon reacted)							
	C_1	C_2-P	C_2-O	C_3-P	C_3-O	C_4-P	C_4-O	C_5-P
5	0.01	0.03	0.06	0.21	0.49	0.10	0.08	0.03
30	0.02	0.03	0.05	0.19	0.51	0.09	0.08	0.04
55	0.02	0.03	0.05	0.18	0.53	0.08	0.08	0.04
80	0.02	0.03	0.05	0.17	0.54	0.08	0.08	0.04
105	0.02	0.02	0.04	0.17	0.55	0.08	0.08	0.04
130	0.02	0.02	0.04	0.17	0.56	0.07	0.08	0.04
155	0.02	0.02	0.04	0.17	0.56	0.07	0.08	0.03
180	0.02	0.02	0.04	0.16	0.57	0.07	0.08	0.03
205	0.02	0.02	0.04	0.16	0.57	0.07	0.08	0.03
230	0.02	0.02	0.04	0.16	0.57	0.07	0.08	0.03
255	0.02	0.02	0.04	0.16	0.58	0.07	0.08	0.03
280	0.02	0.02	0.04	0.15	0.58	0.07	0.08	0.03
305	0.02	0.02	0.04	0.15	0.58	0.07	0.08	0.03
330	0.02	0.02	0.04	0.15	0.58	0.07	0.08	0.03
355	0.02	0.02	0.04	0.15	0.59	0.07	0.08	0.03
380	0.02	0.02	0.04	0.15	0.59	0.07	0.08	0.03
405	0.02	0.02	0.04	0.15	0.59	0.06	0.08	0.03
430	0.02	0.02	0.04	0.15	0.59	0.06	0.08	0.03
455	0.02	0.02	0.04	0.14	0.59	0.06	0.08	0.03
480	0.02	0.02	0.04	0.14	0.60	0.06	0.08	0.03
505	0.02	0.02	0.04	0.14	0.60	0.06	0.08	0.03
530	0.02	0.02	0.04	0.14	0.60	0.06	0.08	0.03
555	0.02	0.02	0.04	0.14	0.60	0.06	0.09	0.03
580	0.02	0.02	0.04	0.14	0.60	0.06	0.09	0.03
605	0.02	0.02	0.04	0.14	0.60	0.06	0.09	0.03
630	0.02	0.02	0.04	0.14	0.60	0.06	0.09	0.03
655	0.02	0.02	0.04	0.14	0.60	0.06	0.09	0.03
680	0.02	0.02	0.04	0.14	0.61	0.06	0.09	0.03
705	0.02	0.02	0.04	0.14	0.61	0.06	0.09	0.03
730	0.02	0.02	0.04	0.14	0.61	0.06	0.09	0.03

Table S4. Product selectivity of hexane cracking over 1.0-ETPS/Al-deAl-Y on a carbon basis

Time on stream (min)	Selectivity (moles carbon of product/moles carbon reacted)							
	C_1	C_2-P	C_2-O	C_3-P	C_3-O	C_4-P	C_4-O	C_5-P
5	0.01	0.03	0.05	0.20	0.50	0.09	0.07	0.04
30	0.01	0.03	0.05	0.18	0.52	0.09	0.08	0.05
55	0.02	0.03	0.05	0.16	0.54	0.08	0.08	0.05
80	0.02	0.02	0.04	0.16	0.56	0.08	0.08	0.04
105	0.02	0.02	0.04	0.16	0.57	0.08	0.08	0.04
130	0.02	0.02	0.04	0.15	0.57	0.08	0.08	0.04
155	0.02	0.02	0.04	0.15	0.57	0.08	0.08	0.04
180	0.02	0.02	0.04	0.15	0.58	0.07	0.08	0.04
205	0.02	0.02	0.04	0.15	0.58	0.07	0.08	0.04
230	0.02	0.02	0.04	0.14	0.59	0.07	0.08	0.04
255	0.02	0.02	0.04	0.14	0.59	0.07	0.08	0.04
280	0.02	0.02	0.04	0.14	0.59	0.07	0.08	0.04
305	0.02	0.02	0.04	0.14	0.59	0.07	0.08	0.04
330	0.02	0.02	0.04	0.14	0.59	0.07	0.08	0.04
355	0.02	0.02	0.04	0.14	0.60	0.07	0.08	0.04
380	0.02	0.02	0.04	0.14	0.60	0.07	0.08	0.04
405	0.02	0.02	0.04	0.13	0.60	0.07	0.08	0.04
430	0.02	0.02	0.04	0.13	0.60	0.07	0.08	0.04
455	0.02	0.02	0.04	0.13	0.60	0.06	0.08	0.04
480	0.02	0.02	0.04	0.13	0.60	0.06	0.08	0.04
505	0.02	0.02	0.04	0.13	0.61	0.06	0.08	0.04
530	0.02	0.02	0.04	0.13	0.61	0.06	0.08	0.04
555	0.02	0.02	0.04	0.13	0.61	0.06	0.08	0.04
580	0.02	0.02	0.04	0.13	0.61	0.06	0.08	0.04
605	0.02	0.02	0.04	0.13	0.61	0.06	0.08	0.04
630	0.02	0.02	0.04	0.13	0.61	0.06	0.08	0.04
655	0.02	0.02	0.04	0.13	0.61	0.06	0.08	0.04
680	0.02	0.02	0.04	0.13	0.61	0.06	0.08	0.04
705	0.02	0.02	0.04	0.12	0.61	0.06	0.08	0.04
730	0.02	0.02	0.04	0.12	0.62	0.06	0.08	0.04

Table S5. Product selectivity of hexane cracking over unmodified deAl-Y on molecular basis

Time on stream (min)	Selectivity (moles product/moles hexane reacted)								
	C_1	C_2-P	C_2-O	C_3-P	C_3-O	C_4-P	C_4-O	C_5-P	H_2
5	0.10	0.09	0.21	0.45	0.92	0.14	0.12	0.03	0.18
30	0.12	0.09	0.19	0.40	0.98	0.13	0.12	0.04	0.22
55	0.12	0.10	0.18	0.37	1.03	0.12	0.12	0.04	0.26
80	0.13	0.10	0.18	0.35	1.05	0.11	0.12	0.04	0.28
105	0.13	0.10	0.18	0.34	1.07	0.10	0.12	0.04	0.30
130	0.13	0.10	0.17	0.33	1.09	0.10	0.13	0.04	0.31
155	0.13	0.10	0.17	0.32	1.10	0.10	0.13	0.04	0.32
180	0.13	0.10	0.17	0.31	1.11	0.09	0.13	0.04	0.33
205	0.14	0.10	0.17	0.31	1.12	0.09	0.13	0.04	0.33
230	0.14	0.10	0.17	0.30	1.13	0.09	0.13	0.03	0.34
255	0.14	0.10	0.17	0.30	1.14	0.09	0.13	0.03	0.35
280	0.14	0.08	0.14	0.30	1.17	0.09	0.13	0.04	0.37
305	0.14	0.08	0.14	0.29	1.17	0.08	0.13	0.03	0.37
330	0.14	0.08	0.14	0.29	1.18	0.08	0.13	0.03	0.38
355	0.15	0.08	0.14	0.28	1.19	0.08	0.13	0.03	0.38
380	0.15	0.08	0.14	0.28	1.19	0.08	0.13	0.03	0.39
405	0.15	0.08	0.14	0.27	1.20	0.08	0.13	0.03	0.39
430	0.15	0.08	0.14	0.27	1.20	0.08	0.13	0.03	0.40
455	0.15	0.08	0.14	0.27	1.21	0.07	0.13	0.03	0.40
480	0.15	0.08	0.14	0.27	1.21	0.07	0.13	0.03	0.40
505	0.15	0.08	0.14	0.26	1.22	0.07	0.13	0.03	0.41
530	0.15	0.08	0.14	0.26	1.22	0.07	0.14	0.03	0.41
555	0.15	0.08	0.14	0.26	1.22	0.07	0.14	0.03	0.41
580	0.15	0.08	0.13	0.26	1.23	0.07	0.14	0.03	0.42
605	0.15	0.08	0.13	0.25	1.23	0.07	0.14	0.03	0.42
630	0.15	0.08	0.13	0.25	1.24	0.07	0.14	0.03	0.42
655	0.15	0.07	0.13	0.25	1.24	0.07	0.14	0.03	0.42
680	0.15	0.07	0.13	0.25	1.24	0.07	0.14	0.03	0.43
705	0.16	0.08	0.14	0.25	1.27	0.04	0.14	0.03	0.45
730	0.16	0.08	0.14	0.25	1.27	0.04	0.14	0.03	0.45

Table S6. Product selectivity of hexane cracking over 0.5-ETPS/Al-deAl-Y on molecular basis

Time on stream (min)	Selectivity (moles product/moles hexane reacted)								
	C_1	C_2-P	C_2-O	C_3-P	C_3-O	C_4-P	C_4-O	C_5-P	H_2
5	0.09	0.08	0.17	0.41	0.98	0.14	0.11	0.04	0.24
30	0.09	0.08	0.16	0.37	1.02	0.13	0.12	0.05	0.27
55	0.10	0.08	0.16	0.36	1.05	0.12	0.12	0.04	0.29
80	0.10	0.08	0.15	0.35	1.07	0.12	0.12	0.04	0.31
105	0.10	0.07	0.13	0.34	1.10	0.12	0.12	0.04	0.33
130	0.10	0.07	0.13	0.34	1.11	0.11	0.12	0.04	0.34
155	0.10	0.07	0.13	0.33	1.12	0.11	0.12	0.04	0.35
180	0.10	0.07	0.13	0.32	1.13	0.11	0.12	0.04	0.36
205	0.11	0.07	0.13	0.32	1.14	0.10	0.12	0.04	0.36
230	0.11	0.07	0.13	0.32	1.15	0.10	0.12	0.04	0.37
255	0.11	0.07	0.13	0.31	1.15	0.10	0.12	0.04	0.37
280	0.11	0.07	0.13	0.31	1.16	0.10	0.13	0.04	0.37
305	0.11	0.07	0.12	0.31	1.16	0.10	0.13	0.04	0.38
330	0.11	0.07	0.12	0.30	1.17	0.10	0.13	0.04	0.38
355	0.11	0.07	0.12	0.30	1.17	0.10	0.13	0.04	0.39
380	0.11	0.07	0.12	0.30	1.17	0.10	0.13	0.04	0.39
405	0.11	0.07	0.12	0.29	1.18	0.09	0.13	0.04	0.39
430	0.11	0.07	0.12	0.29	1.18	0.09	0.13	0.04	0.40
455	0.11	0.07	0.12	0.29	1.19	0.09	0.13	0.04	0.40
480	0.11	0.07	0.12	0.29	1.19	0.09	0.13	0.04	0.40
505	0.11	0.07	0.12	0.28	1.20	0.09	0.13	0.04	0.40
530	0.11	0.07	0.12	0.28	1.20	0.09	0.13	0.04	0.41
555	0.11	0.07	0.12	0.28	1.20	0.09	0.13	0.04	0.41
580	0.11	0.07	0.12	0.28	1.20	0.09	0.13	0.04	0.41
605	0.11	0.07	0.12	0.28	1.20	0.09	0.13	0.04	0.41
630	0.11	0.07	0.12	0.28	1.21	0.09	0.13	0.04	0.41
655	0.12	0.07	0.12	0.27	1.21	0.09	0.13	0.04	0.42
680	0.12	0.07	0.12	0.27	1.21	0.09	0.13	0.04	0.42
705	0.12	0.07	0.12	0.27	1.21	0.09	0.13	0.04	0.42
730	0.12	0.07	0.12	0.27	1.21	0.09	0.13	0.04	0.42

Table S7. Product selectivity of hexane cracking over 1.0-ETPS/Al-deAl-Y on molecular basis

Time on stream (min)	Selectivity (moles product/moles hexane reacted)								
	C_1	C_2-P	C_2-O	C_3-P	C_3-O	C_4-P	C_4-O	C_5-P	H_2
5	0.09	0.08	0.16	0.39	1.00	0.14	0.11	0.05	0.26
30	0.09	0.08	0.15	0.36	1.04	0.13	0.12	0.05	0.29
55	0.09	0.08	0.15	0.33	1.08	0.12	0.12	0.06	0.32
80	0.10	0.06	0.12	0.32	1.12	0.12	0.12	0.05	0.35
105	0.10	0.06	0.12	0.31	1.13	0.12	0.12	0.05	0.36
130	0.10	0.06	0.12	0.31	1.14	0.11	0.12	0.05	0.37
155	0.10	0.06	0.12	0.30	1.15	0.11	0.12	0.05	0.38
180	0.10	0.06	0.12	0.29	1.16	0.11	0.12	0.05	0.38
205	0.10	0.06	0.12	0.29	1.17	0.11	0.12	0.05	0.39
230	0.10	0.06	0.12	0.29	1.17	0.11	0.12	0.05	0.39
255	0.10	0.06	0.12	0.29	1.18	0.11	0.12	0.05	0.40
280	0.10	0.06	0.12	0.28	1.18	0.10	0.12	0.05	0.40
305	0.10	0.06	0.12	0.28	1.19	0.10	0.12	0.05	0.41
330	0.10	0.06	0.12	0.28	1.19	0.10	0.12	0.05	0.41
355	0.10	0.06	0.12	0.27	1.19	0.10	0.12	0.05	0.41
380	0.10	0.06	0.12	0.27	1.19	0.10	0.12	0.05	0.41
405	0.10	0.06	0.12	0.27	1.20	0.10	0.13	0.05	0.42
430	0.10	0.06	0.12	0.27	1.20	0.10	0.13	0.05	0.42
455	0.10	0.06	0.12	0.27	1.20	0.10	0.13	0.05	0.42
480	0.10	0.06	0.12	0.26	1.21	0.10	0.13	0.05	0.42
505	0.11	0.06	0.12	0.26	1.21	0.10	0.13	0.05	0.43
530	0.11	0.06	0.12	0.26	1.21	0.10	0.13	0.05	0.43
555	0.11	0.06	0.12	0.26	1.21	0.10	0.13	0.05	0.43
580	0.11	0.06	0.12	0.26	1.22	0.09	0.13	0.05	0.43
605	0.11	0.06	0.12	0.26	1.22	0.09	0.13	0.05	0.43
630	0.11	0.07	0.12	0.25	1.22	0.09	0.13	0.05	0.44
655	0.11	0.07	0.12	0.25	1.22	0.09	0.13	0.04	0.44
680	0.11	0.06	0.12	0.25	1.23	0.09	0.13	0.05	0.44
705	0.12	0.07	0.12	0.27	1.21	0.09	0.13	0.04	0.42
730	0.12	0.07	0.12	0.27	1.21	0.09	0.13	0.04	0.42

NMR of post-reaction catalysts

Solid-state 1D direct-excitation ^{1}H NMR spectra of unmodified deAl-Y and 1.0-ETPS/Al-deAl-Y were acquired to aid in assignment of signals from post-reaction deAl-Y ^{1}H NMR spectra. These spectra are shown in Figure S6 and show a variety of ^{1}H signals associated with the zeolite framework. A ^{1}H NMR signal at 1.7 ppm is assigned to silanol groups located on the external surface and at defects in the zeolite crystal structure. A shoulder at 2.5 ppm is assigned to AlOH species from extraframework aluminum species. ^{1}H NMR signals at 3.9 and 4.4 ppm are assigned to Bronsted acid ^{1}H located in the supercage and sodalite cage of zeolite Y, respectively.[41] Notably, these framework associated signals are all consistent in intensity and lineshape for the two materials, indicating ETPS deposition does not result in significant

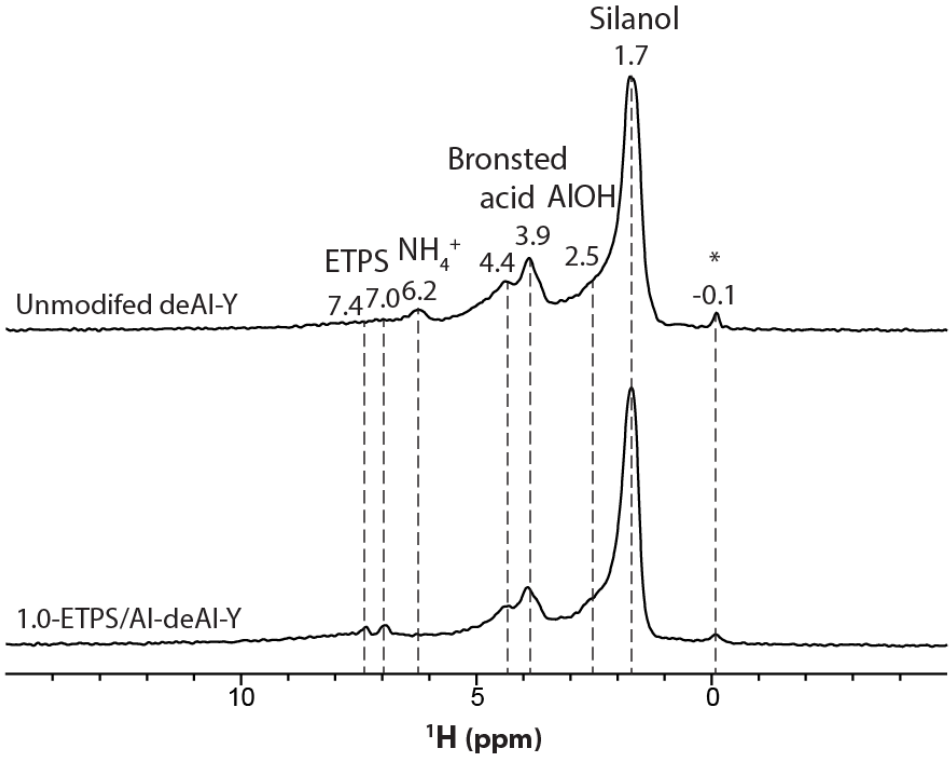

Figure S6. Solid-state 1D direct-excitation ^{1}H MAS NMR of dehydrated unmodified deAl-Y and 1.0-ETPS/Al-deAl-Y. The spectra were acquired at 11.7 T and 30 kHz MAS at room temperature. The asterisk (*) denotes an artifact from vacuum grease contamination.

changes to the overall distribution of Bronsted acid sites and silanols. In the ^{1}H NMR spectrum of unmodified deAl-Y, a signal is detected at 6.2 ppm which is attributed to residual NH_4^+ from the calcination to the H^+-form. In the ^{1}H NMR spectrum of 1.0-ETPS/Al-deAl-Y, weak signals at 7.0 and 7.4 ppm are attributed to residual phenyl groups left over after calcination of ETPS molecules.

Solid-state 2D ^{1}H–^{1}H single-quantum double-quantum (SQ-DQ) NMR spectra were acquired for post-reaction deAl-Y materials at selected time points to aid in signal assignments. These spectra show intensity only from pairs of ^{1}H species in very close proximity. Correlations between ^{1}H species in the same chemical environment appear on the double-diagonal line in the spectrum. Correlations between ^{1}H species with different chemical shifts appear reflected across the diagonal at a double-quantum shift of the sum of the two single-quantum chemical shifts. Solid-state 2D ^{1}H-^{1}H SQ-DQ NMR spectra of unmodified deAl-Y and 1.0-ETPS/Al-deAl-Y after 0.5 and 2 h of hexane cracking at 400 ºC are shown in Figure S7. Broadly, these spectra show on-diagonal intensity ranging from 0.8 to 10.2 ppm associated with a variety of aliphatic, olefinic, and aromatic ^{1}H moieties on adsorbed hydrocarbons and also silanols at 1.6 ppm. ^{1}H NMR signal intensity broadens around the diagonal in the aromatic region at 8.7 ppm and from 2.0-4.7 ppm, indicating multiple types of adsorbed ^{1}H in these regions that are in close proximity, but do not have resolved signals in the spectra. One prominent off-diagonal correlation at DQ 11.7 ppm between ^{1}H chemical shifts at 8.7 and 3.0 ppm is observed in all spectra. Based on this, the ^{1}H NMR signal at 3.0 ppm is assigned to methyl groups on aromatic rings. Notably, there is greater signal intensity at SQ 10.2 ppm in the spectrum acquired of unmodified deAl-Y after 2 h of hexane cracking in Figure 7C than

the other spectra, consistent with other observations of increased build up of polyaromatic coke species on the unmodified deAl-Y during the first few hours on stream.

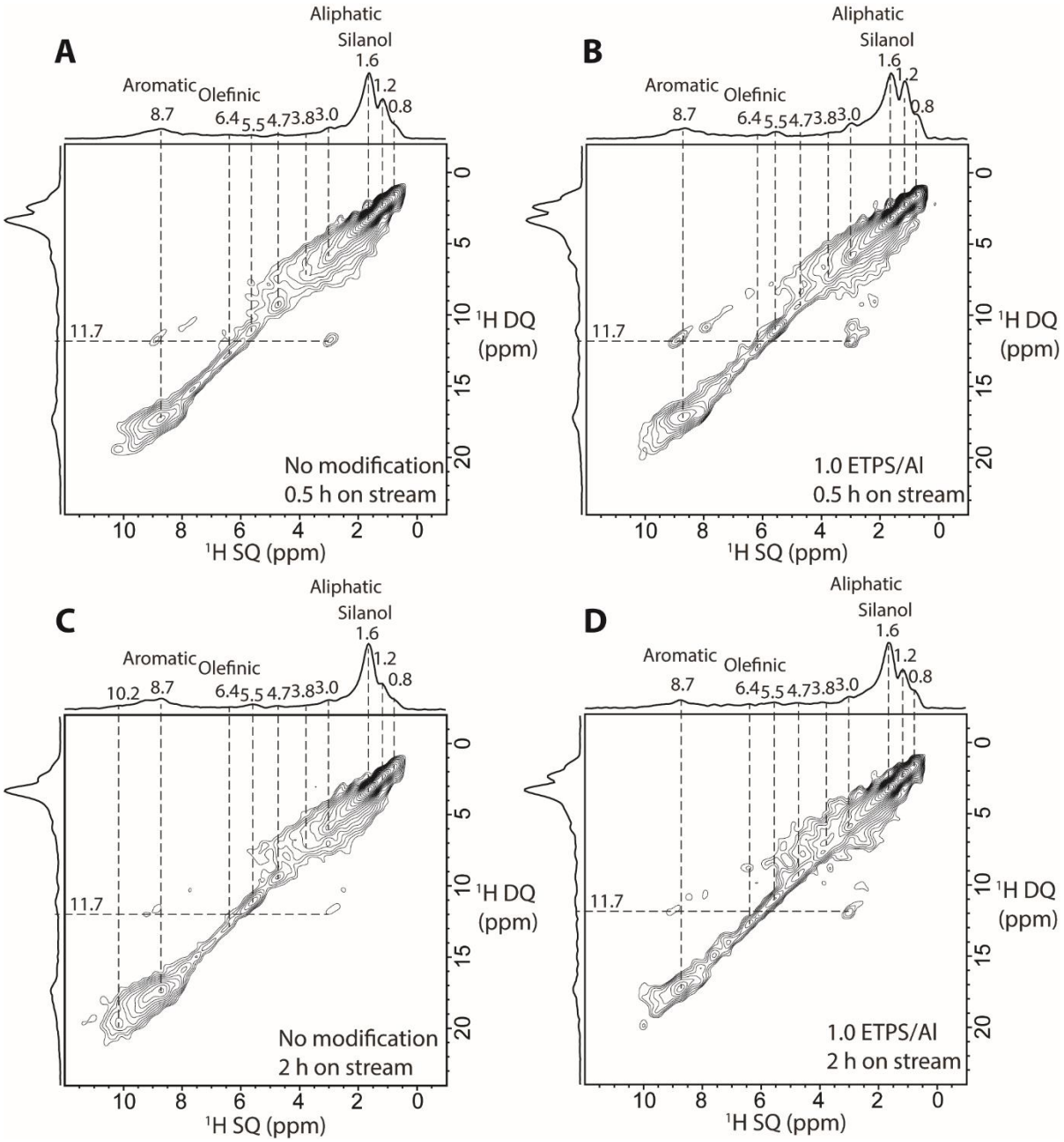

Figure S7. Solid-state 2D ^{1}H-^{1}H single-quantum double-quantum NMR spectra of (A) unmodified deAl-Y after 0.5 h of hexane cracking, (B) 1.0-ETPS/Al-deAl-Y after 0.5 h of hexane cracking, (C) unmodified deAl-Y after 2 h of hexane cracking, and (D) 1.0-ETPS/Al-deAl-Y after 2 h of hexane cracking. Spectra were acquired at 11.7 T and 30 kHz MAS at room temperature.

Solid-state $^{1}H\{^{27}Al\}$ S-RESPDOR NMR analyses were undertaken to characterize the distributions of adsorbed hydrocarbon species near aluminum species in unmodified deAl-Y and 1.0-ETPS/Al-deAl-Y after hexane cracking at 400 ºC. In these REDOR-type analyses, two spectra are acquired. In one spectrum, all ^{1}H species are observed (S_0). A second spectrum is acquired under the same conditions, but with irradiation of ^{27}Al nuclei that results in depletion of NMR signal from ^{1}H species that have strong dipole-dipole couplings with nearby ^{27}Al nuclei (S). A difference spectrum is taken by subtracted S from S_0. This difference spectrum shows intensity only from ^{1}H species with dipole-dipole couplings to ^{27}Al. The proportional loss of intensity in the S spectrum is given by the equation.

$$\Delta S = \frac{S_0 - S}{S_0}$$

This ΔS quantity provides information on the relative average strength of dipole couplings to ^{27}Al for different ^{1}H NMR signals, and can be influenced by distance between nuclei, mobility, the number of proximate nuclei, and also the fraction of ^{1}H species corresponding to an NMR signal that are in close proximity to ^{27}Al species. This is critical for interpreting REDOR-type analyses, as the absolute intensity observed in the difference spectrum can be misleading.

S_0, S, and ΔS spectra of unmodified deAl-Y and 1.0-ETPS/Al-deAl-Y after 0.5, 1, 2, 4, and 8 h of hexane cracking at 400 ºC are shown in Figures S8 and S9. Due to the complex distributions of adsorbed ^{1}H species on the catalyst post-reaction, a confident deconvolution of the observed ^{1}H NMR signals could not be performed. Instead, bands of signal from –0.5 to 1.0, 1.0 to 2.3, 2.3 to 4.0, 4.0 to 5.0, 5.0 to 7.3, and 7.3 and 11.0 were integrated for the S_0 and S spectra of each material to produce ΔS values. These signal bands roughly line up with where assignments of methyl groups, silanol moieties, AlOH moieties, Bronsted acid moieties, olefin species, and aromatic species were observed and assigned in Figure 5. However, the ^{1}H NMR

signal distributions are complex, so these signal bands are not unique assignments. In general, the ΔS values from both catalysts for the region from –0.5 to 1.0 range from 1-3%, for the region from 1.0-2.3 range from 13-18%, for the region from 2.3-4.0 range from 25-37%, for the region from 5.0-7.3 range from 17-33%, and for the region from 7.3-11.0 range from 21-26%. These values show no significant trends with time on stream or differences between the two materials, indicating that the strength of adsorption for ^{1}H species in these regions is relatively constant. Notably, the signal region assigned to methyl groups from –0.5-1.0 ppm has a very low ΔS value compared to other regions. This is not unexpected, as methyl groups will have high mobility, and methyl groups in these signal regions are typically at the end of aliphatic chains, and thus likely are not near regions of organic molecules that are strongly adsorbed near aluminum species. Interestingly, some trends are observed for the signal region from 4.0-5.0 ppm assigned to Bronsted acid moieties. For 1.0-ETPS/Al-deAl-Y, the ΔS depletion of this signal region ranges from 48% to 60%, with no significant trend. This high value is consistent with Bronsted acid ^{1}H species with very strong dipole-dipole couplings to framework Al species. In contrast, for unmodified deAl-Y the ΔS attenuation is 28% and 36% after 0.5 h and 1 h on stream, respectively, before increasing to range from 41% to 56% at longer times on stream. These lower values at short reaction times could be interpreted as resulting from some Bronsted acid sites complexing with adsorbed species, displacing the ^{1}H chemical shift. At longer reaction times, these species no longer stay adsorbed upon quenching the reaction to room temperature, resulting in more Bronsted acid ^{1}H signal intensity.

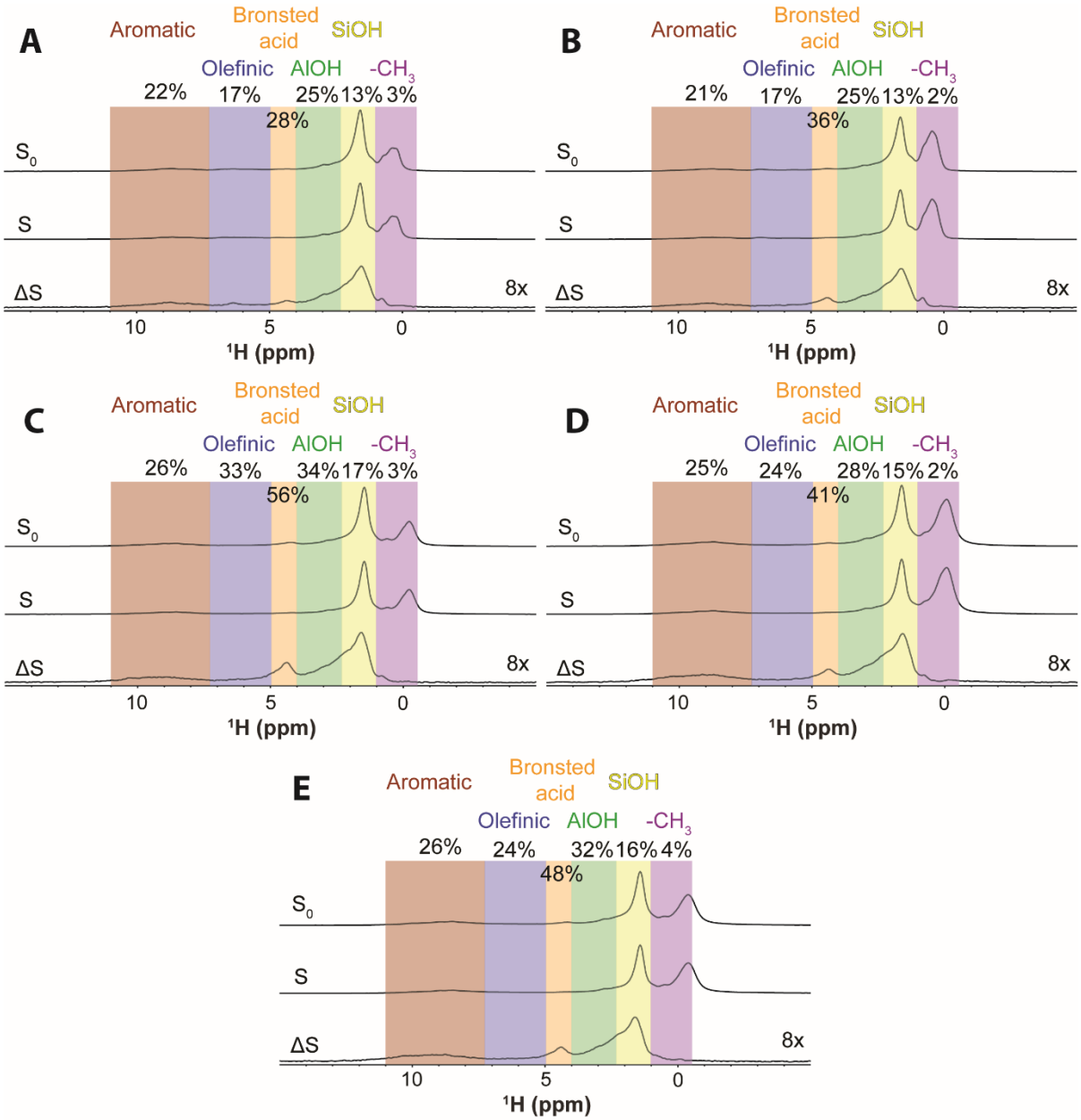

Figure S8. Solid-state 2D $^{1}H\{^{27}Al\}$ S-RESPDOR NMR S_0, S, and resulting difference spectra of unmodified deAl-Y after (A) 0.5 h, (B) 1 h, (C) 2 h, (D), 4 h, and (E) 8 h of hexane cracking at 400 °C at the conditions discussed above. The colored bands represent regions that were integrated to assess dephasing of different types of ^{1}H species. The percentages are the amount of signal dephased in each region due to the REDOR effect as given by $(S_0 - S)/S_0$. The spectra were acquired at 11.7 T and 30 kHz MAS at room temperature.

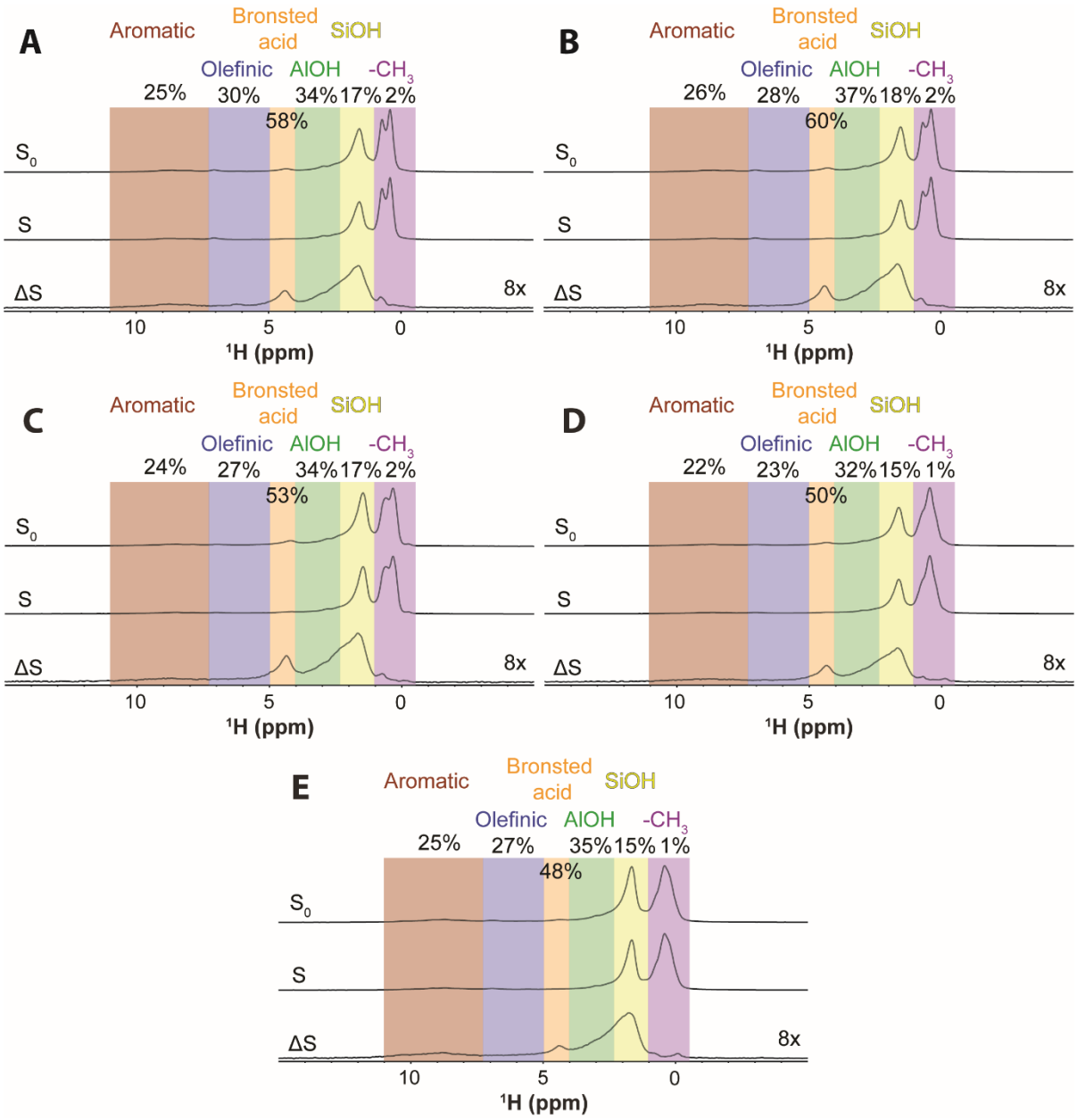

Figure S9. Solid-state 2D $^{1}H\{^{27}Al\}$ S-RESPDOR NMR S_0, S, and resulting difference spectra of 1.0-ETPS/Al-deAl-Y after (A) 0.5 h, (B) 1 h, (C) 2 h, (D), 4 h, and (E) 8 h of hexane cracking at 400 °C at the conditions discussed above. The colored bands represent regions that were integrated to assess dephasing of different types of ^{1}H species. The percentages are the amount of signal dephased in each region due to the REDOR effect as given by $(S_0 - S)/S_0$. The spectra were acquired at 11.7 T and 30 kHz MAS at room temperature.

References

(1) Vogt, E. T. C.; Whiting, G. T.; Dutta Chowdhury, A.; Weckhuysen, B. M. Chapter Two - Zeolites and Zeotypes for Oil and Gas Conversion. In *Advances in Catalysis*; Jentoft, F. C., Ed.; Academic Press, 2015; Vol. 58, pp 143–314. https://doi.org/10.1016/bs.acat.2015.10.001.

(2) Haw, J. F. Zeolite Acid Strength and Reaction Mechanisms in Catalysis. *Physical Chemistry Chemical Physics* **2002**, *4* (22), 5431–5441. https://doi.org/10.1039/B206483A.

(3) Breck, D. W. *Zeolite Molecular Sieves: Structure, Chemistry, and Use*; Wiley: New York, 1973.

(4) Di Iorio, J. R.; Nimlos, C. T.; Gounder, R. Introducing Catalytic Diversity into Single-Site Chabazite Zeolites of Fixed Composition via Synthetic Control of Active Site Proximity. *ACS Catalysis* **2017**, *7* (10), 6663–6674. https://doi.org/10.1021/acscatal.7b01273.

(5) Deimund, M. A.; Harrison, L.; Lunn, J. D.; Liu, Y.; Malek, A.; Shayib, R.; Davis, M. E. Effect of Heteroatom Concentration in SSZ-13 on the Methanol-to-Olefins Reaction. *ACS Catalysis* **2016**, *6* (2), 542–550. https://doi.org/10.1021/acscatal.5b01450.

(6) Fraenkel, D.; Levy, M. Comparative Study of Shape-Selective Toluene Alkylations over HZSM-5. *Journal of Catalysis* **1989**, *118* (1), 10–21. https://doi.org/10.1016/0021-9517(89)90296-0.

(7) Mendes, P. S. F.; Silva, J. M.; Ribeiro, M. F.; Daudin, A.; Bouchy, C. Synergies, Cooperation and Other Effects: A Review for Hydroconversion Catalysts. *Catalysis Today* **2020**, *356*, 260–270. https://doi.org/10.1016/J.CATTOD.2019.08.055.

(8) Williams, B. A.; Babitz, S. M.; Miller, J. T.; Snurr, R. Q.; Kung, H. H. The Roles of Acid Strength and Pore Diffusion in the Enhanced Cracking Activity of Steamed Y Zeolites. *Applied Catalysis A: General* **1999**, *177* (2), 161–175. https://doi.org/10.1016/S0926-860X(98)00264-6.

(9) Vogt, E. T. C.; Weckhuysen, B. M. Fluid Catalytic Cracking: Recent Developments on the Grand Old Lady of Zeolite Catalysis. *Chemical Society Reviews* **2015**, *44* (20), 7342–7370. https://doi.org/10.1039/c5cs00376h.

(10) van Donk, S.; Janssen, A. H.; Bitter, J. H.; de Jong, K. P. Generation, Characterization, and Impact of Mesopores in Zeolite Catalysts. *Catalysis Reviews* **2003**, *45* (2), 297–319. https://doi.org/10.1081/CR-120023908.

(11) Pérez-Ramírez, J.; Christensen, C. H.; Egeblad, K.; Christensen, C. H.; Groen, J. C. Hierarchical Zeolites: Enhanced Utilisation of Microporous Crystals in Catalysis by Advances in Materials Design. *Chem. Soc. Rev.* **2008**, *37* (11), 2530–2542. https://doi.org/10.1039/B809030K.

(12) Na, K.; Jo, C.; Kim, J.; Cho, K.; Jung, J.; Seo, Y.; Messinger, R. J.; Chmelka, B. F.; Ryoo, R. Directing Zeolite Structures into Hierarchically Nanoporous Architectures. *Science* **2011**, *333* (6040), 328–332. https://doi.org/10.1126/science.1204452.

(13) Messinger, R. J.; Na, K.; Seo, Y.; Ryoo, R.; Chmelka, B. F. Co-Development of Crystalline and Mesoscopic Order in Mesostructured Zeolite Nanosheets. *Angewandte Chemie - International Edition* **2015**, *54* (3), 927–931. https://doi.org/10.1002/anie.201408623.
(14) Zhu, J.; Zhu, Y.; Zhu, L.; Rigutto, M.; van der Made, A.; Yang, C.; Pan, S.; Wang, L.; Zhu, L.; Jin, Y.; Sun, Q.; Wu, Q.; Meng, X.; Zhang, D.; Han, Y.; Li, J.; Chu, Y.; Zheng, A.; Qiu, S.; Zheng, X.; Xiao, F.-S. Highly Mesoporous Single-Crystalline Zeolite Beta Synthesized Using a Nonsurfactant Cationic Polymer as a Dual-Function Template. *J. Am. Chem. Soc.* **2014**, *136* (6), 2503–2510. https://doi.org/10.1021/ja411117y.
(15) Zhang, X.; Liu, D.; Xu, D.; Asahina, S.; Cychosz, K. A.; Agrawal, K. V.; Al Wahedi, Y.; Bhan, A.; Al Hashimi, S.; Terasaki, O.; Thommes, M.; Tsapatsis, M. Synthesis of Self-Pillared Zeolite Nanosheets by Repetitive Branching. *Science* **2012**, *336* (6089), 1684–1687. https://doi.org/10.1126/science.1221111.
(16) Na, K.; Choi, M.; Park, W.; Sakamoto, Y.; Terasaki, O.; Ryoo, R. Pillared MFI Zeolite Nanosheets of a Single-Unit-Cell Thickness. *J. Am. Chem. Soc.* **2010**, *132* (12), 4169–4177. https://doi.org/10.1021/ja908382n.
(17) Dai, H.; Shen, Y.; Yang, T.; Lee, C.; Fu, D.; Agarwal, A.; Le, T. T.; Tsapatsis, M.; Palmer, J. C.; Weckhuysen, B. M.; Dauenhauer, P. J.; Zou, X.; Rimer, J. D. Finned Zeolite Catalysts. *Nat. Mater.* **2020**, *19* (10), 1074–1080. https://doi.org/10.1038/s41563-020-0753-1.
(18) Hao, W.; Zhang, W.; Guo, Z.; Ma, J.; Li, R. Mesoporous Beta Zeolite Catalysts for Benzylation of Naphthalene: Effect of Pore Structure and Acidity. *Catalysts* **2018**, *8* (11), 504. https://doi.org/10.3390/catal8110504.
(19) Adawi, H. I.; Odigie, F. O.; Sarazen, M. L. Alkylation of Poly-Substituted Aromatics to Probe Effects of Mesopores in Hierarchical Zeolites with Differing Frameworks and Crystal Sizes. *Mol. Syst. Des. Eng.* **2021**, *6* (11), 903–917. https://doi.org/10.1039/D1ME00062D.
(20) Rieg, C.; Li, Z.; Kurtz, A.; Schmidt, M.; Dittmann, D.; Benz, M.; Dyballa, M. A Method for the Selective Quantification of Brønsted Acid Sites on External Surfaces and in Mesopores of Hierarchical Zeolites. *J. Phys. Chem. C* **2021**, *125* (1), 515–525. https://doi.org/10.1021/acs.jpcc.0c09384.
(21) Vogt, E. T. C.; Fu, D.; Weckhuysen, B. M. Carbon Deposit Analysis in Catalyst Deactivation, Regeneration, and Rejuvenation. *Angewandte Chemie International Edition* **2023**, *62* (29), e202300319. https://doi.org/10.1002/anie.202300319.
(22) Guisnet, M.; Magnoux, P. Coking and Deactivation of Zeolites: Influence of the Pore Structure. *Applied Catalysis* **1989**, *54* (1), 1–27. https://doi.org/10.1016/S0166-9834(00)82350-7.
(23) Guisnet, M.; Magnoux, P. Organic Chemistry of Coke Formation. *Applied Catalysis A: General* **2001**, *212* (1), 83–96. https://doi.org/10.1016/S0926-860X(00)00845-0.

(24) Bibby, D. M.; Milestone, N. B.; Patterson, J. E.; Aldridge, L. P. Coke Formation in Zeolite ZSM-5. *Journal of Catalysis* **1986**, *97* (2), 493–502. https://doi.org/10.1016/0021-9517(86)90020-5.
(25) Kim, J.; Choi, M.; Ryoo, R. Effect of Mesoporosity against the Deactivation of MFI Zeolite Catalyst during the Methanol-to-Hydrocarbon Conversion Process. *Journal of Catalysis* **2010**, *269* (1), 219–228. https://doi.org/10.1016/j.jcat.2009.11.009.
(26) Lee, K.; Lee, S.; Jun, Y.; Choi, M. Cooperative Effects of Zeolite Mesoporosity and Defect Sites on the Amount and Location of Coke Formation and Its Consequence in Deactivation. *Journal of Catalysis* **2017**, *347*, 222–230. https://doi.org/10.1016/j.jcat.2017.01.018.
(27) Adawi, H. I.; Zheng, Y.; Sarazen, M. L. Underpinnings of Carbonaceous Deposition among Structurally Diverse Hierarchical Zeolites during Hydrocarbon Upgrading. *Crystal Growth & Design* **2023**, *23* (4), 2675–2688. https://doi.org/10.1021/acs.cgd.2c01488.
(28) Cejka, J.; ĺilková, N.; Wichterlová, B.; Eder-Mirth, G.; Lercher, J. A. Decisive Role of Transport Rate of Products for Zeolite Para-Selectivity: Effect of Coke Deposition and External Surface Silylation on Activity and Selectivity of HZSM-5 in Alkylation of Toluene. *Zeolites* **1996**, *17* (3), 265–271. https://doi.org/10.1016/0144-2449(96)00006-1.
(29) Zheng, S.; Heydenrych, H. R.; Jentys, A.; Lercher, J. A. Influence of Surface Modification on the Acid Site Distribution of HZSM-5. *J. Phys. Chem. B* **2002**, *106* (37), 9552–9558. https://doi.org/10.1021/jp014091d.
(30) Zheng, S.; Jentys, A.; Lercher, J. A. Xylene Isomerization with Surface-Modified HZSM-5 Zeolite Catalysts: An in Situ IR Study. *Journal of Catalysis* **2006**, *241* (2), 304–311. https://doi.org/10.1016/j.jcat.2006.04.026.
(31) Akiyama, S.; Mochizuki, H.; Yamazaki, H.; Yokoi, T.; Tatsumi, T.; Kondo, J. N. The Effective Silylation of External Surface on H-ZSM5 with Cyclic Siloxane for the Catalytic Cracking of Naphtha. *Molecular Catalysis* **2017**, *433*, 48–54. https://doi.org/10.1016/j.mcat.2016.12.005.
(32) Losch, P.; Boltz, M.; Bernardon, C.; Louis, B.; Palčić, A.; Valtchev, V. Impact of External Surface Passivation of Nano-ZSM-5 Zeolites in the Methanol-to-Olefins Reaction. *Applied Catalysis A: General* **2016**, *509*, 30–37. https://doi.org/10.1016/j.apcata.2015.09.037.
(33) Zhu, T.; Liang, H.; Zhang, B.; Tian, Y.; Liu, G. Controllably Tailoring External Surface Sites of Nanosheet HZSM-5 for Maximizing Light Olefins in Catalytic Cracking of n-Decane. *Chinese Journal of Chemical Engineering* **2021**, *38*, 276–285. https://doi.org/10.1016/J.CJCHE.2021.04.015.
(34) Chapellière, Y.; Daniel, C.; Tuel, A.; Farrusseng, D.; Schuurman, Y. Kinetics of N-Hexane Cracking over Mesoporous HY Zeolites Based on Catalyst Descriptors. *Catalysts* **2021**, *11* (6), 652. https://doi.org/10.3390/catal11060652.

(35) Babitz, S. M.; Williams, B. A.; Miller, J. T.; Snurr, R. Q.; Haag, W. O.; Kung, H. H. Monomolecular Cracking of N-Hexane on Y, MOR, and ZSM-5 Zeolites. *Applied Catalysis A: General* **1999**, *179* (1–2), 71–86. https://doi.org/10.1016/S0926-860X(98)00301-9.

(36) Massiot, D.; Fayon, F.; Alonso, B.; Trebosc, J.; Amoureux, J. P. Chemical Bonding Differences Evidenced from J-Coupling in Solid State NMR Experiments Involving Quadrupolar Nuclei. *Journal of Magnetic Resonance* **2003**, *164* (1), 160–164. https://doi.org/10.1016/S1090-7807(03)00134-4.

(37) Schmithorst, M. B.; Prasad, S.; Moini, A.; Chmelka, B. F. Direct Detection of Paired Aluminum Heteroatoms in Chabazite Zeolite Catalysts and Their Significance for Methanol Dehydration Reactivity. *J. Am. Chem. Soc.* **2023**, *145* (33), 18215–18220. https://doi.org/10.1021/jacs.3c05708.

(38) Berkson, Z. J.; Hsieh, M.; Smeets, S.; Gajan, D.; Lund, A.; Lesage, A.; Xie, D.; Zones, S. I.; McCusker, L. B.; Baerlocher, C.; Chmelka, B. F. Preferential Siting of Aluminum Heteroatoms in the Zeolite Catalyst Al-SSZ-70. *Angewandte Chemie International Edition* **2019**, *58* (19), 6255–6259. https://doi.org/10.1002/anie.201813533.

(39) Hensen, E. J. M.; Poduval, D. G.; Magusin, P. C. M. M.; Coumans, A. E.; Veen, J. A. R. van. Formation of Acid Sites in Amorphous Silica-Alumina. *Journal of Catalysis* **2010**, *269* (1), 201–218. https://doi.org/10.1016/j.jcat.2009.11.008.

(40) Valla, M.; Rossini, A. J.; Caillot, M.; Chizallet, C.; Raybaud, P.; Digne, M.; Chaumonnot, A.; Lesage, A.; Emsley, L.; van Bokhoven, J. A.; Copéret, C. Atomic Description of the Interface between Silica and Alumina in Aluminosilicates through Dynamic Nuclear Polarization Surface-Enhanced NMR Spectroscopy and First-Principles Calculations. *J. Am. Chem. Soc.* **2015**, *137* (33), 10710–10719. https://doi.org/10.1021/jacs.5b06134.

(41) Schroeder, C.; Hansen, M. R.; Koller, H. Ultrastabilization of Zeolite Y Transforms Brønsted-Brønsted Acid Pairs into Brønsted-Lewis Acid Pairs. *Angewandte Chemie International Edition* **2018**, *57* (43), 14281–14285. https://doi.org/10.1002/anie.201808395.

(42) Böhlmann, W.; Michel, D.; Roland, J. ^{1}H NMR Studies of the Mobility of Olefins Adsorbed in Zeolites of Type NaX. *Magnetic Resonance in Chemistry* **1999**, *37* (13), S126–S134. https://doi.org/10.1002/(SICI)1097-458X(199912)37:13<S126::AID-MRC560>3.0.CO;2-1.

(43) Rongbao, L.; Zengmin, S.; Bailing, L. Structural Analysis of Polycyclic Aromatic Hydrocarbons Derived from Petroleum and Coal by ^{13}C and ^{1}H-N.M.R. Spectroscopy. *Fuel* **1988**, *67* (4), 565–569. https://doi.org/10.1016/0016-2361(88)90355-9.

(44) Castaño, P.; Elordi, G.; Olazar, M.; Aguayo, A. T.; Pawelec, B.; Bilbao, J. Insights into the Coke Deposited on HZSM-5, Hβ and HY Zeolites during the Cracking of Polyethylene. *Applied Catalysis B: Environmental* **2011**, *104* (1), 91–100. https://doi.org/10.1016/j.apcatb.2011.02.024.

(45) Hsieh, P. Y.; Widegren, J. A.; Slifka, A. J.; Hagen, A. J.; Rorrer, R. A. L. Direct Measurement of Trace Polycyclic Aromatic Hydrocarbons in Diesel Fuel with ^{1}H and ^{13}C NMR Spectroscopy: Effect of PAH Content on Fuel Lubricity. *Energy Fuels* **2015**, *29* (7), 4289–4297. https://doi.org/10.1021/acs.energyfuels.5b01193.

(46) Zhao, Z.; Xu, S.; Hu, M. Y.; Bao, X.; Peden, C. H. F.; Hu, J. Investigation of Aluminum Site Changes of Dehydrated Zeolite H-Beta during a Rehydration Process by High-Field Solid-State NMR. *J. Phys. Chem. C* **2015**, *119* (3), 1410–1417. https://doi.org/10.1021/jp509982r.

(47) Lu, X.; Lafon, O.; Trébosc, J.; Amoureux, J. P. Detailed Analysis of the S-RESPDOR Solid-State NMR Method for Inter-Nuclear Distance Measurement between Spin-1/2 and Quadrupolar Nuclei. *Journal of Magnetic Resonance* **2011**, *215*, 34–49. https://doi.org/10.1016/j.jmr.2011.12.009.

(48) Wang, C.; Wang, Q.; Xu, J.; Qi, G.; Gao, P.; Wang, W.; Zou, Y.; Feng, N.; Liu, X.; Deng, F. Direct Detection of Supramolecular Reaction Centers in the Methanol-to-Olefins Conversion over Zeolite H-ZSM-5 by ^{13}C-^{27}Al Solid-State NMR Spectroscopy. *Angewandte Chemie International Edition* **2016**, *55* (7), 2507–2511. https://doi.org/10.1002/anie.201510920.

(49) Perras, F. A.; Padmos, J. D.; Johnson, R. L.; Wang, L. L.; Schwartz, T. J.; Kobayashi, T.; Horton, J. H.; Dumesic, J. A.; Shanks, B. H.; Johnson, D. D.; Pruski, M. Characterizing Substrate-Surface Interactions on Alumina-Supported Metal Catalysts by Dynamic Nuclear Polarization-Enhanced Double-Resonance NMR Spectroscopy. *Journal of the American Chemical Society* **2017**, *139* (7), 2702–2709. https://doi.org/10.1021/jacs.6b11408.

(50) Wang, C.; Chu, Y.; Xu, J.; Wang, Q.; Qi, G.; Gao, P.; Zhou, X.; Deng, F. Extra-Framework Aluminum-Assisted Initial C−C Bond Formation in Methanol-to-Olefins Conversion on Zeolite H-ZSM-5. *Angewandte Chemie International Edition* **2018**, *57* (32), 10197–10201. https://doi.org/10.1002/anie.201805609.

(51) Fung, B. M.; Khitrin, A. K.; Ermolaev, K. An Improved Broadband Decoupling Sequence for Liquid Crystals and Solids. *Journal of Magnetic Resonance* **2000**, *142* (1), 97–101. https://doi.org/10.1006/JMRE.1999.1896.

(52) Massiot, D.; Fayon, F.; Capron, M.; King, I.; Le Calvé, S.; Alonso, B.; Durand, J.-O.; Bujoli, B.; Gan, Z.; Hoatson, G. Modelling One-and Two-Dimensional Solid-State NMR Spectra. *Magnetic Resonance in Chemistry* **2002**, *40*, 70–76. https://doi.org/10.1002/mrc.984.

(53) Iuga, D.; Schäfer, H.; Verhagen, R.; Kentgens, A. P. M. Population and Coherence Transfer Induced by Double Frequency Sweeps in Half-Integer Quadrupolar Spin Systems. *Journal of Magnetic Resonance* **2000**, *147* (2), 192–209. https://doi.org/10.1006/jmre.2000.2192.

(54) Elena, B.; de Paëpe, G.; Emsley, L. Direct Spectral Optimisation of Proton-Proton Homonuclear Dipolar Decoupling in Solid-State NMR. *Chemical Physics Letters* **2004**, *398* (4–6), 532–538. https://doi.org/10.1016/j.cplett.2004.09.122.
(55) Jaeger, C.; Hemmann, F. EASY: A Simple Tool for Simultaneously Removing Background, Deadtime and Acoustic Ringing in Quantitative NMR Spectroscopy—Part I: Basic Principle and Applications. *Solid State Nuclear Magnetic Resonance* **2014**, *57–58*, 22–28. https://doi.org/10.1016/J.SSNMR.2013.11.002.
(56) Saalwächter, K.; Lange, F.; Matyjaszewski, K.; Huang, C. F.; Graf, R. BaBa-Xy16: Robust and Broadband Homonuclear DQ Recoupling for Applications in Rigid and Soft Solids up to the Highest MAS Frequencies. *Journal of Magnetic Resonance* **2011**, *212* (1), 204–215. https://doi.org/10.1016/J.JMR.2011.07.001.
(57) Hu, B.; Trébosc, J.; Amoureux, J. P. Comparison of Several Hetero-Nuclear Dipolar Recoupling NMR Methods to Be Used in MAS HMQC/HSQC. *Journal of Magnetic Resonance* **2008**, *192* (1), 112–122. https://doi.org/10.1016/j.jmr.2008.02.004.
(58) Engelhardt, G.; Lohse, U.; Samoson, A.; Mägi, M.; Tarmak, M.; Lippmaa, E. High Resolution ^{29}Si N.M.R. of Dealuminated and Ultrastable Y-Zeolites. *Zeolites* **1982**, *2* (1), 59–62. https://doi.org/10.1016/S0144-2449(82)80042-0.
(59) Grobet, P. J.; Geerts, H.; Tielen, M.; Martens, J. A.; Jacobs, P. A. Framework and Non-Framework Al Species in Dealuminated Zeolite Y. In *Studies in Surface Science and Catalysis*; Karge, H. G., Weitkamp, J., Eds.; Zeolites as Catalysts, Sorbents and Detergent Builders; Elsevier, 1989; Vol. 46, pp 721–734. https://doi.org/10.1016/S0167-2991(08)61025-3.
(60) Wouters, B. H.; Chen, T.-H.; Grobet, P. J. Reversible Tetrahedral−Octahedral Framework Aluminum Transformation in Zeolite Y. *J. Am. Chem. Soc.* **1998**, *120* (44), 11419–11425. https://doi.org/10.1021/ja982082l.
(61) Galarneau, A.; Villemot, F.; Rodriguez, J.; Fajula, F.; Coasne, B. Validity of the T-Plot Method to Assess Microporosity in Hierarchical Micro/Mesoporous Materials. *Langmuir* **2014**, *30* (44), 13266–13274. https://doi.org/10.1021/la5026679.
(62) Boréave, A.; Auroux, A.; Guimon, C. Nature and Strength of Acid Sites in HY Zeolites: A Multitechnical Approach. *Microporous Materials* **1997**, *11* (5), 275–291. https://doi.org/10.1016/S0927-6513(97)00047-3.

Chapter 5

Methods for characterizing evolution of local framework chemical environments during zeolite crystallization

This chapter is a discussion of a discontinued project from early in my Ph.D. with Dr. Philipp Selter, Dr. Xiaojun Zeng, Prof. Bradley F. Chmelka, and Prof. Galen Stucky from UC Santa Barbara and Dr. Subramanian Prasad and Dr. Ahmad Moini from the BASF Corporation and is adapted from various reports and presentations from that project, including the final report for the project. The primary purpose of writing this chapter is to collect the preliminary results we acquired in one place so that future group members can use them as a springboard for experimental plans in future projects. My contributions to this work include experimental design, performing and analyzing solid-state NMR measurements, and writing. Dr. Xiaojun Zeng performed syntheses along with X-ray diffraction and scanning transmission electron microscopy experiments. Dr. Philipp Selter aided in performing and analyzing solid-state NMR measurements.

Abstract

Aluminosilicate zeolites are used as catalysts in a wide variety of heterogeneous reaction chemistries. As we shift towards new feedstocks for hydrocarbon conversion reactions in response to climate change, new catalysts are required in order to fully utilize these more sustainable carbon sources. New activities and selectivities can be achieved over aluminosilicate zeolites by biasing the aluminum distributions in the zeolite framework, which controls the locations and types of active sites. However, competing kinetic and thermodynamic factors make it hard to predict how changes in synthesis conditions will modify aluminum distributions. Here, on a series of standard chabazite syntheses, we demonstrate

advanced solid-state nuclear magnetic resonance (NMR) methods to examine the evolution of the aluminosilicate framework and interactions with structure-directing agents (SDA) which partially determine aluminum siting during synthesis. Solid-state 2D ^{29}Si{^{1}H} HETCOR NMR spectra provide information on SDA interactions with the fully crystalline zeolite framework and disordered framework species during synthesis. Solid-state 2D ^{27}Al–^{29}Si *J*-HMQC NMR spectra reveal how aluminosilicate chemical environments evolve during crystallization. Lastly, *in situ* ^{29}Si NMR methods are demonstrated to track the evolution of ^{29}Si local chemical environments during zeolite crystallization under hydrothermal synthesis conditions. These measurements are accompanied by standard powder X-ray diffraction, scanning electron microscopy, and 1D NMR analyses to track the crystallization of the chabazite zeolite. These methods are anticipated to be useful for understanding complex zeolite syntheses.

Introduction

Zeolites are a class of microporous, crystalline aluminosilicates which are used in a wide variety of industrial applications including air separations, water softening, and oil refining.[1–3] The diverse applications of zeolites are made possible due to two features of zeolites. For one, there are over 200 distinct zeolite framework topologies that have been synthesized.[4] This range of framework topologies enables selection of a pore structure that has pore diameters and void sizes suitable for precise size exclusion or to stabilize specific reaction transition states and heavily bias reaction selectivity. Second, the four-coordinate aluminum incorporated in the zeolite framework results in localized negative charges on the zeolite framework, which are charge-balanced by cations present in the pores of the zeolite.[5] These cations act as the adsorption sites or catalysts for various processes performed using zeolites. Exchanging in different cations results in different reaction properties for the same zeolite

framework type. For example, the small-pore zeolite chabazite is used for methanol upgrading to hydrocarbons in the H^+-exchanged form but is active for the selective catalytic reduction of NO_x by NH_3 in the Cu^{2+}-exchanged form.[6–8]

Controlling the distributions of aluminum heteroatoms incorporated into the zeolite framework during synthesis is desirable to control the locations and distributions of exchangeable cation active sites. This potentially would enable the design of catalysts with improved selectivity or stability. Zeolite synthesis is typically performed in a sealed reactor under hydrothermal conditions around 150 ºC. A mixture of aluminum and silicon sources is mixed with a solution containing both inorganic and organic cations, which act as structure-directing agents (SDA).[5] These SDA molecules determine the zeolite framework topology and also charge-balance negative charges resulting from aluminum incorporation into the framework. Thus, selection of SDA molecules exerts some control over the distributions of aluminum atoms in a synthesized zeolite.[9] Computational studies have shown that different SDA molecules thermodynamically favor aluminum insertion into different framework sites or local paired configurations.[10–13] However, kinetic effects during zeolite crystallization also play a role in aluminum distributions and complicate the ability to design zeolite syntheses based on computational studies of the SDA thermodynamics.[14]

A recent focus of zeolite synthesis in the academic community is on methods for transforming one zeolite crystal structure into another. One example of this process is interzeolite conversion (IZA), where a zeolite is used as an aluminum and silicon source in zeolite synthesis of a different framework topology.[15–18] Zeolite Y (FAU framework type) is commonly used, as it is available in large abundance due to its ubiquitous use as a component in hydrocarbon cracking catalysts.[19,20] It has been observed that different aluminum

distributions are accessible with interzeolite conversion syntheses than from traditional syntheses involving separate silicon and aluminum sources.[17] It has been proposed that this may be due to differences in dissolution and recrystallization kinetics, or alternatively that the zeolite source does not fully dissolve before transforming into the target zeolite crystal structure.[21] Tracking this evolution is challenging. Another active topic in zeolite synthesis is assembly-disassembly-organization-reassembly (ADOR) syntheses, where a zeolite framework is selectively disassembled, and additional structure-directing agents are added to produce a different framework structure.[22–24] This is typically used to access challenging-to-synthesize zeolite framework topologies and may facilitate the synthesis of additional topologies.[25]

Advanced characterization methods are necessary to understand the complex combination of dissolution and crystallization processes happening during IZA and ADOR processes, and how aluminum distributions are biased during these syntheses. Here, a series of advanced 2D NMR methods are demonstrated on standard chabazite syntheses to track formation of the aluminosilicate chabazite framework in both acidic and basic synthesis regimes. In addition, *in situ* NMR methods for tracking zeolite crystallization are demonstrated. These methods could be applied to state-of-the-art zeolite synthesis techniques to better design future zeolite syntheses.

Results and Discussion

To understand the evolution of local chemical environments in a zeolite framework, a series of standard chabazite syntheses were performed. Chabazite was selected due to its relative simplicity with only one tetrahedral site, which makes analysis of the crystalline material by solid-state NMR straightforward. In addition, chabazite is currently heavily

researched due to its industrial relevance for use as a diesel engine NO_x emission control catalyst. Three chabazite syntheses were investigated. First, a siliceous chabazite (no aluminum heteroatoms) was synthesized in fluoride media, necessary to produce the siliceous structure.[26] Second, the same synthesis was performed, but with Al_2O_3 added as an aluminum source to produce an aluminosilicate chabazite.[27] Lastly, a standard chabazite synthesis under basic conditions was performed with a small molecule aluminum source, aluminum isopropoxide.[28] All syntheses utilized N,N,N-trimethyl-1-adamantammonium hydroxide (TMAdaOH) as an organic structure-directing agent (OSDA).

In order to assess the evolution of the crystal structure as a function of time, syntheses were quenched at various time points and characterized. Powder X-ray diffraction (XRD) was used to characterize the long-range crystallinity of the resulting solids as a function of time to quickly assess the extent of crystal formation. Figure 1A and B show powder XRD patterns for a siliceous chabazite synthesis after 24 h and 84 h of hydrothermal synthesis, respectively. The powder XRD pattern of the 24-h synthesis material exhibits a few sharp reflections consistent with formation of chabazite along with a broad underlying feature consistent with an amorphous material, indicating partial crystallinity. In comparison, the powder XRD pattern of the 84-h synthesis material exhibits only sharp reflections consistent with a chabazite structure, indicating complete zeolite crystallization.

To compare the local ordering of 24-h and 84-h synthesis siliceous chabazite and interactions of the framework with occluded OSDA species, 2D solid-state $^{29}Si\{^{1}H\}$ HETCOR NMR analyses were performed on both materials. These analyses reveal pairs of ^{29}Si and ^{1}H nuclei that are coupled through dipole-dipole interactions, which provide information on through-space proximity of the nuclei. The 2D solid-state $^{29}Si\{^{1}H\}$ HETCOR NMR spectrum of 24-h synthesis siliceous chabazite is shown in Figure 1C. This spectrum shows a distribution

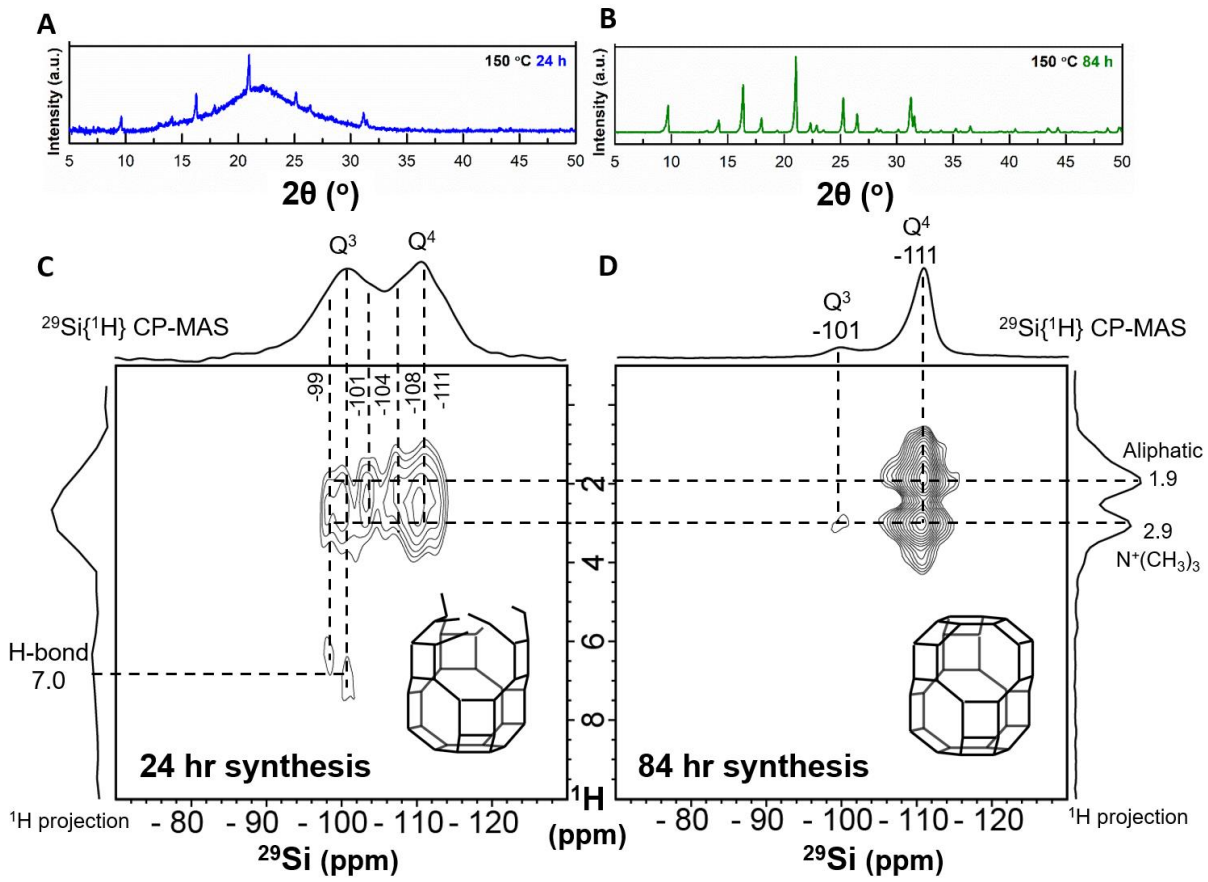

Figure 1. XRD powder pattern of siliceous chabazite sample after (A) 24 h and (B) 84 h of hydrothermal synthesis. 2D ^{29}Si{^{1}H} HETCOR of siliceous chabazite after (C) 24 h and (D) 84 h of hydrothermal synthesis. The solid-state ^{29}Si{^{1}H} HETCOR were acquired at 11.7 T, 298 K and 12.5 kHz MAS on hydrated samples. Insets show partially and fully crystallized chabazite cages.

of ^{29}Si NMR signals ranging from –99 to –111 ppm, corresponding to Q^4 and Q^3 moieties, correlated with ^{1}H NMR signals that, while unresolved, cover a signal range consistent with the quaternary ammonium headgroup and aliphatic body of TMAdaOH. TMAdaOH ^{1}H signal assignments are based on ^{1}H and ^{13}C NMR spectra of TMAdaOH shown in Figure S1. In addition, Q^3 ^{29}Si NMR signals at –99 and –101 ppm show a weak correlation to a ^{1}H NMR signal at 7.0 ppm, attributed to hydrogen-bonding with surface water. In contrast, the 2D 2D solid-state ^{29}Si{^{1}H} HETCOR NMR spectrum of 84-h synthesis siliceous chabazite exhibits two well-resolved ^{29}Si NMR signals at –111 and –101 ppm attributed to Q^4 and Q^3 species,

respectively. The Q^4 ^{29}Si NMR signal at –111 ppm is correlated with ^{1}H NMR signals at 1.9 and 2.9 ppm, corresponding to aliphatic and quaternary ammonium headgroup moieties on TMAdaOH, respectively. The Q^3 ^{29}Si NMR signal at –101 ppm is weakly correlated with the ^{1}H NMR signal at 2.9 ppm attributed to TMAdaOH headgroup ^{1}H species, consistent with silanol nests charge-balancing the cationic headgroup of TMAdaOH.

Similar analyses were undertaken for HF-synthesis aluminosilicate chabazite after 12 h and 72 h of hydrothermal synthesis. After 12 h of hydrothermal synthesis, the obtained powder XRD pattern on the solid product exhibits sharp reflections indexable to chabazite along with a broad feature consistent with an amorphous component (Figure 2A). In contrast, the powder XRD pattern in Figure 2B of HF-synthesis aluminosilicate chabazite after 72 h of hydrothermal synthesis exhibits only sharp features consistent with a complete synthesis of pure chabazite-phase material. The 2D solid-state ^{29}Si{^{1}H} HETCOR NMR spectrum of 12-h HF-synthesis aluminosilicate chabazite in Figure 2C shows broad Q^3 and Q^4-assigned ^{29}Si NMR signals ranging from –101 to –111 ppm correlated with broad ^{1}H features ranging from 1.9 to 4.0 ppm. This signal intensity is attributed to a combination of TMAdaOH ^{1}H species and surface water. In addition, Q^3 ^{29}Si NMR signals at –101 and –102 ppm are correlated with ^{1}H NMR signals 7.2 ppm that are attributed to hydrogen bonding with surface water. Notably, in contrast to the 2D solid-state ^{29}Si{^{1}H} HETCOR NMR spectrum of 24-h synthesis siliceous chabazite in Figure 1C, this spectrum exhibits an additional region of ^{29}Si NMR signal intensity at –106 ppm which is attributed to Q^4(1Al) moieties, indicating incorporation of aluminum species into the forming zeolite. Figure 2D shows the 2D solid-state ^{29}Si{^{1}H} HETCOR NMR spectrum of 72-h HF-synthesis aluminosilicate chabazite. The 1D ^{29}Si{^{1}H} CP-MAS NMR spectrum shown above the 2D spectrum shows three well resolved ^{29}Si NMR signals at –111,

–106, and –101 ppm attributed to Q^4(0Al), Q^4(1Al), and Q^3 moieties, respectively. The 2D correlation map reveals that the Q^4(0Al) ^{29}Si NMR signal is correlated with ^{1}H NMR signals at 1.9 and 2.9 ppm attributed to aliphatic and quaternary ammonium headgroup ^{1}H species on TMAdaOH. In addition, the Q^4(1Al) ^{29}Si NMR signal at –106 ppm is correlated with a quaternary ammonium headgroup signal at 2.9 ppm, consistent with the charged headgroup balancing negative charges introduced to the framework by aluminum incorporation.

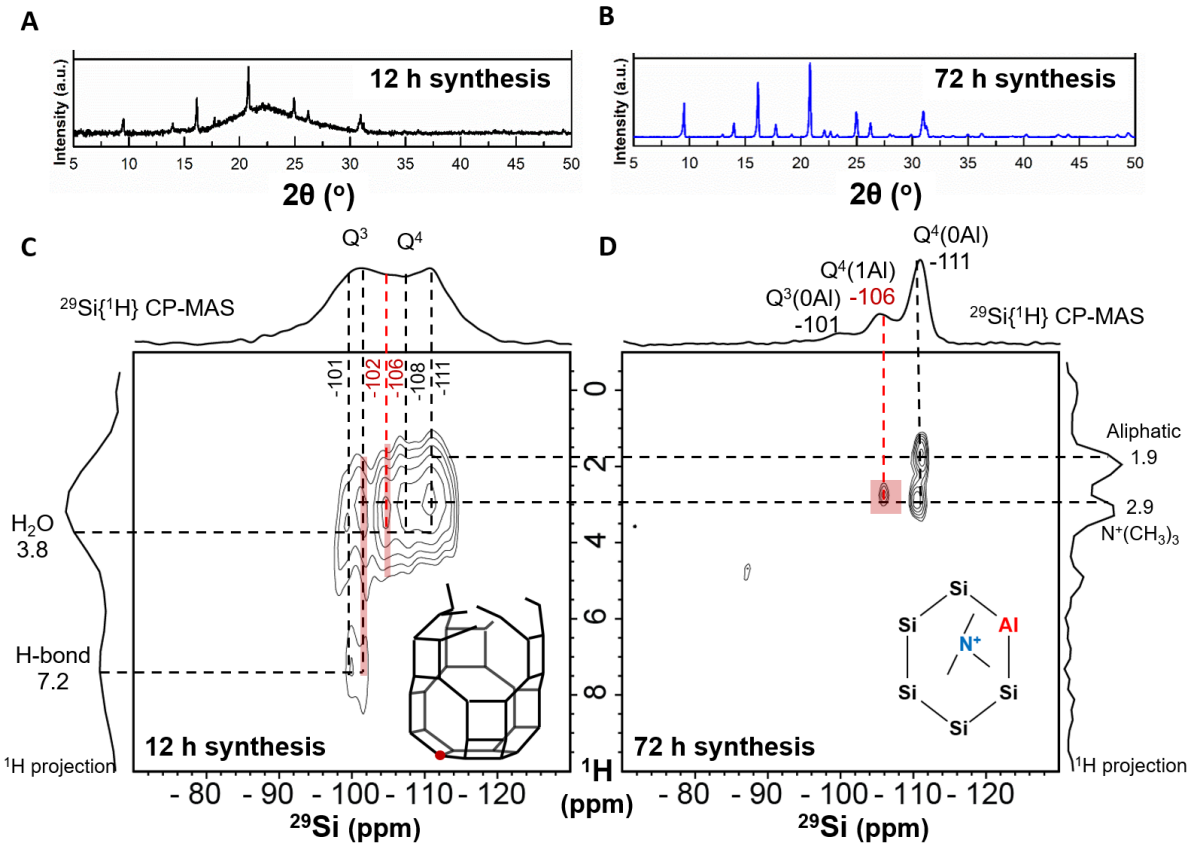

Figure 2. (A) XRD powder pattern of aluminosilicate chabazite sample after (A) 12 h and (B) 72 h of hydrothermal synthesis. (C) 2D ^{29}Si{^{1}H} HETCOR NMR of aluminosilicate chabazite after (C) 12 h or (D) 72 h of hydrothermal synthesis. The solid-state ^{29}Si{^{1}H} HETCOR were acquired at 11.7 T, 298 K and 12.5 kHz MAS on hydrated samples. Lines and regions highlighted in red indicate signals not detected in siliceous chabazite. The inset in (c) shows a partially crystallized chabazite cage with an Al heteroatom (red). The inset in (d) shows the headgroup of a TMAda$^+$ interacting with framework Al.

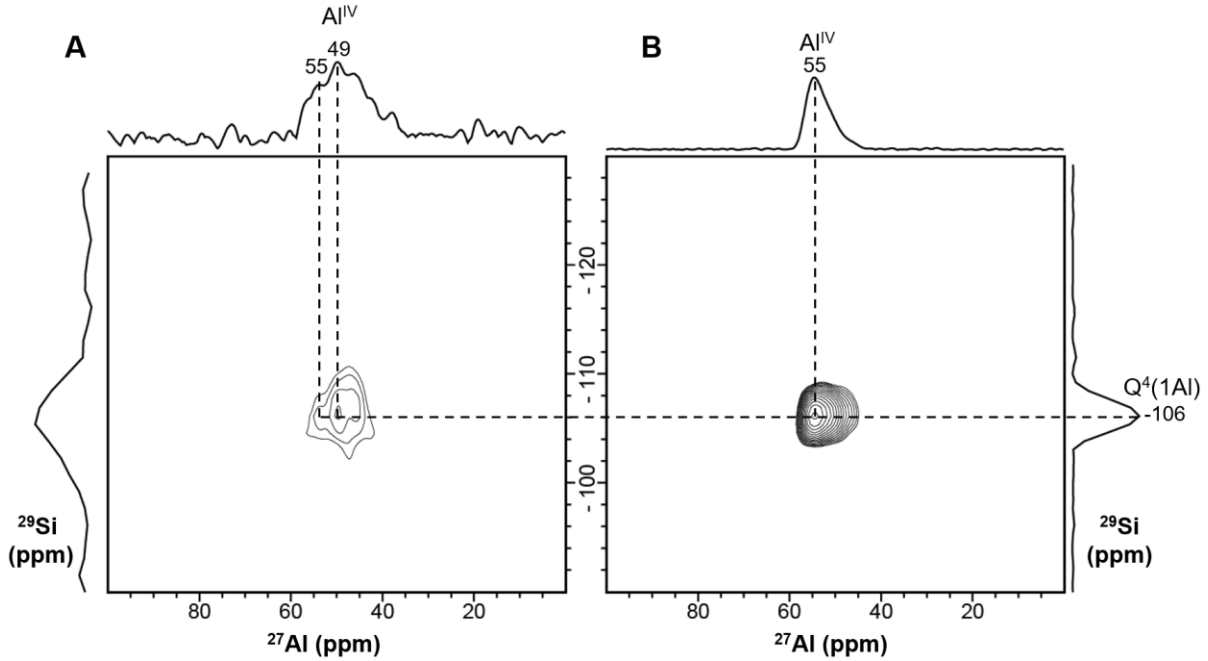

Figure 3. (A) Solid-state 2D ^{27}Al–^{29}Si *J*-mediated HMQC spectrum of the aluminosilicate chabazite product after 12 h of hydrothermal synthesis, revealing correlated signal intensity that corresponds to ^{27}Al heteroatoms that are covalently bonded to ^{29}Si atoms in the zeolite framework. (B) Solid-state 2D ^{27}Al{^{29}Si} *J*-mediated HMQC spectrum of the aluminosilicate chabazite product after 72 h of hydrothermal synthesis. Both spectra were acquired at 100 K and 8 kHz MAS.

To assess the incorporation of aluminum species into the siliceous framework during the HF-synthesis of aluminosilicate chabazite, solid-state 2D ^{27}Al–^{29}Si *J*-mediated HMQC spectra were acquired of 12-h and 72-h HF-synthesis aluminosilicate chabazite. These analyses show regions or correlated signal from ^{29}Si and ^{27}Al moieties coupled by through-bond scalar (*J*-) couplings, resulting in intensity only from ^{29}Si and ^{27}Al moieties correlated through ^{29}Si–O–^{27}Al bonds.[29] The solid-state 2D ^{27}Al–^{29}Si *J*-mediated HMQC spectrum of 12-h HF-synthesis aluminosilicate chabazite shown in Figure 3A reveals a complex distribution of ^{27}Al NMR signals centered at 55 and 49 ppm, attributed to Al^{IV} species, correlated with a ^{29}Si NMR signal at –106 ppm which is attributed to Q^4(1Al) moieties. In contrast, the solid-state 2D ^{27}Al–^{29}Si *J*-mediated HMQC spectrum of 72-h HF-synthesis aluminosilicate chabazite shows only

a narrow ^{27}Al NMR signal at 55 ppm, attributed to Al^{IV}, correlated with a ^{29}Si NMR signal at –106 ppm attributed to Q^4(1Al) moieties. Thus, the ^{27}Al NMR signal at 55 ppm observed in the solid-state 2D ^{27}Al–^{29}Si *J*-mediated HMQC spectrum of the 12-h HF-synthesis aluminosilicate is assigned to aluminum incorporated in the crystalline chabazite framework, while the ^{27}Al NMR signal at 49 ppm is attributed to aluminum species incorporated into more disordered silica environments.

In industrial settings, HF-based syntheses are rarely used due to safety concerns, so most zeolites are synthesized under highly basic conditions. An aluminosilicate zeolite synthesis under basic conditions was undertaken, and the synthesis was quenched at different time points to examine the formation of zeolite crystals. In contrast to the HF syntheses, small molecule silicon and aluminum sources were used. Figure 4A shows powder XRD patterns for the basic-synthesis aluminosilicate chabazite after the synthesis was halted after different amounts of time. The non-soluble solids show sharp diffractions peaks consistent with a chabazite crystal structure. Figure 4B shows average crystallite sizes as determined by scanning electron microscopy as a function of synthesis time, and indicates that the final crystallite size was achieved after 24 h. Interestingly, in this synthesis, it was found that washing the resulting product with water removed all non-crystalline chabazite material. To better understand the evolution of these water-soluble species, the basic-synthesis aluminosilicate chabazite materials were also characterized without rinsing away water-soluble species. Figure 4C shows solid-state 1D ^{29}Si{^{1}H} cross polarization NMR spectra for unwashed basic-synthesis aluminosilicate chabazite after 3, 6, and 12 h of synthesis. After 3 h and 6 h of synthesis, the only ^{29}Si NMR signals observed are two sharp signals at –98.6 and –99.6 ppm. These signals are consistent with previous reports of small anionic silica species in

solution and may represent building blocks of chabazite synthesis.[30] After 12 h of synthesis, these two signals persist, and relatively weak ^{29}Si NMR signals at –111 and –105 ppm consistent with chabazite Q^4(0Al) and Q^4(1Al) moieties are observed, consistent with a substantial conversion of precursors to chabazite at this time point.

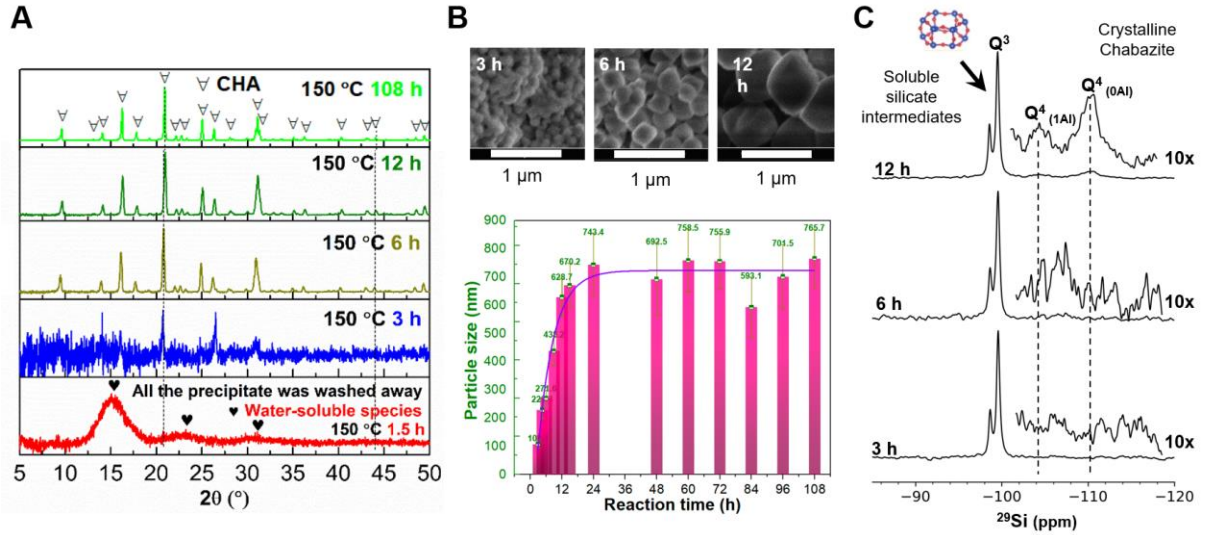

Figure 4. (A) Wide-angle X-ray diffraction patterns of a series of products produced by quenching a aluminum-containing chabazite synthesis with a final Si/Al of 20 after different hydrothermal synthesis times. The samples were washed to remove water-soluble species prior to measurement. (B) SEM images for the same samples, along with a histogram showing the average particle size at different hydrothermal synthesis times. (C) Solid-state 1D ^{29}Si{^{1}H} CPMAS spectra acquired at room temperature for a series of products collected from the same hydrothermal chabazite synthesis mixture after different times, but prior to the removal of water-soluble species.

To better understand the relationship of the small silicate species observed with a ^{29}Si NMR signal of –98.6 and –99.6 ppm to the evolving zeolite framework, a 2D solid-state ^{29}Si{^{1}H} HETCOR NMR spectrum of the 12-h basic-synthesis aluminosilicate chabazite was acquired and is shown in Figure 5. Three ^{29}Si NMR signals are observed at –111, –105, and –99 ppm. The signals at –111 and –105 ppm are assigned to chabazite Q^4(0Al) and Q^4(1Al) moieties, respectively. The ^{29}Si NMR signal at –99 ppm is assigned to a convolution of the signals previously observed at –98.6 and –99.6 ppm, which are unresolved in this experiment.

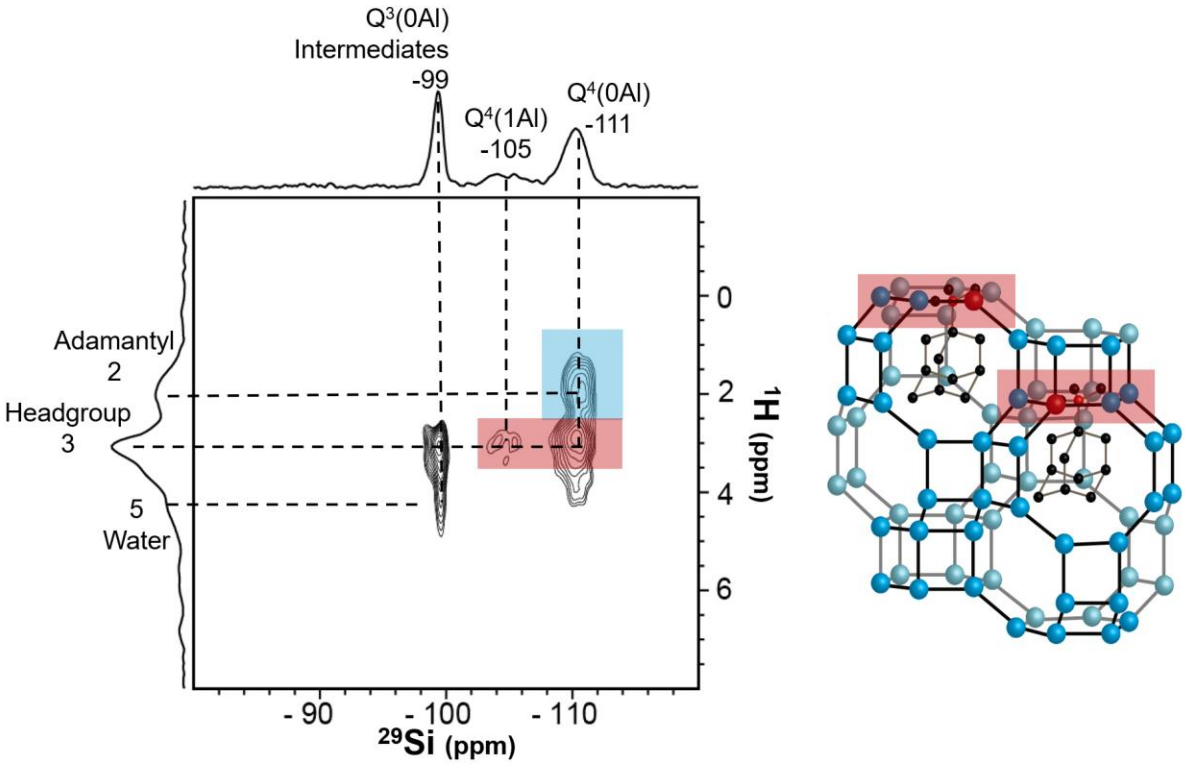

Figure 5. (Left) Solid-state 2D ^{29}Si{^{1}H} HETCOR NMR spectrum acquired at room temperature, 8 kHz MAS and with a 1 ms contact time of an aluminosilicate product after 12 h of hydrothermal chabazite synthesis (see corresponding results in Figure 4), (Right) Stick-and-ball model of a chabazite cage with occluded TMAda^{+} molecules charge-balancing framework Al atoms. The red and blue bands highlight interactions between the cationic head-groups and hydrophobic adamantyl moieties of the TMAda^{+} OSDA with different ^{29}So moieties of the crystallizing chabazite framework.

The Q^4(0Al) signal at –111 ppm shows strong correlations to ^{1}H NMR signals at 1.9 and 2.9 ppm, assigned to TMAdaOH aliphatic species and the TMAdaOH quaternary ammonium headgroup, respectively. The ^{29}Si NMR signal at –105 ppm assigned to Q^4(1Al) moieties shows a strong correlation to the ^{1}H NMR signal at 2.9 ppm assigned to the quaternary ammonium headgroup of TMAdaOH, consistent with the OSDA cation charge-balancing the inserted framework aluminum, as shown in the structural diagram of Figure 5. The Q^3 intermediates at a ^{29}Si NMR signal of –99 ppm exhibit correlations to ^{1}H NMR signals at 2.9 and 4.8 ppm

assigned to the quaternary ammonium headgroup of TMAdaOH and water, respectively. This provides evidence that TMAdaOH stabilizes these small silicate cations.

Along with the *ex situ* characterization methods discussed in this chapter, it is desirable to characterize the evolution of framework species during zeolite syntheses *in situ* under hydrothermal conditions. During the project, UCSB received an NMR probehead with a custom rotor setup designed to be used under temperatures and pressures like those used for zeolite synthesis.[31] While the project ended before *in situ* experiments tracking zeolite crystallization could be completed, preliminary NMR measurements with the high-temperature, high-pressure NMR system were performed. Figure 6 shows 1D ^{29}Si NMR spectra acquired of the basic aluminosilicate zeolite synthesis mixture. After inserted into the rotor at room temperature, the synthesis mixture shows sharp ^{29}Si NMR signals at –98.6 and –99.6 ppm, consistent with previous room temperature observations. When heated to 150 ºC, a typical zeolite synthesis temperature, ^{29}Si NMR reveals broad signals at –98 and –89 ppm,

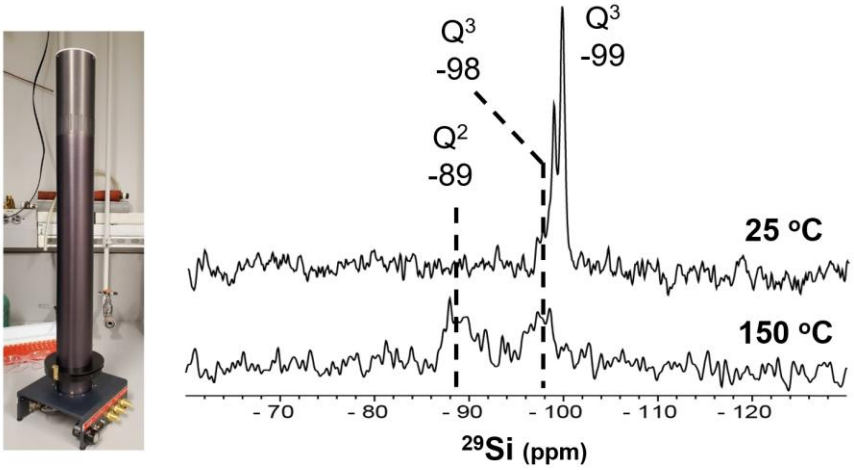

Figure 6. (Left) *In situ* NMR probehead that arrived at UCSB during the project. (Right) Direct-excitation *in situ* ^{29}Si NMR spectra acquired at 25 ºC and at 150 ºC and 5 kHz MAS of a chabazite synthesis mixture at the start of the hydrothermal reaction. The spectra were acquired from a sample sealed in a special NMR MAS rotor capable of withstanding the temperature and pressure of zeolite synthesis conditions.

assigned to Q^3 and Q^2 species that evolve upon heating to reaction conditions. This observation underscores the importance of performing measurements *in situ* under synthesis conditions, as the distributions of species that are stable at room temperature will not necessarily be the same species that are stable at elevated temperatures.

Conclusions

Zeolite syntheses involve complex interactions between structure-directing agents. Here, for various standard chabazite syntheses, NMR methods for characterizing interactions between evolving framework species and structure-directing agents are discussed. 2D ^{29}Si{^{1}H} HETCOR NMR spectra provide information on both disordered and ordered ^{29}Si moieties during zeolite synthesis. In addition, 2D ^{27}Al–^{29}Si *J*-HMQC spectra reveal the evolution of incorporated framework aluminum species in aluminosilicate chabazite. These advanced methods are accompanied by time-resolved powder XRD, SEM, and ^{29}Si NMR to track zeolite syntheses. Lastly, *in situ* NMR methods for tracking zeolite crystallization are demonstrated. These techniques could provide information on how different novel zeolite syntheses modify framework aluminum distributions during synthesis.

In the future, this work could be built upon to examine novel zeolite syntheses. For example, methods to synthesize various zeolites by interzeolite conversion, where a zeolite is used as the silicon and aluminum source in synthesis, have been recently reported in the literature. The relative rates of simultaneous dissolution and crystallization are not well understood in these systems, and it is still debated whether these zeolite precursors are dissolved into single Si or Al atom species, or if small anionic structures from the dissolving zeolite persist in solution and recrystallize as the target zeolite. In addition, assembly-disassembly-organization-reassembly (ADOR) zeolite synthesis processes, where one

framework-type is synthesized, then the synthesis is modified to access a difficult-to-synthesize zeolite framework structure, are complex. These methods could provide better understanding of the atomic-level interactions that guide these complex syntheses in order to enable more rational design of these processes.

Supporting Information

Materials and Methods

Synthesis. Siliceous chabazite samples for crystallization studies were synthesized by Dr. Xiaojun Zeng. The final synthesis mixture had the molar ratio 1 SiO_2:0.75 TMAdaOH:0.75 HF:4.5 H_2O. First a 25 wt% TMAdaOH aqueous solution was combined with TEOS. This solution was stirred at room temperature for 12 h, then heated to 70 ºC to evaporate water until the appropriate molar ratio was reached. After evaporation, the appropriate amount of HF was added, and the solution was stirred for another 12 h at room temperature. The sample was then placed in a high-pressure vessel and heated to 150 ºC while allowing pressure to naturally build. Hydrothermal synthesis at 150 ºC was performed for various amounts of time as reported in the results and discussion section. After hydrothermal synthesis, the sample was rapidly cooled then was vacuum filtered and rinsed with excess water. The solids after filtration were used in all characterization experiments reported here.

HF-synthesis aluminosilicate chabazite samples were prepared by the same method as the siliceous chabazite samples, but with the addition of Al_2O_3 as an Al source. The appropriate amount of Al_2O_3 powder was added to the initial TMAdaOH-TEOS synthesis mixture at the beginning of the synthesis. The molar ratio of this synthesis was 1 SiO_2:0.025 Al_2O_3:0.75 TMAdaOH:0.75 HF:4.5 H_2O.

The basic-synthesis aluminum-containing chabazite was prepared under hydrothermal conditions using a gel precursor with molar composition of 1 SiO_2:0.025 aluminum isopropoxide:0.75 TMAdaOH: 4.5 H_2O. Typically, 0.34 g of aluminum isopropoxide (AIP, Aldrich) was dissolved in 42.27 g of *N,N,N*-trimethyl-1-adamantylammonium hydroxide (TMAdaOH, 25 wt% in water solution, Sachem). Subsequently, 13.89 g of tetraethoxysilane

(TEOS, Sigma-Aldrich) were added and stirred for 12 h. A portion of the water was then evaporated to reduce the H_2O content of the reaction mixture, after which it was placed in a Teflon-lined stainless steel autoclave (30 mL in volume) for hydrothermal reaction at 423 K for different lengths of time (1.5~108 h). The resulting product was washed with deionized water and dried in a vacuum oven.

Basic characterization. The phase and crystallinity of Al-CHA zeolites were evaluated by powder X-ray diffraction (XRD, Malvern Panalytical, Empyrean, Cu Kα radiation). The morphology and microstructure of the sample were characterized by scanning electron microscopy using a FEI Nova Nano 650 SEM.

Solid-state NMR spectroscopy. Solid-state 1D $^{29}Si\{^1H\}$ CP-MAS and 2D $^{29}Si\{^1H\}$ and $^{13}C\{^1H\}$ HETCOR experiments were acquired on a 11.7 T Bruker Avance-II NMR spectrometer operating at frequencies of 500.2 MHz for ^1H, 125.8 MHz for ^{13}C and 99.4 MHz for ^{29}Si. The spectrometer was equipped with a Bruker 4 mm HX double resonance probehead and samples were packed in zirconia rotors with Kel-F caps. A 5.0 ms contact time was used for $^{29}Si\{^1H\}$ CP-MAS experiments. $^{29}Si\{^1H\}$ HETCOR experiments were acquired using a 1.0 ms contact time and a recycle delay of 1.0 s. $^{13}C\{^1H\}$ HETCOR experiments were acquired using a 0.5 ms contact time and a recyle delay of 1.0 s. All HETCOR experiments were acquired using eDUMBO homonuclear decoupling during the ^1H evolution period to enhance resolution in the indirect dimension.[32] Experiments were performed at room temperature with 12.5 kHz magic angle spinning.

Solid-state 2D ^{27}Al–^{29}Si *J*-HMQC were acquired on a Bruker 9.4 T Avance-III NMR spectrometer operating at 400.2 MHz for ^1H, 104.3 MHz for ^{27}Al, and 79.5 MHz for ^{29}Si. This spectrometer was equipped with a Bruker variable temperature 3.2 mm HXY triple resonance

probehead and a cooling cabinet. Samples for solid-state 2D ^{27}Al–^{29}Si *J*-HMQC experiments were packed in zirconia rotors with Kel-F drive caps. These experiments were performed with a 1.0 recycle delay. These experiments were performed under 8 kHz magic angle spinning at 95 K.

Solution-state 1D ^{13}C and ^{1}H single-pulse NMR experiments were carried out on Bruker Avance NMR spectrometer equipped with a narrow bore magnet charged to 11.7 T and set to 500.2 MHz for ^{1}H and 125.8 MHz for ^{13}C. A 25 wt% aqueous TMAdaOH solution was measured in a 5 mm solution-state NMR tube.

Additional Data

To confidently assign NMR signals related to the TMAdaOH structure-directing agent, NMR experiments were performed to identify the chemical shifts of its ^{13}C and ^{1}H moieties. Figure S1A shows a solution-state ^{1}H NMR spectrum of TMAdaOH in water. Along with a ^{1}H signal attributed to water at 4.7 ppm, ^{1}H signals attributed to TMAdaOH are observed at 2.9, 2.2, 1.9, and 1.6 ppm and are assigned as shown in the figure. Similar assignments for ^{13}C are found from the solution-state ^{13}C NMR spectrum shown in Figure S1B. To understand the ^{1}H resolution that could be expected for TMAdaOH occluded in the zeolite pores, a solid-state 2D ^{13}C{^{1}H} HETCOR NMR spectrum of the fully-synthesized siliceous chabazite was acquired and is shown in Figure S1C. The observed correlations are as expected given the assignments in Figure S1A and B.

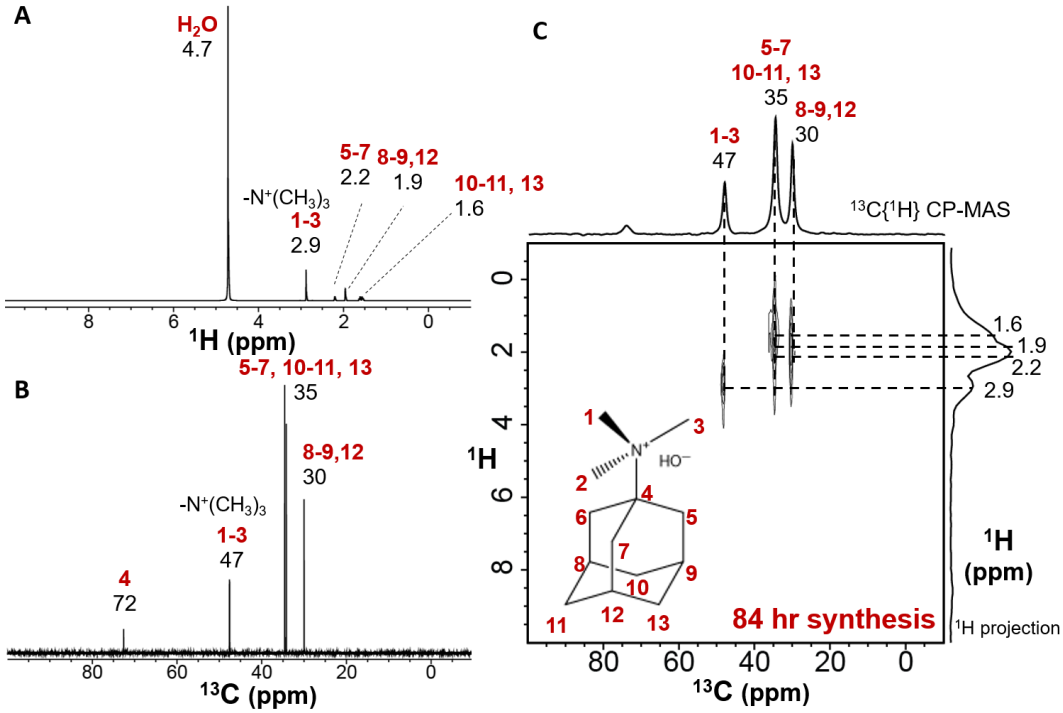

Figure S1. (A) Solution-state ^{1}H NMR spectrum of 25 wt% aqueous TMAdaOH. (B) Solution-state ^{13}C NMR spectrum of 25 wt% aqueous TMAdaOH. (C) 2D ^{13}C{^{1}H} HETCOR of siliceous chabazite revealing TMAdaOH occluded in the zeolite nanopores. All spectra were acquired at 11.7 T and 298 K. The solid-state ^{13}C{^{1}H} HETCOR was acquired under 12.5 kHz MAS.

References

(1) Rege, S. U.; Yang, R. T. Limits for Air Separation by Adsorption with LiX Zeolite. *Ind. Eng. Chem. Res.* **1997**, *36* (12), 5358–5365. https://doi.org/10.1021/ie9705214.

(2) Ghobarkar, H.; Schäf, O.; Guth, U. Zeolites—from Kitchen to Space. *Progress in Solid State Chemistry* **1999**, *27* (2–4), 29–73. https://doi.org/10.1016/S0079-6786(00)00002-9.

(3) Vogt, E. T. C.; Weckhuysen, B. M. Fluid Catalytic Cracking: Recent Developments on the Grand Old Lady of Zeolite Catalysis. *Chemical Society Reviews* **2015**, *44* (20), 7342–7370. https://doi.org/10.1039/c5cs00376h.

(4) Guo, P.; Yan, N.; Wang, L.; Zou, X. Database Mining of Zeolite Structures. *Crystal Growth and Design* **2017**, *17* (12), 6821–6835. https://doi.org/10.1021/acs.cgd.7b01410.

(5) Breck, D. W. *Zeolite Molecular Sieves: Structure, Chemistry, and Use*; Wiley: New York, 1973.

(6) Deimund, M. A.; Harrison, L.; Lunn, J. D.; Liu, Y.; Malek, A.; Shayib, R.; Davis, M. E. Effect of Heteroatom Concentration in SSZ-13 on the Methanol-to-Olefins Reaction. *ACS Catalysis* **2016**, *6* (2), 542–550. https://doi.org/10.1021/acscatal.5b01450.

(7) Nova, I.; Tronconi, E. *Urea-SCR Technology for deNOx After Treatment of Diesel Exhausts*; Nova, I., Tronconi, E., Eds.; Fundamental and Applied Catalysis; Springer New York: New York, NY, 2014. https://doi.org/10.1007/978-1-4899-8071-7.

(8) Beale, A. M.; Gao, F.; Lezcano-Gonzalez, I.; Peden, C. H. F.; Szanyi, J. Recent Advances in Automotive Catalysis for NO_x Emission Control by Small-Pore Microporous Materials. *Chemical Society Reviews* **2015**, *44* (20), 7371–7405. https://doi.org/10.1039/c5cs00108k.

(9) Román-Leshkov, Y.; Moliner, M.; Davis, M. E. Impact of Controlling the Site Distribution of Al Atoms on Catalytic Properties in Ferrierite-Type Zeolites. *The Journal of Physical Chemistry C* **2011**, *115* (4), 1096–1102. https://doi.org/10.1021/jp106247g.

(10) Di Iorio, J. R.; Gounder, R. Controlling the Isolation and Pairing of Aluminum in Chabazite Zeolites Using Mixtures of Organic and Inorganic Structure-Directing Agents. *Chemistry of Materials* **2016**, *28* (7), 2236–2247. https://doi.org/10.1021/acs.chemmater.6b00181.

(11) Di Iorio, J. R.; Li, S.; Jones, C. B.; Nimlos, C. T.; Wang, Y.; Kunkes, E.; Vattipalli, V.; Prasad, S.; Moini, A.; Schneider, W. F.; Gounder, R. Cooperative and Competitive Occlusion of Organic and Inorganic Structure-Directing Agents within Chabazite Zeolites Influences Their Aluminum Arrangement. *Journal of the American Chemical Society* **2020**, *142* (10), 4807–4819. https://doi.org/10.1021/jacs.9b13817.

(12) Di Iorio, J. R.; Nimlos, C. T.; Gounder, R. Introducing Catalytic Diversity into Single-Site Chabazite Zeolites of Fixed Composition via Synthetic Control of Active Site

Proximity. *ACS Catalysis* **2017**, *7* (10), 6663–6674. https://doi.org/10.1021/acscatal.7b01273.

(13) Schwalbe-Koda, D.; Kwon, S.; Paris, C.; Bello-Jurado, E.; Jensen, Z.; Olivetti, E.; Willhammar, T.; Corma, A.; Román-Leshkov, Y.; Moliner, M.; Gómez-Bombarelli, R. A Priori Control of Zeolite Phase Competition and Intergrowth with High-Throughput Simulations. *Science* **2021**, *374* (6565), 308–315. https://doi.org/10.1126/science.abh3350.

(14) Lee, S.; Nimlos, C. T.; Kipp, E. R.; Wang, Y.; Gao, X.; Schneider, W. F.; Lusardi, M.; Vattipalli, V.; Prasad, S.; Moini, A.; Gounder, R. Evolution of Framework Al Arrangements in CHA Zeolites during Crystallization in the Presence of Organic and Inorganic Structure-Directing Agents. *Crystal Growth and Design* **2022**, *22* (10), 6275–6295. https://doi.org/10.1021/ACS.CGD.2C00856.

(15) Inoue, T.; Itakura, M.; Jon, H.; Oumi, Y.; Takahashi, A.; Fujitani, T.; Sano, T. Synthesis of LEV Zeolite by Interzeolite Conversion Method and Its Catalytic Performance in Ethanol to Olefins Reaction. *Microporous and Mesoporous Materials* **2009**, *122* (1), 149–154. https://doi.org/10.1016/j.micromeso.2009.02.027.

(16) Devos, J.; A. Shah, M.; Dusselier, M. On the Key Role of Aluminium and Other Heteroatoms during Interzeolite Conversion Synthesis. *RSC Advances* **2021**, *11* (42), 26188–26210. https://doi.org/10.1039/D1RA02887A.

(17) Robijns, S.; Devos, J.; Donckels, T.; de Oliveira-Silva, R.; De Witte, N.; Sakellariou, D.; Van Assche, T. R. C.; Dusselier, M. Steering Interzeolite Conversion with Alkali Metal Cations: Lithium Maximizes Al Proximity in SSZ-13 Zeolite Genesis. *Crystal Growth and Design* **2023**, *23* (1), 289–299. https://doi.org/10.1021/ACS.CGD.2C01009.

(18) Goel, S.; Zones, S. I.; Iglesia, E. Synthesis of Zeolites via Interzeolite Transformations without Organic Structure-Directing Agents. *Chem. Mater.* **2015**, *27* (6), 2056–2066. https://doi.org/10.1021/cm504510f.

(19) Itakura, M.; Goto, I.; Takahashi, A.; Fujitani, T.; Ide, Y.; Sadakane, M.; Sano, T. Synthesis of High-Silica CHA Type Zeolite by Interzeolite Conversion of FAU Type Zeolite in the Presence of Seed Crystals. *Microporous and Mesoporous Materials* **2011**, *144* (1), 91–96. https://doi.org/10.1016/j.micromeso.2011.03.041.

(20) Diaz Arroyo, R.; Pascual, J.; Jensen, K.; Hwang, S.-J.; Zones, S. I. Studies on the Conversion of FAU Zeolites to SSZ-13: The Rate Advantage of Having Both Si and Al in the FAU Reagent. *Crystal Growth & Design* **2023**, *23* (9), 6318–6330. https://doi.org/10.1021/acs.cgd.3c00219.

(21) Liu, Z.; Chokkalingam, A.; Miyagi, S.; Yoshioka, M.; Ishikawa, T.; Yamada, H.; Ohara, K.; Tsunoji, N.; Naraki, Y.; Sano, T.; Okubo, T.; Wakihara, T. Revealing Scenarios of Interzeolite Conversion from FAU to AEI through the Variation of Starting Materials. *Physical Chemistry Chemical Physics* **2022**, *24* (7), 4136–4146. https://doi.org/10.1039/D1CP03751J.

(22) Eliášová, P.; Opanasenko, M.; S. Wheatley, P.; Shamzhy, M.; Mazur, M.; Nachtigall, P.; J. Roth, W.; E. Morris, R.; Čejka, J. The ADOR Mechanism for the Synthesis of New Zeolites. *Chemical Society Reviews* **2015**, *44* (20), 7177–7206. https://doi.org/10.1039/C5CS00045A.
(23) Zhang, J.; Veselý, O.; Tošner, Z.; Mazur, M.; Opanasenko, M.; Čejka, J.; Shamzhy, M. Toward Controlling Disassembly Step within the ADOR Process for the Synthesis of Zeolites. *Chem. Mater.* **2021**, *33* (4), 1228–1237. https://doi.org/10.1021/acs.chemmater.0c03993.
(24) Morris, S. A.; Bignami, G. P. M.; Tian, Y.; Navarro, M.; Firth, D. S.; ÄŒejka, J.; Wheatley, P. S.; Dawson, D. M.; Slawinski, W. A.; Wragg, D. S.; Morris, R. E.; Ashbrook, S. E. In Situ Solid-State NMR and XRD Studies of the ADOR Process and the Unusual Structure of Zeolite IPC-6. *Nature Chemistry* **2017**, *9* (10), 1012–1018. https://doi.org/10.1038/nchem.2761.
(25) Yue, Q.; Steciuk, G.; Mazur, M.; Zhang, J.; Petrov, O.; Shamzhy, M.; Liu, M.; Palatinus, L.; Čejka, J.; Opanasenko, M. Catching a New Zeolite as a Transition Material during Deconstruction. *J. Am. Chem. Soc.* **2023**, *145* (16), 9081–9091. https://doi.org/10.1021/jacs.3c00423.
(26) Miyamoto, M.; Nakatani, T.; Fujioka, Y.; Yogo, K. Verified Synthesis of Pure Silica CHA-Type Zeolite in Fluoride Media. *Microporous and Mesoporous Materials* **2015**, *206* (C), 67–74. https://doi.org/10.1016/j.micromeso.2014.12.012.
(27) Eilertsen, E. A.; Arstad, B.; Svelle, S.; Lillerud, K. P. Single Parameter Synthesis of High Silica CHA Zeolites from Fluoride Media. *Microporous and Mesoporous Materials* **2012**, *153*, 94–99. https://doi.org/10.1016/j.micromeso.2011.12.026.
(28) Zones, S. I. Zeolite SSZ-13 and Its Method of Preparation, 1985.
(29) Massiot, D.; Fayon, F.; Alonso, B.; Trebosc, J.; Amoureux, J. P. Chemical Bonding Differences Evidenced from J-Coupling in Solid State NMR Experiments Involving Quadrupolar Nuclei. *Journal of Magnetic Resonance* **2003**, *164* (1), 160–164. https://doi.org/10.1016/S1090-7807(03)00134-4.
(30) Harris, R. K.; Knight, C. T. G. Silicon-29 NMR Studies of Aqueous Silicate Solutions. Part IV Tetraalkylammonium Hydroxide Solutions. *Journal of Molecular Structure* **1982**, *78* (3–4), 273–278. https://doi.org/10.1016/0022-2860(82)80013-6.
(31) Walter, E. D.; Qi, L.; Chamas, A.; Mehta, H. S.; Sears, J. A.; Scott, S. L.; Hoyt, D. W. Operando MAS NMR Reaction Studies at High Temperatures and Pressures. *Journal of Physical Chemistry C* **2018**, *122* (15), 8209–8215. https://doi.org/10.1021/acs.jpcc.7b11442.
(32) Elena, B.; de Paëpe, G.; Emsley, L. Direct Spectral Optimisation of Proton-Proton Homonuclear Dipolar Decoupling in Solid-State NMR. *Chemical Physics Letters* **2004**, *398* (4–6), 532–538. https://doi.org/10.1016/j.cplett.2004.09.122.

Chapter 6

Conclusions and future perspectives

Zeolites are used as catalysts in a wide range of industrial catalytic processes. When catalytic sites are associated with cations in the zeolite pores, framework aluminum distributions play an important role in controlling the distributions of active sites, which can have significant effects on the activity and selectivity of the zeolite catalyst. As such, developing synthesis-structure-function relationships for zeolite catalysts is desirable for the design of next generation catalysts to help meet energy transition goals. However, the structure piece of this relationship, meaning an understanding of distributions of aluminum heteroatoms in aluminosilicate zeolites, is often challenging to elucidate due to the complex non-periodic and non-stoichiometric distributions of these heteroatoms. This dissertation sought to close this knowledge gap. I have demonstrated that advanced solid-state nuclear magnetic resonance (NMR) spectroscopy techniques, in combination with other advanced characterization techniques and adsorption and reaction studies, can provide useful information on both local and macroscopic distributions of aluminum heteroatoms in zeolites which can aid in explaining differences in reaction properties. Here is a brief summary of the conclusions from each chapter in this thesis along with commentary on future directions for each project.

Chapter 2: Direct detection of paired aluminum heteroatoms in chabazite zeolite catalysts and their significance for methanol dehydration activity

For methanol dehydration reactions over the small-pore zeolite chabazite, closely paired aluminum configurations with aluminum atoms separated by one silicon atom (second-nearest-neighbor paired configuration) and aluminum atoms separated by two silicon atoms (third-nearest-neighbor paired configurations) have been suggested to improve rates of

reaction relative to isolated aluminum species.[1,2] However, detecting these paired aluminum configurations and comparing their quantities between zeolites is challenging. For two chabazite materials with the same bulk aluminum content that standard methods show to have similar levels of paired aluminum configurations, it was found that their methanol dehydration activity was notably different. Solid-state 2D ^{27}Al–^{29}Si through-bond NMR correlation analyses were used to detect differences in second-nearest-neighbor paired configuration levels between the two zeolites. In addition, solid-state 2D ^{29}Si–^{29}Si through-bond NMR correlation analyses were used to detect differences in third-nearest-neighbor paired configuration levels between the two zeolites. Higher levels of paired aluminum configurations were detected in the zeolite with higher methanol dehydration activity.

An obvious future extension of this work would be to apply these techniques to other zeolite framework types. In chabazite, all tetrahedral sites in the zeolite lattice are equivalent, resulting in a relatively straightforward-to-interpret ^{29}Si NMR spectrum thanks to all siliceous Q^4 species having the same ^{29}Si chemical shift. The medium pore zeolite MFI (commercially known as ZSM-5) has 12 distinct tetrahedral sites, which all have slightly different ^{29}Si chemical shifts. If the techniques demonstrated in this chapter could be performed on MFI zeolites with sufficient resolution to identify different tetrahedral sites based on ^{29}Si NMR chemical shifts, information could be obtained not only on the pairing of aluminum species, but also the tetrahedral sites that the paired aluminum species occupy.

An additional extension of the work would be to compare these NMR methods more rigorously with literature-reported methods for detecting aluminum pairing by titration of divalent cations.[3–5] The NMR methods discussed in this chapter require specialized equipment and are time-consuming; however, they provide unambiguous information on paired aluminum

levels. In contrast, divalent cation titration methods are straightforward to perform in any chemistry wet lab but provide ambiguous information in terms of what sites they truly exchange into. An extensive study combining divalent cation titrations with simulations to suggest types of exchange sites for each cation combined with these NMR methods would produce fantastic practical knowledge for understanding paired aluminum distributions in zeolites.

Chapter 3: Understanding distributions of copper and aluminum species in an aged copper chabazite deNO$_x$ catalyst

Cu^{2+}-exchanged chabazite (Cu-CHA), a small-pore zeolite, is used industrially as a deNO$_x$ catalyst in diesel exhaust systems. A significant challenge with these catalysts is sensitivity to high-temperature hydrothermal conditions, which results in a loss of activity over the lifetime of the catalyst.[6] The molecular origins of this deactivation, along with the types of active sites that are resistant to deactivation and present after severe hydrothermal treatment are not well understood. Here, advanced characterization techniques were combined to provide insights into the evolution of copper and framework aluminum species as a result of aging. Scanning transmission electron microscopy reveals the formation of nanoscale Cu clusters after hydrothermal treatment, consistent with loss of active single-atom Cu species. Solid-state NMR of Cu-CHA catalysts with different aging conditions after inducing the reduction half-cycle of the deNO$_x$ reaction redox cycle reveal differences in distributions of adsorbed species and in the fractions of framework aluminum species in paired aluminum configurations, suggesting that paired aluminum configurations are stabilized under hydrothermal conditions. In addition, ^{15}N exchange NMR analyses on adsorbed species reveal that site-exchange kinetics evolve upon aging in ways consistent with preservation of closely paired aluminum species.

An important extension of this work will be to perform these analyses—particularly analyses of paired aluminum in the zeolite framework after hydrothermal treatment—on Cu-CHA catalysts prepared in a variety of ways, with different framework Al contents, Cu/Al ratios, and zeolite synthesis methods. Varying these parameters will provide a better understanding of what types of species are preserved upon hydrothermal treatment. In particular, chabazite syntheses that have been suggested to result in different types of paired aluminum configurations (e.g. pairing in 8-member ring vs. 6-member ring) should be investigated, as this will provide more fine grained insights on the types of framework aluminum species stabilized by Cu^{2+} under hydrothermal conditions.[7–9]

Chapter 4: External-surface acid sites in a dealuminated zeolite and their role in coking

Many hydrocarbon conversion reactions, including the cracking of large molecules to smaller, more useful chemical intermediates are performed over H^+-exchanged zeolites, where H^+ cations charge-balancing the zeolite framework act as Bronsted acid sites to catalyze reactions. Often zeolites used as catalysts in these reactions are modified to have mesopores in order to improve mass transport and make acid sites accessible to larger reactant species.[10] However, the distributions of acid sites and types of framework moieties exposed to the mesopore surface are challenging to characterize. Here, solid-state 2D ^{27}Al–^{29}Si NMR correlation analyses reveal distinct spectroscopic signatures for mesopore-defect acid sites. It is demonstrated that these moieties can be modified by an organosilane deposition, resulting in a catalyst with lower initial activity due to loss of active sites but less susceptibility to coke formation in a hexane cracking reaction. ^1H NMR analyses of catalysts after hexane cracking reveal differences in the types of polyaromatic species formed on an unmodified or silylated catalyst, indicating that bulkier coke species form at mesopore surface active sites. These

analyses provide important information for the design of zeolite catalysts where avoiding coke formation is desirable.

Similar methods explored here could be applied to different industrially-relevant zeolite catalysts. Methods other than silylation are typically employed in industrial settings to modify zeolite catalysts and improve their selectivity. For example, phosphorus modification is often used to modify activity of cracking catalysts.[11] However, the atomic-level effects of phosphorus modification are not well understood. Similar NMR methods would be well-suited to establishing changes in aluminum distributions as a result of phosphorus modification, and similar studies to characterize adsorbed species post-reaction would help in understanding the atomic-level origins of changes in reaction properties. Another system of interest is zeolite catalyst composites. Zeolite catalysts used industrially are typically mixed with a binder material, which can have catalytic activity.[12] Similar methods could help to understand the types and locations of sites in a zeolite composite catalyst that are most important for desirable reaction properties.

Chapter 5: Methods for characterizing evolution of local framework chemical environments during zeolite crystallization

Understanding how different zeolite syntheses influence aluminum distributions is important for the intelligent design of zeolite catalysts. Here, we demonstrate NMR methods suitable for studying these distributions and the influence of synthesis for a series of standard chabazite syntheses. Solid-state 2D ^{29}Si-^{1}H NMR correlation analyses reveal interactions between organic structure-directing agents and framwork moieties and the evolution of these interactions with synthesis time. Solid-state 2D ^{27}Al-^{29}Si NMR correlation analyses reveal the evolution of framework ^{27}Al-O-^{29}Si moieties as a function of synthesis time. *In situ* NMR

methods are also demonstrated for tracking the evolution of framework species under elevated-temperature hydrothermal reaction conditions.

The methods demonstrated here could be applied to new, complex zeolite syntheses where the dissolution and recrystallization of aluminosilicate species is believed to play an important role in controlling zeolite framework-type selection and aluminum heteroatom distributions. For example, interzeolite conversion methods utilize zeolites as both aluminum and silicon sources.[13,14] In addition, assembly-disassembly-organization-reassembly zeolite crystallization processes access unique crystal structures through selective modification of synthesized zeolites.[15,16] With both of these syntheses, the methods outlined here would provide important information on the relationships between initial zeolite framework moieties and final zeolite framework moieties, and also how these evolving structures interact with structure-directing agents.

References

(1) Di Iorio, J. R.; Nimlos, C. T.; Gounder, R. Introducing Catalytic Diversity into Single-Site Chabazite Zeolites of Fixed Composition via Synthetic Control of Active Site Proximity. *ACS Catalysis* **2017**, *7* (10), 6663–6674. https://doi.org/10.1021/acscatal.7b01273.

(2) Marsden, G.; Kostetskyy, P.; Sekiya, R. S.; Hoffman, A.; Lee, S.; Gounder, R.; Hibbitts, D.; Broadbelt, L. J. Quantifying Effects of Active Site Proximity on Rates of Methanol Dehydration to Dimethyl Ether over Chabazite Zeolites through Microkinetic Modeling. *ACS Materials Au* **2022**, *2* (2), 163–175. https://doi.org/10.1021/ACSMATERIALSAU.1C00057/.

(3) Dědeček, J.; Kaucky, D.; Wichterlová, B.; Gonsiorová, O. Co^{2+} Ions as Probes of Al Distribution in the Framework of Zeolites. ZSM-5 Study. *PCCP* **2002**, *4*, 5406–5413. https://doi.org/10.1039/b203966b.

(4) Nimlos, C. T.; Hoffman, A. J.; Hur, Y. G.; Lee, J.; Di Iorio, J. R.; Hibbitts, D. D.; Gounder, R. Experimental and Theoretical Assessments of Aluminum Proximity in MFI Zeolites and Its Alteration by Organic and Inorganic Structure-Directing Agents. *Chemistry of Materials* **2020**, *32* (21), 9277–9298. https://doi.org/10.1021/acs.chemmater.0c03154.

(5) Chen, K.; Abdolrahmani, M.; Horstmeier, S.; Pham, T. N.; Nguyen, V. T.; Zeets, M.; Wang, B.; Crossley, S.; White, J. L. Brønsted–Brønsted Synergies between Framework and Noncrystalline Protons in Zeolite H-ZSM-5. *ACS Catalysis* **2019**, *9* (7), 6124–6136. https://doi.org/10.1021/ACSCATAL.9B01583.

(6) Gao, F.; Szanyi, J. On the Hydrothermal Stability of Cu/SSZ-13 SCR Catalysts. *Applied Catalysis A: General* **2018**, *560*, 185–194. https://doi.org/10.1016/j.apcata.2018.04.040.

(7) Di Iorio, J. R.; Gounder, R. Controlling the Isolation and Pairing of Aluminum in Chabazite Zeolites Using Mixtures of Organic and Inorganic Structure-Directing Agents. *Chemistry of Materials* **2016**, *28* (7), 2236–2247. https://doi.org/10.1021/acs.chemmater.6b00181.

(8) Di Iorio, J. R.; Li, S.; Jones, C. B.; Nimlos, C. T.; Wang, Y.; Kunkes, E.; Vattipalli, V.; Prasad, S.; Moini, A.; Schneider, W. F.; Gounder, R. Cooperative and Competitive Occlusion of Organic and Inorganic Structure-Directing Agents within Chabazite Zeolites Influences Their Aluminum Arrangement. *Journal of the American Chemical Society* **2020**, *142* (10), 4807–4819. https://doi.org/10.1021/jacs.9b13817.

(9) Schwalbe-Koda, D.; Kwon, S.; Paris, C.; Bello-Jurado, E.; Jensen, Z.; Olivetti, E.; Willhammar, T.; Corma, A.; Román-Leshkov, Y.; Moliner, M.; Gómez-Bombarelli, R. A Priori Control of Zeolite Phase Competition and Intergrowth with High-Throughput Simulations. *Science* **2021**, *374* (6565), 308–315. https://doi.org/10.1126/science.abh3350.

(10) Vogt, E. T. C.; Weckhuysen, B. M. Fluid Catalytic Cracking: Recent Developments on the Grand Old Lady of Zeolite Catalysis. *Chemical Society Reviews* **2015**, *44* (20), 7342–7370. https://doi.org/10.1039/c5cs00376h.
(11) Van Der Bij, H. E.; Weckhuysen, B. M. Phosphorus Promotion and Poisoning in Zeolite-Based Materials: Synthesis, Characterisation and Catalysis. *Chemical Society Reviews* **2015**, *44* (20), 7406–7428. https://doi.org/10.1039/c5cs00109a.
(12) Lakiss, L.; Kouvatas, C.; Gilson, J.-P.; Valtchev, V.; Mintova, S.; Fernandez, C.; Bedard, R.; Abdo, S.; Bricker, J. Atomic-Insight into Zeolite Catalyst Forming—an Advanced NMR Study. *J. Phys. Chem. C* **2021**, *125* (36), 20028–20034. https://doi.org/10.1021/acs.jpcc.1c05501.
(13) Devos, J.; Bols, M. L.; Plessers, D.; Goethem, C. V.; Seo, J. W.; Hwang, S. J.; Sels, B. F.; Dusselier, M. Synthesis-Structure-Activity Relations in Fe-CHA for C-H Activation: Control of Al Distribution by Interzeolite Conversion. *Chemistry of Materials* **2020**, *32* (1), 273–285. https://doi.org/10.1021/ACS.CHEMMATER.9B03738.
(14) Devos, J.; A. Shah, M.; Dusselier, M. On the Key Role of Aluminium and Other Heteroatoms during Interzeolite Conversion Synthesis. *RSC Advances* **2021**, *11* (42), 26188–26210. https://doi.org/10.1039/D1RA02887A.
(15) Eliášová, P.; Opanasenko, M.; S. Wheatley, P.; Shamzhy, M.; Mazur, M.; Nachtigall, P.; J. Roth, W.; E. Morris, R.; Čejka, J. The ADOR Mechanism for the Synthesis of New Zeolites. *Chemical Society Reviews* **2015**, *44* (20), 7177–7206. https://doi.org/10.1039/C5CS00045A.
(16) Morris, S. A.; Bignami, G. P. M.; Tian, Y.; Navarro, M.; Firth, D. S.; ÄŒejka, J.; Wheatley, P. S.; Dawson, D. M.; Slawinski, W. A.; Wragg, D. S.; Morris, R. E.; Ashbrook, S. E. In Situ Solid-State NMR and XRD Studies of the ADOR Process and the Unusual Structure of Zeolite IPC-6. *Nature Chemistry* **2017**, *9* (10), 1012–1018. https://doi.org/10.1038/nchem.2761.

Appendix A

Limitations to current NMR methods for analyzing differences in aluminum distributions in zeolites as observed in ZSM-5

This chapter is adapted from work performed in collaboration with Sopuruchukwu Ezenwa and Prof. Rajamani Gounder at Purdue University and Professor David Hibbitts at the University of Florida, which has been submitted to *Science*. My role in this project was to perform solid-state NMR analyses on zeolite samples provided from the Gounder group to assess differences in the aluminum distributions between zeolites made through different syntheses. During the project, we made several observations on factors limiting the resolution of the NMR spectra we were analyzing that did not make it into the final paper. These observations are not of the sort that would be worth writing a publication about; however, they may be educational and demonstrative for future graduate students looking to do NMR of zeolites, so I'm including them here as an appendix.

Abstract

Aluminum heteroatoms in aluminosilicate zeolite frameworks determine the locations of exchangeable actions in the zeolite pores that act as active sites for a variety of reaction chemistries. Controlling the distributions of aluminum heteroatoms between different tetrahedral sites is desirable to control the catalytic properties of the material. However, characterizing these distributions is challenging. Here, we use solid-state nuclear magnetic resonance spectroscopy to characterize the framework aluminum species present in MFI zeolites prepared with different structure-directing agents. Small differences in solid-state 1D direct-excitation ^{27}Al MAS NMR spectra are observed. In addition, material differences that

result in observed differences in NMR signal resolution in zeolites are discussed. These results may inform future studies of aluminum tetrahedral site distributions in zeolites.

Introduction

Zeolites, a crystalline, microporous class of aluminosilicates, are used industrially for a wide range of reaction chemistries.[1–3] The diverse reaction properties of zeolites are in part due to exchangeable cations in the pores which charge balance framework aluminum heteroatoms. These cations act as the catalytic sites in zeolites.[4] H^+ cations exchanged into the zeolite pores act as strong Bronsted acid sites and are active for a wide range of hydrocarbon conversion reactions. For example, the medium pore zeolite MFI is used for toluene alkylation to various xylenes.[5,6] The distribution of para-, meta-, and ortho-xylenes that are produced is determined in part by the voids in which the active catalytic sites sit, as steric hindrances will determine which isomers form favorably.[7] The zeolite MFI has 12 unique tetrahedral sites, so in theory if the distributions of aluminum heteroatoms could be controlled during zeolite synthesis, it might be possible to produce toluene alkylation catalysts with differing isomer selectivity.[8]

Detecting differences in aluminum tetrahedral site distributions in complex zeolite topologies like MFI is not straightforward. Scattering methods and electron microscopy have challenges distinguishing between aluminum and silicon atoms due to their similar atomic mass, though some progress has been made recently in special cases.[9,10] In theory, solid-state nuclear magnetic resonance (NMR) is well-suited to detect differences in these distributions, as the technique is nucleus-specific and sensitive to differences in local bonding environments.[11] Indeed, solid-state ^{29}Si NMR has been used in the past to resolve tetrahedral site chemical shifts in MFI.[12] However, inclusion of aluminum heteroatoms in a zeolite

framework results in distortions in lattice parameters to accommodate the heteroatoms, which manifest as anisotropic broadening of framework ^{29}Si and ^{27}Al NMR signals. In addition, ^{27}Al is a quadrupolar nucleus, resulting in a non-Gaussian lineshape that can be complicated to interpret.[13]

Here, we show NMR analyses of a series of synthesized MFI materials made with different structure-directing agent (SDA) molecules hypothesized to result in different framework tetrahedral-site aluminum distributions. We comment on small differences in the distributions of ^{27}Al NMR signal observed for different MFI materials. In addition, observed factors affecting ^{27}Al NMR signal resolution are discussed, and the efficacy of 2D ^{27}Al–^{29}Si NMR correlation analyses in differentiating between these different tetrahedral site distributions is also commented on.

Results and discussion

In order to determine if differences in aluminum tetrahedral site distributions between different syntheses of MFI zeolites could be detected by ^{27}Al NMR, a series of solid-state 1D direct-excitation ^{27}Al MAS NMR spectra were collected for a series of MFI zeolites, as shown in Figure 1. Four different organic structure-directing agent mixtures were used. Samples labeled ‘TPA’ were synthesized with tetrapropylammonium as an OSDA. Samples labeled ‘EDA’ were synthesized with a mixture of tetrapropylammonium and ethylenediamine. Samples labeled ‘DABCO’ were synthesized with a mixture of 1,4-diazabicycle[2,2,2]octane and methylamine. Samples labeled ‘TPA-C666’ were synthesized with an OSDA with the formula of C_6H_{13}-$N^+(CH_3)_2C_6H_{12}$-$N^+(CH_3)_2C_6H_{13}$. Samples labeled ‘C’ are commercial. Table S1 and S2 summarize the SDAs and heteroatoms used in each synthesis along with final compositions. Full details of the synthesis will be available in the published work. The solid-

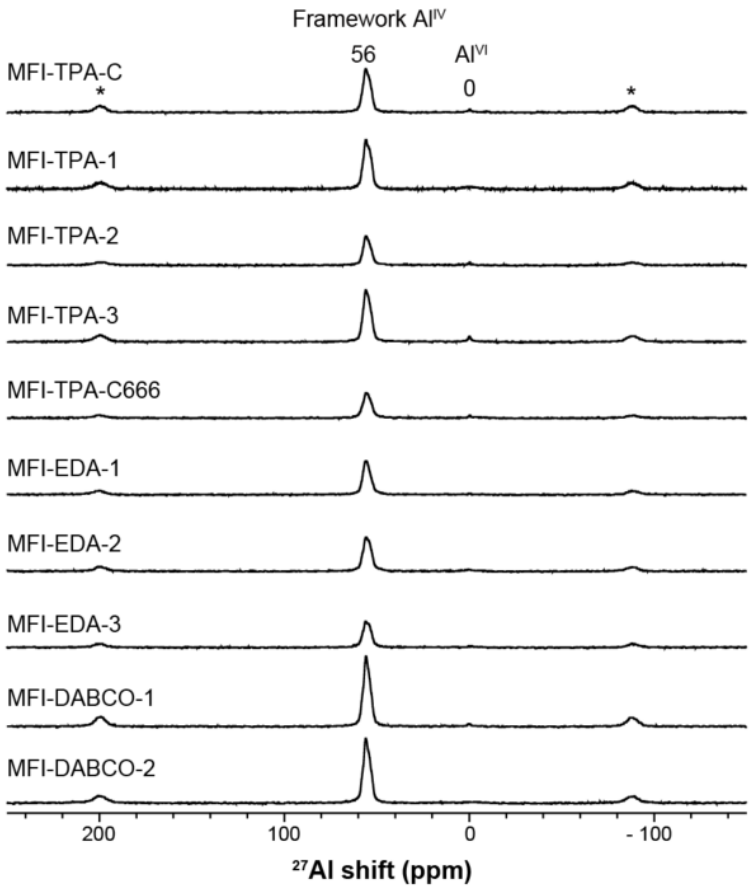

Figure 1. Solid-state 1D direct-excitation ^{27}Al MAS NMR of series of MFI zeolites synthesized with different structure directing agents. Spinning sidebands of the $^{27}Al^{IV}$ signal at 56 ppm are denoted by asterisks (*). All samples were measured in the H^+-form and were fully hydrated. Spectra were acquired at 18.8 T and 30 kHz MAS at room temperature.

state 1D direct-excitation ^{27}Al NMR spectra shown in Figure 1 all exhibit two regions of NMR signal. ^{27}Al NMR signal intensity centered at 56 ppm is assigned to framework Al^{IV}, while intensity centered at 0 ppm is assigned to Al^{VI}, created either from dealumination during calcination or resulting from hydration effects on framework aluminum. In all materials, the vast majority of the ^{27}Al NMR signal observed is from framework $^{27}Al^{IV}$. Slight variations in intensity and lineshape are evident in this region.

To investigate the differences of ^{27}Al NMR signal lineshape, the Al^{IV} signal region is shown for overlaid MFI aluminosilicate zeolites synthesized with the four different discussed

OSDA mixtures. These zoomed in spectra reveal that the $^{27}Al^{IV}$ signal intensity is made up of several partially resolved NMR signals at 53, 54, 56, and 58 ppm. These signals are attributed to aluminum in different tetrahedral sites. However, due to the large number of tetrahedral sites in the MFI crystal structure, these signals cannot be confidently assigned. Examining the differences in the four overlaid spectra, there are minor differences in some of the features, particularly the shoulder at 54 ppm, suggesting that the different OSDA mixtures may bias the aluminum heteroatom tetrahedral site distributions.

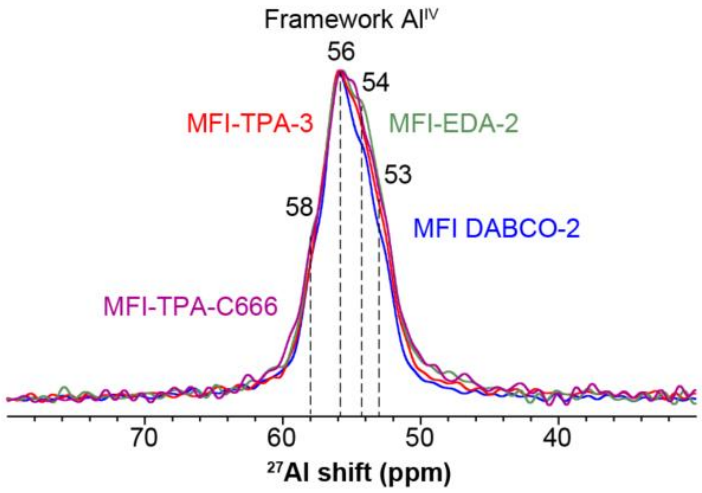

Figure 2. Solid-state 1D direct-excitation ^{27}Al MAS NMR spectra of hydrated MFI zeolites focused on the Al^{IV} region comparing the lineshapes for MFI-TPA-3 (red), MFI-EDA-2 (green), MFI-DABCO-2 (blue), and MFI-TPA-C666 (purple). All spectra were acquired at 18.8 T and 30 kHz MAS at room temperature.

The majority of MFI zeolites measured in this study had a bulk Si/Al of 50–60. However, to obtain an understanding on heteroatom content might affect ^{27}Al NMR signal resolution, a commercial MFI sample with a Si/Al = 134, labeled MFI-C2. The ^{27}Al NMR spectrum of this materials is compared to the other measured commercial MFI (MFI-C, Si/Al = 43) in Figure 3. The solid-state 1D direct-excitation ^{27}Al NMR spectrum of MFI-C2 shows four relatively well-resolved ^{27}Al NMR signals at 58.2, 56.2, 54.4, and 52.7 ppm, similar to the identified signals in Figure 2. The solid-state 1D direct-excitation ^{27}Al NMR spectrum of

MFI-C shows a similar distribution of Al^{IV} signals. However, the four regions of $^{27}Al^{IV}$ intensity are much more poorly resolved. There are likely two reasons for this. For one, substitution of aluminum into the MFI framework results in distorted tetrahedra, as aluminum substitution results in localized negative charges on the framework which must be charge-balanced by cations. These distortions result in a broader distribution of bond angles for aluminum or silicon tetrahedra in the same chemical environment, which manifests itself as anisotropic broadening of the $^{27}Al^{IV}$ NMR signals. In addition, higher concentrations of aluminum heteroatoms may result in stronger dipole-dipole couplings between ^{27}Al nuclei, which would result in broadening of observed signals.

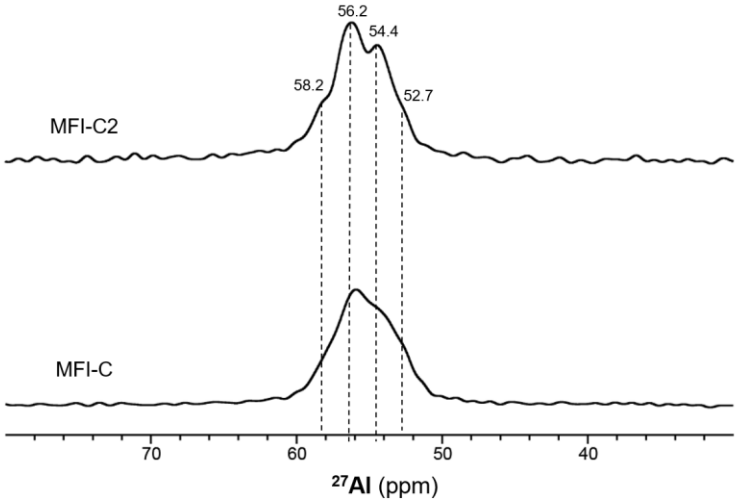

Figure 3. Solid-state 1D direct-excitation ^{27}Al MAS NMR spectra of two commercial MFI materials with different bulk Si/Al ratios. Both samples were hydrated prior to measurement. Spectra were acquired at 18.8 T and 30 kHz MAS at room temperature.

While the majority of MFI materials measured had similar Si/Al ratios, some of the MFI also contained boron heteroatoms in addition to aluminum heteroatoms. Figure 4A shows solid-state 1D direct-excitation ^{27}Al MAS NMR spectra of two MFI synthesized with TPA. MFI-TPA-1 has only aluminum heteroatoms, while MFI-TPA-2 has both aluminum and boron heteroatoms. In the solid-state 1D direct-excitation ^{27}Al MAS NMR spectrum of MFI-TPA-1,

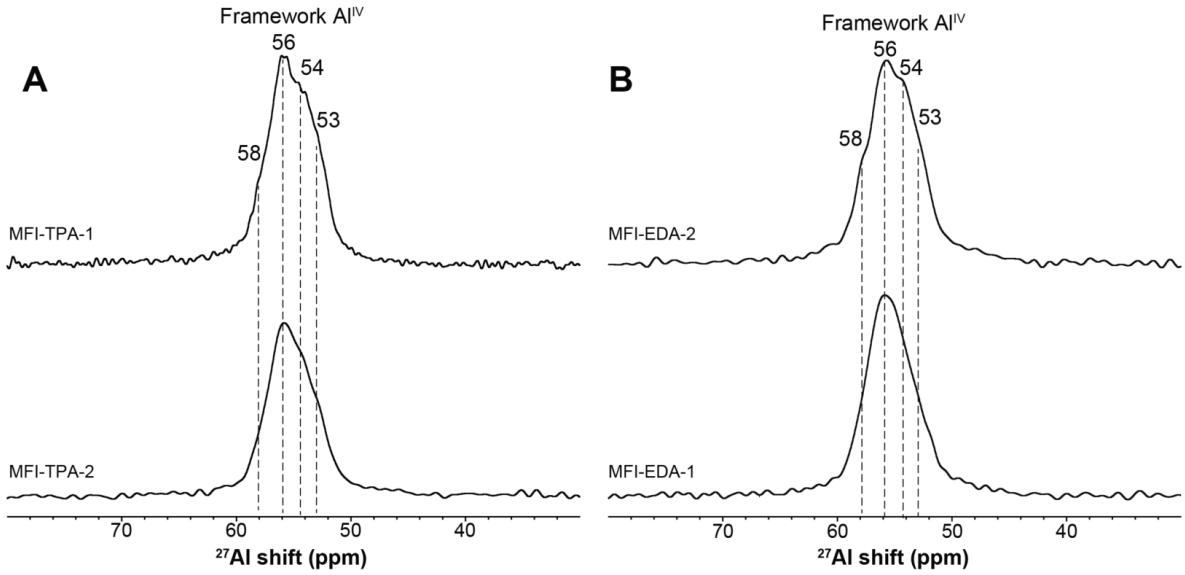

Figure 4. Solid-state 1D direct-excitation ^{27}Al MAS NMR spectra of (A) two MFI materials synthesized with TPA as a structure-directing agent and (B) two MFI materials synthesized with EDA as a structure-directing agent. The materials in the top row have only aluminum as heteroatoms and the materials in the bottom row have both aluminum and boron as heteroatoms. All MFI materials were measured hydrated. Spectra were acquired at 18.8 T and 30 kHz MAS at room temperature.

multiple regions of $^{27}Al^{IV}$ NMR signal can be partially resolved at 53, 54, 56, and 58 ppm. In contrast, this partial resolution is lost in MFI-TPA-2. Figure 4B shows a similar comparison for two MFI samples synthesized with EDA. MFI-EDA-2 has only aluminum heteroatoms, while MFI-EDA-1 has both aluminum and boron heteroatoms. The solid-state 1D direct-excitation ^{27}Al MAS NMR spectrum of MFI-EDA-2 shows four partially resolved $^{27}Al^{IV}$ signals at 53, 54, 56, and 58 ppm. In contrast, much of this resolution is lost in the analogous spectrum of MFI-EDA-1. These spectra reveal that inclusion of boron heteroatoms negatively affects the resolution of ^{27}Al NMR signals from framework moieties. Similar to a change in aluminum heteroatom content, this is likely due to increased variation of tetrahedral bond angles to accommodate the heteroatoms into the four-coordinate MFI framework.

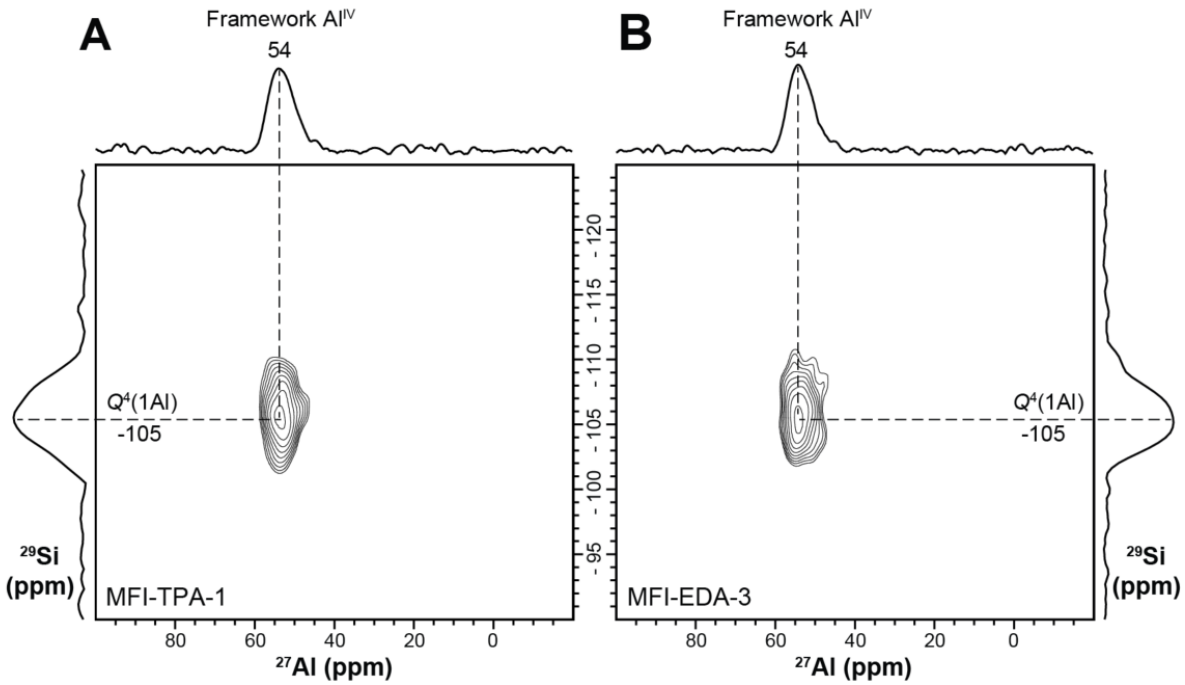

Figure 5. Solid-state 2D ^{27}Al–^{29}Si *J*-HMQC MAS NMR spectra of (A) MFI-TPA-1 and (B) MFI-EDA-3. Both materials were measured hydrated. Projected ^{27}Al intensity is shown at the top of each spectrum and projected ^{29}Si intensity is shown on the vertical axis. The spectra were acquired at 9.4 T, 100 K, and 8 kHz MAS.

The connectivity of framework aluminum within the zeolite framework can be further understood through solid-state 2D ^{27}Al–^{29}Si *J*-mediated MAS NMR correlation spectra. Each spectrum represents a 2D frequency map of correlated signals that arise only from ^{27}Al and ^{29}Si nuclei that are *J*-coupled through ^{27}Al–O–^{29}Si covalent bonds. Such spectra thus provide information on the locations and distributions of framework Al atoms based on differences in their local bonding environments with *J*-coupled ^{29}Si moieties. Representative solid-state 2D ^{27}Al–^{29}Si *J*-mediated correlation NMR spectra of MFI-TPA-1 and MFI-EDA-3 are shown in Figure 5A,B. Both spectra show a region of correlated intensity between a signal at 54 ppm in the ^{27}Al dimension, corresponding to four-coordinate framework ^{27}Al^{IV} species, and a signal centered at –105 ppm (ranging from –102 ppm to –111 ppm) in the ^{29}Si dimension, assigned to a distribution of Q^4(1Al) ^{29}Si chemical framework environments. The relatively broad

distribution of ^{29}Si intensity associated with these Q^4(1Al) species results from a distribution of nearby Al T-site occupancies that produce local differences in Q^4(1Al) bonding environments. Due to the large number of T-sites in MFI, subtly different 2D signals from *J*-coupled ^{27}Al–O–^{29}Si moieties are not resolved between the two MFI samples, further underscoring the challenges of experimentally detecting differences in aluminum T-site distributions.

Conclusions

Solid-state NMR was employed to attempt to determine differences in distributions of aluminum heteroatoms between tetrahedral sites in MFI after syntheses with different structure-directing agents. While small differences in distributions of ^{27}Al NMR signal attributed to framework Al^{IV} were observed for different samples, the resolution of NMR signals was not sufficient to confidently assign signal to different tetrahedral sites. It was observed that differences in heteroatom content, whether aluminum content or boron content in an aluminoborosilicate, result in differences in resolution of framework Al^{IV} ^{27}Al NMR signals. 2D ^{27}Al–^{29}Si *J*-HMQC spectra were acquired, but also did not have the resolution necessary to distinguish between different aluminum tetrahedral sites. Given the partially resolved signals observed in these measurements, higher field measurements could potentially provide improved resolution of the ^{27}Al^{IV} signal region.

Supporting Information

Materials and methods

Samples were obtained in the H^+-form from the Gounder group at Purdue University. Synthesis details can be found in the published manuscript on this project.

Solid-state one-dimensional (1D) direct-excitation ^{27}Al NMR spectra were acquired on fully hydrated zeolite samples using a Bruker Avance NMR spectrometer at a field of 18.8 T using 2.5 mm zirconia rotors and acquired under magic-angle-spinning (MAS) conditions of 30 kHz at room temperature. Prior to the ^{27}Al MAS NMR measurements, samples were stored in a sealed container containing a saturated solution of potassium chloride for at least 24 h (~85% relative humidity) to ensure consistent hydration. An 83.3 kHz 15° pulse was used to excite the central transition of the ^{27}Al nuclei. A 0.2 s recycle delay was used between pulses, which was found to be sufficient for the ^{27}Al nuclei to fully relax between scans. 16384 scans were acquired for each spectrum, except for the spectrum of MFI-C2, for which 65536 scans were acquired. The ^{27}Al MAS NMR spectra were referenced to an aqueous solution of 0.5 M $Al(NO_3)_3$ at 0 ppm.

Solid-state 2D *J*-mediated ^{27}Al–^{29}Si *J*-HMQC NMR spectra were acquired at 9.4 T and 100 K on a 400 MHz Bruker Ascend NMR spectrometer equipped with a triple-resonance NMR probehead using 3.2 mm zirconia rotors spinning at a MAS frequency of 8 kHz [14]. Samples were hydrated as described above prior to measurement. For each 2D spectrum, the indirect dimension was acquired with 32 increments of 2048 scans with a t_1 increment of 250 μs and a recycle delay of 1 s between scans. 25 kHz radiofrequency pulses were applied to ^{29}Si nuclei, and 16.7 kHz radiofrequency pulses were applied to ^{27}Al nuclei. A 1-ms double-frequency-sweep shaped pulse was applied to ^{27}Al nuclei before the initial 90° pulse of the *J*-

HMQC sequence. This pulse was swept between 100 kHz and 1 MHz relative to the carrier frequency. ^{29}Si chemical shifts were indirectly referenced to tetramethylsilane at 0 ppm using tetrakis(trimethylsilyl)silane as a secondary standard at –9.84 ppm. ^{27}Al NMR chemical shifts were referenced to an aqueous solution of 0.5 M $Al(NO_3)_3$ at 0 ppm. All references were measured at room temperature.

Additional data

Tables S1 and S2 summarize the synthesis parameters relevant for the different MFI syntheses and also the bulk properties of all characterized materials.

Table S1. Summary of organic and inorganic SDA content of as-synthesized MFI zeolites discussed here

		SDA content per unit cell[b] / mol (unit cell)$^{-1}$				
Sample	C/N[a]	TPA	EDA	DABCO	MA	Na^+
MFI-TPA-1	n.m.	3.8	-	-	-	-
MFI-TPA-2	11.0	4.0	-	-	-	-
MFI-TPA-3	n.m.	3.6	-	-	-	2.4
MFI-TPA-C666	n.m.	-	-	-	-	-
MFI-EDA-1	2.3	1.5	5.0	-	-	-
MFI-EDA-2	4.2	2.0	2.4	-	-	-
MFI-EDA-3	3.9	1.7	2.4	-	-	-
MFI-DABCO-1	2.7	-	-	3.7	1.1	1.1
MFI-DABCO-2	2.8	-	-	4.5	0.9	0.2

[a]Determined by CHN elemental analysis. Uncertainties are ±10%.
[b]Calculated from total organic weight loss using TGA (for TPA^+ only synthesis) and C/N using CHN analysis (for EDA/TPA^+ and DABCO/MeN synthesis). Uncertainties are ±10%.

Table S2. Summary of characterization of MFI zeolites discussed here

Sample	Si/Al_{tot}	Si/B_{tot}[a]	Al per u.c.[b]	B per u.c.[b]	H^+/Al_{tot}[c]	Al^{IV}/Total NMR visible Al [d]
MFI-TPA-C	43	-	2.2	-	0.85	0.98
MFI-TPA-C2	134	-	0.7	-	0.92	
MFI-TPA-1	50	-	1.9	-	1.01	0.96
MFI-TPA-2	59	48	1.6	2.0	0.84	0.97
MFI-TPA-3	55	-	1.7	-	0.97	0.96
MFI-TPA-C666	47	-	1.9	-	0.81	0.97
MFI-EDA-1	53	26	1.7	3.5	1.02	0.99
MFI-EDA-2	58	-	1.6	-	0.92	0.97
MFI-EDA-3	49	-	2.0	-	0.70	0.97
MFI-DABCO-1	44	-	2.1	-	0.95	0.98
MFI-DABCO-2	44	-	2.1	-	0.87	0.98

[a]Determined from ICP-OES (Si, Al, B) or AAS (Al). Uncertainties are ±10%.
[b]Calculated from elemental analysis and unit cell formula.
[c]Determined from liquid-phase NH_4^+ ion exchange followed by NH_3 TPD.
[d]Determined using ^{27}Al SS MAS NMR. Integrated Al^{IV} intensity includes the ^{27}Al NMR signal at 56 ppm and spinning sidebands shown in Figure S30. Additional spinning sidebands associated with the $^{27}Al^{IV}$ signal likely exist outside of the measured NMR spectral frequencies but are expected to have minor effects on the reported fractions. Uncertainties are ±0.05.

References

(1) Vogt, E. T. C.; Weckhuysen, B. M. Fluid Catalytic Cracking: Recent Developments on the Grand Old Lady of Zeolite Catalysis. *Chemical Society Reviews* **2015**, *44* (20), 7342–7370. https://doi.org/10.1039/c5cs00376h.

(2) Lei, H.; Rizzotto, V.; Guo, A.; Ye, D.; Simon, U.; Chen, P. Recent Understanding of Low-Temperature Copper Dynamics in Cu-Chabazite NH_3-SCR Catalysts. *Catalysts* **2021**, *11* (1), 1–20. https://doi.org/10.3390/CATAL11010052.

(3) Al-Khattaf, S.; Rabiu, S.; Tukur, N. M.; Alnaizy, R. Kinetics of Toluene Methylation over USY-Zeolite Catalyst in a Riser Simulator. *Chemical Engineering Journal* **2008**, *139* (3), 622–630. https://doi.org/10.1016/j.cej.2007.09.019.

(4) Breck, D. W. *Zeolite Molecular Sieves: Structure, Chemistry, and Use*; Wiley: New York, 1973.

(5) Smirniotis, P. G.; Ruckenstein, E. Alkylation of Benzene or Toluene with MeOH or C2H4 over ZSM-5 or Beta. Zeolite: Effect of the Zeolite Pore Openings and of the Hydrocarbons Involved on the Mechanism of Alkylation. *Ind. Eng. Chem. Res.* **1995**, *34* (5), 1517–1528. https://doi.org/10.1021/ie00044a002.

(6) Wu, H.; Liu, M.; Tan, W.; Hou, K.; Zhang, A.; Wang, Y.; Guo, X. Effect of ZSM-5 Zeolite Morphology on the Catalytic Performance of the Alkylation of Toluene with Methanol. *Journal of Energy Chemistry* **2014**, *23* (4), 491–497. https://doi.org/10.1016/S2095-4956(14)60176-5.

(7) Fraenkel, D.; Levy, M. Comparative Study of Shape-Selective Toluene Alkylations over HZSM-5. *Journal of Catalysis* **1989**, *118* (1), 10–21. https://doi.org/10.1016/0021-9517(89)90296-0.

(8) Nimlos, C. T.; Hoffman, A. J.; Hur, Y. G.; Lee, J.; Di Iorio, J. R.; Hibbitts, D. D.; Gounder, R. Experimental and Theoretical Assessments of Aluminum Proximity in MFI Zeolites and Its Alteration by Organic and Inorganic Structure-Directing Agents. *Chemistry of Materials* **2020**, *32* (21), 9277–9298. https://doi.org/10.1021/acs.chemmater.0c03154.

(9) Pinar, A. B.; Rzepka, P.; Knorpp, A. J.; McCusker, L. B.; Baerlocher, C.; Huthwelker, T.; Bokhoven, J. A. van. Pinpointing and Quantifying the Aluminum Distribution in Zeolite Catalysts Using Anomalous Scattering at the Al Absorption Edge. *Journal of the American Chemical Society* **2021**, *143* (43), 17926–17930. https://doi.org/10.1021/JACS.1C06925.

(10) Shen, B.; Wang, H.; Xiong, H.; Chen, X.; Bosch, E. G. T.; Lazić, I.; Qian, W.; Wei, F.; Xiong, H. Atomic Imaging of Zeolite-Confined Single Molecules by Electron Microscopy. *Nature* **2022**, *607*, 703–707. https://doi.org/10.1038/s41586-022-04876-x.

(11) Levitt, M. H. *Spin Dynamics: Basics of Nuclear Magnetic Resonance*, 2. ed., repr.; Wiley: Chichester, 2011.

(12) Fyfe, C. A.; Strobl, Harald.; Kokotailo, G. T.; Kennedy, G. J.; Barlow, G. E. Ultrahigh-Resolution Silicon-29 Solid-State MAS NMR Investigation of Sorbate and

Temperature-Induced Changes in the Lattice Structure of Zeolite ZSM-5. *J. Am. Chem. Soc.* **1988**, *110* (11), 3373–3380. https://doi.org/10.1021/ja00219a005.

(13) Chen, K.; Gan, Z.; Horstmeier, S.; White, J. L. Distribution of Aluminum Species in Zeolite Catalysts: ^{27}Al NMR of Framework, Partially-Coordinated Framework, and Non-Framework Moieties. *Journal of the American Chemical Society* **2021**, *143* (17), 6669–6680. https://doi.org/10.1021/JACS.1C02361.

(14) Massiot, D.; Fayon, F.; Alonso, B.; Trebosc, J.; Amoureux, J.-P. Chemical Bonding Differences Evidenced from J-Coupling in Solid State NMR Experiments Involving Quadrupolar Nuclei. *Journal of Magnetic Resonance* **2003**, *164* (1), 160–164. https://doi.org/10.1016/S1090-7807(03)00134-4.

Appendix B

Simple microreactor design for use basic kinetic studies and *ex situ* characterization of adsorbates

This appendix covers the design of a home-built reactor that was built during my Ph.D. in order to perform basic reaction studies like those discussed in Chapter 4. The reactor was built based on designs from the Christopher Lab at UCSB with the help of Alan Stoev, an undergraduate student in the Department of Chemical Engineering during my time at UCSB. The overall design of the reactor, and the purpose for certain design choices, is discussed. In addition, operation of the on-line mass chromatograph is covered. Potential future improvements to the reactor system are also covered.

Introduction

In order to provide greater impact to structural studies of zeolites, it is desirable to measure catalytic properties of the characterized zeolites. While this can be done through collaborations, as in Chapter 3, a desire to measure adsorbates on spent catalysts with very careful handling conditions led to a decision to build a reactor for gas-phase flow reactions in the Chmelka lab. This reactor was used for the measurements discussed in Chapter 4. The test reaction discussed in Chapter 4, hexane cracking, is relatively simple in terms of experimental setup, since there is only one reactant and it is liquid-phase at room temperature. Thus, the reactor design is fairly straightforward. However, in a desire to ensure this piece of equipment which required significant time and financial investment to build during my Ph.D. continues to get used after I leave, I am providing a detailed description here for future graduate students to review, if necessary.

Design of reactor system

The simple reactor system built during my Ph.D. is suitable for ambient pressure gas-phase flow reaction chemistries. The reactor itself is a one-foot long ¼'' stainless steel tube, in which catalyst powder can be suspended between plugs of quartz wool in the center of the reactor tube. Each end of the reactor tube is fitted with a ball valve such that the reactor tube can easily be sealed after reaction if desired for transit of the spent catalyst to an inert atmosphere. ¼'' quartz tubes can easily be swapped for the stainless-steel tube if gas reactivity with stainless steel is a concern. This stainless-steel tube is placed inside of a homebuilt furnace to heat the catalyst bed to the desired reaction temperature. The furnace consists of a block of stainless steel split into two pieces with a hole bored through the center to accommodate the reactor tube. The two sides of the stainless-steel block can be precisely connected thanks to two bore holes for connecting pins. The block also has holes bored into it for insertion heater plugs, and a hole for a thermocouple. This stainless-steel block functions as a large thermal mass that maintains an even temperature once the reactor has been heated to the desired temperature. The stainless-steel block is encased in an enclosure of one-inch-thick calcium silicate as an insulator which is wrapped in aluminum foil to minimize radiative and convective losses. The temperature of the furnace is regulated by a commercial temperature controller which is attached to a insertion heating plug in a hole in the stainless steel block along with a K-type thermocouple placed in contact with the exterior of the stainless-steel reactor tube near the plug of catalyst.

Gas lines in and out of the reactor tube consist of 1/8'' stainless-steel tubing. Two mass flow controllers provide input flow for two different inlet lines, which mix prior to the reactor tube. One of the inlet lines flows through a bubbler to provide saturated vapor flows of

reactants that are liquid at room temperature. The purpose of the second inlet line is to control the dilution of the saturated vapor flow and gain better control of inlet mass flow rates by decoupling inlet reactant flow from total flow. Three-way valves allow for bypass of the bubbler if gas reactants or used or if a pretreatment is desired with no reactant flow at the same flowrate as the final reactant flowrate. Three-way valves also enable bypass of the reactor if necessary, or to characterize the reactant feed stream without flow through the reactor. Downstream of the reactor, the product stream flows to an online gas chromatograph equipped with an autosampler to enable regular sampling of the product distribution. The full design of this system with details on conditions used during the hexane reaction studies discussed in Chapter 4 is shown in Figure 1.

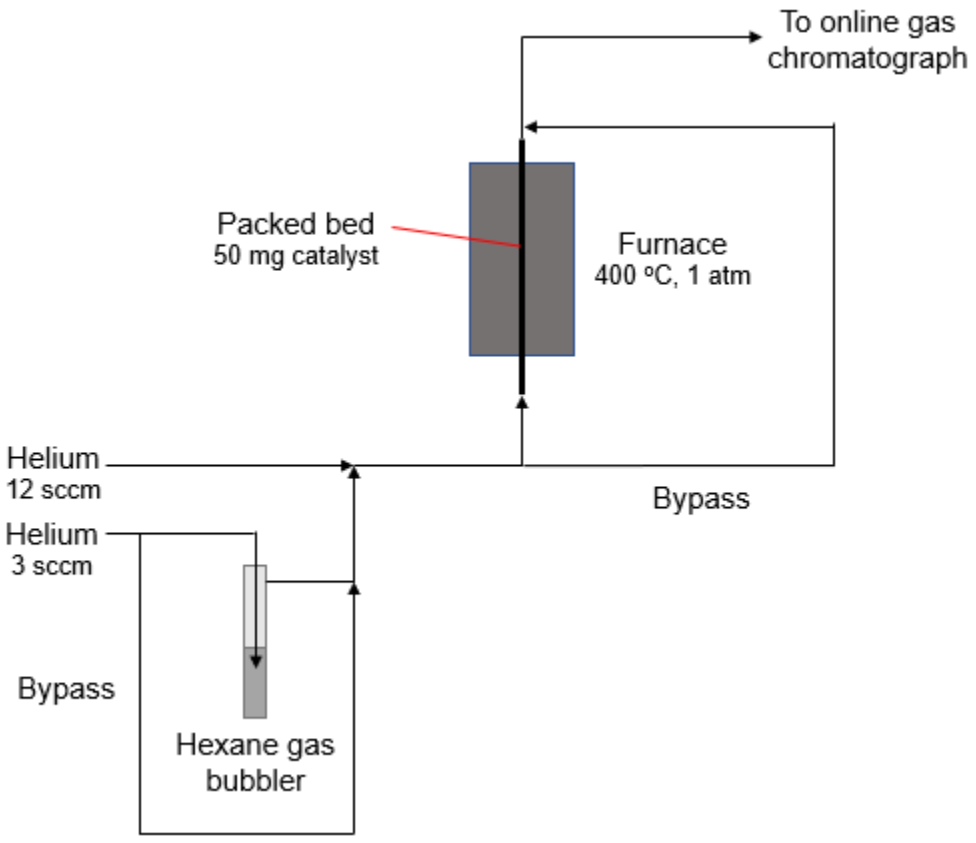

Figure 1. Reactor design as configured for the hexane cracking reaction studies in Chapter 4.

Operation of the reactor

The reactor setup is fairly straightforward; however, there are a few aspects that are important for consistent operation. Prior to insertion into the reactor tube, the catalyst powder should be sieved through two sieves of different sizes. The middle fraction should be used. This ensures that mas transport effects related to particle size and bed pressure drop will be approximately the same between different catalysts and runs. This sieved catalyst should be suspended between two plugs of quartz wool approximately halfway along the reactor tube, with efforts made to not compress the catalyst and change the packing. The tube should then be inserted into the furnace, with care taken to make sure the plug of catalyst is centered in the furnace block.

The furnace can maintain a stable temperature of 400 ºC for long reaction studies (>24 h). Temperatures of 500 ºC can be achieved but often cause issues with parts of the heating system if this temperature is maintained for too long. A relatively slow heating ramp should be used to avoid damaging the catalyst—typically less than 2 ºC/min for zeolite catalysts. This heating ramp should be performed under flow conditions to sweep away any adsorbed water that desorbs during the temperature ramp.

As previously mentioned, if using a bubbler to provide a saturated vapor stream from a liquid-phase reactant, dilution can be used to control the partial pressure of the reactant. There are two reasons to do this. For one, this ensures that condensation of reactants on the walls of tubing will not cause mass transport issues in the interpretation of the data. In addition, if water is evolved as a product of the reaction, it is important to ensure that the water vapor partial pressure is not sufficient to cause condensation downstream of the reactor. Condensation of

water is a major issue, as many organic compounds are soluble in water and thus the gas phase product distributions detected will be inaccurate.

The gas chromatograph

An online gas chromatograph (GC) equipped with a flame ionization detector (FID) is equipped to the system to characterize product distributions. A GC works by separating a mixture of gases into components, which enter a detector at different time points, producing distinct time-resolved signals. This separation is performed by flowing the gas that enters the GC through a long capillary tube packed with a material the gas mixture must diffuse through. Based on a combination of size and affinity for the adsorbent in the capillary column, products diffuse at different rates.[1] By careful selection of temperature at which the separation occurs, a program can be created that successfully separates all products with enough time resolution such that each signal can be individually quantified. For different product mixtures, it is likely necessary to change the packing material of the capillary column. Different capillary columns can be bought online and readily swapped out of the GC.

After exiting the capillary column, product species flow into a detector, which can be used to quantify the amounts of each product. The GC hooked up to the system is equipped with an FID. In an FID, gases are burned in a hydrogen flame. Ions formed during the combustion are attracted to a negatively-charged detector plate. The contact of ionized gases with the collector plate results in a current which is proportional to the number of ions contacting the plate, resulting in a time-resolved electrical signal proportional to the amount of ions.[1] As an FID works by combustion to produce ions in a hydrogen flame, it does not detect non-combustible gases, nor does it detect hydrogen gas.

The GC and FID must be calibrated to an expected product mixture. This serves two purposes. For one, it is important to run standards to properly identify when products will elute from the column using a given temperature program. In addition, it is good to verify the correct calibration of the FID to ensure measured amounts of gases are quantitative. To calibrate the GC, known quantities of gases anticipated to be in the product stream should be measured. For common gas mixtures (e.g. short chain linear alkanes, short chain linear alkenes) a reference gas mixture can typically be purchased and measured by serial dilution. For other gases, flows of varying concentration can be run in bypass of the reactor to the GC.

After calibration, operation of the GC to characterize product distributions is user friendly. The GC is equipped with an autosampler system. Product gas flows through a 1 mL sample loop. During normal operation, gas flows through the loop and vents into the fume hood. When a sample is taken, a valve shifts the gas flow such that a carrier gas pushes the products occupying the 1 mL sample loop into the capillary column, ensuring a consistent volume of sample is taken for each measurement. The computer program controlling the GC can be configured such that a sample will automatically be taken after a given amount of dead time between measurements. Time-resolved signals from the FID can readily be integrated and then assigned and translated into amounts of product based on calibrations.

Future improvements

The current reactor setup could be improved in several ways. For one, the current method of introducing liquid-phase reactants using a bubbler requires consideration of vapor pressure to control flowrate and relies on maintaining a relatively constant temperature in the lab to keep the flowrate constant. In addition, this makes it exceedingly difficult to perform reactions involving multiple liquid-phase reactants. This could be improved by purchasing a

pump system to introduce a controlled amount of liquid reactant into the gas stream at a constant rate. This would overcome temperature considerations, and liquid mixtures could also be used as long as they are introduced at a rate significantly below their vapor pressures.

In addition, the insertion heating plugs currently used in the reactor are somewhat unreliable. These heaters purchased from McMaster Carr seem to have had issues with degradation of quality insurance over the past few years. Some heaters will last for a very long time, others will die after one or two uses. These are not expensive, so replacement is not a big deal. However, it is likely that other sources for purchasing these exist and that heaters purchased from other sources may be more reliable.

Lastly, the setup of the GC could be improved. As mentioned previously, the GC is equipped with an FID, which is only sensitive to flammable gases. It is possible to have a GC setup such that an FID and a thermal conductivity detector (TCD) are run in series. The TCD is not as sensitive as the FID; however, it is sensitive to non-flammable gases. This combination would ensure that mass balances can always be closed. It is likely possible to ship the GC back to the supplier and get them to install an additional detector for a relatively low price. Installing only one detector and also the lack of controlled liquid injection were choices made during the building of the reactor system to keep costs down. If the reactor system will be used long-term, these additions are worth the costs.

References

(1) McNair, H. M.; Miller, J. M.; Snow, N. H. *Basic Gas Chromatography*, Third edition [2019 edition].; Wiley: Hoboken, NJ, USA, 2019.

Appendix C

Considerations for dehydrating zeolites and adsorbing species onto dry zeolites for *ex situ* analysis

Over the course of my Ph.D., I devoted a considerable amount of time and effort to successfully prepping zeolite samples for measurement by NMR and other characterization methods where exposure of the zeolite to oxygen and water vapor in the air after sample prep would render the measurement pointless. In the hopes that others will not need to recreate my efforts, I've collected a series of protocols here that I have found consistently result in moisture-free samples for spectroscopic analysis.

Dehydration of zeolites

Zeolites readily adsorb water from the atmosphere at incredibly low partial pressures.[1] This water forms a hydration shell around charge-balancing cations, modifying their local chemical environment. For example, adsorption of 1 H_2O molecule per Bronsted acid site in a H^+-zeolite is sufficient to significantly change the ^1H NMR spectrum of the zeolite.[2] As such, it is important to characterize spectroscopic features in zeolites related to cations and adsorbed species in the absence of water, unless trying to replicate reaction conditions where water would be present. This can be done by preparing zeolite samples for analysis in an inert atmosphere. However, there are opportunities for water adsorption both before transferring the dehydrated sample into the glovebox and during transfer of the prepared sample holder from the glove box to the instrument.

Zeolite dehydration preparation for spectroscopic analysis is typically done in a one-ended tube furnace with a sealable glass vessel attached to a vacuum line. The sample in the glass vessel is placed in the tube furnace with a thermocouple near the sample, and a vacuum

is pulled on the glassware. In our experience, a vacuum of 0.5 kPa is sufficient for dehydration. It is important to verify at this stage that the glassware will hold a vacuum (i.e. there are no leaks through seals in the glassware. The sample is then heated slowly, preferably less than 2 ^{o}C/min for zeolites to avoid framework damage during water desorption. A temperature of 450 ^{o}C is sufficient to drive off all adsorbed water species from the zeolite after a hold of ~2 h, though there is no harm in maintaining this temperature for longer and it is often convenient to run the full dehydration temperature program overnight. Caution should be taken to ensure that only quartz glassware is used for this sample treatment. Standard Pyrex glassware will warp under these temperature conditions and may even implode.

To ensure no re-adsorption of water through back diffusion, the dehydration glassware should be sealed at temperature, after which the tube furnace can be rapidly cooled. The sealed vessel can then be transferred to a glovebox, taking care to not repressurize the vessel during transit. Once in the glovebox, the glassware can be repressurized and the sample can be transferred to a separate vial for storage. It is generally a good idea to wrap the seal of the sample vial with Teflon tape as an extra barrier against moisture if other people are using the glovebox as well.

Dehydrated zeolite samples should be packed into sample tubes in the glovebox. For solid-state NMR, the rotor should be packed, and the cap should be placed on the rotor in the glovebox. The rotor should then be placed in a vial in the glovebox and sealed with Teflon tape. This vial can then be removed from the glovebox. Working quickly, the vial should be taken to the spectrometer and inserted into the probe. The MAS system should immediately be used to start spinning the rotor in inert N_2 gas. This process can be completed in a couple of minutes, but generally the sample should be okay for up to 10 min outside of the glovebox or

probe, assuming it is in the sealed vial. Once the rotor has been spun up, ^{1}H NMR can be performed to evaluate if the sample is dehydrated. Many published sources of ^{1}H NMR of zeolites exist online and can be used to assess if the sample is dehydrated.[2] It should be noted that occasionally the N_2 gas used in the Spectroscopy Facility at UCSB contains trace moisture, as this N_2 gas is generated from boiloff and may get contaminated. This will be evident by NMR, as ^{1}H NMR spectra taken at regular intervals will show a slow hydration process. While this is rare, it is best to wait a day and try measurements again if this occurs.

For measurements done in glass tubes that are exposed to the atmosphere during analysis, such as EPR, the provided cap for the sample tube will not be sufficient to prevent slow zeolite rehydration. Instead, after loading dehydrated zeolite into these tubes they can be sealed with an epoxy resin in the glove box. Many two component resins are available for purchase online that can be injected with a nozzle into the top of the EPR tube. The sealed EPR tube should be stored in the glove box for 24 h before measurement to ensure sufficient resin curing has occurred. We have left EPR tubes filled with Cu^{2+}-exchanged zeolite powder on the counter for months and obtained consistent EPR spectra with spectra obtained right after removal from the glovebox.

These dehydration protocols can be quite frustrating for new users, as the only way to verify dehydration is to attempt a measurement. However, with sufficient practice it is possible to consistently obtain dehydrated zeolites for analysis by these protocols.

Adsorption of gaseous species onto zeolites

Often it is desirable to spectroscopically characterize adsorbates on zeolites, either reactant molecules or probe molecule adsorbates. For species that are gas phase at room temperature, this is relatively straightforward. The zeolite sample should first be dehydrated as

described previously. After dehydration, the sample should be cooled to the desired adsorption temperature. It is generally a good idea at this point to use a liquid nitrogen cold finger trap on the vacuum line to prevent back diffusion of water vapor to the sample. A lecture bottle of the gas of interest can be hooked up to the vacuum system and plugs of adsorbate can be dosed to the system until the desired pressure is reached. The pressure can be monitored to ensure that equilibrium has been reached between the gas and adsorbed phases. After equilibrium has been reached, the excess adsorbate should be removed by vacuum, and the glassware should be vacuum cycled by inert. The sample can then be transferred into a glovebox and packed for measurement as described above.

Adsorption of liquid species onto zeolites

Species that are liquid at room temperature can be easily adsorbed in a similar system as long as the vapor pressure is relatively high. The glassware should be fitted with a rubber septum instead of the normal glass cap. We have found that the septum with vacuum grease creates a good seal. After dehydration and cooling as described above, liquid species can be injected to the glassware under vacuum as described above. It is generally a good idea to backfill the syringe with inert gas prior to filling it with liquid in an effort to reduce the amount of air that gets pulled into the glassware upon injection. Care should be taken to use a small enough amount of adsorbate that it will fully vaporize inside the glassware. If necessary, multiple injections can be used to fully saturate the zeolite sample. After injection, the glassware should be vacuum cycled several times to remove excess physisorbed species on the interior surface of the glassware. The sample can then be transferred to the glovebox and packed for measurement as described above.

Measurement of post-reaction spent catalysts

It is sometimes desirable to characterize distributions of adsorbed species on a zeolite catalyst after reaction, as shown in Chapter 4. The reactor discussed in Appendix B is set up so that the spent catalyst can easily be transferred to a glovebox for characterization prep without exposure to ambient air. After a certain time point in the reaction, the reactor can be sealed by turning two ball valves on either side of the reactor tube. The reactor can then be disassembled, and the sealed reactor tube can be transferred to the glovebox. The reactor tube can then be disassembled, and the spent catalyst can be stored in a sealed vial.

References

(1) Breck, D. W. *Zeolite Molecular Sieves: Structure, Chemistry, and Use*; Wiley: New York, 1973.

(2) Wang, M.; Jaegers, N. R.; Lee, M. S.; Wan, C.; Hu, J. Z.; Shi, H.; Mei, D.; Burton, S. D.; Camaioni, D. M.; Gutiérrez, O. Y.; Glezakou, V. A.; Rousseau, R.; Wang, Y.; Lercher, J. A. Genesis and Stability of Hydronium Ions in Zeolite Channels. *Journal of the American Chemical Society* **2019**, *141* (8), 3444–3455. https://doi.org/10.1021/jacs.8b07969.